

**THÈSE DE DOCTORAT DE L'ETABLISSEMENT
UNIVERSITÉ BOURGOGNE FRANCHE-COMTÉ**

PRÉPARÉE AU LABORATOIRE INTERDISCIPLINAIRE CARNOT DE BOURGOGNE

**École doctorale n° 553
Carnot Pasteur**

Doctorat de Physique

par

Adrian AGREDA

Electrical Control of the Nonlinear Properties of Plasmonic Nanostructures

These présentée et soutenue à Dijon le 09 mars 2020

Composition du jury :

Eric Finot	Professeur à l'Université de Bourgogne	Président
Bruno Palpant	Professeur à l'Université Paris-Saclay	Rapporteur
Céline Fiorini	Chercheur au CEA	Rapportrice
Anne-Laure Baudrion	Maître de Conférences Univ. Technologie de Troyes	Examinatrice
Arnaud Stolz	Maître de Conférences à Université d'Orléans	Examinateur
Alexandre Bouhelier	Directeur de recherche CNRS, Univ. Bourgogne	Directeur de Thèse

Title: Electrical Control of the Nonlinear Properties of Plasmonic Nanostructures

Keywords: Nonlinear plasmonics, Nano-optics, Nanowires, Nonlinear photoluminescence, Optical antennas, Nanophotonics

Abstract:

This work brings nano-electronics and nano-photonics technologies together to create an electron-plasmon device whose linear and nonlinear optical properties are electrically controlled. Here, we present the first demonstration of nonlinear photoluminescence modulation by electrical means in an uncluttered configuration. To this purpose, plasmonic nanoantennas are interfaced with electrical connections inducing localized regions of electron accumulation and depletion and therefore affecting the optical response. Additionally, a complete analysis of the nonlinear photoluminescence in plasmonic nanowires is carried out. The delocalization and transport of nonlinearities provided by such structures allow the remote activation of the signals. Different aspects including the underlying mechanisms behind the electrical modulation and the processes dictating the nonlinear photoluminescence generation are systematically explored.

Titre: Contrôle électrique Des Propriétés Non Linéaires De Nanostructures Plasmoniques

Mots-clés: Plasmonique, Nano-optique, Nanofils, Photoluminescence non linéaire, Antennes optiques, Nanophotonique

Résumé:

Ce travail rassemble les technologies de nanoélectronique et de nano-photonique pour créer un dispositif électro-plasmonique dont les propriétés optiques linéaires et non linéaires sont contrôlées électriquement. Ici, nous présentons la première démonstration de la modulation de photoluminescence non linéaire par des moyens électriques dans une configuration épurée. à cette fin, les nanoantennes plasmoniques sont interfacées avec des connexions électriques induisant des régions localisées d'accumulation et de déplétion d'électrons et affectant ainsi la réponse optique. De plus, une analyse complète de la photoluminescence non linéaire dans les nanofils plasmoniques est réalisée. La délocalisation et le transport des non-linéarités apportées par de telles structures permettent l'activation à distance des signaux. Différents aspects, dont les mécanismes sous-jacents à la modulation électrique et les processus dictant la génération de photoluminescence non linéaire, sont systématiquement explorés.

Acknowledgements

In the following, I would like to thank all the people whose direct or indirect help and support were crucial for the completion of my research during these more than three years.

In the first place, I wish to express my deepest gratitude to my supervisor and mentor Alexandre Bouhelier for giving me the great opportunity to work in his group, for his guidance, and support and for making our joint work a satisfying experience. I have really enjoyed working in an environment that provided me with autonomy but also where he was always available for discussion and assistance.

I would like to acknowledge Céline Fiorini and Bruno Palpant for kindly accepting being rapporteurs of my manuscript. Thanks to Anne-Laure Baudrion, Eric Finot and Arnaud Stolz for giving me the honor of having them as part of my thesis jury.

A special thank is dedicated to Sviatlana Viarbitskaya. She introduced me to the experimental setup and initiated me in the nanofabrication protocols. I also really appreciate her contributions and ideas. I wish to express my regards to Gerard Colas des Francs who provided very good support with theoretical calculations. I am thankful to Olivier Demichel, Romain Hernandez and Benoît Cluzel for giving helpful ideas. Thanks to Laurent Markey and Juan Arocas for the technical support and training in the nanofabrication facilities. A particular acknowledgement goes to Elly Lacroute for the administrative and paperwork support. I would also like to pay my special regards to G.V.P. Kumar for hosting me multiple times in India and giving me the opportunity to work at his lab in IISER Pune. Thanks also to Deepak Sharma for the help, experimental support and great ideas during my stays in India and during his times in Dijon.

I wish to also mention my friends and lab co-workers Mickäel Buret, Marie Gourier, Arindam Dasgupta, Reinaldo Chacón, Daniela Barrios, Xavier Laforgue, Vincent Dorier, Xiao Yu, Konstantin Malchow, Raminfar Al Rafrain, Andreea Crisbasan, Dimitrii Rusakov. I have to say they contributed to make these times great.

I have no enough words to thank my wife Laura for always being open to listen and to help me in the adversities I encountered while transiting this sinuous path. I thank her for her love and mainly for her patience.

And finally to my family who was always very supportive. To my parents for their unconditional support and trust. Thanks for raising me with freedom and encouraging me to always go for more and reach my goals.

Contents

General introduction	1
1 Nonlinear photoluminescence in optical antennas	3
1.1 Introduction	3
1.2 Optical antennas	4
1.2.1 The origin of optical antennas	4
1.2.2 Optical vs. classical antennas	5
1.2.3 Surface plasmon polaritons	6
1.2.4 Localized surface plasmons	6
1.2.5 A metal nanoparticle: the simplest optical antenna	7
1.2.6 Optical antennas design	8
1.2.7 Optical antennas applications	8
1.3 Optical properties of metals: the case of gold	9
1.4 Optical nonlinearities in plasmonic antennas	12
1.4.1 Luminescence from metals	13
1.4.1.1 A macroscopic perspective. Two-photon absorption and the $\chi^{(3)}$ susceptibility.	14
1.4.1.2 N-PL seen as a multi-photon absorption process	18
1.4.1.3 N-PL seen as a thermal radiation process	20
1.4.1.4 N-PL as an inelastic scattering process	22
1.4.1.5 N-PL: a multifaceted process	22
1.5 Conclusion	23
2 Electrical command of the linear and nonlinear responses of plasmonic antennas	25
2.1 Introduction	25
2.2 Active devices based on plasmonic metals	25
2.2.1 Electrically controlled plasmonic devices	26
2.3 Experimental methods	29
2.3.1 Fabrication of the electrically controlled plasmonic device	30
2.3.1.1 Optical gap antennas fabrication	30
2.3.1.2 Contacting the optical antennas	31
2.3.2 Nonlinear photoluminescence confocal microscopy	32

2.4	Controlling the Nonlinear Photoluminescence	33
2.4.1	Evolution of the N-PL yield with the electric field	36
2.4.2	Optical antenna as a nanocapacitor	38
2.4.3	Response time of the N-PL modulation	40
2.4.4	Excitation polarization. Another degree of control	43
2.5	Nonlinear photoluminescence modulation mechanisms	44
2.5.1	Possible effects on the hot carriers generation	44
2.5.2	Changes on the Electronic temperature and the N-PL emission	45
2.5.2.1	Spectral changes of the N-PL with the electric field	46
2.5.2.2	Delayed N-PL response by a trap charging effect	47
2.5.3	Electric field-induced surface modification and the optical nonlinearities	48
2.6	Electrical control of the dark-field linear scattering	49
2.7	Conclusion	53
3	Nonlinear optical transport in plasmonic nanowires	55
3.1	Introduction	55
3.2	Fabrication techniques and nonlinear wide-field microscopy	56
3.3	Excitation of delocalized N-PL in gold nanowires	57
3.4	Unraveling the N-PL delocalization	59
3.4.1	Propagation lengths	60
3.4.2	N-PL plasmons coupling	62
3.4.3	Emission mechanisms of the delocalized N-PL	65
3.4.3.1	Wavevector distribution of the N-PL	66
3.4.3.2	Polarization resolved wavevector distribution of the N-PL in AuNWs	69
3.4.3.3	Polarized N-PL emission of AuNWs	70
3.5	Spatially resolved N-PL spectral emission	71
3.6	Remote electrical control of the N-PL emission	74
3.6.1	Single-crystalline nanostructures and the control of complex higher order modes	76
3.7	Conclusion	76
4	Control of the nonlinear properties of silver nanowires: towards the realization of plasmonic routers	79
4.1	Introduction	79
4.2	Experimental methods	79
4.2.1	Silver nanowires' synthesis	80
4.2.2	Higher SPP modes detection by leakage radiation	81
4.3	Modal distribution and nonlinear optical emission in silver nanowires	81
4.3.1	Optical nonlinearities in silver nanowires	84
4.3.2	Linear and nonlinear modal distribution in AgNWs	85
4.4	Conclusion	88
	Summary & outlook	91
	List of publications	105
	List of conference contributions	107

General Introduction

The ubiquity of nonlinearities in real systems is a well accepted fact supported with a long history. Indeed, the theory of nonlinear dynamics in the context of mechanical systems dates back to the penultimate century. However, nonlinear photonics did not take off but after the laser invention opened the required access to strong optical fields in 1960. Since then, the evolution of this area of research has been driven by an ever-increasing interest in different areas going from fundamental studies of the light-matter interaction to the design of components and devices with applications in biomedicine and human safety, telecommunications and biotechnology. Most important, the research interest is now focused on novel strategies to guide and propagate nonlinear optical signals as well as the active enhancement and tunability of such nonlinear responses in miniaturized dimensions [1]. In this connection, the present thesis tackles both aspects by electrically and spatially controlling nonlinear photoluminescence (N-PL) in optical nanoantennas.

Antennas are almost ubiquitous in our daily life. In this more and more wireless-dependent world they have become one of the most important constituents of many connected devices. From the radio invention to the widespread use of mobile phones the sending and receiving of electromagnetic waves at different frequencies using antennas has been a significant part of humanity. Antennas transduce efficiently electromagnetic near-fields (NF) to far-fields (FF) in the case of a transmitting antenna and FFs to NFs in the case of a receiving antenna [2]. As the antennas' physical dimensions depend on their operation frequency, the typical size scale of radio frequency (RF) antennas goes from hundred meters to a few millimeters. Consequently, operating at higher frequencies results in physically smaller antennas and more confined fields, with the added value of higher bandwidths and higher data rates. Importantly, the latest advances in photonics and nanotechnology allow to explore the effect of pushing the operating frequency towards the visible and infrared range. As a matter of fact, optical antennas are ruled by plasmonic effects resulting from collective oscillations of free electrons at the interface between dielectrics and metals known as surface plasmons. Along with strong spatial confinement, plasmonic excitations in optical antennas can increase the yield of nonlinear processes which are essential for the achievement of complex operations in the manipulation of light.

In fact, the birth of nonlinear plasmonics was marked by the associated huge enhancement needed for highly efficient nonlinear optics. The first experiments relating nonlinearities with plasmonics were done at the beginning of the 1980s by a few research groups including the work of Wokaun *et al* in second harmonic generation [3] followed later by Ricard, Hache and co-workers and their study in metal nanoparticles and the surface-mediated effects [4, 5]. Concurrently, enhanced second harmonic generation and nonlinear photoluminescence from rough-

ened noble metals films were related to plasmon resonances taking place at the surface [6, 7].

This doctoral work deals with N-PL generated in gold and silver nanostructures after near infrared pulsed illumination. Remarkably, in spite of the vast presence of N-PL in the literature in the context of imaging applications, its fundamental underlying mechanisms are still at discussion. Experimental evidence points to a recombination process following multi-photon absorption in addition to thermal radiation of an out-of-equilibrium hot-electron distribution [8–10]. Here, roughly making the comparison with previous studies on N-PL and plasmonic nanostructures, we go a step higher by including the electrical activation and command of the optical nonlinear response.

Active plasmonics and more particularly electrically-active plasmonics are not new. Coincidentally, their origins also date back to the 1980s with the development of light modulators [11], where the surface plasmon excitation or the refractive index of the surrounding medium were respectively mechanically or electrically controlled. In the nonlinear regime, however, actively-controlled surface plasmon-based phenomena are much more recent and have been primarily pushed by the advances in nano-fabrication techniques achieved during this century.

In our study, the enhanced optical and static electric fields at the feed gap of bow-tie optical antennas favor the efficient generation and electrical modulation of N-PL in a compact electro-plasmonic device. Furthermore, different nanostructural configurations allow us to undertake the problem of controlling local and non-local N-PL emission in zero- and one-dimensional metal nanostructures. Remarkably, the experiments shown here are easily extendable to the more general two-dimensional situation.

Besides presenting clear evidence of the electrical command of the nonlinear response, this thesis interrogates firstly about the processes ruling the nonlinear photoluminescence and secondly about the compatibility of such processes with the achieved electrical modulation. In this context, **Chapter 1** introduces the necessary fundamental concepts of plasmonics along with a complete overview on optical antennas, their design, history and applications. Additionally, we make a deep examination of the different experimental and theoretical evidences supporting the established streams of thought around nonlinear photoluminescence in metals. **Chapter 2** introduces the electro-plasmonic device in question and the necessary fabrication protocols to meet the standards. It particularly addresses the question of locally modulating optical signals by applying strong static electric fields across the gap of optically excited bow-tie antennas. A complete analysis of the different parameters affecting the modulation is made, including the strength of the field, optical power, polarization, among others. At the end, several hypothesis possibly explaining the modulation are contrasted and consequently validated or discarded by the scrutiny of the experimental results.

As the canonical optical antenna, a simple metal nanowire is the starting point towards the realization of more complex devices. In that regard, **Chapter 3** investigates the spatial distribution of N-PL emission in gold nanowires including polarization, spectral and wavevector analysis. Notably, combining the electrical control and optical enhancement brought by bow-tie antennas and the nonlinear transporting features of gold nanowires, remotely generated N-PL is successfully modulated. Finally, **Chapter 4** is an effort to take the control of nonlinearities to higher and more complex plasmonic modes. To this end, synthesized silver nanowires serve now as bearers of the nonlinear optical signals. A general conclusion close the manuscript highlighting the key points of every chapter.

Our device represents the first demonstration of nonlinear photoluminescence electrical modulation and as it will be seen, it could contribute although in a limited way, to the field of optical information processing in optoelectronics and photonic circuitry.

Nonlinear photoluminescence in optical antennas

1.1 Introduction

Optical antennas are a relatively new concept in photonics. They allow to control and manipulate electromagnetic fields at optical frequencies at scales smaller than the diffraction limit. Depending on their design and intrinsic properties, optical antennas can operate in the linear or in the nonlinear regimes. The latter, although relatively unexplored, provides interesting and technologically important phenomena such as frequency conversion, all-optical signal processing, modulation and switching [12–15]. Therefore, nonlinear optical antennas not only serve as transmitters or receivers but additionally allow to further control and enhance the interaction between localized and propagating fields. In particular, the large field enhancement provided by optical antennas has been successfully used to exploit different coherent and incoherent nonlinear processes in metals such as second harmonic generation (SHG) [16], third harmonic generation (THG) [17], four-wave mixing (FWM) [18] and nonlinear photoluminescence (N-PL) [7, 8, 10] which is of special importance in our research.

Linear photoluminescence from copper and gold was first reported in 1969 by Aram Mooradian [19]. Fifty years later, it is still matter of discussion and there is no clear agreement on the underlying mechanisms. Nonlinear photoluminescence results from the pulsed infrared excitation of plasmonic metal structures. It produces a continuum in the visible and near-infrared part of the spectrum [20]. Many studies have been made to clarify the mechanisms behind this phenomena [7–10, 21–24]. On the one hand, N-PL emission can be macroscopically described by considering the third order susceptibility $\chi^{(3)}$ because of its resemblance to two-photon absorption [25–29]. On the other hand, from a microscopic point of view, several physical mechanisms have been proposed. Traditionally, radiative electron-hole recombinations following multi-photon absorption is assumed as the main responsible for N-PL. Recently, photoluminescence has been proposed as the result of hot-electron intraband luminescence [9]. Electrons within the *sp*-band interact with the laser and reach temperatures of several thousand Kelvin. This hot-electron gas is able to emit as a subdiffraction incandescent light source. Light emission from metals has also been considered as electronic Raman scattering [30]. N-PL is then a complex process possibly mediated by different mechanisms [10].

The aim of this chapter is to give a general description of optical antennas, their properties and the nonlinearities resulting from their interaction with electromagnetic fields, making emphasis in the case of gold optical antennas and the generated nonlinear photoluminescence.

1.2 Optical antennas

A short definition for optical antenna would be a nanoscale element that converts efficiently free propagating optical radiation into localized energy in volumes smaller than its own dimensions and vice versa [2]. Engineering of optical antennas seeks the control and optimization of the energy transfer between a localized source (transmitter or receiver) and free radiation fields at the nanoscale. Despite the direct analogy with radio frequency (RF) antennas, there are other factors that certainly make optical antennas different from their RF counterpart. Firstly because metals stop being perfect conductors at optical frequencies due to high losses [31]. Secondly, because dielectric-metallic interfaces can sustain surface plasmon polaritons [32]. For instance, the conversion efficiency of nonlinear optical processes is negligible in bulk metals [33, 34], nevertheless, at the nanoscale it can be resonantly enhanced by several orders of magnitude via the excitation of collective surface charge oscillations in the metal known as localized surface plasmons. This feature along with an intrinsic broadband response and very small footprint make the spectrum of applications very wide. It includes surface enhanced Raman scattering (SERS) [35, 36], sensing [37, 38], photodetection [39], lasing [40, 41], light emission [42–45], optical information processing [31, 46], photovoltaics [47, 48] among others. In this section, a brief overview of the different designs, applications and most important features of optical antennas is presented.

1.2.1 The origin of optical antennas

Logically, the introduction of the first antennas came some years after the demonstration of the mathematical and physical basis for the electromagnetic waves in 1864 by James Clerk Maxwell, the so called Maxwell's equations. First, Heinrich Hertz in 1887 with the fabrication of the antenna and ten years later in 1897 Guglielmo Marconi with the radio systems invention started the relatively fast development of antenna theory. The first written evidence of the use of the word *antenna* as an electromagnetic transmitter dates back to 1898 in a paper by Blondel [49]. Electronics advances in the beginning of the twentieth century allowed several advances on more sophisticated radio systems. World War II brought with it the development of microwave devices and the radar systems. By the 1980s, radio communications were already massively deployed [50].

Looking at the history of optical antennas it is clear that the central motivation for their development came from microscopy. In the 1920s decade Edward Hutchinson Synge, inspired by the development of dark-field microscopy, had some visionary ideas about localized fields in the vicinity of small particles [51]. Many years later, in 1985, John Wessel possibly inspired by the invention of scanning tunneling microscopy and the discovery of SERS, stated that a particle may serve as an antenna that receives an incoming electromagnetic field [52]. In 1988, Pohl and Fischer demonstrated experimentally these antenna effects using a gold-coated polystyrene particle as a local light source [53]. By the end of the 1990s, looking for a near-field optical probe with a higher efficiency than tapered fibers, Robert Grober et al. studied a bow-tie antenna at the end of a waveguide. They demonstrated confinement of a tenth of a wavelength with 30% transmission efficiency [54]. This work also suggested that such antennas could be fabricated for visible frequencies, which motivated several new experimental efforts. Since then this field has been growing rapidly and various geometries of antennas have been explored theoretically and experimentally.

1.2.2 Optical vs. classical antennas

Optical antennas have the same fundamental principles as classical antennas. For example, charge oscillations in a dipole antenna result in fields generated at the surface of the antenna with transfer of signal and power to the surrounding medium. Let's take as example a classical electric antenna where the center dipole is fed with an AC current oscillating with a period T , figure 1.2.1 shows this charge oscillation mechanism [55]. At $t = 0$, the external AC source accelerates the charges towards the top and bottom halves of the antenna, charges start to accumulate at the ends and the electric field points from the positive to the negative charges. At $t = T/4$, charges start to move towards the opposite ends under the action of the oscillating AC and the field takes a semicircular shape. Changes on the AC polarity are obviously followed by a consequent change on charge and electric field polarity. When the cycle is completed, a full wavelength of field is radiated. The same example just explained can be applied to nanostructures and incident optical fields coupled to the electrons on the surface.

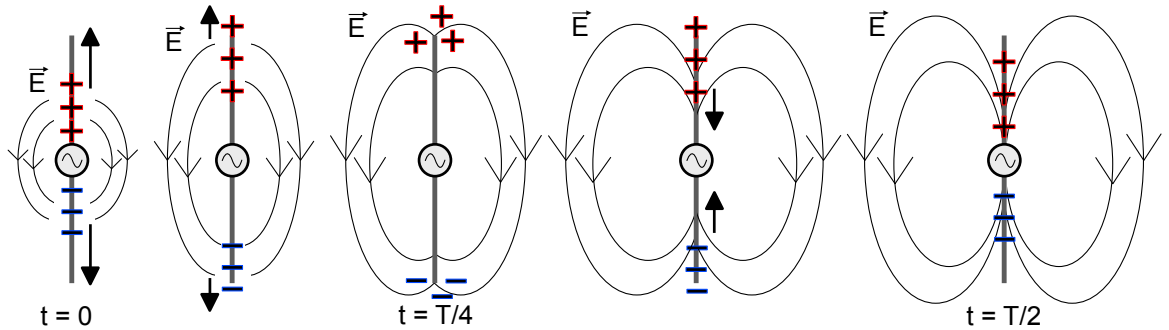


Fig. 1.2.1. Charge oscillations on a dipole as a function of time. In the case of an electric dipole, the driving current is supplied externally in the circuit. For optical antennas, the oscillations are generated by the incident EM field. Inspired by [55].

In optical antennas, the first clear difference with the classical counterpart is the fact that there is no AC source operating at visible frequencies, meaning that only displacement currents are at play. Nonetheless, the main deviation lies on the assumption of a perfect conducting metal. It is well known that metals cease to have this property in the visible wavelength regime where losses become significantly higher.

Electromagnetic fields penetrate certain distance into the metals (skin depth). Assuming a plane wave incident in the z -direction and wave vector \vec{k} , $|\vec{k}| = (\omega/c)(n + i\kappa)$, the electric field within the metal can be expressed as:

$$\vec{E}(\vec{r}, t) = \vec{E}_0(\vec{r}, t)e^{i\omega(zn/c-t)}e^{-z/\delta} \quad (1.2.1)$$

with the attenuation of the field determined by the skin depth $\delta = c/\omega\kappa = \lambda/2\pi\kappa$ and the complex optical index $n + i\kappa = \sqrt{\varepsilon_1 + i\varepsilon_2}$, where ε_1 and ε_2 are the real and the imaginary parts of the dielectric function.

At radio frequencies, the skin depth is negligible compared to the antenna dimensions. For instance, gold exhibits $\delta = 7 - 75 \mu\text{m}$ at the MHz regime [56] whereas it is on the range of $25 - 40 \text{ nm}$ for the near infrared and visible part of the spectrum [57]. Therefore, at optical frequencies the skin depth is appreciable and material properties, such as the real and imaginary part of its dielectric constant are now relevant for the antenna performance. Furthermore, such small values of δ imply that the electrons in the metal become a plasma at the air-medium interface strongly coupled to the incident light (surface plasmon polaritons).

1.2. Optical antennas

1.2.3 Surface plasmon polaritons

Surface plasmons polaritons (SPPs) are dispersive electromagnetic waves coupled to the electron plasma of a metal at a dielectric interface [58,59]. They can be understood as a mixed state between an electromagnetic wave and surface charges that results from the interaction between light and the conduction electrons.

The plasmon excitation study is derived from Maxwell's equations [60], which are solved for the dielectric and the metal separately. For simplicity, an infinite flat metallic surface is considered as shown in figure 1.2.2.

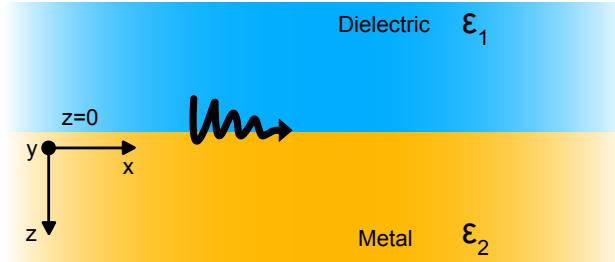


Fig. 1.2.2. Interface along the $x - y$ plane between a metal and a dielectric.

The continuity conditions of the transversal and parallel field components at the interface between the dielectric (1) and the metal (2) impose the absence of transverse-electric (TE) modes in both half-spaces [59]. The transverse-magnetic mode of the field propagating along the x -axis follows an exponential form. The dispersion relation is then

$$k_x^2 = \frac{\varepsilon_1 \varepsilon_2}{\varepsilon_1 + \varepsilon_2} k^2 \Rightarrow k_x = \sqrt{\frac{\varepsilon_1 \varepsilon_2}{\varepsilon_1 + \varepsilon_2}} k \quad (1.2.2)$$

where $k = \omega/c$ is the vacuum wavevector of light at angular frequency ω .

The dispersion relation 1.2.2 in addition to the dielectric function allow to extract the most relevant features of SPPs. For instance, localized modes (SPPs) can only exist at metal-dielectric interfaces. Furthermore, the penetration depth of the fields into the dielectric is typically around half the wavelength in the medium, while in the metal it is given by the skin depth. In other words, electromagnetic fields at the interface experience a fast decay along the transverse direction leading to sub-wavelength concentration of these fields. This is without a doubt the most relevant property of SPPs, guiding and confining light to scales smaller than the diffraction limit have attracted a lot of attention in the context of nanophotonics.

Surface plasmon polaritons excitation results in propagation in all the in-plane directions. However, the specific shape of metal nanostructures determine and restrain such propagation. For instance, SPPs can be guided using plasmonic waveguides where SPPs propagate in a certain direction while being confined in the others. Different structural configurations include nanoparticle arrays [61], thin metal films [62], metal stripes [63], metal nanowires [64,65] (see chapter III and IV), grooves [66], nanoslits [67], among many others. Furthermore, some sub-wavelength nanostructures interacting with electromagnetic fields such as simple nanoparticles can sustain local plasmon modes as presented below.

1.2.4 Localized surface plasmons

In practice, light cannot be directly coupled to SPPs, nevertheless, in a metal nanoparticle, the closed geometrical boundaries can sustain localized oscillations of the surface charge density [58]. Such oscillations are the second fundamental excitation of plasmonics and are known

as localized surface plasmons. In contrast with SPPs, LSPs are non-propagating excitations. The high intensity and sensitivity of the plasmon resonance are the core of many applications.

Localized surface plasmon modes can be more easily understood from the polarizability α_p of metal nanoparticles which relates the incoming displacement electric field \vec{E}_0 with the electric dipole moment $\vec{p} = \alpha_p \vec{E}_0$. The polarizability depends on the dielectric function of the metal, the surrounding medium, the particle size and shape and on the frequency. In the following, all these aspects will be more profoundly discussed.

1.2.5 A metal nanoparticle: the simplest optical antenna

Many features make metal nanoparticles the key building blocks in nano-optics. Besides providing a mean to couple external light into plasmons, metal nanoparticles offer a way to tune the energy of the plasmon excitations and to highly localize the fields in their vicinity. In other words, they fit perfectly the definition of an optical antenna. Geometrically simple, spherical metal nanoparticles give an easy understanding of the basic concepts of optical antennas. Antenna parameters such as the received and radiated power, the directivity, the efficiency, the local density of states (LDOS) or the aperture are easy to derive from this straightforward geometry [49].

An important feature of plasmonic nanoparticles is the polarizability α_p defined as [68]

$$\alpha_p = 4\pi R^3 \frac{\varepsilon_s - \varepsilon_d}{\varepsilon_s + 2\varepsilon_d} \quad (1.2.3)$$

where R is the nanoparticle radius, ε_s is the dielectric function of the sphere and ε_d the dielectric constant of the surrounding medium.

Similar to the dispersion relation (eq. 1.2.2) in a flat geometry, α_p grows for small values of the metal dielectric function diverging for $\varepsilon_s = -2\varepsilon_d$. This situation represents the appearance of resonances in the nanoparticle at incident wavelengths matching the plasmonic modes supported by the nanoparticle. In general, gold and silver nanoparticles usually show LSP resonances in the visible range of the spectrum. In spite of the limitation of equation 1.2.3 to spherical geometries, the presence of localized surface plasmon resonances (LSPRs) in metal particles of any shape and size can be deduced from full electrodynamic calculations (analytically [69, 70] or numerically [71, 72]).

As it will be seen throughout the thesis, when optical antennas are illuminated at the resonant wavelength, the charge interaction at the surface produce intense optical fields which are strongly confined to sub-wavelength spatial dimensions. These intense localized fields can be tailored by varying different parameters such as the shape of the nanostructures or the distance between them, even small shape variations may influence the resonance condition. In fact, nowadays research on optical antennas is widely focused on predicting, manipulating, characterizing, and concentrating optical field intensity in a certain preferred location using plasmonic structures. In spite of the scale invariant property of the Maxwell's equations, it is not the case for the resonance conditions, they are strongly influenced by the materials properties, i.e. the dielectric function ε .

Metal nanoparticles and in general optical antennas show to significantly increase the efficiency of nonlinear optical interactions. Strong spatial confinement and enhancement of the fields generated on the nanostructures make interesting nonlinear optical phenomena arise. Therefore, the engineering and design of the optical antennas are particularly important in the achievement and optimal enhancement of the optical responses. In the next section, some of the most used designs are presented along with their own particularities.

1.2. Optical antennas

1.2.6 Optical antennas design

At first glance, the criteria for designing plasmonic nano-optical antennas is the enhancement of optical near fields in concentrated and small volumes (hot-spots). As for microwave antennas, the resonance conditions for optical antennas depend on their geometry and the surrounding medium [55, 73, 74]. Nevertheless, as already mentioned, inherent losses in metals at optical frequencies bring more complexity to the engineering of these parameters. For single particles, the field enhancements are not very strong (≈ 5 for a 20 nm gold sphere and ≈ 50 for a 60 nm long gold nanorod [75]). On the contrary, very strong enhancements take place in the case of dimer junctions thanks to the mixing of the plasmons of the two entities [76].

Many optical antenna configurations have been theoretically and experimentally analyzed in order to achieve different functionalities. They have been largely inspired by the well-developed RF antenna theory. Dimer antenna structures (Fig. 1.2.3(a)) and dipole antennas (1.2.3(b)) offer hot-spot generation and in general, narrow gaps between sharp structures like bowties (Fig. 1.2.3(c)) have proven to be very effective for this purpose [77, 78]. More complex designs as Yagi-Uda antennas have been developed too, similar to its RF analog, they consist on multiple elements parallelly disposed as shown in Fig. 1.2.3(d).

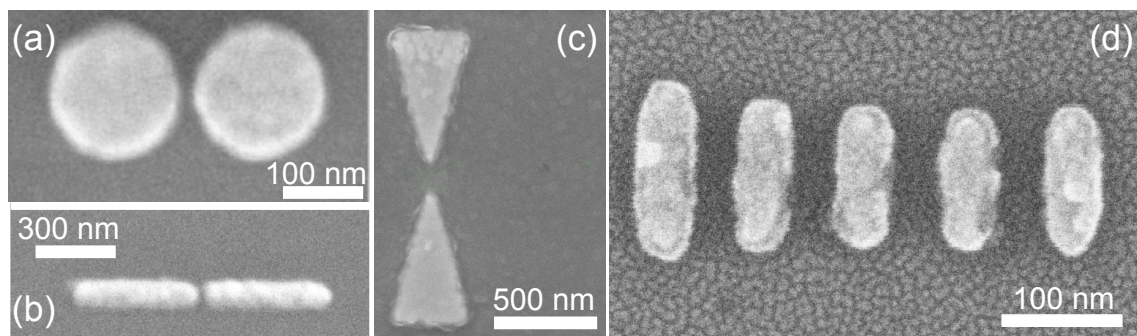


Fig. 1.2.3. Scanning electron micrographs of different optical antenna designs. (a) Hertzian dimer antenna. Reprinted with permission from [79]. Copyright 2012 American Chemical Society. (b) Dipole antenna. Reprinted with permission from [80]. Copyright 2008 by the American Physical Society. (c) Bowtie antenna and (d) Yagi-Uda antenna. SEM image courtesy of Xiao Yu, PhD student at the ICB lab.

Yagi-Uda configurations provide high directionality on the signal thanks to the interplay between its constituent elements. Oligomers of plasmonic particles are generally used to induce strong directivity and control of the scattering and extinction spectra [81]. All these emission properties come from the particular excitation of the electromagnetic modes in the nanostructure [34]. Optical antennas are also able to perform transduction between electrical currents and optical radiation, serving as an optical interconnect [82].

1.2.7 Optical antennas applications

We have already discussed some of the great features of optical antennas which are mainly focused on the control, manipulation, localization and enhancement of optical fields into a subdiffraction limited volume. These characteristics have allowed to consider the use of optical antennas in a broad range of applications.

The high enhancement capabilities of nanoantennas come from the large and highly localized fields produced at their vicinity, making sensing and light harvesting one of the most promising areas for optical antennas. Optical antennas are typically placed on the active region of the device, where, under certain resonance conditions, their large cross-sections, the plasmon near

field and the tailored photon density of states (DOS) allow to enhance the performance of photodetectors or photovoltaic cells [39, 83, 84].

The study of several relevant processes in biology needs very reduced detection volumes. Decoding the complex relationship between individual cell components seems possible in the framework of optical antennas [85]. By using nanoantennas, it is possible to monitor small changes on the refractive index of the specimens and detect molecular interactions [86]. Optical antennas have also been used to enhance the sensitivity of photoluminescence and vibrational spectroscopy [35] as well as controlling the fluorescent emission from single quantum dots [2]. The inherently weak Raman scattering cross sections are boosted by the action of the enhanced fields surrounding the nanostructures allowing single molecule detection [87].

Optical trapping has also been proposed in the context of optical antennas using them as optical tweezers [88]. Heating effects as a consequence of the resonant excitation of metallic nanoparticles could have therapeutic applications on the treatment of tumors [89].

Furthermore, wireless broadcasting using nanoantennas was theoretically proven to perform better than a plasmonic waveguide in optical communications [90] and more recently, an on-chip wireless near-infrared link between an optical and a rectifying antenna was demonstrated [91].

Although the applications listed so far reveal the great potential of optical antennas in a broad range of domains, the vast majority of them are electrically passive. Furthermore, nanoantenna-based active devices have been mainly controlled by modifying the surrounding medium properties and therefore changing the antenna resonances [92]. However, the electrical manipulation of intrinsic linear and nonlinear optical processes happening at the nanoantennas is essential for uncluttered optoelectronic utilization including information and signal processing. In this context, this thesis presents experimental results of an electrically controlled nonlinear nanophotonic device based on optical antennas.

In terms of fabrication materials, the use of nonlinear ones like metals or dielectrics in the design of optical antennas emerges as a promising way for the generation and control of optical information. As presented in the next section, metals and in particular gold offer relatively high efficiency due to their intrinsic nonlinearities along with high optical and chemical stability.

1.3 Optical properties of metals: the case of gold

Metals are elements with relatively low ionization energies and with many free electrons. These free electrons give to the metals their typical properties such as their high conductivity and they dictate almost completely the interaction of metals with electromagnetic radiation.

The optical response of metals is well described by a complex dielectric function $\varepsilon(\omega)$ that depends on the frequency of the incident light and, evidently, on the material band structure (electron transitions). There are mainly two mechanisms contributing to $\varepsilon(\omega)$ [32, 68]:

- **The quasi-free conduction electrons motion on the metal.** The near-parabolic form of the *sp*-band allows to approximate these electrons as free electrons. The mechanism of the intraband electronic conduction is accurately described by the Drude-Sommerfeld theory; it depicts the electrons as a gas of independent, quasi-free particles that are accelerated by an external electric field and slowed down after a mean free time τ through collisions with metal ions. The Drude-Sommerfeld theory determines the dielectric function $\varepsilon(\omega)$ of a macroscopic metal considering the behavior of a single conduction electron and multiplying it by the number of electrons in the metal. It yields, according to the Drude-Sommerfeld theory, to

1.3. Optical properties of metals: the case of gold

$$\varepsilon(\omega)_{\text{Drude}} = 1 - \frac{\omega_p^2}{\omega(\omega + i\gamma)} \quad (1.3.1)$$

where $\gamma = 1/\tau$ is the collision frequency and represents the damping suffered by the electrons in the material with τ the relaxation constant. The plasma frequency ω_p , in terms of the effective mass m_e , the electron density N , the electron charge e and the vacuum permittivity ε_0 , is given by $\omega_p = \sqrt{Ne^2/\varepsilon_0 m_e}$. The relaxation constant τ can be calculated from the electron mean free path l and the Fermi velocity v_F , $\tau = l/v_F$. Which for bulk gold at room temperature is roughly [93]

$$\tau_{\text{Au}} = \frac{l_{\text{Au}}}{v_{F_{\text{Au}}}} = \frac{3.8 \times 10^{-8} \text{ m}}{1.4 \times 10^6 \text{ m/s}} = 27 \text{ fs} \quad (1.3.2)$$

The Drude-Sommerfeld model, which only takes into account conduction electrons, is able to predict the optical properties in the infrared. Nevertheless, the bound electrons, completely ignored by the model, start to play a role in the visible regime. For this range of wavelengths, the photons have energy enough to promote electrons from the lower-lying bands to the conduction band. The model can be extended to include the next contribution by means of Lorentz-like terms.

- **The interband transitions of the electrons.** When the energy of the incoming photon exceeds the band gap energy of the metal, it can promote bound electrons to the conduction band of the metal. This effect leads to

$$\varepsilon(\omega)_{\text{Interband}} = \frac{\Delta\varepsilon\Omega_p^2}{\Omega_p^2 - \omega^2 - i\Gamma\omega} \quad (1.3.3)$$

where $\Omega_p = \sqrt{\tilde{N}e^2/m\varepsilon_0}$ and Γ are the plasma frequency and the damping terms for the bound electrons. \tilde{N} is now the density of bound electrons. Importantly, $\Delta\varepsilon$ takes into account the weight of the particular interband transition to the dielectric function. Evidently the more interband transitions are included the more accurate is the model.

In figures 1.3.1(a) and 1.3.1(b) the real and imaginary parts of the dielectric functions of gold are plotted for the visible and near-infrared parts of the spectrum [68]. Here, $\varepsilon(\omega)$ is calculated using the data from [94] (black dots), the Drude and Drude-Lorentz fits to the experimental values are shown as red and blue lines respectively. The measurements of such optical data are strongly dependent on experimental conditions like the morphology and fabrication processes making the choice very difficult.

As told before, the dielectric function is fairly well estimated for $\lambda > 650 \text{ nm}$ by both models. For this range of wavelengths, the large negative value of the real part dominates, mainly because of the fast response of the conduction electrons. As quasi-free particles, they can screen the external electromagnetic excitation avoiding the penetration of fields into the metal. At shorter wavelengths, the interband transitions induce a decrease on $|\text{Re}\{\varepsilon\}|$ and an increase of $|\text{Im}\{\varepsilon\}|$ (electromagnetic energy dissipation within the metal). The Drude model clearly fails in reproducing this behavior that is partially corrected by including a Lorentz term. The more Lorentzian terms are added in the fitting for $\varepsilon(\omega)$ the more accurate will be the model for shorter and shorter wavelengths.

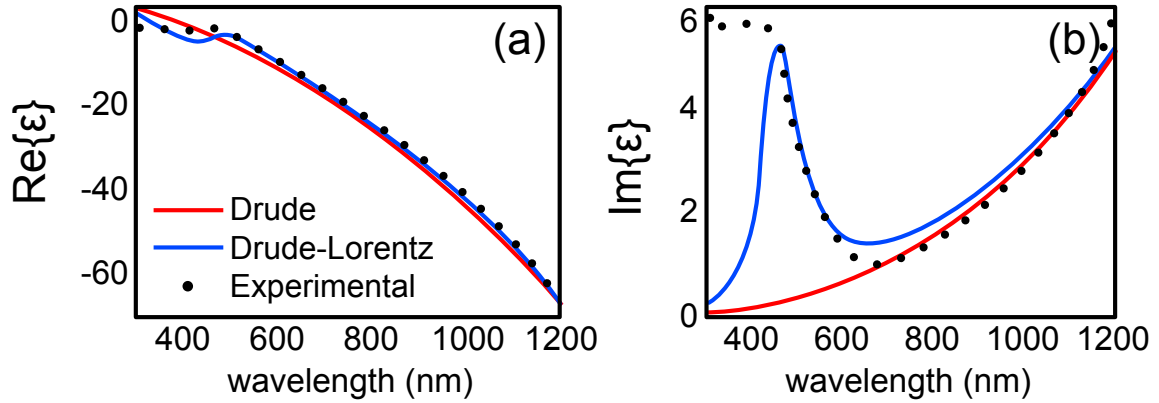


Fig. 1.3.1. Real and imaginary parts of the dielectric function for gold in the optical regime. Black dots correspond to experimental data. The red and blue lines correspond to fits to the Drude and Drude-Lorentz models. Reprinted with permission from [68]. Copyright 2011 American Chemical Society.

Solid materials have their own energy band structures. In metals the energy bands overlap allowing electrons to flow through the material easily in a quasi-continuum of allowed energies. Furthermore, monovalent metals such as silver, copper or gold have partially filled valence bands with a high electron population density near the Fermi energy which results in a large conductivity [95]. Figure 1.3.2(a) shows the band structure of gold.

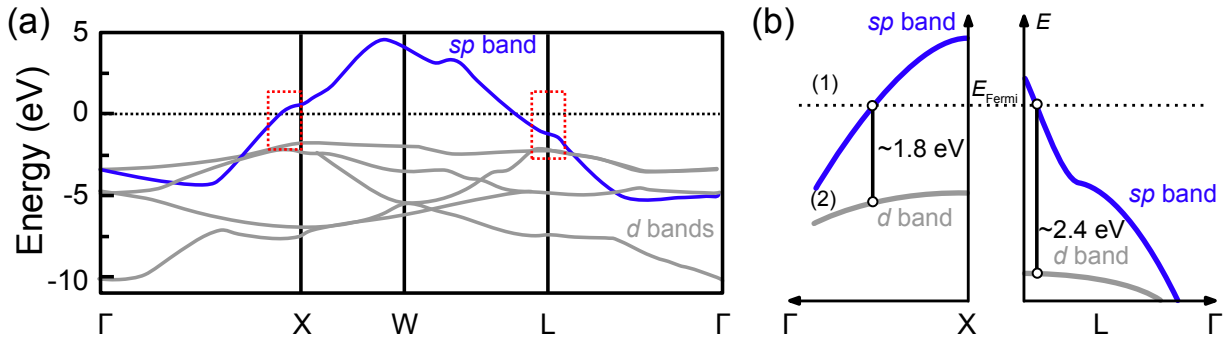


Fig. 1.3.2. (a) Approximative band structure of gold. The red dashed squares point to its interband transitions (b). Adapted from [8] and [23].

In the specific case of gold, it is a noble metal and belongs to the 11th group of the periodic table. It has completely filled atomic d -subshells ($3d$; $4d$ and $5d$), with its core electrons in the inert gas configuration. All gold metallic properties come from the lone valence electron in the half filled atomic s -subshells ($4s$; $5s$ and $6s$). If we look at the band structure of gold, it displays five d -bands below the Fermi level E_F in which are located the ten d -electrons. The lone s -electron forms an sp -band that is filled up to E_F . This band has near parabolic form, i.e. the electron moves quasi-free. The sp -band structure defines the characteristic properties of these metals, such as their thermal and electrical conductivity. To induce an electronic transition between the d -bands and the conduction band, the photon energy $\hbar\omega$ has to be larger than the interband energy $E_G = \hbar\omega_G$. In the case of gold, this energy is $E_G \approx 1.8$ eV and corresponds to the X point of the first Brillouin zone [25]. See fig. 1.3.2(b) showing the interband transitions that occur near the X and L points in the first Brillouin zone.

1.4 Optical nonlinearities in plasmonic antennas

Optical nonlinear effects in optical antennas could offer a way to generate, process and control optical signals within very small distances, with reduced power consumption and much faster than today's electronic devices [96]. Typically, nonlinear conversion requires a phase matching process to occur and the nonlinear response from individual atoms or molecules is coherently summed up. Usually nonlinear crystals carry out this task successfully, thanks to their specific design (symmetry) and their size much larger than the wavelength, the interaction volume is increased and the nonlinear response enhanced. However, they are completely discarded in practical on-chip implementation due to their bulky nature.

Silicon and diverse nonlinear waveguides also offer a wide variety of nonlinearities originating from the interaction of optical fields with electrons and phonons. However, the large wavelength-like scale size of photonic devices along with an inherently weak optical response hinder future applications in integrated nanophotonics and optoelectronics which require extremely reduced dimensions and efficient performance [97].

Plasmonic antennas, on the other hand, could overcome these limitations. They are fabricated with noble metals offering extremely high intrinsic optical nonlinearities. For instance, the third-order nonlinear susceptibility of gold is more than two orders of magnitude larger than the susceptibility of most nonlinear optical crystals [32]. The nonlinear conversion efficiency of metal nanostructures is obviously not mediated by phase matching but resonantly enhanced by localized surface plasmon resonances. Furthermore, sub-wavelength dimensions of plasmonic antennas provide additional degrees of freedom to control the nonlinear responses, which are highly influenced by the shape of the nanostructures. As presented before and additionally to the deep sub-wavelength confinement, plasmonic antennas can also enhance the emission, manipulation and detection of optical signals. In summary, plasmonic antennas are a convenient and flexible candidate to increase nonlinear effects and reduce the footprint and power consumption with very fast response times.

The study and consequently the design principles of nonlinear optical antennas are based on the well-known nonlinear optics theory that remained unexplored until the discovery in 1961 of second harmonic generation in a piezoelectric crystal by Peter Franken *et al.* [98] just after the construction of the first laser by Theodore Harold Maiman [99]. Plenty of textbooks and publications are focused on nonlinear optics and specially in the nonlinear response of bulk materials and their surfaces.

The continuous improvement of nanoscience and nanotechnology has allowed the systematic study of nonlinear effects in the context of nanophotonics and plasmonics with the scope on novel optoelectronic applications. Nowadays, it is possible to reproducibly fabricate samples with smaller dimensionality and with extreme control using different techniques such as soft lithography, two-photon lithography, self assembly, focused ion beam milling, nanosphere lithography among others [100–108]. Additionally, the measurement of the nonlinear optical responses from discrete and controllable structures is now completely achievable [8, 109]. Taking advantage of this level of fabrication control and measurement precision, the influence of individual physical parameters in nonlinear processes has been determined [15]. The research interests of the community regarding plasmonic nonlinearities are primarily focused on the four main phenomena mentioned at the beginning of the chapter (N-PL, SHG, THG, 4WM). Nonetheless, nonlinear plasmonics is still an emerging field with many unexplored aspects.

In a rough sense, nonlinear optics exploit the nonlinear relationship between the exciting electric field \vec{E} and the polarization \vec{P} . This relationship is mostly linear for weak excitation fields and almost all optical antennas operate in this regime. Nevertheless, for strong excitations, the response of \vec{P} with \vec{E} is no longer linear, which gives rise to interesting and

technologically important phenomena.

The nonlinear relation between \vec{P} and \vec{E} can be conveniently expressed in the dipole limit as a power series expansion

$$\vec{P}(\omega) = \varepsilon_0 \left[\chi^{(1)} \vec{E} + \chi^{(2)} \vec{E} \vec{E} + \chi^{(3)} \vec{E} \vec{E} \vec{E} + \dots \right] \quad (1.4.1)$$

where the susceptibilities $\chi^{(n)}$ are tensors of rank $n + 1$. Inserting this polarization \vec{P} into the Maxwell's equations will produce a set of nonlinear differential equations.

When the light-matter interaction is weak, we can approximate the response of a charged nanoparticle to a driven harmonic oscillator. Nevertheless, when excitation fields become stronger (e.g. pulsed lasers), this is no longer valid and the model has to be extended with anharmonic terms. The inclusion of quadratic or higher anharmonic terms in the equation of motion will give rise to solutions that oscillate not only at the fundamental frequency but also at higher order frequencies [34].

The charge oscillations at new frequencies induce polarization currents $J(t)$ producing electromagnetic radiation at those frequencies. Taking the example of second harmonic generation under the action of a driving field $E(t) = E \cos(\omega t)$, the resulting nonlinear polarization is [34]

$$P^{(2)}(t) = \varepsilon_0 \chi^{(2)} E^2 + 2\varepsilon_0 \chi^{(2)} E^2 \cos(2\omega t) \quad (1.4.2)$$

in this case, $\chi^{(2)}$ is assumed to be time independent or dispersion-free for simplicity. The first term represents the induced static field (optical rectification) and the second term SHG.

Proceeding in a similar way, the third order polarization is [34]

$$P^{(3)}(t) = \varepsilon_0 \chi^{(3)} E^3(t) = \frac{1}{4} \varepsilon_0 \chi^{(3)} E^3 \cos(3\omega t) + \frac{3}{4} \varepsilon_0 \chi^{(3)} E^3 \cos(\omega t) \quad (1.4.3)$$

where the first term is linked to third harmonic generation and the second term relates to the refractive index change known as Kerr nonlinearity.

1.4.1 Luminescence from metals

Under certain irradiation conditions, metals can emit light. A particular light emission mechanism often attributed to photoluminescence was first reported in 1969 by Aram Mooradian [19]. Although it was 50 years ago, the origin of this process is still under debate and continues to be the focus of recent research. At that time, the emission spectrum was measured when gold and copper samples were excited with light from an argon ion laser and a high pressure mercury vapor arc lamp at 488 nm or 514 nm. The result was a broad emission spectrum of light with the peaks centered close to the interband absorption of the metals (≈ 2.0 eV for copper and ≈ 2.2 eV for gold, see fig. 1.3.2) and consequently considered as the result of radiative recombination of conduction electrons with d -band holes. Linear with respect to the excitation power it has been referred as one-photon luminescence.

Nonlinear photoluminescence arises under infrared radiation and was first observed as a broadband background in experiments on surface enhanced second harmonic generation [20]. In 1986, photoluminescence was characterized in smooth and rough surfaces of gold, copper and silver by Boyd et al. [7], finding that local field enhancement due to surface plasmon resonance is a prerequisite for strong photoluminescence and ratifying the radiative interband transitions as the responsible underlying mechanism. N-PL was considered as a process induced by multi-photon absorption.

In contrast with the one-photon luminescence case, N-PL has generally showed an excitation power dependence close to quadratic for the up-converted emission (shorter wavelength side of

1.4. Optical nonlinearities in plasmonic antennas

the excitation). As a consequence, N-PL has been thought as a two-photon absorption process followed by the recombination of conduction band electrons with d -band holes (Two-photon luminescence or TPL). In some experimental conditions, such nonlinearity can reach higher orders, thus by correspondence, higher photon-absorption processes have been assumed [21,22]. For the down-converted emission (spectral range above the excitation wavelength), a linear excitation power dependence was found [8]. It was considered as the result of luminescent electronic transitions within the sp -band i.e. intraband luminescence.

The interest on metals photoluminescence lies on its broadband and extremely local emission allowing access to multiple wavelengths in very small volumes. These properties have found applications in sensing [110], spectroscopy [111], imaging [112] and, as presented later, could be useful in optoelectronics too. Such great interest on the metals photoluminescence processes and applications, has led to new hypothesis about the underlying mechanisms and scrutinized the well established (one)multi-photon absorption theory. For instance, it has been proposed to exclude interband transitions as the cause of one-photon luminescence and include alternatively the radiative decay of the surface plasmons, which are generated after fast inter-conversion from excited electron-hole pairs initially created at the excitation wavelength [113]. Some other works include the effect of the surface plasmons and the thermalization of excited electrons [114]. Recently, one-photon luminescence has been interpreted as a Purcell-effect-enhanced radiative recombination of hot carriers [115]. Regarding N-PL, a model based on sp -band heating steered by photon absorption and photoluminescence from intraband transitions within the energy distribution of a hot electron gas has been proposed [9]. Very recently, hot carriers and photoluminescence have been shown to play a key role in the up-converted emission [116]. Another theory, argues that the observed emission should not be interpreted as photoluminescence but as electronic inelastic light scattering (Raman scattering) [30,117,118]. Furthermore, a different type of up-converted luminescence has been shown for gold nanostructures possibly involving interband transitions coupled with phonons or localized vibrations of neighboring atoms [119]. This section seeks to give a comprehensive overview of the main different perspectives of the N-PL starting from a general macroscopic point of view and the third order nonlinear susceptibility $\chi^{(3)}$ and presenting then the possible microscopic mechanisms responsible for this phenomenon.

1.4.1.1 A macroscopic perspective. Two-photon absorption and the $\chi^{(3)}$ susceptibility.

N-PL and other nonlinear optical responses as THG and four-wave mixing (4WM) can be macroscopically described in terms of the third order nonlinear susceptibility. Whereas 4WM is proportional to $\text{Re}[\chi^{(3)}]$, N-PL is proportional to $\text{Im}[\chi^{(3)}]$. In the particular case of N-PL seen as a two-photon absorption process, let us consider the average rate of the dissipated energy in the material, which according to the Poynting theorem is [34]

$$P_{abs} = - \int_V \langle \vec{j}(\vec{r}, t) \times \vec{E}(\vec{r}, t) \rangle dV \quad (1.4.4)$$

where the angle brackets ($\langle \dots \rangle$) refer to the average in time and $\vec{j} = d\vec{P}/dt$ is the polarization current density induced by a time-varying polarization density. We can assume \vec{E} time-harmonic, i.e. $\vec{E}(\vec{r}, t) = \text{Re}[\vec{E}(\vec{r}, \omega)e^{-i\omega t}]$, so the average in time in Eq. 1.4.4 yields to P_{abs} non-zero only if \vec{j} and \vec{E} oscillate at the same frequency [34]. Rewriting Eq. 1.4.4

$$P_{abs} = -\frac{1}{2} \int_V \text{Re}[\underbrace{\vec{j}(\vec{r}, \omega)}_{-i\omega\vec{P}(\vec{r}, \omega)} \times \vec{E}^*(\vec{r}, \omega)] dV = \frac{\omega}{2} \int_V \text{Im}[\vec{P}(\vec{r}, \omega) \times \vec{E}^*(\vec{r}, \omega)] \quad (1.4.5)$$

The lowest order term $\vec{P}^{(1)}$ in Eq. 1.4.1 is related to $\chi^{(1)}$ and is responsible for linear absorption [34].

$$P_{abs}^{(1)} = \frac{\omega}{2} \int_V \text{Im} [\chi^{(1)}(\omega)] \vec{E}(\vec{r}, \omega) \vec{E}^*(\vec{r}, \omega) dV \quad (1.4.6)$$

The second order term associated with $\chi^{(2)}$ oscillates at zero and 2ω frequencies, consequently it does not contribute to P_{abs} . The next contribution to P_{abs} is the $\chi^{(3)}$ term which is responsible for two-photon absorption [34]

$$\vec{P}^{(3)} = \chi^{(3)} \vec{E}(\vec{r}, \omega) \vec{E}(\vec{r}, \omega) \vec{E}^*(\vec{r}, \omega) \quad (1.4.7)$$

Introducing this nonlinear contribution into the Eq. 1.4.5

$$P_{abs}^{(3)} = \frac{\omega}{2} \int_V \text{Im} [\chi^{(3)}] \vec{E}(\vec{r}, \omega) \vec{E}^*(\vec{r}, \omega) \vec{E}(\vec{r}, \omega) \vec{E}^*(\vec{r}, \omega) dV \quad (1.4.8)$$

In the case of an extended isotropic material irradiated by a plane wave this reduces to [34]

$$P_{abs}^{(3)} \sim \text{Im} [\chi^{(3)}] \left| \vec{E}(\vec{r}, \omega) \right|^4 \quad (1.4.9)$$

The first observation on equation 1.4.9 is that absorption is associated only with odd orders of χ . It also shows clearly the quadratic dependence on the incident intensity, which has led, in addition to some experimental evidence to be shown later in the chapter, to the interpretation of N-PL as a two-photon absorption mediated process.

Figure 1.4.1 shows some examples of the different kind of resonances and excited state dynamics which may contribute to incoherent nonlinearities and to large values of $\text{Im}[\chi^{(3)}]$ [120]. Two-, three- and four-level systems coupled by one-photon and two-photon resonances or by the sequential two-photon absorption are presented.

Unlike white-light continuum [121], harmonics generation [122, 123], and frequency mixing [124] which are inherently coherent phenomena with respect to the driving fields [125], nonlinear photoluminescence shows to be incoherent and to follow the sequential absorption of single photons (Figure 1.4.1(c)). Many of the reported values of $\chi^{(3)}$ are highly different throughout the literature mainly because of the inadequate assumption of an instantaneous nonlinear response among other issues [27]. The non-instantaneous behavior has been extensively demonstrated in pump-probe, two-pulse correlation and pulse-duration experiments [22–24].

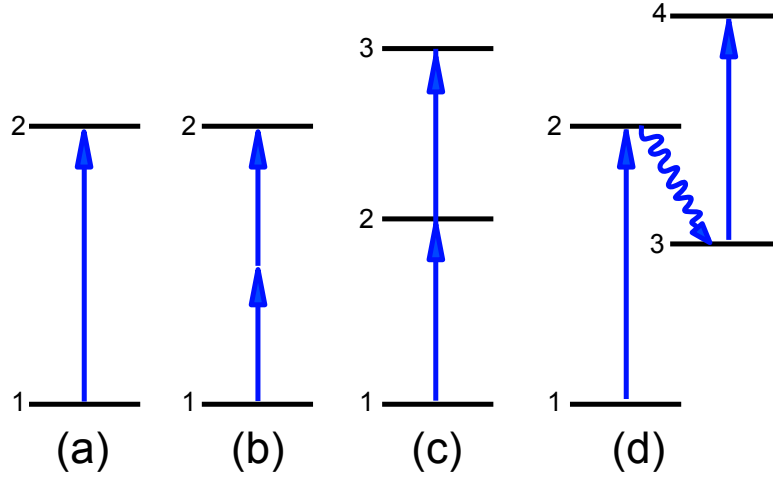


Fig. 1.4.1. Resonances and excited-state dynamics contributing to the $\chi^{(3)}$ nonlinearities. (a) one-photon absorption, (b) direct two-photon resonance mediated by a virtual state, (c) resonant sequential two-photon absorption, (d) relaxed sequential absorption. Adapted with permission from [120]. Copyright 1994 American Chemical Society

The nonlinearity of metals can be interpreted as the result of the smearing of the electron distribution produced by intense optical absorption [126, 127]. As a consequence, the interband and intraband transition probabilities change with the subsequent variation of the dielectric permittivity. The two temperature model has accurately explained the dynamics of such process by describing the temporal evolution of the electron gas and the lattice and their energy balance [127, 128]. This model has also indicated a nonlinear response dominated by a delay mechanism. A theoretical formulation of a delayed $\chi^{(3)}$ based on an extended version of the two temperature model and semi-classical theory of optical transitions in solids has been proposed [28]. Nonetheless, the possible contributions to the nonlinearities are still ambiguous and a precise description of the mechanisms is still lacking. In the next, a summary of the different electronic contributions to the third order nonlinearity established so far is presented.

Electronic contributions to $\chi^{(3)}$

Assuming nonlinear photoluminescence as a third order process, let us go from a macroscopic to a microscopic description by looking into the mechanisms that govern it. We will make special emphasis in the various electronic contributions to $\chi^{(3)}(\omega, -\omega, \omega)$ and how the optical properties of metal can be modified by \vec{E} . The following estimations were made by Hache and coworkers in an extensive study on optical nonlinearities in small metal particles and metal colloids [25].

The first contribution to the optical nonlinear response comes from the conduction *sp*-electrons. It is strongly size dependent and numerical estimates of this contribution show it to be quite small (10^{-10} e.s.u. for 50 Å metal colloids). Thus, this contribution involves only the conduction band and is called *the conduction electron intraband contribution*.

A second mechanism is provided by interband transitions. We are interested in the vicinity of the surface plasmon resonance peak ($\lambda \approx 530$ nm), where part of the absorption is due to *d*-electrons which can be promoted to the *sp*-band. Most of the *d*-electrons involved in this transition come from the vicinity of the X point in the Brillouin zone. Like any electronic transitions, these transitions between a *d*-band and the *sp*-band saturate at high intensity. They may be considered as being superpositions of two-level transitions. Absorption saturation then leads to a $\chi^{(3)}$ susceptibility which is mainly imaginary, with $\text{Im}[\chi^{(3)}]$ negative. Strictly speaking, this is valid only for photon energies that are close to the interband transition threshold in the mentioned Brillouin zone [129]. Numerical estimations place this value around -10^{-8} e.s.u. We have to remark that *the interband contribution* is also size independent down to very small

sizes.

A third mechanism is also important (see Fig. 1.4.2): through absorption, the laser pulse transfers energy to the conduction electrons whose low specific heat allows to raise them to elevated temperatures creating hot electrons. Electrons rapidly reach an equilibrium temperature among each other, but this electronic temperature is larger than the lattice temperature. The thermal equilibrium between the lattice and these electrons is reached in a timescale on the order of a few picoseconds. The high temperature of the hot electrons produces a deformation of the Fermi-Dirac occupation probabilities near the Fermi energy (part of the one-electron levels below the Fermi level being emptied whereas part of the levels above the Fermi level become occupied), modifying the absorption coefficient of d -electrons that finally leads to an imaginary and positive $\chi^{(3)}$. The d -electrons involved in this process are located in the vicinity of the L point of the Brillouin zone. Numerical estimations of the *hot electron contribution* to $\chi^{(3)}$ give values of the order of 10^{-7} e.s.u. This contribution is also size independent. However, it holds for an energy range close to the surface plasmon resonance and picosecond-order pulse widths. For the seek of generality, calculations have been extended to a wider spectral range, different pulse widths and excitation magnitudes [129].

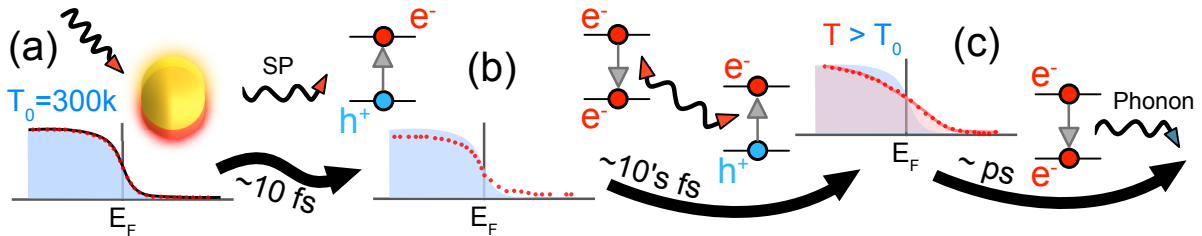


Fig. 1.4.2. Schematic representation of the hot electron generation in gold nanostructures. (a) A gold nanostructure is initially in thermal equilibrium at $T = T_0$. (b) A femtosecond laser pulse generates surface plasmons in the particle which exponentially decay into hot electrons and holes within ≈ 10 fs. (c) Coulomb electron-electron interactions lead to the decay of the most energetic electrons in a few tenths of femtoseconds and eventually relax back to ambient temperature in the picosecond scale thanks to the coupling with phonons. Shaded areas represent the initial Fermi-Dirac distribution of electronic states, points indicate the occupancies of different energy levels. The solid curve in (c) is the Fermi-Dirac distribution at a higher temperature T . Adapted with permission from [130]. Copyright 2016 American Chemical Society.

To summarize, the theory states that the main two mechanisms leading to a change in the $\chi^{(3)}$ susceptibility of gold are the saturation of the interband transition and the creation of hot conduction electrons. Both processes involve interband absorption but from different parts of the Brillouin zone as well as they correspond to different signs for the imaginary part of $\chi^{(3)}$ and have different anisotropies too [26]. The third order nonlinear optical response varies in a complex way and depends on many parameters that are difficult to control experimentally. Thermal effects are some of them and can significantly vary the optical properties of metals [26].

Additional thermal effects

There is a common agreement on the link between the dynamics of the nonlinear optical response and the dynamics of thermal effects. One of the mechanisms contributing to the thermal effects has been already evoked and has to do with Fermi smearing mechanism after optical absorption. Additionally, the electron-phonon and electron-electron scatterings may also exhibit an electronic temperature dependence [131, 132]. Furthermore, the interaction of electrons with the surface becomes a significant relaxation channel in nanoparticles [133]. The metal lattice heating after the coupling with the electron gas induces a metal density

1.4. Optical nonlinearities in plasmonic antennas

modification thus affecting the optical properties too [134]. Finally, the thermal energy diffusion towards the surrounding host heats the whole material.

The macroscopic treatment of the nonlinear photoluminescence of metals provides a broad perspective of the process. Nevertheless, it fails to precisely describe it quantitatively [125]. The first reason lies on the calculations of the bulk gold susceptibility, which are very complex and with contradictory results in the literature [27]. Secondly, the field enhancement at the nanoscale is highly dependent on the geometrical properties of the nanostructures and very difficult to evaluate accurately under different experimental conditions [135,136]. And lastly, in order to precisely analyze the optical response, the magnitude of the plasmonic enhancement must be known with high accuracy since the efficiency of multiphoton processes scales nonlinearly [77,137]. In the following, we will turn our focus to the underlying physics generating the nonlinear photoluminescence and the main different perspectives around it.

1.4.1.2 N-PL seen as a multi-photon absorption process

The first evidence of a multi-photon absorption interpretation dates back from 1982 when Boyd *et al.* established significant differences between the emission excited by one- and what they called multi-photon absorption [138]. Briefly, they found multi-photon luminescence to be more sensitive to the local fields than one-photon luminescence yielding different spectra. In a second experiment by the same research group [7], the number of photons involved in the multi-photon excitation was inferred from the high-energy cutoff of the spectrum, which was located at the two(three)-photon energy suggesting that the luminescence was initiated by two(three)-photon absorption for gold and copper (silver). They confirmed this by measuring the power dependence of the luminescence and finding a quadratic result. We reproduced the experiment on gold nanostructures with bow-tie shape under near-infrared excitation. The experimental setup will be more deeply explained in the next chapter. Essentially, a tightly focused femtosecond laser beam at $\lambda_0 = 810\text{nm} \approx 1.53\text{ eV}$ illuminates the nanostructures and generates N-PL which is collected and sent to a spectrometer. Figure 1.4.3(a) shows the measured N-PL spectrum for different incident powers or irradiance E at the laser focus.

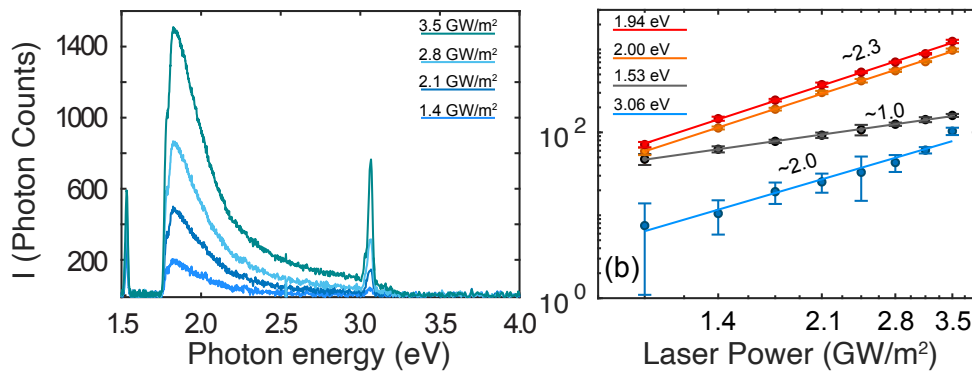


Fig. 1.4.3. (a) Emission spectra of gold nanostructures for different excitation powers. (b) Log-log plot of the N-PL intensity dependence on the excitation power with its corresponding slope. The laser intensities have been proportionally reduced to avoid overlapping of the curves.

The emission extends, as usual, from the visible to the infrared range with higher intensities at lower photon energies (cut by filters in the setup at $\lambda = 700\text{ nm} \approx 1.77\text{ eV}$). Peaks centered around $\lambda = 405\text{ nm} \approx 3.06\text{ eV}$ and $\lambda = 810\text{ nm} \approx 1.53\text{ eV}$ correspond to second harmonic generation and scattered photons at the laser energy in the setup respectively. In

figure 1.4.3(b), a log-log plot shows the power dependence of the N-PL intensity I for two different photon energies, the nearly quadratic dependence is again confirmed ($I \propto E^{2.3}$). For reliability purposes, the power dependence of the linearly scattered laser photons and the frequency doubled photons are included.

Nonlinear photoluminescence has proven to be a delayed mechanism which involves a sequence of distinct optical interactions. According to the multi-photon absorption approach, first two photons are absorbed sequentially and then one photon is emitted. More specifically, a photon excites an electron producing an intraband transition within the sp -band, another photon excites an electron from the d -band to a hole in the sp -band. The lifetime of the intermediate state after the first photon absorption rules the N-PL dynamics [23].

Several other studies have been focused on higher order absorption processes. Three-photon absorption was reported in single gold nanoparticles [139], and four-photon nonlinearities were measured in resonant gold antennas [22, 121]. Restricting N-PL as a third-order nonlinearity, it can be generally described as a three-step process as depicted in Fig. 1.4.4:

- (i) Excitation of electrons from the occupied d -bands to the unoccupied states of the sp -band to generate electron-hole pairs. Two photons are absorbed sequentially.
- (ii) Subsequent intraband scattering of electrons and holes on the picosecond timescale with partial energy transfer to the phonon lattice, moving the electrons closer to the Fermi level.
- (iii) Electron-hole recombination resulting in non-radiative processes or the emission of luminescence.

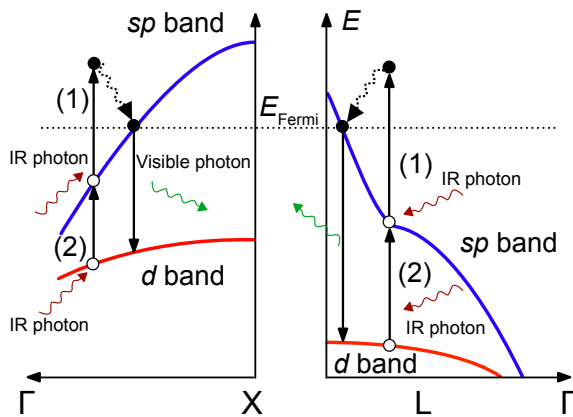


Fig. 1.4.4. Representative band diagram for gold near the X and L symmetry points in the first Brillouin zone. The first IR photon (1) excites an electron in the sp -band, while the second (2) excites an electron from the d -band to the sp -band. Electron-electron and electron-hole scattering events move the electrons closer to the Fermi level. Visible emission is generated when the electron relaxes from the sp -band back to the d -band. Adapted with permission from [23]. Copyright 2009 by the American Physical Society.

Looking at the N-PL process is noticeable that the radiative relaxation energies match those of the interband separation. For bulk material these energies occur around the X and L points of the Brillouin zone. In the case of small particles where the optical properties are dominated by localized surface plasmon resonances, photoluminescence spectra is observed at the same energy as extinction and scattering spectra, suggesting that the photo-emission is related to the particle plasmons [8, 109] which are well known to enhance a variety of linear and nonlinear optical properties. The same effect has been studied in single nanorods where the strong and narrow surface plasmon resonance in the near-infrared region of the spectrum allows a clearer observation [136].

Although there is a broad agreement on the multi-photon absorption nature of the nonlinear photoluminescence, some other viewpoints have also partially explained this particular phenomenon. As introduced before, recent works point to a universal nature of the light emission in metals involving either hot-electron black-body radiation [9] or resonant electronic Raman scattering [30]. In the next, we outline these two perspectives.

1.4. Optical nonlinearities in plasmonic antennas

1.4.1.3 N-PL seen as a thermal radiation process

As stated before, hot electrons play an important role on the light-matter interaction. Recent scientific data has pointed to a process driven by the hot electron gas emission which acts as a subdiffraction incandescent light source [9]. The nonlinearity of the process is not driven by the absorption as in the multi-photon luminescence approach but in the emission which depends nonlinearly on the electronic temperature.

After exciting silver and gold nanoparticles with a weakly focused laser at $\lambda_0 = 770 \text{ nm}$ ($\approx 1.6 \text{ eV}$), the authors recorded the generated luminescence spectrum. To determine the power dependence, a linear fit was applied, as usual, to a log-log representation of the measured input laser power and the integrated photoluminescence intensities. The extracted slope represents the power-law exponent. In agreement with previous works, for the integrated up-converted part of the emission the obtained value is around $p = 2$ and for the integrated down converted one $p = 1$. Carefully looking at the spectral variations of the emission with the incident power, the authors noted a blue-shift as the power increases suggesting a variation of the power-law exponent p with λ . A more complete and rigorous analysis, consists then on evaluating p for every single wavelength over the whole spectrum, the result is shown in Fig. 1.4.5 where p shows to be directly proportional to the emission wavelength ($p(\lambda) \propto \lambda$). The linearity of $p(\lambda)$ is a consequence of the pulse excitation, which is able to deposit enough energy in the electron gas such that emission occurs before the cooling mediated by electron-phonon scattering. This linear dependence can be explained by the increased availability of high-energy electronic states within the sp -band electron gas.

For comparison, the down-converted emission under continuous-wave illumination with different incident powers is presented too ($p(\lambda) = \text{const} \approx 1$), in this case electron heating is suppressed by phonon scattering and the electronic and lattice temperatures equalize.

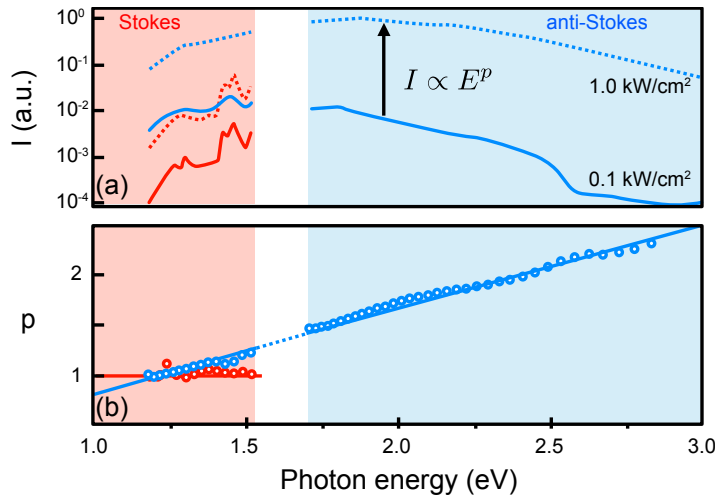


Fig. 1.4.5. (a) Emission spectrum of a single luminescent spot in a silver nanoparticle film being excited at 770 nm by a femtosecond laser (blue) or by a CW laser (red). The solid and the dashed lines represent a laser excitation power of 100 W/cm² and 1 kW/cm² respectively. The blank space in the 1.52 – 1.72 eV range is a consequence of the filtering of the elastically scattered light. (b) Spectrally resolved power-law exponent for the incident laser dependence of the emitted photons. Figure adapted with permission from [9]. Copyright 2015 by the American Physical Society

This result is considered an unequivocal property of the intraband recombination of hot carriers. Using a simple thermodynamic two temperature model, Haug *et al.* were able to estimate the electron gas temperature in the range of 2000 K to 4000 K consistently matching previous theoretical calculations [130,140,141] and femtosecond pump-probe experiments [142].

Additionally, despite the strong modification of the spectral shape by the local density of states which varies from one hot spot to another, fitting it with a Planck-type black-body spectrum gives a consistent comparison.

In the interpretation of Haug *et al.* [9], the electronic temperature and the power-law exponent p are inversely proportional. Autocorrelation experiments substantiate these results [143]. Varying the relative intensity of two temporally separated pulses reveals power-law exponents increasing with the inter-pulse delay. As expected, the electronic temperature is higher for shorter delays and vice-versa. Moreover, spectrally resolved measurements show redder emissions (colder) for the longer delays.

N-PL excited by electrons. A thermal process too.

Generation of hot-electrons is not limited to laser excitation. Broadband light emission can also be generated through electron tunneling in biased tunnel junctions and is generally understood as radiative decay of surface plasmon modes [144]. Surprisingly, in a work on electron-fed optical antennas by Buret *et al.*, part of the emitted photons show an energy exceeding that of the injected electrons thus violating the quantum limit [145]. Also, such overbias light emission can be explained as spontaneous emission of a hot-electron distribution. Estimations of the electronic temperature T_e are shown in figure 1.4.6(a). The model relates T_e with the electrical power injected into the nanostructure in the strong heating regime as [146]

$$k_B T_e \approx (\alpha I_T V_{\text{bias}})^{1/2} \quad (1.4.10)$$

where k_B is the Boltzmann's constant, α is the coupling coefficient and I_T is the tunneling current. These electronic temperatures are comparable to previously reported values for nanoparticles excited with ultra-short laser pulses [147].

Figure 1.4.6(b) shows the light intensity as a function of the inferred electronic temperature. The fit comes from the relationship between thermal emission and blackbody radiation where the Planck spectrum of such radiation $U(\nu, \vec{r})$ is obtained by multiplying the thermal energy $\theta(\nu, T)$ by the local density of states $\rho(\nu, \vec{r})$ [148, 149].

$$U(\nu, \vec{r}) = \rho(\nu, \vec{r}) \theta(\nu, T) = \rho(\nu, \vec{r}) \frac{h\nu}{e^{h\nu/k_B T_e} - 1} \quad (1.4.11)$$

It is important to highlight the highly nonlinear dependence of the light intensity with the electronic temperature. Furthermore the variation for a certain range of temperatures follows a quadratic dependence with the temperature. The similarity with the N-PL emission under pulsed laser excitation is unquestionable and fig. 1.4.10(c) provides further evidence. In this case, the emission spectrum is shown for different bias. The long tail, characteristic of N-PL (see fig. 1.4.3) with higher light intensity for lower energies, is reproduced by this emission process.

1.4. Optical nonlinearities in plasmonic antennas

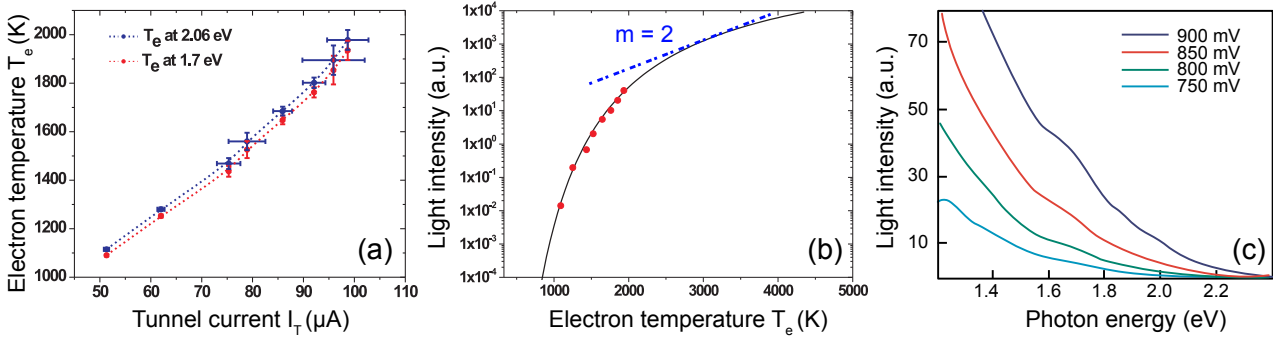


Fig. 1.4.6. Estimated effective electron temperature as a function of the tunnel current for two energies (1.7eV; 2.06eV). (b) Light intensity versus electron temperature (semi-logarithmic scale). The red points are the inferred electron temperature and the solid line is the evolution of the light intensity at 1.7 eV. (c) Emission spectra of the device for different bias voltages. Figure adapted and reprinted with permission from [145]. Copyright 2015 American Chemical Society.

1.4.1.4 N-PL as an inelastic scattering process

Nonlinear photoluminescence in plasmonic nanostructures is a resonant secondary emission process according to reference [118]. In this context, several studies have proposed luminescence and resonant Raman scattering to be fundamentally equivalent [150, 151]. Influenced by this approach, Huang *et al.* [118] quantitatively connect the intensity of the emission with the electronic temperature and conclude that the up-converted emission (anti-Stokes in Raman terminology) generated in gold nanostructures by a NIR pulsed laser excitation is not a process mediated by multi-photon absorption and the subsequent plasmon radiative decay. Instead, they find electronic Raman scattering by a thermal distribution of electronic excitations to be a good description of the emission mechanisms. It is worth noting that the model fails to describe the Stokes part of the spectrum.

Regarding continuous wave excitation, Hugall *et al.* and Xie *et al.* also observe a temperature dependence emission in gold pyramids [117] and gold nanodisks [152] respectively. Both studies link the resulting emission to inelastic light scattering from the electrons within the noble metal nanostructures supporting the plasmon modes. A more general analysis by Mertens *et al.* states that light emission from plasmonic nanostructures is neither interband nor intraband photoluminescence but instead comes from the photo-excitation of electrons to a virtual state followed by re-emission [30].

1.4.1.5 N-PL: a multifaceted process

A more detailed study by Roloff *et al.* [10] in 2017 proposed a complex emission phenomena with different mechanisms depending on the laser excitation range of powers. On the one hand, at low irradiance levels, the up-converted emission clearly follows a power-law with a constant integer exponent around two, a signature of a multi-photon absorption process. In the down-converted part of the spectrum a linear power excitation dependence dominates, probably a signature of electronic Raman scattering. On the other hand, at higher irradiance levels, the nonlinearity exponent depends on the emitted wavelength, indicating the emergence of an irradiation-induced heated electron gas.

As can be seen in Fig. 1.4.7, in the regime of high irradiation, $p(h\nu)$ shows the linear dependence with the emitted photon energy in agreement with the intraband emission model (figure 1.4.5). For low laser powers, p remains constant and around 1 for the down-converted emission and 2 for the up-converted emission.

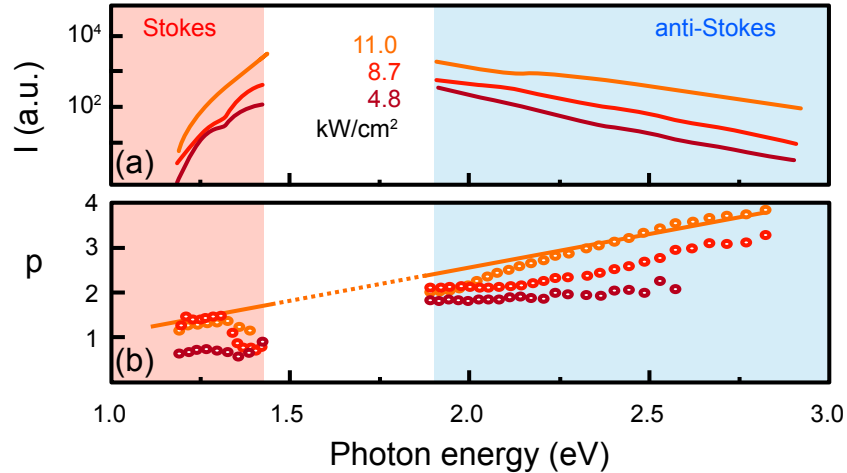


Fig. 1.4.7. (a) Emission spectra of a small particle aggregate on a glass surface for increasing irradiation (dark red, 4.8 kW/cm²; red, 8.7 kW/cm²; orange, 11.0 kW/cm²). Scattered light is cut off by filters. (b) Power-law exponents p for several laser powers over a limited range of irradiation (dark red, 1.8 – 4.9 kW/cm²; red, 2.6 – 8.7 kW/cm²; orange, 4.5 – 11.0 kW/cm²). Adapted with permission from [10]. Copyright 2017 American Chemical Society.

In the same work, a comparison was made between the luminescent interband transitions, the inelastic light scattering and the luminescent intraband transitions models for two different substrates (glass and glass/ITO) as well as the corresponding fit according to each model. Only intraband luminescence seems to be fully compatible with measured values.

As already presented, the nonlinear photoluminescence is still matter of discussion and can be interpreted as the result of a linear, multi-photon or noninteger nonlinear interaction depending on the incident laser power excitation and on the studied spectral range. Many aspects of such optical phenomenon are not fully understood and unveiling the mechanisms behind them remains a theoretical and experimental challenge.

1.5 Conclusion

Summarizing this chapter, the main concepts of the rapidly growing field of linear and nonlinear plasmonics, as well as their close connection to optical antennas have been reviewed. It is unquestionable the role of nanoantennas as a powerful tool for manipulating light in the nanoscale and their broad range of applications. On the other hand, the strong nonlinearities consequence of the large field enhancement in plasmonic metals nanostructures could open the way to scale down the footprint of nonlinear components allowing the development of integrable photonic devices.

Despite the known broad potentiality of nonlinear plasmonics, only a small fraction of the work is focused on decoding the mechanisms behind nonlinear photoluminescence, with most of the studies centered on its imaging capabilities. N-PL has proven to be a complex process that involves several nonlinear phenomena and which fundamental nature is still under discussion. In our study, we have focused mainly on gold thanks to its remarkable stability, relatively low loss in the visible and NIR parts of the spectrum and of course its strong nonlinear photoluminescence.

In the next chapters, the scope will be on going deeper into the nonlinear photoluminescence underlying mechanisms and the convenient control of such mechanisms by modifying the electrical properties.

1.5. Conclusion

Electrical command of the linear and nonlinear responses of plasmonic antennas

2.1 Introduction

Nowadays, electronic transistors have shrunk to a few nanometers allowing for very large scale integration. Nevertheless, there are still some challenges to overcome such as heating effects and a limited processing speed [153]. Conversely, photonics offers very high speed operations but is restricted in size by the law of diffraction in conventional optics [31]. Combining photonics and electronics could lead then to smaller and faster processing devices [154]. In this direction, plasmonics structures emerge as a possible solution to bridge the size mismatch between photonics and electronics [46, 155]. SPPs can concentrate and consequently boost electromagnetic fields to magnitudes comparable to the intra-atomic electric field giving rise to highly localized nonlinear processes [15]. Additionally, nanometer-scale plasmonic lasers based on nanowires or quantum dots may lead to integrated coherent light sources [40, 156]. Furthermore, their conductive nature offers a range of secondary functions and adds another degree of control by applying electric fields or injecting currents. Optical and electrical operation can be performed simultaneously, thereby simplifying many optoelectronic processes. Therefore, plasmonic nanostructures match on the description of a highly size-reduced device capable of bringing electronics and photonics together on a single platform.

In this chapter, some active plasmonic devices are presented including our own work on an hybrid electro-plasmonic device based on gold optical antennas where the fabrication protocol is included. The devices' operation and the physics mechanisms behind it are also explained. In our particular case, we demonstrate the capability to control the optical properties of plasmonic gap antennas by applying static electric fields. As it will be shown in the next sections of the chapter, an applied electric field can modulate the nonlinear emission and to a minor extent the linear scattering. A complete overview of the possible underlying mechanisms of such effects is made. Finally, conclusions are presented.

2.2 Active devices based on plasmonic metals

Metals display a whole range of advantageous physical properties such as high electrical and thermal conductivity, reliable mechanical stability, high temperature stability, and in the case

2.2. Active devices based on plasmonic metals

of plasmonic metals, high confinement of light. This allows metals to perform multiple functions at the same time. However, the design of plasmonic and nanophotonic circuitry involves overcoming two issues: high metal losses and the dynamic manipulation of the SPPs and the subsequent optical responses. For the first issue, several strategies are being explored to mitigate the losses. For instance, the use of media with optical gain provides some improvement in this matter [157, 158]. Advances in fabrication techniques also allow the minimization of defects and surface roughness [159] and thus losses. Furthermore, the plasmonic losses could be compensated by the tinier dimensions of nonlinear plasmonic devices. New plasmonic materials such as complex oxides could also reduce losses providing higher field concentrations and stronger resonances. The second issue is on the focus of this thesis and it is, perhaps, the most critical and interesting step towards the realization of practical applications. Evidently, the achievement of elemental components such as couplers, active multiplexers, modulators or switches requires the on-demand, dynamic and external manipulation of the optical properties. Such manipulation can be directly performed over the plasmonic structures themselves or over their surrounding media [11]. In the first case, the change can be induced either on the intrinsic metal optical properties [160, 161] or by changing the physical interplay between structures (tunable gaps and distances) [162]. In the second case, the active control is based on the sensitive dependence of plasmons on the surrounding environment [163–167]. In this context, multiple efforts are being made to find the most suitable control parameters including optical signals [163, 168, 169], temperature [164, 170–172], magnetic [167] and electric fields [166, 173–178], some of which are presented below. Naturally, every implementation has its pros and cons determined by the specific targeted application and a fair comparison between them is beyond the scope of this thesis. Generally there is a trade off between modulation speed, circuit integrability, stability and modulation depth. For instance, all-optical command provides the benefit to dynamically manipulate coherent linear and nonlinear signals at ultrafast time scales, however, their implementation in a photonic circuit architecture is not viable. Similarly, the command of the temperature imposes difficulties along with the usually slower response. Magnetic-controlled devices, on the other hand, involve the utilization of very high magnetic fields which is certainly not convenient. Fortunately, the dual functionality of plasmonic nanostructures concerning electrical conduction and nanooptical features enables a broad range of electro-optical operation and integration possibilities, mostly given by the predominant use of electric signals in digital devices. In summary, the electrical command of the plasmonic responses could offer an interesting opportunity for active linear and nonlinear optics way beyond the subwavelength scale and could also open up numerous applications in the framework of compact photonic devices for signal and information processing.

2.2.1 Electrically controlled plasmonic devices

So far, few studies explore the control of optical properties on metal nanostructures by electrical means. Usually, a plasmonic metal is interfaced with electro-refractive media such as carrier-injected or depleted semiconductors [174, 179], electro-optic polymers [176] or liquid crystals [165, 180, 181]. In all the cases, the refractive index of the adjacent dielectric medium is modified and can induce a change in the system. Specifically, in ref. [174], the transmission coefficient of a metal-metal oxide semiconductor (MOS)-metal waveguide structure is electrically manipulated. The waveguide supports photonic and plasmonic modes that can interfere. Applying a bias drives the MOS into accumulation modifying the index of the silicon and thus the photonic mode and the transmission. Remarkably, the device is low power consuming and very compact, however, the modulation depth is not very high. Randhawa and co-workers [176] brought about a plasmonic switch based on a dielectric loaded plasmonic ring resonator. The

refractive index of an electro-optic material (doped PMMA) is changed by the action of a modulating voltage via the Pockels effect [92] in which the birefringence is proportional to the electric field. An interesting property of this and other devices based on the Pockels effect is the ultra-low energy required for operation which is not limited in theory.

Regarding liquid crystals, electric fields produce a strong dipolar-like response thanks to their elongated shape which also translates into a large and tunable birefringence. Dickson *et al.* [180] achieve electrical modulation of the optical transmission properties on perforated gold films adjacent to liquid crystals. White light excites SPP modes and an electric field reorients the liquid crystal molecules resulting in changes of the surface plasmon dispersion relation and consequently modifying the excitation conditions. The characteristic response time of this device remains, however, relatively slow.

Active plasmonics is also achieved by electrochemically changing the refractive index of conductive polymers. The electronic structure and dielectric functions of these materials are easily changed by controlling their redox reactions. For instance, the localized surface plasmon resonance shape and position of gold nanoparticle arrays can be fully controlled by switching between oxidized and reduced states of the polymer [166]. A similar mechanism is used to modulate the absorption of an electro-chromic material placed on a nanoslit waveguide propagating SPPs [177]. The material is also switched between absorbing oxidized and transparent reduced states. A limitation of this approach is the electrochemical corrosion of the involved plasmonic nanostructures and the requirement of specific polymers.

Electrical control of the plasmonic properties is commonly accomplished in tunable metasurfaces. In a work of Thyagarajan *et al.* [182], the optical extinction of plasmonic metasurfaces is controlled by electric fields as low as 1 mV/nm triggered by the transport of silver ions.

As demonstrated recently by Maniyara *et al.* [183], applying an electrostatic voltage on ultra thin gold ribbons (3 nm thick) embedded in an ion gel can highly tune their plasmonic resonance ($\Delta\lambda = 200$ nm). The wavelength shift $\Delta\lambda$ results from the substantial change in the effective surface density of conduction electrons. The shift depends on the sign of the applied voltage. Additionally, the optical transmission is also modulated which can be associated with an effective modification of the optical damping.

Another kind of electrically controlled nonlinear plasmonic devices consists on nanoscale cavities formed in metallic structures to enhance the optical fields and to facilitate the application of very high electric fields with chip-level voltage signals. For instance, the manipulation of second harmonic generation by a DC electric field in bulky optical crystals known as electric-field-induced second harmonic generation (EFISH) involves huge voltages and high power lasers in order to be detectable. Contrarily, EFISH in nanostructures is highly sensitive to voltages as small as a few volts thanks to the nanometric separation between the constituent electrodes of the active device [184–186]. Cai *et al.* [178] fabricated a nanocavity consisting of a nanoslit resonator cut through a metal film surrounded by an engineered periodic grating-based optical antenna to enhance the emission (see figure 2.2.1(a)).

Fabry-Pérot resonances of the SPPs combined with the Bragg grating resonance enhance the electromagnetic energy density by a factor of several tens. The slit is around 100 nm wide thus low voltages across result in very high control fields. The nanocavity is filled with a dielectric medium (PMMA, poly-methyl methacrylate) with second- and third-order nonlinear susceptibilities responsible for second harmonic generation and EFISH respectively. The nonlinear polarization and SHG intensity are expressed as

$$I_{2\omega} \propto |P_{2\omega}|^2 \propto |\chi^{(2)} + \chi^{(3)} E_c|^2 I_\omega^2 \quad (2.2.1)$$

where E_c is the control field. Then the RHS of the formula contains a voltage-insensitive term $[\chi^{(2)} I_\omega^2]^2$ that corresponds to ordinary SHG, but also extra voltage-controlled terms

2.2. Active devices based on plasmonic metals

$\{[\chi^{(3)}E_c]^2 + 2\chi^{(2)}\chi^{(3)}E_c\}I_\omega^2$. Figure 2.2.1(b) shows a voltage-dependent nonlinear generation with a linear trend of $\approx 7\%/volt$. The quasi-linear dependence on the control field implies that the cross term $\chi^{(2)}\chi^{(3)}E_c$ dominates over the quadratic term $[\chi^{(3)}E_c]^2$.

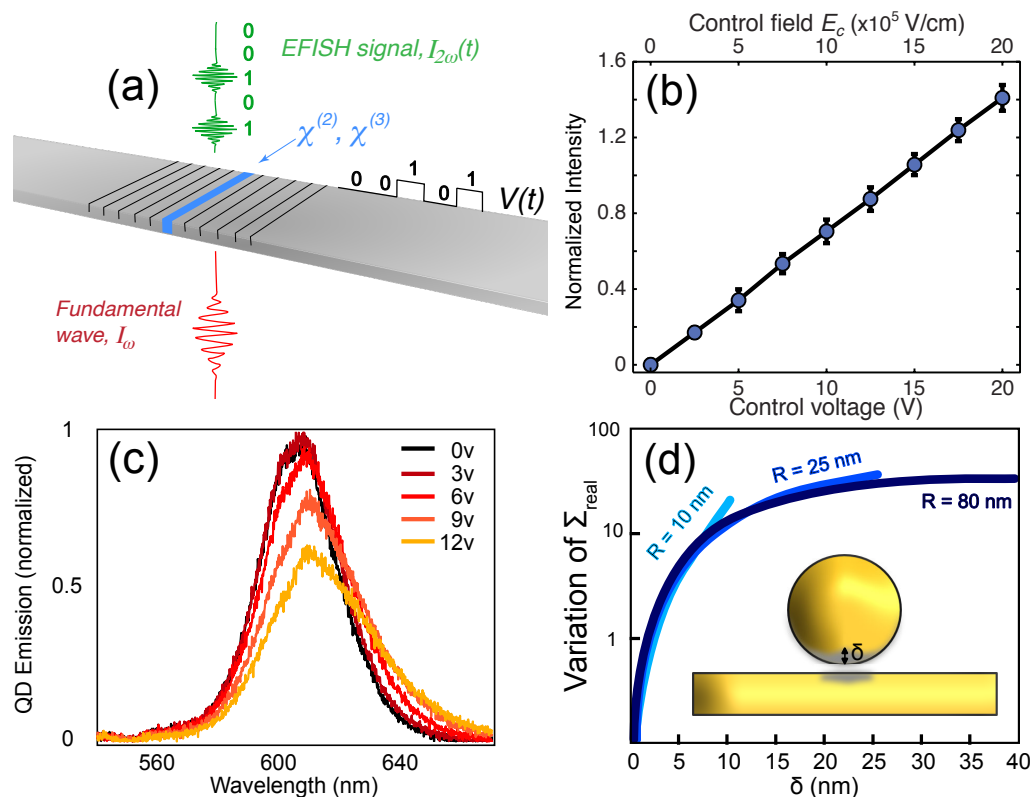


Fig. 2.2.1. (a) Schematic of a plasmonic EFISH device. A gold nanoslit filled with a dielectric medium is surrounded by a grating-based optical antenna. The two electrodes are connected to external circuits for electrical control. (b) Normalized change in the frequency doubled intensity versus the external applied voltage. Figures adapted with permission from [178]. (c) Measured fluorescence emission spectra for different applied DC bias voltages across the nanogap filled with quantum dots. Figure adapted by permission from [184]. Copyright 2011. (d) Dielectric function variation plotted versus δ for three sphere radii, the inset shows the effect of the strong electric field on the sphere. Figure adapted with permission from [160]. Copyright 2016 by the American Physical Society.

A very similar configuration has been also implemented by the same group [184]. Fluorescence emitters (quantum dots) placed within the metallic nanocavity are submitted to moderate bias to change their emission properties. Their radiative strength and spectral peak location are successfully tuned by means of the quantum-confined Stark effect [187] and luminescence quenching as shown in Fig. 2.2.1(c). The applied field across the gap red-shifts and decreases the quantum dots emission. The spectral shift increases quadratically with the voltage and saturates for large voltage values. The intensity drop comes from the electric-field-induced dissociation of electron-hole pairs followed by non-radiative recombination processes [188].

Strong electric fields produced in small junctions have also shown to strongly modify the $\chi^{(3)}$ susceptibility of a gold tip-sample in a scanning tunneling microscope (STM) system thus dynamically affecting the optical response [160]. In this case, junction plasmons are electrically excited by the inelastic electron tunneling of the STM. SPPs scatter to radiation via surface roughness features. The expected light emission is highly affected by the DC field due to local surface charge screening and an effective reduction of the density of free electrons available to take part in the plasmon oscillations. Figure 2.2.1(d) shows the modified dielectric function as

a function of the parameter δ which denotes the position in the electrically affected volume of the sphere as shown in the inset of Fig. 2.2.1(d).

In our particular research, we demonstrate an active plasmonic device based on gold optical gap antennas with different shapes. Figures 2.2.2(a) and (b) show a schematic representation and a graphic image of the actual device respectively. Figures 2.2.2(c,d,e) additionally show scanning electron microscope (SEM) micrographs of the nanoantennas. This configuration brings several advantages in the framework of electro-photonic applications. Firstly, the nanometric size of the gap that defines the antennas allows very high electric fields $10^7 - 10^9$ V/m with relatively low applied voltages (1 – 20 V). Secondly, the geometry of the antenna (see Fig. 2.2.2(e)) enables huge enhancement of the optical fields and consequently improve inherently weak nonlinear processes which, as discussed in section 1.4, provide reduced power consumption and footprints. Moreover, the device can be realized through simple and standard nanofabrication techniques. Discarding the addition of a supplementary electro-refractive material provides further advantages. For example, liquid crystals tend to anchor to the surfaces limiting the alignment with the applied electric field and thus the change on the refractive index [189]. Uncluttered gold nanostructures also circumvent the photo-degradation exhibited by photo-chromic materials [163].

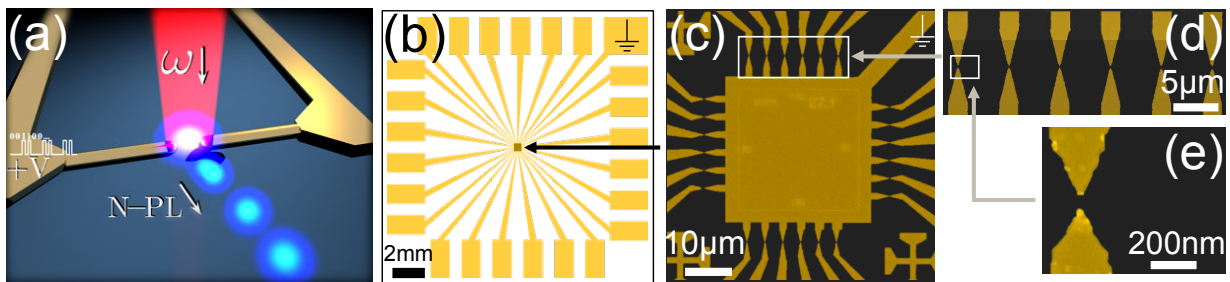


Fig. 2.2.2. Electrically controlled plasmonic device. (a) Schematic representation of the device operation. Two gold electrodes are separated by a nanometric gap to form an optical gap antenna. A femtosecond laser excites the structure and generates N-PL which is modulated by an applied electric field across the gap. (b) Real graphic representation of the plasmonic device. SEM micrographs of (c) all the nanoantennas, (d) zoomed at the top 6 nanoantennas and (e) a single nanoantenna.

In our device, when an electric field is applied through the gap, the nonlinear photoluminescence produced by a pulsed femtosecond laser is deeply modulated. Precise control of the laser position or the polarity of the field allows either to quench or to enhance the nonlinear emission. In a secondary study, the elastically scattered light from the same device is also affected by the electric fields.

In the next section, the experimental methods are completely outlined. The fabrication process as well as the experimental setup are presented in detail.

2.3 Experimental methods

The device is built using a top-down fabrication method based on e-beam and UV lithography and a lift-off process [190]. In particular, two-steps lithography is applied on a standard borosilicate glass cover slip. The smaller features and the nanoantennas are fabricated by electron beam lithography (EBL) with bow-tie shape like the one already showed in figure 2.2.2(e). A subsequent UV lithography (UVL) process defines a set of macroscopic electrodes connected to the nanoantennas.

2.3. Experimental methods

Concerning the experimental setup, the hybrid nature of the device imposes electrical and optical control over it. The system is mainly based on a scanning confocal microscope which allows to construct nonlinear emission maps by systematically exciting point by point the nanostructures and collecting the resulting optical response in a determined area. Wide-field optical imaging is performed too.

2.3.1 Fabrication of the electrically controlled plasmonic device

The nature of the device demands the fabrication of micro- and macro-structures in large areas combined with smaller nanostructured regions. The optical antennas require nanometer scale definition whereas the electrodes from μm to mm are necessary to facilitate the electrical contacting. The micro- and mili-metric scale features are more efficiently defined by high-throughput methods like UVL while serial nanofabrication methods like EBL, although slower, are needed for the nanometric scale features. Consequently, the device is fabricated following several steps combining EBL and UVL: resist coating, e-beam or UV exposure, development, material deposition and finally lift-off of unwanted materials.

In our experiment, optical antennas are generally conceived seeking to maximize the enhancement and concentration of the optical and DC fields respectively. In the case of the bow-tie antennas (see Sec. 1.2.6), they consist of two triangles separated by a small gap and facing tip to tip. Such configuration causes strong and confined field enhancement, it combines the plasmon resonant behavior of coupled nanoparticles pairs with the electromagnetic properties of sharp metal tips [77].

2.3.1.1 Optical gap antennas fabrication

The resist to be exposed consists on a double layer of the commonly used polymethylmethacrylate (PMMA) with different molecular weights (50 kDa and 200 kDa) totaling a thickness of ≈ 200 nm. Both PMMA layers are successively spin-coated on a glass coverslip (see table 2.3.1) and subsequently soft-baked in a hot plate at 150°C for 3 minutes. The double layer forms an undercut profile after exposure thus improving the lift-off. It is worth highlighting the fact that spin coating recipes were recently improved reducing the final speed and thus increasing the final thickness. Furthermore, piranha cleaning of the substrate showed to ameliorate the smoothness of the structures edges.

Table 2.3.1. Recipes for spin coating the two PMMA layers needed for e-beam lithography.

Step	First layer			Second layer		
	Time (s)	Acceleration (rpm/s)	Speed (rpm)	Time (s)	Acceleration (rpm/s)	Speed (rpm)
1	1	100	100	1	100	100
2	5	300	500	5	300	500
3	60	3000	5000	60	3000	4000

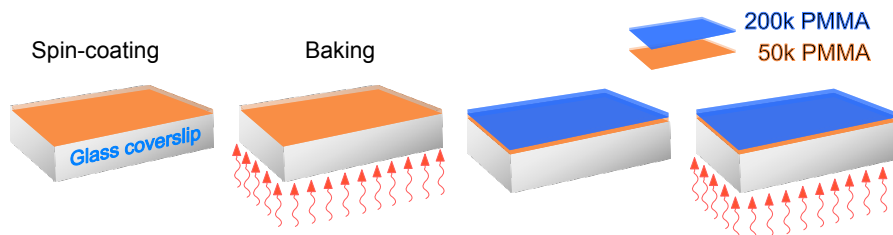


Fig. 2.3.1. Schematic representation of the spin-coating process for a double layer of PMMA.

The electron beam directly writes on the resist coating by using a raster or vector scan (Pioneer, e-line). The desired patterns are directly created from a standard computer-aided design (CAD) to reproduce the structures shown in figure 2.2.2(c). It is composed of 24 nanoantennas and a common ground electrode (top right corner), the crosses are alignment marks to be used for the UV lithography step. As the resist is positive, the exposed areas correspond to the yellow-colored areas in figure 2.2.2(c,d,e). These parts of the resist are removed in the development process by immersing the sample in an organic solvent (Allresist AR 600-56). The development time is precisely controlled by stopping the reaction with another solvent (Allresist AR 600-60). Just after, the patterned PMMA is used as a mask to deposit 3nm of titanium (Ti) and 50nm of gold (Au) by electron-beam and thermal evaporation respectively in a Plassys MEB400 evaporator. The Ti layer is used to improve the adhesion between the glass and the gold layer. Once the metal evaporation is done, the resist is taken off by means of a remover solvent (Allresist AR 600-71).

2.3.1.2 Contacting the optical antennas

Continuing with the fabrication protocol, the second step consists on the macroelectrodes (figure 2.2.2(b)). They allow to electrically connect the nanoantennas and for the seek of time and costs they are built following a standard UV lithography process (SUSS MicroTec MJB4). To start, a negative photoresist (MicroChemicals AZ nLOF 2070) is spin-coated on the coverslip with the previously fabricated nanoantennas following the recipe shown in the table 2.3.2.

Table 2.3.2. Recipes for spin coating the AZ nLOF 2070 photoresist.

Step	Time (s)	Acceleration (rpm/s)	Speed (rpm)
1	1	100	100
2	5	300	500
3	60	2500	3000

The sample is pre-baked at 110°C for 2 minutes. After aligning the nanoantennas and the common ground microelectrodes with the macroelectrodes of the UV mask, the sample is held in hard contact with the mask and exposed to an UV lamp (240 nm – 260 nm) for 2.2 s to deliver ≈ 65 mJ. The exposure is again followed by post-baking for 5 minutes at 110°C and a development process in which AZ MIF 826 (MicroChemicals) is used as developer and deionized water as stopper.

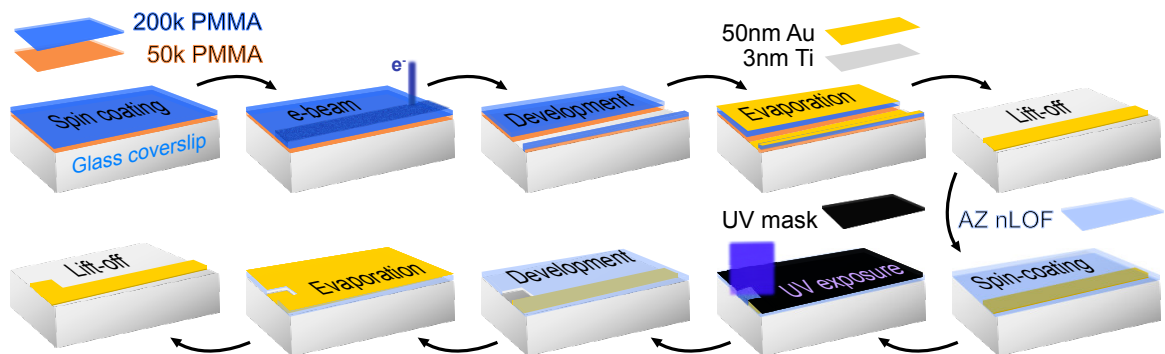


Fig. 2.3.2. Schematic representation of the complete fabrication process of the plasmonic device. A combination of e-beam and UV lithography defines a set of nanoantennas and the connecting electrodes respectively.

2.3. Experimental methods

Once again, titanium (3 nm) and gold (50 nm) are evaporated adopting the same procedure. The lift off is carried out in acetone or NMP (1-Methyl-2-pyrrolidone, commercially available as remover 1165) at 70°C. The complete fabrication process is summarized in figure 2.3.2.

2.3.2 Nonlinear photoluminescence confocal microscopy

Contrarily to traditional widefield optical microscopes, in which the entire sample is illuminated at the same time, in confocal microscopy the sample is scanned relative to a point-like light source (usually a focused laser). A simplified version of the setup is schematically depicted in figure 2.3.3(b). Briefly, an electrical and an optical parts are controlled and monitored respectively by a scanning probe microscope (SPM) control system (RHK SPM1000).

An inverted nonlinear optical microscope equipped with a two-axis piezo-electric (MadCity labs, Nano LP100) allows to map the sample and monitor the N-PL in the focal region. The SPM1000 has several high voltage outputs that provide the control voltages to precisely displace the piezo-stage. While the scanning is taking place, a feedback loop keeps the sample-objective distance constant. The maps are produced by simultaneously exciting and measuring pixel by pixel the nonlinear optical emission of the nanostructures as they are scanned at the laser focal point.

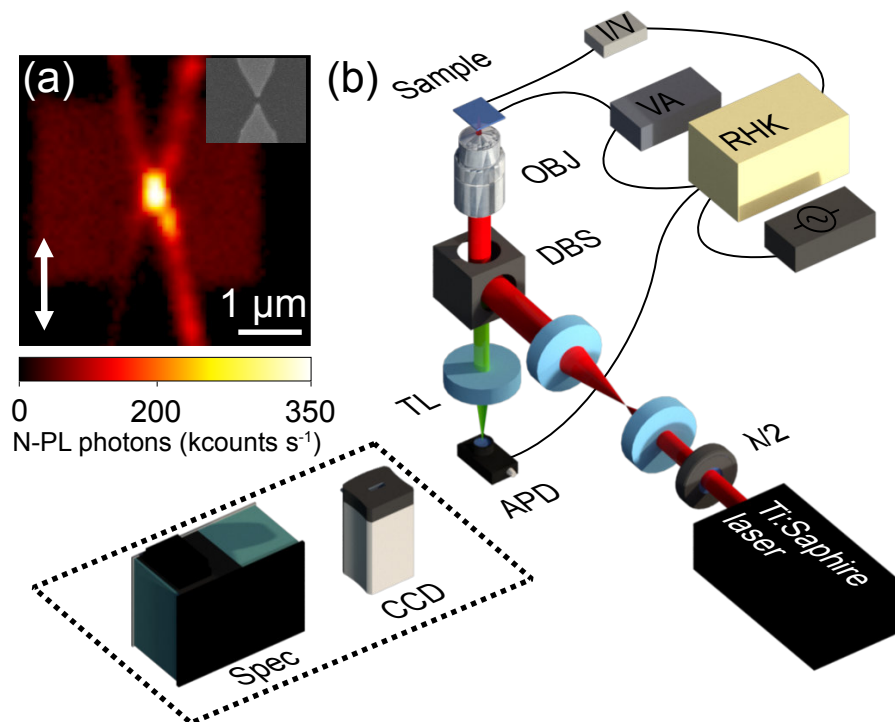


Fig. 2.3.3. (a) Nonlinear photoluminescence confocal map of a bow-tie optical antenna. The inset shows a SEM micrograph of the same structure. (b) Experimental setup. Ti:Sapphire laser (Chameleon, Coherent) at a wavelength of 810nm, ≈ 120 fs pulses and 80 MHz repetition rate. $\lambda/2$ Half wave plate. DBS Dichroic beam splitter, TL Tube lens, APD Avalanche photodiode, OBJ 1.49 100x numerical aperture objective, I/V converter, VA Voltage amplifier, RHK Scanning probe microscope control system, Function generator, Spec Spectrometer, CCD charge-coupled device camera.

Specifically, gold optical gap antennas are excited with a near infrared (NIR) pulsed femtosecond laser (Chameleon, Coherent) centered at $\lambda = 810$ nm. A home-built beam expander filters and increases the beam width to overfill the back lens of a high numerical aperture (NA) oil immersion objective (Nikon, 100x, NA = 1.49) equipped with a correction collar to avoid

aberration due to substrate thickness changes. The beam is tightly focused and assumed to be point-like enough for confocal microscopy, therefore no additional aperture is introduced in the excitation path. The beam power is adjusted using a half-wave plate and a polarized cube, additionally, a set of neutral density filters can be used. Another half-wave plate controls the linearly polarized laser beam angle depending on the antenna orientation. The N-PL is collected through the same objective and separated from the excitation light and from second harmonic generation by a dichroic beam splitter (Chroma) and a long-pass filter respectively. N-PL is then directed to an avalanche photodiode (APD, Perkin Elmer) placed at one of the ports of the microscope. As illustrated in the last chapter, the N-PL emission spans a broad range of wavelengths that certainly overpass the detection range of the APDs. The recorded counts on the APD are a convolution of the photon detection efficiency of the apparatus and the N-PL emission spectrum. In some experiments presented in this work the signal output is switched to other ports of the microscope and directed to a spectrometer (Andor Shamrock SR-303i) equipped with a charge-coupled device (CCD) camera (iDus DU401-BR-DD). A diffraction grating with 800 nm blaze and 150 lines/mm is used to obtain a detection spectral range of ≈ 600 nm. Another port directs the output signal to an additional CCD camera (Hamamatsu C4742-80-12-AG). Second harmonic generation is directed to an extra APD (MPD). The APD detectors are connected to a photon counting port in the SPM1000. Given the nonlinear nature of the N-PL process, most of the optical response is localized to the focus of the laser beam, therefore positioning the APDs at a conjugated plane allows to dispense the use of a detection pinhole [191]. The photon counts registered at the detectors for each pixel generate a 2D image. The resolution limit is given by the point spread function of the system.

Figure 2.3.3(a) shows the N-PL map of a typical optical gap antenna composing the plasmonic device, the color indicates the N-PL intensity in that specific point. The inset shows the corresponding SEM image of the structure and the double arrow indicates the incident polarization. The nonlinear photoluminescence distribution in the map is dominated by emission maxima at the gap region and the edges of the antennas due to stronger field localization. The brighter square around the gap of the bow-tie antenna is produced by electron beam induced contamination, carbonaceous material deposits over the sample surface previously bombarded by the electron beam while doing SEM imaging. N-PL is a nonlinear process particularly adapted for mapping out optical antennas with highly localized fields [49]. Furthermore, N-PL mapping over a gold antenna gives valuable direct information about its diffraction-limited modal distribution [8, 80] as well as the surface plasmon local density of states [192].

On the electrical side, a function generator applies different types of electrical waveforms over a defined set of frequencies with voltage amplitudes ranging 0 – 10 V. For the larger gaps, the amplitude is multiplied by a voltage amplifier. Current tunneling through the gap which may be detected, is recorded with the SPM1000 after being amplified by a current voltage (I/V) converter.

Once the nanoantenna is scanned and the specific DC electric fields are set, the laser is precisely located somewhere in the gap region where the electric and optical fields are the strongest, and where most of the times the N-PL emission is affected by the electric field.

2.4 Controlling the Nonlinear Photoluminescence

As already stated, the excitation of gold nanostructures with a NIR pulsed laser generates N-PL. In the following, the device introduced in the last sections which is capable of modulating the nonlinear response by activating an electric field in optical antennas will be studied. The experiment involves several degrees of freedom (control) on the device operation. Mastering parameters like the geometry of the nanostructure, the incident laser characteristics (wavelength,

2.4. Controlling the Nonlinear Photoluminescence

power, polarization) and the applied DC electric field are critical for a successful command of the nonlinear photoluminescence.

The obvious starting point concerns the geometry of the nanoantenna and consists firstly on finding the critical gap for which the DC field is strong enough to modify the nonlinear emission and moderate enough to avoid the electrical breakdown of the nanostructure. Several nanoantennas were studied and only those with gaps around or smaller than ≈ 100 nm showed modulation of the N-PL at fields within a safe range. Figure 2.4.1 compares two different nanoantennas of the same device with ≈ 100 nm (a,d) and ≈ 150 nm (b,e) gaps. The laser is positioned in the gap region and the time trace of the N-PL is recorded while a voltage ramping from 2.5 – 10 volts and immediately after from 10 – 2.5 volts is applied across the gap of the nanoantennas. The N-PL graphs include the smoothed data using a moving average filter to reduce the noise and make it clearer to the eye. Assuming uniform and planar edges of the antennas, the corresponding electric fields range from $E_{100\text{nm}} \approx 0.25 - 1.0 \times 10^8$ V/m for (a) and from $E_{150\text{nm}} \approx 0.17 - 0.7 \times 10^8$ V/m for (b). In the narrow sense, the precise electric field values are unknown, they will be highly dependent on the specific geometry of each nanoantenna.

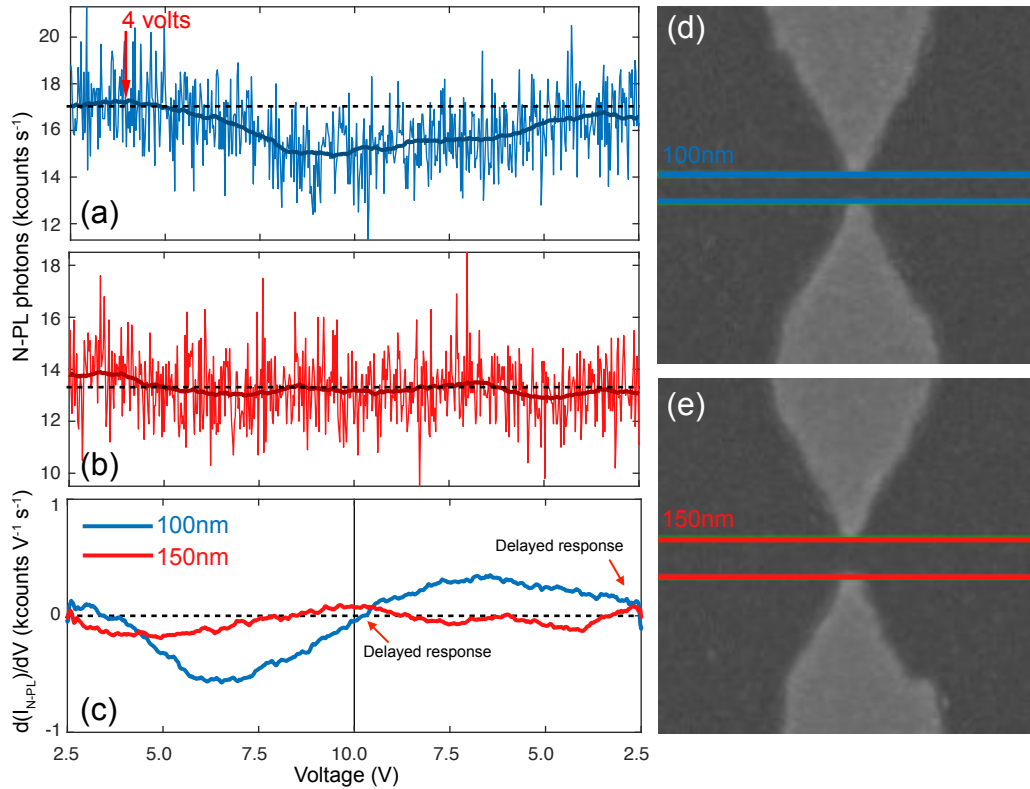


Fig. 2.4.1. Recorded N-PL in the gap region as a function of the applied voltage for nanoantennas with (a) ≈ 100 nm and (b) ≈ 150 nm gaps. (c) Change rate of the N-PL with the voltage applied. (d,e) SEM micrographs of typical studied nanoantennas with gaps similar to (a) and (b). The dotted lines indicate the zero bias N-PL in (a) and (b) and the zero N-PL change rate in (c)

The effect of the electric field on the N-PL is noticeable in the case of (a), at around 4 volts (0.4×10^8 V/m) the nonlinear emission starts to decrease beyond the baseline indicated by a dashed line, the N-PL goes from ≈ 17 kcounts/s down to ≈ 14 kcounts/s roughly following the voltage trend. Contrarily, in the case of the nanoantenna (b), the electric field is not strong enough to have an effect on the N-PL. The N-PL signal oscillates around the baseline value. Furthermore, the instantaneous N-PL change rate with the voltage D_V is extracted by calculating the derivative of the N-PL photon counts as a function of the applied voltage, i.e.

$D_V = d(I_{N-PL})/dV$ (See 2.4.1(c)). As expected for the antenna with the smaller gap, $|D_V|$ increases for voltages values comprised within $4 \text{ V} \lesssim V \lesssim 7.5 \text{ V}$. For greater voltage values the rate diminishes until reaching $D_V = 0$ which corresponds to a critical point and to the minimum N-PL value under the action of a $\approx 10 \text{ V}$ potential. Notably, such critical point does not fully coincide with the voltage sweep inversion point ($V = 10 \text{ V}$). Carefully looking at Fig. 2.4.1(c), it reveals a delayed response of the N-PL modulation with the electric field. Taking into account that the voltage varies at a rate of 1.25 V/s , the delay is roughly on the order of milliseconds in these experimental conditions, further discussions throughout this chapter will clarify this point. Comparatively in the case of the 150 nm gap nanoantenna, the change rate oscillates around the zero value with negligible values dictated by the noise in the signal.

As will be presented in the next sections, many factors influence the final impact of the electric field on the nonlinear emission. However, decreasing the gap size to dimensions below the critical size of 100 nm is crucial to get modulation of the N-PL. For instance, figure 2.4.2 shows another much clearer situation where the N-PL emission is drastically changed by the applied electric field in a nanoantenna with a gap of around 75 nm . In this case, the laser spot is again positioned at the gap region and the N-PL emission is recorded for 10 s while, instead of ramping the electric signal up, the electric field alternates between OFF (0 V/m) and ON ($1.6 \times 10^8 \text{ V/m}$) states. It is evident the sharp variation of the nonlinear emission as soon as the bias is activated at $t = 4 \text{ s}$, the N-PL yield is increased from the base value $I_{N-PL}(E = 0) \approx 280 \text{ kcounts/s}$ up to $I_{N-PL}(E = E_0) \approx 400 \text{ kcounts/s}$. The modulation depth $\Delta_{N-PL}(E = E_0) = 120 \text{ kcounts/s}$ or 43% which is a much greater variation than before. The N-PL change is anew not immediate after the voltage is applied or withdrawn. The time trace of Fig. 2.4.2 demonstrates an asymmetric dynamics with slower response times when removing the electric field.

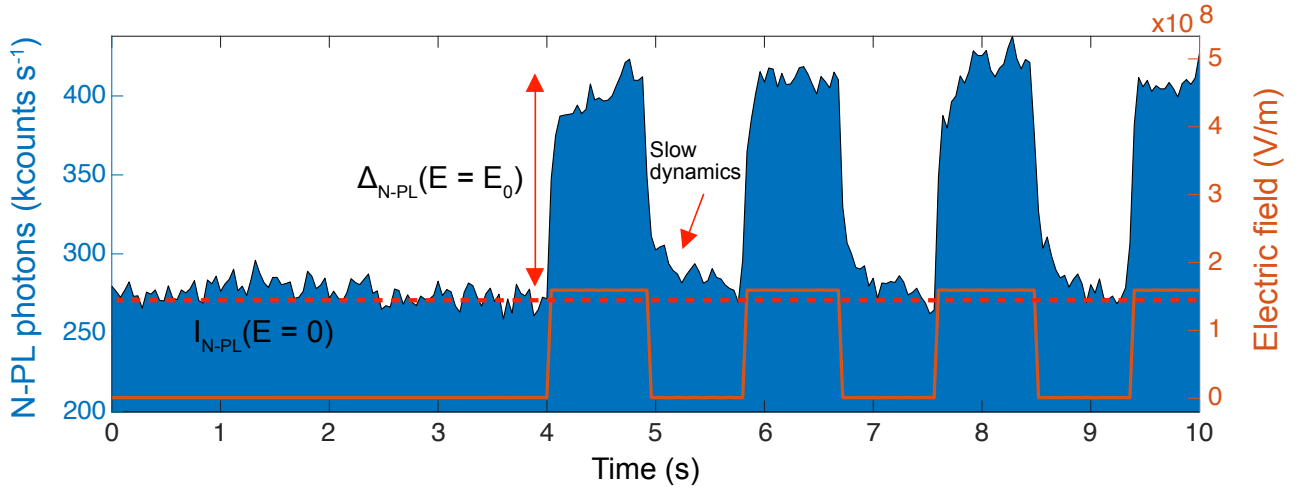


Fig. 2.4.2. In blue, the time trace of the N-PL emission (left ordinate axis) for a 75 nm gap nanoantenna. In orange, the applied squared electrical signal (right ordinate axis). The red dashed line and the double red arrow indicate approximately the values of $I_{N-PL}(E = 0)$ and $\Delta_{N-PL}(E = E_0)$ respectively.

At this stage of the discussion, let us review the implications of the results shown so far. Firstly, the data shows unequivocally the successful modulation of the N-PL in the vicinity of the optical antennas' gap by the simple effect of high electric fields across them, providing thus an external electrical handle to manipulate the nonlinear activity. Secondly, the underlying electrical mechanism responsible for modifying the N-PL occurs at a certain voltage threshold since there is no evidence of N-PL modulation for $V < 4 \text{ V}$ in the particular experiment

2.4. Controlling the Nonlinear Photoluminescence

summarized in Fig. 2.4.1. However, many questions must be addressed. For instance, the modulation process has a relatively slow dynamics compared to the extremely fast intrinsic response time of the involved nonlinear optical processes [22, 23]. Furthermore, the bias effect on the N-PL showed in fig. 2.4.1 is completely reversed with respect to the one showed in fig. 2.4.2. In the first case, the voltage weakens the N-PL emission whereas in the latter it induces an increment. This and some other issues will be further discussed throughout the chapter.

2.4.1 Evolution of the N-PL yield with the electric field

In figure 2.4.3(a), the effect of the variation of the electric field on the generated N-PL in the 75 nm gap of an optical antenna is presented. The amplitude of a squared electrical input is varied in the range of 4 – 20 V ($0.5 - 2.7 \times 10^8$ V/m) with a period of 1 s and an average laser power of 1.4 GW/m^2 . The inset of the figure is a confocal N-PL map of the nanoantenna previously constructed in order to locate the highest emission points and precisely fix the excitation laser in those positions, the blue arrow indicates the laser position for that specific acquired data set. Here and in the rest of the chapter, the polarization is set to maximize the N-PL modulation (indicated by double white arrow). The contour of the nanoantenna is outlined with dashed lines for better perception. As the DC field decreases ($0 \text{ s} \leq t \leq 10 \text{ s}$), the modulation depth decreases until it reaches a threshold voltage and disappears. From that point, the electric field starts to increase again ($10 \text{ s} \leq t \leq 20 \text{ s}$) and the modulation comes up. Fig. 2.4.3(b) summarizes the trend of the mean N-PL as a function of the applied electric field estimated during the on-state of the voltage duty cycle. The gray zone and the dotted line at $222 \text{ kcounts s}^{-1}$ is the mean flux of the N-PL calculated in the time sequence when the signal is unperturbed by the voltage. The right axis shows the modulation depth $\Delta_{\text{N-PL}}(E = E_0)$ normalized by the N-PL intensity at no bias applied $I_{\text{N-PL}}(E = 0)$ resulting in a relative modulation Δ_r . The modulation goes from 5% up to 23% of $I_{\text{N-PL}}(E = 0)$. A linear fit gives an approximate value of 8% variation of the N-PL yield per every 60 MV/m increment on the DC field. This trend varies in many situations, depending on the excitation point and on the nanoantenna it can reach modulations up to 400% within the same range of electric fields ($\approx 2 \times 10^8 \text{ V/m}$).

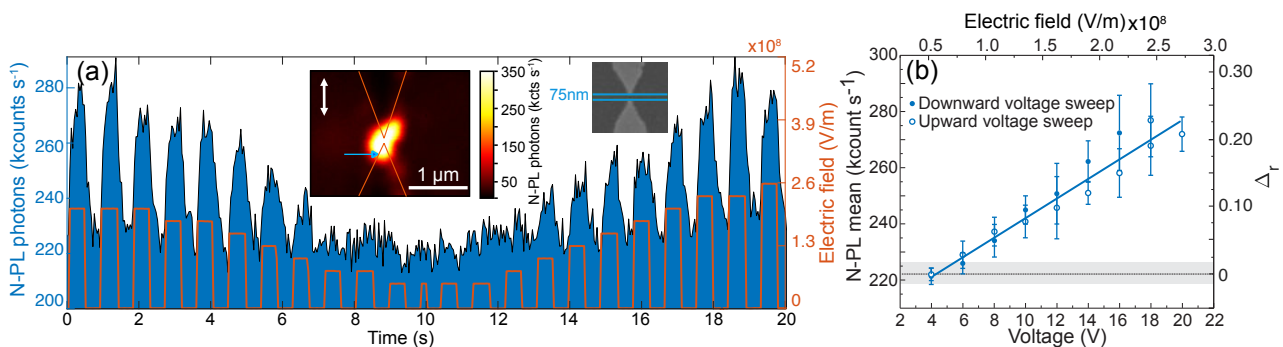


Fig. 2.4.3. (a) Time trace of the N-PL emission (blue shaded area and left axis) of the optical antenna under different applied electric fields (orange, right axis). The inset is a confocal map of the N-PL emission of the same optical antenna. The orange lines help the eye to see the nanostructure location. The blue arrow points to the acquisition area of the N-PL. A SEM image is also shown. (b) Evolution of N-PL mean rate (left axis) and the relative modulation depth Δ_r (right axis) during the on-state as a function of the voltage applied (lower scale) or electric field (upper scale) for the two voltage sweeps illustrated in (a). The horizontal dotted line and the gray zone indicate the off-state N-PL value and its standard deviation evaluated from $8 \text{ s} < t < 12 \text{ s}$ in (a). The solid line is a linear fit taking into account the complete data set.

The data obtained during the upward and downward sweep are reproducible indicating that neither the sampled voltage range nor the laser power irreversibly degraded the optical gap antenna. The dashed line is a linear fit to the data indicating that there is a proportionality between the amplitude of the bias and the nonlinear rate, a handle which may prove useful for realizing a commanded device.

The N-PL modulation efficiency is directly related to the exact location of the excitation beam with respect to the antenna feed gap. Typically, for a given bias voltage and gap size, the strength of the modulation strongly depends on the adjustment of the diffraction-limited observation area. Figures 2.4.4(a,b,c,d,e) show the time evolution of the N-PL signal when the sample is displaced to excite different locations around the feed gap as represented in Fig. 2.4.4(f). The electric field amplitude is kept constant and follows again a squared shape switching between ON and OFF states. In this experiment the gap is 75 nm. The dotted lines in the graphs indicate the approximate off-state N-PL rate (null amplitude). In Fig. 2.4.4(a), the displacement of the sample with respect to the focus favors the generation of N-PL signal on the positive electrode (point ‘a’) and the behavior observed in Fig. 2.4.2 and 2.4.3, where the on-state enhances the N-PL signal, is retrieved (in-phase). In Fig. 2.4.4(b), the sample is now slightly displaced to facilitate the N-PL response from the grounded electrode (point ‘b’). Clearly, the N-PL rate and the electric signal are now out-of-phase, the N-PL is no longer enhanced by the electric field but suffers from a significant reduction of its rate compared to its steady state value at $V = 0$ V. Changing the sample position to favor the laser focus incidence on the point ‘c’ and then on the point ‘d’ brings the response back to the in-phase and out-of-phase situations respectively (see Fig. 2.4.4(c) and Fig. 2.4.4(d)). This inversion of the N-PL modulation is systematically observed in several nanoantennas, the closer the focus is to the biased electrode, the more probable to get an in-phase response and vice versa. Such behavior suggests a process influenced by the symmetry of the system hence by the polarity of the field.

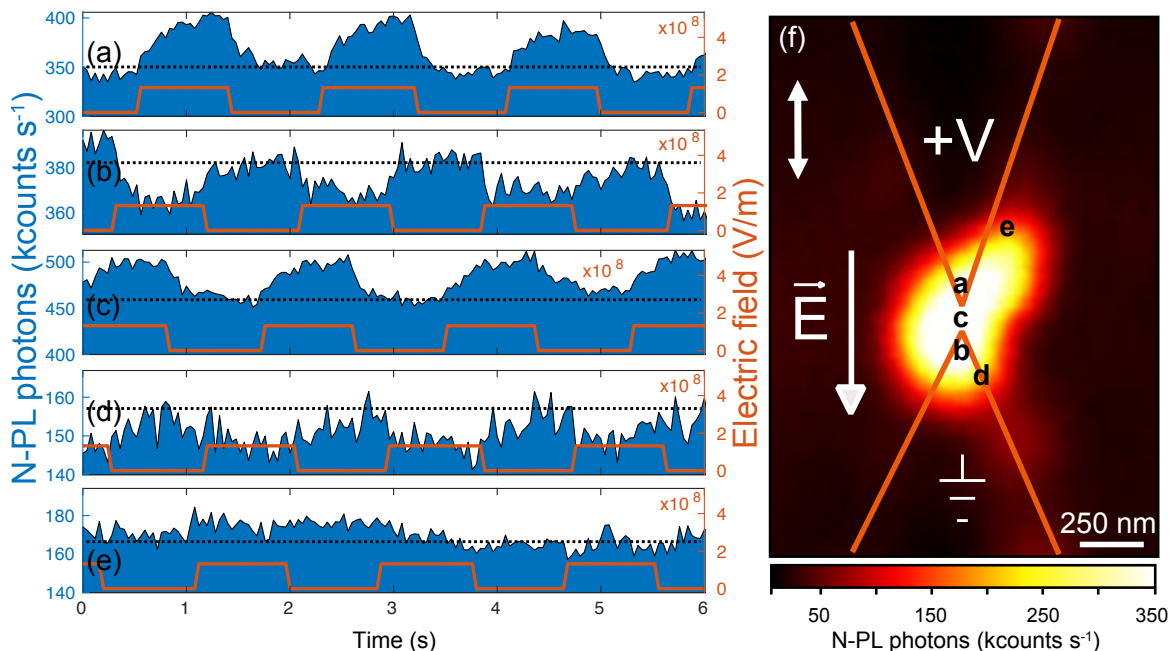


Fig. 2.4.4. (a,b,c,d,e) Corresponding time traces of the N-PL for each marked position in (b). The horizontal dashed line showing the approximated OFF state of the N-PL emission. (f) Confocal map of the N-PL emission of a 75 nm gap nanoantenna. The nanostructure is traced with orange lines. Each excitation point (laser tip position) is indicated with letters. The incident laser polarization is indicated by the double arrow.

2.4. Controlling the Nonlinear Photoluminescence

It is worth noting that the laser beam diameter exceeds the gap of the nanoantenna, meaning that both sides can be excited at the same time, then the observed modulation is the result of the addition of the two opposite responses and three different situations can occur: (i) both sides have inverted modulation depth (null net modulation), (ii) the biased side has better modulation (in-phase net modulation), (iii) the grounded side has better modulation (out-of-phase net modulation).

The second main observation points to the fact that the modulation strength will vary significantly depending on the excitation point as can be seen in Fig. 2.4.4(a,b,c,d,e). When the laser focus is away from the gap region (point ‘e’) the modulation is absent. This suggests a process ruled by the high electric field generated at the vicinity of the gap region.

If the inversion of the N-PL modulation is symmetric with respect to the side of the nanoantenna, the same effect should be noticeable by inverting the electric field polarity while keeping the sample position fixed (overlapping the ground electrode). This is indeed the case depicted in Fig. 2.4.5(a). The polarity of the field is systematically switched passing from a positive voltage (0 – 20V or 2.7×10^8 V/m) to a negative variation. The positive bias quenches the signal whereas the negative bias gives rise to an enhanced nonlinear signal.

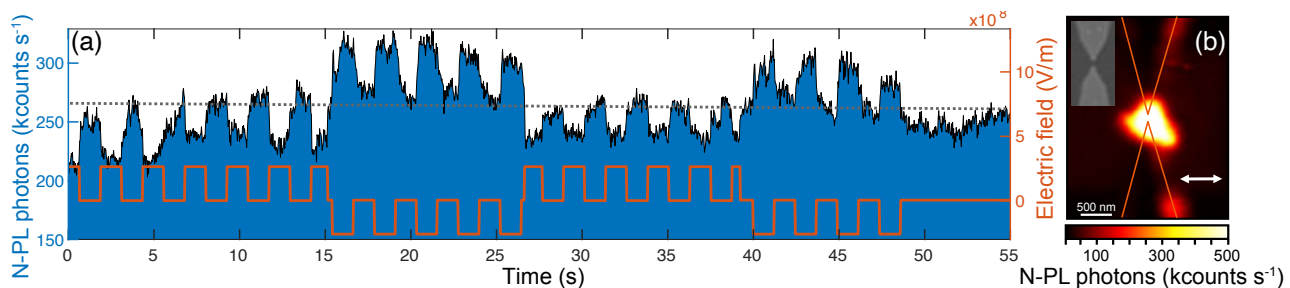


Fig. 2.4.5. Effect of the electric field polarity inversion on the recorded N-PL emission in the gap of a bow-tie antenna (100 nm gap). (a) Time trace of the N-PL and the electric signal. The dotted horizontal line refers to the no bias state. (b) N-PL confocal map of the nanoantenna. The inset shows an SEM micrograph of the antenna. The double arrow indicates the incident laser polarization.

To summarize, the modulation of the N-PL happens at locations of the antenna with the highest DC electric fields. Furthermore, the N-PL yield is directly related to the excited electrode. This inevitably interrogates on the role played by the displaced free electrons under the action of the electric field and implies that, as in an electric capacitor, the accumulation and depletion of charges can be important.

2.4.2 Optical antenna as a nanocapacitor

By obvious reasoning, an electrically contacted optical gap antenna acts as a nanocapacitor, in which the developed electric field across the gap causes the accumulation and depletion of free electrons on the grounded and biased terminals of the nanoantenna, respectively. In a simplified treatment, as an electric field is applied, the charges will accumulate in a plane of zero thickness at the air/electrode interface near to the gap. In reality, it has been shown that the displaced charges occupy a finite space on the order of a few angstroms [193] and a capacitance correction factor is needed [194]. Nevertheless, the well-known linear capacitance formula follows such approximation and is accurate enough for most of the structures. A quick calculation considering a parallel plates capacitor with an area of $A = (80 \times 50) \text{ nm}^2$ and a distance between the plates of $d = 50 \text{ nm}$ gives

$$C = \epsilon_0 \epsilon_r \frac{A}{d} = 1.8 \times 10^{-18} \text{ F} \quad (2.4.1)$$

where ϵ_0 is the permittivity of free space and ϵ_r is the relative permittivity of the dielectric medium between the plates. In this case, the terminals are on top of glass and their end faces are separated by air. Therefore, it is convenient to define an effective medium with $\epsilon_{\text{eff}} = (\epsilon_{\text{air}} + \epsilon_{\text{glass}})/2 \approx 2.5$.

More precisely, a modelization using finite element method (FEM) software package COMSOL Multiphysics[®] is developed in order to obtain the charge distribution inside the nanostructure (See Fig. 2.4.6(a)). It considers an ideal nanocapacitor with perfectly conductive electrodes, smooth interfaces and bow-tie shape mimicking the nanoantennas of the electroplasmionic device. The boundary conditions are as follows. Two gold terminals with a potential difference of 10 V between them are separated by a 50 nm gap. The gold structures are on a silica glass substrate ($W \times D \times H = 1.5 \mu\text{m} \times 1.5 \mu\text{m} \times 100 \text{ nm}$) and embedded in air. Figures 2.4.6(b,c,d) show a zoomed picture of the gap region with the calculated electric potential, field and charge distributions respectively. As expected, the norm of the field and consequently the charge density increases in the gap region. Figure 2.4.6(e) shows more precisely the charge density in the semicircle formed at the very end of the electrode reaching values close to 10^{-2} C/m^2 .

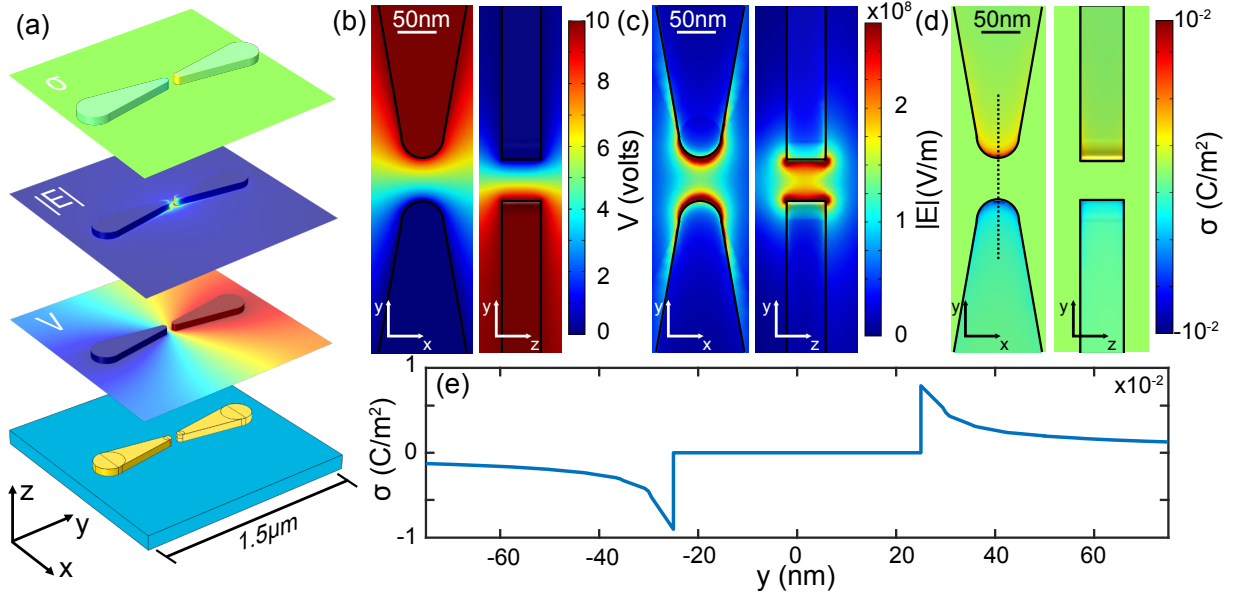


Fig. 2.4.6. COMSOL Multiphysics[®] simulation of a nanocapacitor with shape and dimensions similar to the studied nanoantennas. (a) Model configuration and different performed calculations. Electric (b) potential, (c) field and (d) surface charge density distribution in the gap region of the nanocapacitor. (e) Surface charge density along the dotted line indicated in (d).

Despite the apparent low values of $|\sigma|$ ($\approx 250 e^-$ at the end face of the electrode), studies have demonstrated modification of nonlinear optical responses induced by surface charge densities as low as $\sigma = 10^{-3} \text{ C/m}^2$ [195]. In that specific case, electric field induced second harmonic generation from colloidal gold nanoparticles in water is changed by the addition of salt solutions and consequently by the surface charge density variations.

Going back to the capacitance of the nanoantenna, we can precisely compute it using the COMSOL Multiphysics[®] model which results in $C = 6.5 \times 10^{-18} \text{ F}$ and is very close to our approximative calculation. The total induced charge per volt is then around 7 aC.

Again, calculating the capacitance at the nanoscale has several implications not taken into account in this simplified model. Additionally, in the calculations of C a perfectly smooth shape is assumed which is not totally true. However, it is possible to consider the accumulation of charges at the gap region as the main responsible for the N-PL modification.

2.4. Controlling the Nonlinear Photoluminescence

In this context and in accordance with a charge-discharge mechanism, the resulting response time of the process will be *a-priori* the convolution of the resistance-capacitance (RC) time constant τ_C of the circuit, the response time of the instruments and detectors τ_{IRF} and the intrinsic response time of the nonlinear photoluminescence $\tau_{\text{N-PL}}$. It is possible to estimate the response time of the system and thus τ_C with the nominal impedance. In this respect, $R = 50 \Omega$ and therefore $\tau_C = R \cdot C = 0.3 \text{ fs}$.

2.4.3 Response time of the N-PL modulation

Nonlinear photoluminescence is the result of very fast mechanisms. Two-pulse correlation and pulse duration dependence experiments on N-PL confirm its sub-picosecond dynamics ($\tau_{\text{N-PL}} < 1 \text{ ps}$) [22, 23]. On the other hand, the instrument response function (IRF) of the detectors is around a few nanoseconds. Additionally, the total response time of the system is limited by the electronic response time of the electrical components used which should be in the nanosecond scale too.

To explore the latency of the modulation, the response of the N-PL is recorded while a train of 10 V pulses with different durations are activated (See Fig. 2.4.7).

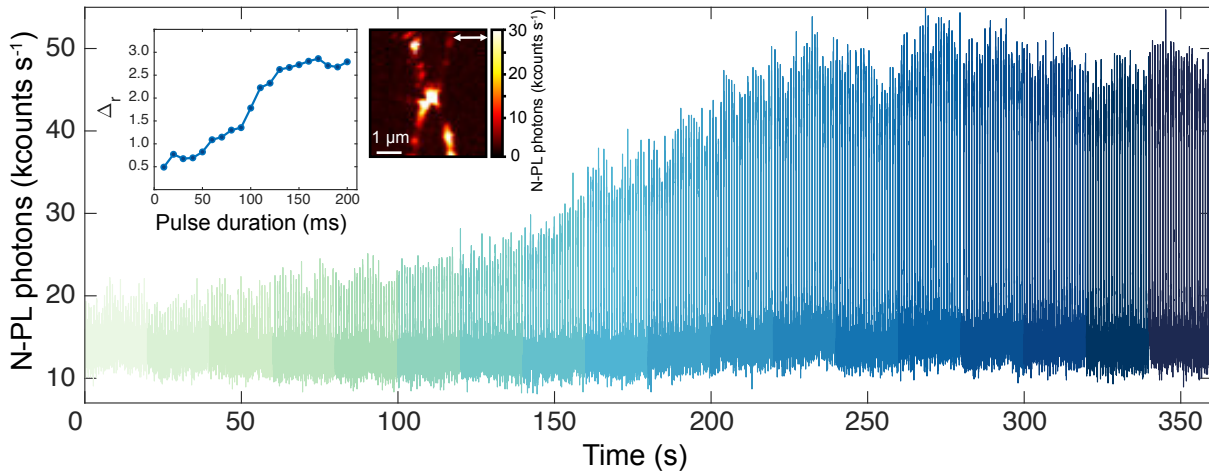


Fig. 2.4.7. Time trace of the recorded N-PL in a $\approx 80 \text{ nm}$ gap under the action of time-varying 10 V pulses. Each color represents a different electrical pulse duration starting at 30 ms and increasing in 10 ms steps until reaching 200 ms. The insets show the dependence of the N-PL modulation depth as a function of the pulse duration and a N-PL confocal map of the studied nanoantenna.

Here, the evolution of the N-PL is monitored as the pulse duration increases starting at $t_{\text{pulse}} = 30 \text{ ms}$. Each color represents an increment of 10 ms, the darker the color the longer the pulse duration. Surprisingly, the amplitude of the modulation is highly affected by the pulse duration until it reaches an asymptotic value around $t_{\text{pulse}} = t_t = 130 \text{ ms}$. This indicates that pulses shorter than such threshold value are not long enough to completely boost the N-PL, pointing inevitably to a relatively slow process with a response time $\tau_{\Delta} > t_t$.

To go further, standard pulse measurements like the N-PL rise time, fall time and pulse width are performed as shown in Fig. 2.4.8. In the case of in-phase modulation, the rise time t_{rise} is defined as the amount of time that N-PL takes to go from low to high values once the voltage is applied. Contrarily, the fall time t_{fall} is the amount of time it takes to go from the high to the low values once the voltage is withdrawn. Both quantities are measured from 10% to 90% in the case of N-PL rising and from 90% to 10% in the case of falling. This helps to eliminate any irregularities at the pulse's transition corners. For illustration purposes, the blue- and red-shaded areas in the Fig. 2.4.8(a) indicate the rise and fall time of the recorded N-PL

during the action of a 200 ms electric pulses train. The pulse width is, on the other hand, the amount of time the N-PL takes to go from low to high and back to low again. Mostly called full width at half maximum (FWHM), it is measured at half of the full modulation depth (See inset of Fig. 2.4.8(b)).

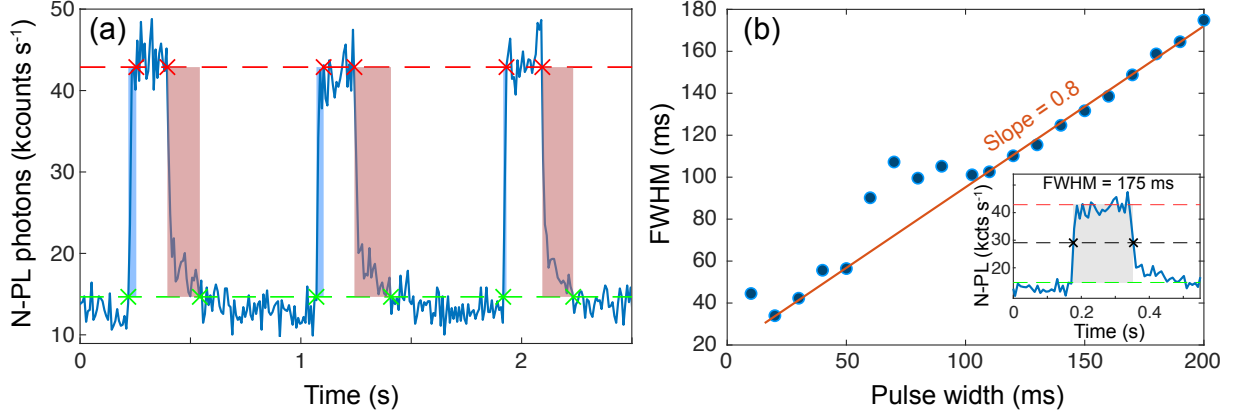


Fig. 2.4.8. (a) Rise (blue-shaded area) and fall (red-shaded areas) times measured on a highly time-resolved trace of the N-PL under the action of 10 V and 200 ms pulses. The red and green crosses indicate the referential points for the high and low values of the N-PL respectively. (b) Evolution of the FWHM of the N-PL pulses with the electric pulse duration. The inset shows the measured points for an N-PL pulse under the action of a 200 ms and 10 V pulse.

The observed N-PL pulses are asymmetric in shape, i.e. the time it takes to activate the N-PL change (t_{rise} in this case) is much shorter than the time it takes to relax back to its initial electric field-free value (t_{fall}). Averaging the calculated rise and fall times for the time trace shown in Fig. 2.4.8(a) leads to $t_{\text{rise}} \approx 20.1$ ms and $t_{\text{fall}} \approx 110.4$ ms in accordance with the modulation weakening for $t_{\text{pulse}} < 130$ ms.

Fig. 2.4.8(b) evaluates the change on the N-PL FWHM with the electric pulse duration. For $t_{\text{pulse}} \lesssim t_t$, the FWHM of the N-PL shows some instability due to the relative short duration of the electric pulse. However, as expected, it increases with t_{pulse} and follows a trend close to 80% of the electric pulse duration.

When the modulation is out-of-phase, i.e. the ON-state quenches the signal, the asymmetry of the N-PL pulses reverses and $\tau_{\text{fall}} < \tau_{\text{rise}}$ as illustrated in Fig. 2.4.9(a,b).

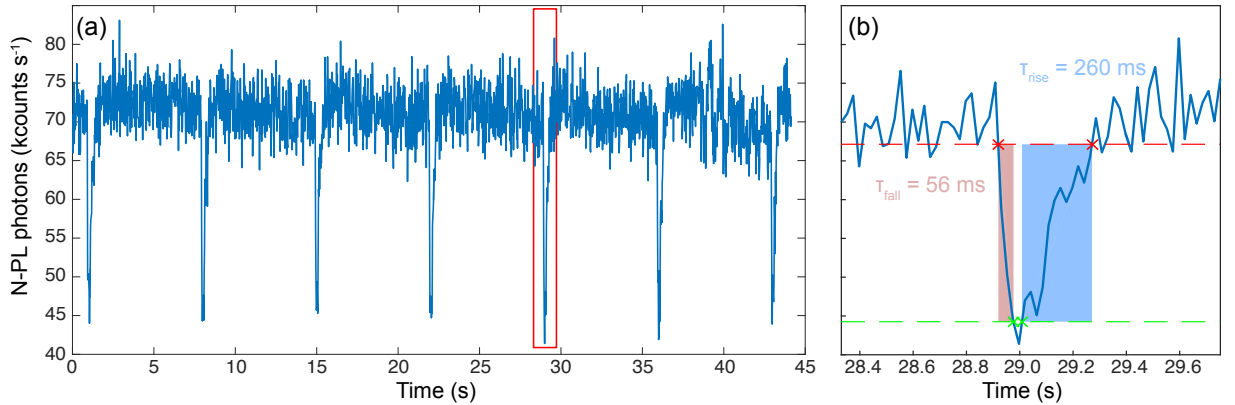


Fig. 2.4.9. (a) time trace of the emitted N-PL of a nanoantenna under the action of 8 V and 200 ms pulses. (b) Rise (blue-shaded area) and fall (red-shaded areas) times measured on a highly time-resolved trace of the N-PL indicated by the red square on (a). The red and green crosses indicate the referential points for the high and low values of the N-PL respectively.

2.4. Controlling the Nonlinear Photoluminescence

Although rise and fall times are longer in this quenched modulation case ($\tau_{\text{fall}} = 56 \text{ ms}$; $\tau_{\text{rise}} = 260 \text{ ms}$), the slower response time is clearly always associated to the settle down of the N-PL when the voltage goes to 0 V.

In general, the response time of the N-PL modulation is in the range of tens of milliseconds which is much longer than the time constants of the system elements ($\tau_C, \tau_{\text{N-PL}}, \tau_{\text{TRF}}$). Different parameters like the particular shape of the nanoantenna or the laser power considerably affect the latency of the modulation. Low laser powers lead to very slow response times reaching in some cases a timescale of seconds. A direct comparison between two incident laser powers is shown in Fig. 2.4.10. The top graph corresponds to the time trace of the N-PL for the higher power case and is very similar to the modulated N-PL signals shown before with sub-second response times. Conversely, the bottom graph shows the lower power case which, interestingly, displays very long τ_{rise} . Once the voltage is applied ($t \approx 5 \text{ s}$) the N-PL signal is rapidly quenched, however, the ON-OFF switching in the bias signal ($5 \text{ s} < t < 10 \text{ s}$) does not return the N-PL signal back to its initial value but after several seconds with no voltage applied ($t \approx 14 \text{ s}$). Both data sets were subsequently acquired at the same position on the nanoantenna and under the same bias conditions. In other words, the different response times are unequivocally a direct consequence of the change on the excitation power.

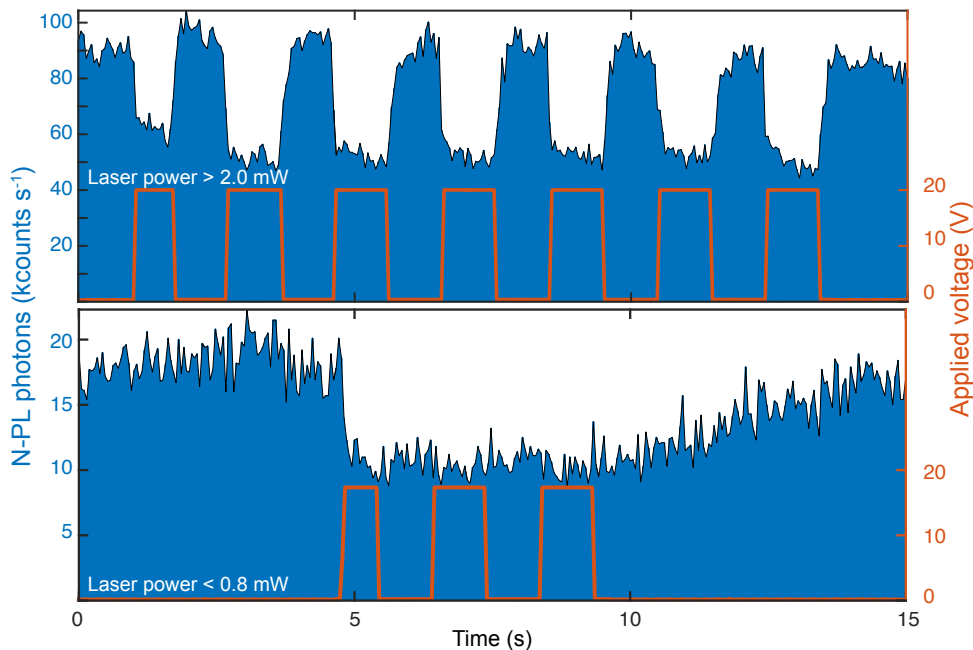


Fig. 2.4.10. N-PL time trace of an optical antenna for two incident laser powers and under the action of a squared time-varying voltage function with an amplitude of 20 V and a period $T = 2 \text{ s}$.

The results showed above with different modulation time responses suggest that the kinetics of the N-PL modulation mechanisms is driven by a combination of fast and slow processes. The first hypothesis that would match such slow processes points to temperature or electrostriction effects. Furthermore, the dielectric nature of the substrate could allow charge trapping effects which certainly change the electrostatic mechanisms presented in section 2.4.2. Final sections of the chapter systematically compare and rule out some of these aspects.

Continuing with the laser effects on the modulation, let us now explore the consequences of the variation of the polarization on the N-PL modulation efficiency.

2.4.4 Excitation polarization. Another degree of control

The N-PL modulation is examined as a function of the polarization angle of the incident laser beam. Figure 2.4.11 shows the recorded N-PL under the effect of a squared electric signal systematically varying from 0 V to -20 V ($|E_0| \approx 2 \times 10^8$ V/m). The incident polarization is gradually changed from parallel to perpendicular with respect to the nanoantenna orientation. In principle and regardless of the DC field, the maximum N-PL intensity enhancement is reached when the incident laser field orientation matches the plasmon resonances of the excited nanostructure [80, 121]. Such resonances are nontrivial given the fluctuations of the geometry imparted by the nanofabrication process.

Moreover, a careful look at the N-PL evolution with the polarization reveals changes on the relative modulation depth Δ_r for different laser polarizations. More efficient N-PL yield does not necessary induces stronger modulation or vice versa. Δ_r varies in the range of $\approx 19\% - 30\%$ with respect to the field-free value. On the other hand, the absolute variation of the N-PL emission remains practically constant (≈ 50 counts/s), however this figure is indicative. A large variability has been observed depending on the nanoantenna and also between positions of the laser focus at the same nanoantenna.

It is worth noting the persistence of the phase between the N-PL modulation and the electric field, i.e. the N-PL intensity increases every time the electric field is activated (in-phase). This is not always the case and variations in the polarization of the incident laser beam have shown to induce, under some conditions, a phase-shift from in-phase to out-of-phase or vice versa. The explanation lies on the symmetry of the system and the extension of the excitation point. Turning the polarization can activate resonances on one side of the nanoantenna enhancing the nonlinear response and reduce or completely suppress it on the other side.

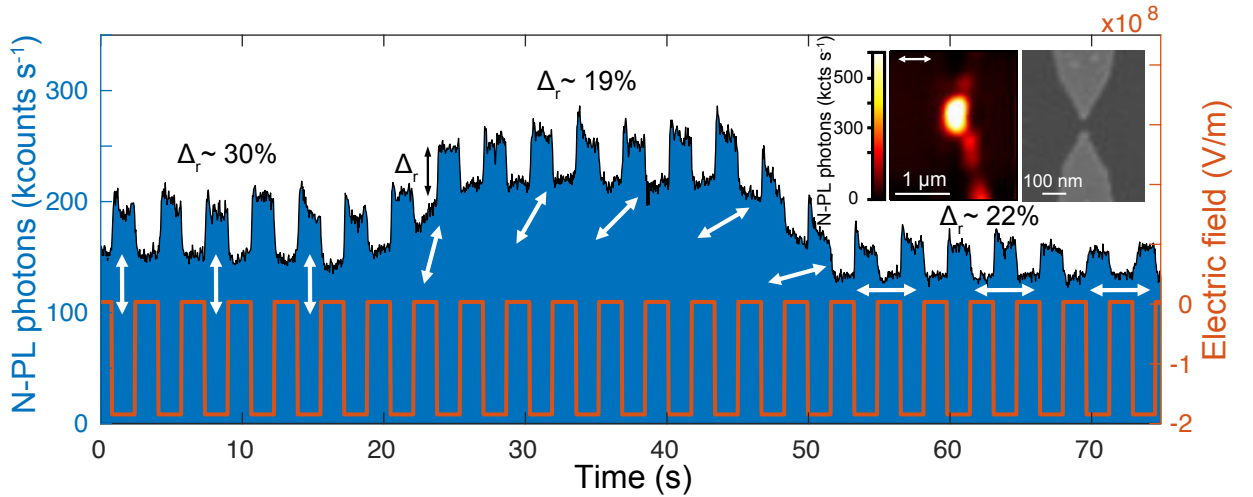


Fig. 2.4.11. Time trace of the recorded N-PL under the action of a 20 V squared electric signal for different incident laser polarizations. The relative modulation depth is pointed out as Δ_{N-PL} . The white arrows show the polarization state with respect to the nanoantenna shown in the inset at that specific time. An N-PL confocal map and a SEM micrograph of the nanoantenna are shown in the inset.

Once again, such variation in response to a change in the excitation polarization suggests a localized process strongly affected by the resulting landscape of the N-PL emission. In the next, some possible underlying mechanisms of the N-PL modulation are proposed from different perspectives.

2.5 Nonlinear photoluminescence modulation mechanisms

Deciphering the N-PL electrical modulation implies taking into account several processes. Starting with the photon absorption (hot electrons generation) and proceeding then with the resulting broadband hot electron emission, the different underlying mechanisms and the possible consequences of carrier density changes are overviewed and contrasted in the following. Extrinsic processes possibly affecting the N-PL yield like mechanical or charging effects occurring on the metal as well as in the glass substrate are also considered.

2.5.1 Possible effects on the hot carriers generation

The generation of hot carriers takes place following absorption in metals. As a matter of fact, let us start by contemplating the scenario where the absorption efficiency is modified by the action of a DC field. As shown in Sec. 2.4.2 such electric field forms a nanocapacitor and induces a relatively high concentration of electrons and holes at the very end of the structures probably affecting the light matter interaction.

There are basically four absorption mechanisms [196]: interband absorption, electron-electron scattering assisted absorption, phonon and defect assisted absorption and surface collision assisted absorption or Landau damping. Out of all these mechanisms, only the last two actually generate efficiently energetic enough hot carriers [196, 197]. Figures 2.5.1(a,b) depict these two absorption processes in a simplified band structure of a metal. Both figures show two states (① and ②) with different momenta \vec{k}_1 and \vec{k}_2 and energies E_1 and E_2 respectively. The difference in momentum between these two states is too large to be supplied by a SPP or a photon, thus momentum must be provided by a defect or a phonon K_{ph} (Fig. 2.5.1(a)). Otherwise, the electron transition to another energy state requires momentum transfer to the interface, i.e. the electron is reflected with the surface (fig 2.5.1(b)).

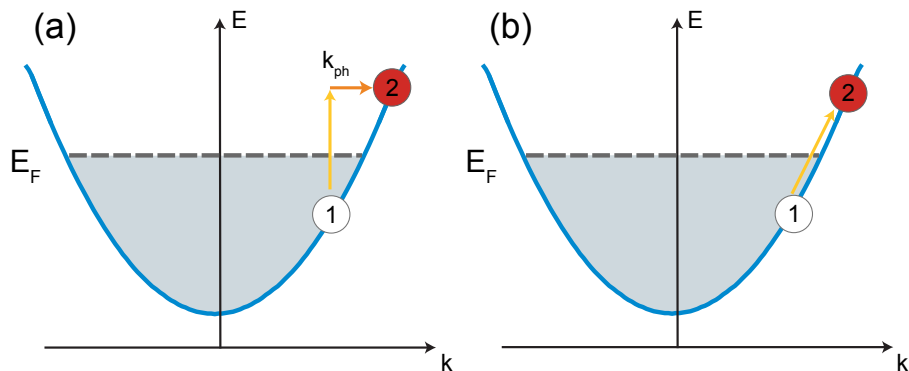


Fig. 2.5.1. (a) Phonon and (b) surface collision assisted absorption of a quantum of electromagnetic energy $\hbar\omega$ in a metal.

Both the surface-induced Landau damping rate as well as the electron-phonon scattering rate (thermalization time) depend on the free electron density. That is, the increased (decreased) surface charge leads to enhanced (reduced) electronic interactions. For instance, small particles show greater scattering rates compared to larger particles due to the higher surface to bulk ratio where the screening of electrons is lower [198]. Furthermore, the spatial distribution of surface charges in nanospheres quantitatively affects the thermalization rate [199].

The considerations mentioned above partially validate the electric-field driven modified absorption hypothesis. Nevertheless, the vast majority of the irradiated bowtie is not affected by the electric field and thus by the surface charge density changes. Studies of gold surfaces

under the influence of an external field show a strong dielectric response thanks to the large density of states at the Fermi level, charges screen very effectively the external electric field. Therefore, the field is barely felt by the second atomic layer of the surface [200,201]. Besides, an ultrashort laser pulse falling on a metal surface is partially absorbed producing hot electrons in a thicker skin layer (several nanometers depth) [202] which certainly limits and discards a major effect of the static electric field on the absorption processes.

Immediately after the electrons are promoted to energies far above the Fermi level, various relaxation processes occur. First, electron-electron scattering between electrons above and below the Fermi level leads to thermalization of the hot electrons in a scale of tens of femtoseconds. Following thermalization, the electronic temperature equalizes the lattice temperature via acoustic phonon emission in the picosecond scale [130,140]. Such dynamics implies that electrons remain “hot” for some time and as such they can radiate as a blackbody. In this context, the question of the static electric field affecting the emission rather than the absorption process emerges. Additionally and contrarily to absorption, the emission process is restricted to the surface of the structure, therefore it is more sensitive to surface charge density changes.

2.5.2 Changes on the Electronic temperature and the N-PL emission

Allow us now to assume that the absorbed energy does not depend on the bias, i.e. the dielectric permittivity remains unchanged under the action of the DC electric field. In this perspective, the change on the N-PL efficiency would come from fluctuations on the effective electronic temperature. Perner *et al.* show in [142] that the electron-surface scattering rate is strongly enhanced as the electronic temperature increases. This is mainly due to the high density of initial (populated) and final (unpopulated) states at the same energy. This is again emphasized in the work of Kanavin *et al.* [203] where the energy dynamics in a metal under ultrashort laser excitation is treated from the two-temperature model approach. Interestingly, electron-phonon and electron-electron collisions become important in the high electronic temperature regime. Furthermore, the electronic temperature T_e at an instant t shows to be directly affected by the electron density N_e , i.e. [203]

$$T_e \approx \frac{FT_F}{N_e v_F \sqrt{\hbar \varepsilon_F t}} \quad (2.5.1)$$

where F is the laser fluence, and T_F , ε_F and v_F are the Fermi temperature, energy and velocity respectively. Naturally, the electron density must also affect the SHG emission. However, SHG mechanisms are considerably different and the influence of the carrier density, in the context presented here, is rather limited as confirmed by our experiments.

Applying the static electric field across the nanoantenna gap modifies the electron density

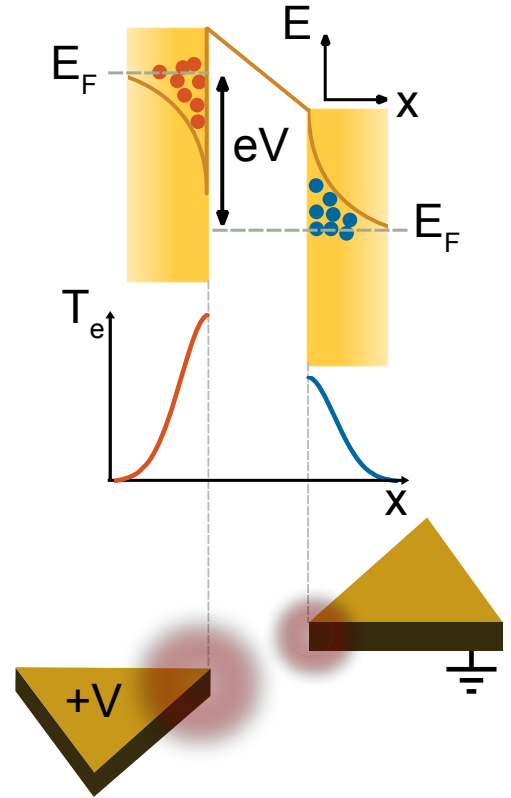


Fig. 2.5.2. Simplified diagram of the charge accumulation and electron temperature effects on the nanoantennas N-PL emission.

2.5. Nonlinear photoluminescence modulation mechanisms

N_e . At the same time, the femtosecond laser pulse creates a hot electron gas at T'_e . Depending on the irradiated electrode there is an asymmetry in the reached electronic temperature, the biased side with a lack of electrons is “hotter” at the gap interface than the grounded side which has an excess of carriers. This situation is better exemplified in Fig. 2.5.2, the energy levels are displaced by the action of the voltage difference between the two electrodes. The charges accumulate within the Thomas-Fermi screening length or the Wigner-Seitz radius [204] (a very few atomic layers at most) and have a direct effect on the nanoantennas’ emitted N-PL. Furthermore, this is in full agreement with the spatially- and field polarity-sensitive N-PL modulation shown in Fig. 2.4.4 and 2.4.5 respectively. There, excitation favoring the biased electrode (lack of electrons) induces higher N-PL emission, whereas pointing at the grounded electrode (excess of electrons) reduces the yield. Now, recalling figure 1.4.6(b), there is a highly nonlinear dependence of the spontaneous emission intensity as a function of the electronic temperature, relatively small variations of T_e may then lead to strong variations on the N-PL intensity. In this respect, an important aspect obviously concerns the electronic temperature under different bias conditions.

2.5.2.1 Spectral changes of the N-PL with the electric field

The N-PL spectrum is recorded under different electrical stress conditions in the gap region of the antenna. More specifically, figure 2.5.3 compares the N-PL broadband emission in the range of $500 \text{ nm} < \lambda < 650 \text{ nm}$ when a 10 V potential and when no bias are applied. The integration time here is $t = 500 \mu\text{s}$ and the incident power is fixed at $1 \text{ GW}/\text{m}^2$ at the focus of the laser. Increasing the voltage produces a consistent increase of the N-PL intensity. In connection with the arguments presented just before, second harmonic generation peak remains constant for both cases (see inset).

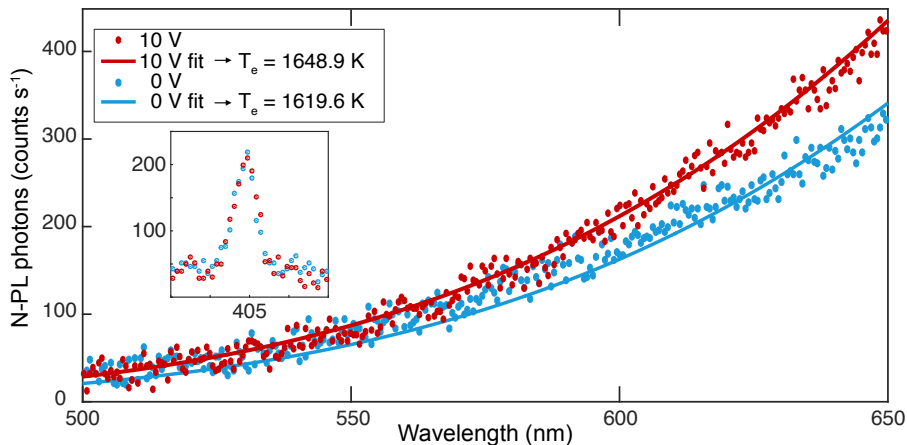


Fig. 2.5.3. N-PL spectra of an optical gap antenna under different applied voltages. The inset shows the spectra at the corresponding SHG wavelength.

According to Planck’s law, the spectral radiance $I(\lambda, T_e)$ of a blackbody is given by

$$I(\lambda, T_e) = \Upsilon \frac{2hc^2}{\lambda^5} \frac{1}{e^{hc/\lambda k_B T_e} - 1} \quad (2.5.2)$$

where c is the speed of light and Υ is a specific parameter that encodes the emissivity of the material and the tooling factor. A simple fitting model allows to estimate the electronic temperature by adjusting the relative intensity of the spectra giving temperatures of $T_e(0 \text{ V}) = 1619.6 \text{ K}$ and $T_e(10 \text{ V}) = 1648.9 \text{ K}$ for the unbiased and biased cases respectively. Moreover, both

temperatures are in the same order of magnitude as previously reported values for electronic temperatures reached after pulsed laser excitation [9, 205, 206].

As expected, small changes in T_e ($\Delta T_e \approx 30$ K) produce noticeable variations of the light intensity. In addition, limiting the electronic temperature dependence to the electron density using Eq. 2.5.1 gives a rough estimation of the necessary additional charge ΔN_e to produce such temperature variations. A quick calculation results in $\Delta N_e \approx 1 \text{ e}^-/\text{nm}^3$ which can be extended to a surface charge density and the reasoning is based on the assumption that the carriers are restricted to the Thomas-Fermi screening length for gold

$$r_{\text{TF}}(\text{Au}) = (3\pi^2 N_e)^{1/6} \sqrt{\frac{\pi \hbar}{4m_e e^2}} \approx \frac{1}{2} \left(\frac{a_0^3}{N_e} \right)^{1/6} = 0.06 \text{ nm} \quad (2.5.3)$$

where a_0 is the Bohr radius and m_e and e are the electron mass and charge respectively. Correspondingly, the surface electron density within r_{TF} is then

$$\Delta N_{e_{\text{TF}}} = \Delta N_e \times r_{\text{TF}} = 9.6 \times 10^{-3} \text{ C/m}^2 \quad (2.5.4)$$

Interestingly, this value is very close to the surface charge calculations for the bowtie nanocapacitor of Sec. 2.4.2 ($\sigma \approx 10^{-2} \text{ C/m}^2$). This result has to be carefully analyzed given that, besides T_e , the complete electronic dynamics of the metal is affected by the carrier density. However, it provides a referential point of comparison and locates the hot-electron modulation hypothesis within the framework of physically possible dynamics.

2.5.2.2 Delayed N-PL response by a trap charging effect

As repeatedly explained throughout the chapter, N-PL involves very fast processes (femtoseconds scale). In contrast, already shown experimental data reveals at least two different time responses, one of them producing a relatively delayed latency of the N-PL modulation. Inevitably, such dynamics hints the presence of additional mechanisms not taken into account so far. For instance, charge trapping mechanisms have shown to increase the response time of many processes. In fact, second harmonic generation in Si – SiO₂ interfaces is strongly affected by the carrier trapping and detrapping dynamics [207]. Notably, a femtosecond level process like SHG [208] is modulated in a time scale of several seconds. It is then worth highlighting the dielectric nature of the substrate and the possibility of charge trapping at the glass (SiO₂) and at the metal-glass interface due to the high electrical stress applied on the nanoantennas.

Traps are generated by charge carriers under high electric fields which can brake the interatomic bonds. These and other structural defects introduce energy levels to the glass and act as a potential well capable of trapping charge carriers. In spite of the insulating nature of the glass, during stress there is a chance of electron transport and injection to occur in the oxide followed by the generation of traps and negative or positive charge trapping. In fact, these processes involve different conduction mechanisms well summarized in the work of [209] and briefly introduced below (see Fig. 2.5.4).

Primarily, *Fowler-Nordheim tunneling* (i) occurs when electrons with energy lower than the height of the metal-glass barrier tunnel through it when the electric-field intensity is strong enough. All along this process, the charge carriers also exchange energy with phonons. In the case of electrons with energies above the barrier, i.e. hot electrons produced by the high laser peak power, they can penetrate into the glass in a process known as *thermionic emission* (ii). Likewise, *the Poole-Frenkel effect* (iii) allows the slow movement of electrons by local thermionic emission when their energy is higher than the barrier between two trap sites. *Direct tunnel emission* (iv) instead, takes place when the electrodes separation is sufficiently thin

2.5. Nonlinear photoluminescence modulation mechanisms

(< 5 nm). Finally, local tunneling allows the *jumping* (v) of electrons with energies below the barrier from one trap to another.

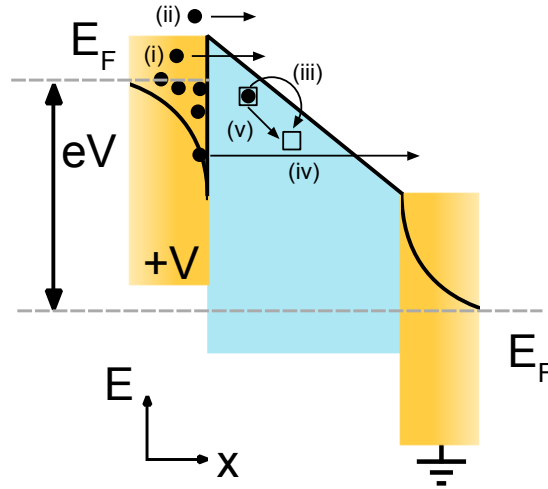


Fig. 2.5.4. Different types of electron emission in a metal insulator metal (MIM) system. (i) Fowler-Nordheim tunneling. (ii) Thermionic emission. (iii) Poole-Frenkel effect. (iv) Direct tunnel emission. (v) Jumping. Modified from [209].

In this scenario, there is a non-negligible possibility that the trapped charges in the substrate would affect the local static electric field across the gap and hold the surface charge density (screening charges) in the gold electrodes for a longer period of time. In an effort to minimize the substrate influence, air-suspended nanoantennas were fabricated. Nonetheless, different issues limited their implantation in the electro-plasmonic device.

Another phenomenon explaining the N-PL modulation by a DC field and that would match the slow response time is obviously the morphological modification of the nanoantennas. On the one hand, glass electrostriction occurring at the substrate is discarded given that it is proportional to the square of the electric field strength [210] which is incompatible with the observed asymmetry of the modulation with respect to the field polarity. On the other hand, induced surface changes on the gold structures constitutes a possibility that cannot be *a priori* ignored.

2.5.3 Electric field-induced surface modification and the optical nonlinearities

Plasmonic processes are very sensitive to the surface characteristics [211], changes on the surface state can greatly enhance the surface interactions. Furthermore, as demonstrated by Boyd *et al.* in 1986, weak N-PL signal can be enhanced by several orders of magnitude when generated at roughened metal surfaces [7].

Surface roughness is obviously affected by the temperature, in fact, surface melting and surface roughening are very related, both implicate a disordering of the surface layers. Additionally, external electric fields have also shown to change the surface features. For example, the outermost atomic layers of gold nanocones are distorted in the presence of a very strong electric field at room temperature [201]. The process is totally reversible, the surface atomic structure of the surface returns back to its initial position within a few seconds once the bias is withdrawn. Simulations by the same group in gold nanoparticles lead to shape elongation along with the disordering of atoms at the surface forming defects and confirming a surface roughening effect.

Comparing with our observations, this process occurs under considerably higher electric fields (> 10 V/nm). However, the structure of the nanoantennas is not perfectly smooth and nanometer-sized apexes show to strongly enhance the local electric fields [212]. Moreover, the combination of high temperatures and strong electric fields shows to change the surface structure too [200], the interplay between the laser incidence and the DC electric field is then relevant.

Still, surface or morphological changes should induce strong variations of the second harmonic generation which is highly sensitive to the surface configuration. As shown before in Fig. 2.5.3 this is not the case and it is again confirmed by Fig. 2.5.5 which simultaneously compares the appropriately filtered signals of N-PL and SHG emitted from the gap region while applying a squared voltage function varying from 0 – 7 V.

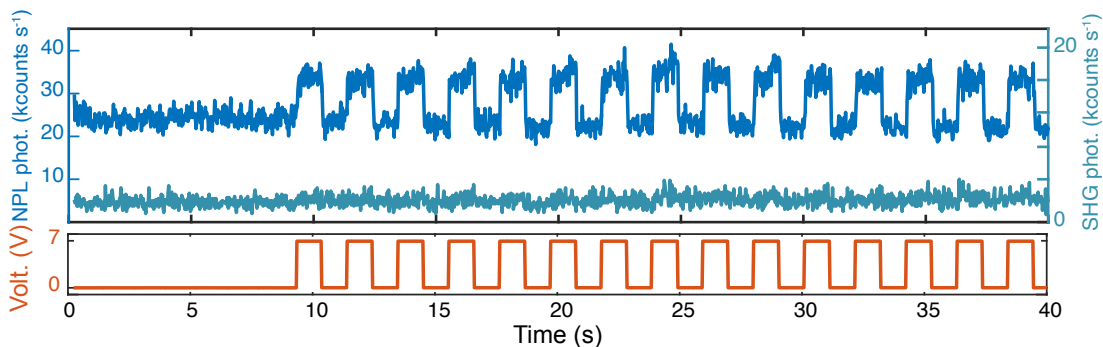


Fig. 2.5.5. Time traces of both SHG and N-PL signals as a 7 V amplitude square waveform is applied.

Clearly, N-PL is largely modulated from ≈ 25 kcounts/s up to ≈ 40 kcounts/s whereas SHG remains under the noise threshold with no noticeable variation. Hence, the question about the modulation mechanisms seems to inevitably point to the intrinsic dynamics of the N-PL phenomenon influenced and delayed by the charging mechanisms occurring in the glass substrate.

In the seek of evidence about the control of plasmonic properties by electrical means, let us focus now on the linear light scattering response of the device which, besides, provides an added value in terms of operation versatility. The reasoning behind is based on the fact that the influence of the linear optical properties on the nonlinearities is well established and supported by several experimental studies. A key question points then to the relationship between the N-PL modulation and the linear optical response of the gold nanoantennas.

2.6 Electrical control of the dark-field linear scattering

The first observation of a relationship between linear and nonlinear optics dates back to the 1960s when Miller established an important relation between the linear and nonlinear optical susceptibilities widely known as Miller’s rule [33, 213]. He empirically found that the ratio between the second order nonlinear susceptibility and the product of linear susceptibilities of a material is nearly constant. This rule holds for coherent signals and a wide variety of materials including noble metals [214]. It is based on the anharmonic oscillator description of nonlinearities [215]. In the field of plasmonics, several efforts have been made in different systems to relate the nonlinear and linear far-field properties at the fundamental and converted wavelengths [216, 217]. Moreover, a linear-nonlinear hybrid method known as nonlinear effective susceptibility method has been already proposed to relate the nonlinear conversion efficiency

2.6. Electrical control of the dark-field linear scattering

of a plasmonic system to its linear near-field properties [218, 219]. However, the relationship between linear and nonlinear optical responses in the framework of plasmonics is affected by the emission characteristics and intrinsic optical resonances given by the particular device geometry. Moreover, as pointed out in Sec. 1.4.1.1, nonlinear susceptibilities calculations are still ambiguous and lack precision.

In an effort to relate linear and nonlinear plasmon-mediated processes and motivated by the successful modulation of gold N-PL, the linear response of the same optical antennas subjected to static electric fields is explored in the following.

Spectral measurements using dark-field microscopy techniques are performed to explore the action of the electric field on the optical linear response of the nanoantennas. Dark-field microscopy is a technique that allows to exclusively collect the light scattered from the sample features. There are mainly two microscope configurations for dark-field, one based on reflection and another based on transmission. In both setups, broadband light passes through a condenser which produces a hollow cone of light focused at the sample. Evidently, to have the full spectral response of the nanoantenna a broadband source is necessary. In the transmission setup, in order to collect only the scattered light and filter the excitation light out, the objective on the other side of the sample must have smaller numerical aperture than the innermost components of the light cone produced by the condenser. In the case of a reflection configuration, the same objective serves to excite and collect the response.

In our particular measurement setup, transmission dark-field microscopy is carried out using the built-in tungsten halogen lamp of a Nikon Eclipse TE2000-U inverted microscope (T-DH dia-illuminator) which is focused on the sample surface by a Nikon 0.80-0.95 NA dark-field condenser. The scattered light from the nanoantennas is then collected using a Nikon variable aperture (NA = 0.5-1.3) 100x oil immersion objective. The position of the condenser is adjusted such that the array of nanoantennas on one side of the device is illuminated homogeneously. A polarizer is introduced in the excitation path and is oriented such that the scattering in the gap of the nanoantennas is maximum. The collected scattered light is then sent to the spectrometer as shown in the setup section (Sec. 2.3.2).

The spectral set in Fig. 2.6.1 shows the typical dark-field spectra of a biased nanogap as the voltage is increased/decreased. As emphasized in section 1.2.5, the resonance varies depending on the specific geometric features and nanoscale variations in the geometry.

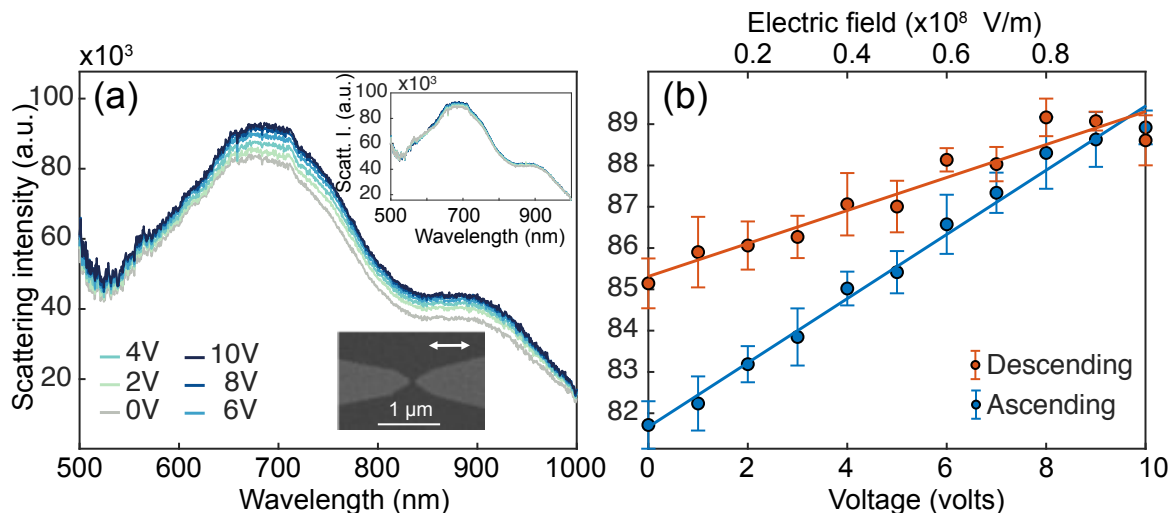


Fig. 2.6.1. (a) Dark-field spectra as the voltage across the gap of a bow-tie antenna is ramped-up. The insets show a SEM micrograph of the nanoantenna and the spectra for the subsequent ramping down. (b) Cross-section at $\lambda = 650$ nm of (a).

In principle, smaller gaps should lead to slightly redder resonances. The second observation is the damping of the scattering intensity at $\lambda \approx 510$ nm. Previous studies have attributed it to the pronounced interband transition of gold in this spectral range where the absorption and therefore the Ohmic losses become important [220]. Note that an accurate description of the dark-field spectra from every nanoantenna is a difficult task given the different scattering features they can have.

Figure 2.6.1 systematically shows changes on the dark-field spectra of a biased nanoantenna as the voltage is varied. The voltage is ramped up from 0 – 10 V just before being ramped back down to zero in 1 V steps (See inset). Only even values of the applied voltage are shown to have a better view. Every spectrum is the averaged result of five successive acquisitions for each voltage value. The changes on the dark-field spectra are restricted to the intensity, there are no apparent spectral shifts. Recalling section 1.2.5 and Mie theory, the plasmon resonance position is ruled by the real part of the dielectric function while the resonance linewidth or full width half maximum (FWHM) is controlled by the imaginary part [69].

Additionally, Fig. 2.6.1(b) presents the cross sections of Fig. 2.6.1(a) at a fixed $\lambda = 650$ nm. The changes on the scattering intensity are confirmed, the higher the voltage, the higher the linear scattering.

Recalling the last sections, the observed nonlinear optical response is usually delayed by a few tenths of milliseconds (seconds in some experimental conditions). This is again the case for the linear scattered light. If we compare the ramping up and down of the voltage both curves differ in intensity as the voltage is set back to zero. The change rate when ramping the voltage up is 0.78 V^{-1} while ramping it down is 0.40 V^{-1} which roughly represents half of the rising change rate. This is a direct consequence of the slow time response, the system takes some time to get back to its precedent values once the electric field stress is reduced (descending voltage). The possible mechanisms behind this slow response time can be again linked to a charge trapping-detrapping phenomenon due to the high DC electric fields applied.

The changes on the spectra are a direct and exclusive consequence of the applied bias and the validation is presented in the following (see Fig. 2.6.2).

With the spectrometer in image mode and the diffraction grating at the zero-order reflection (the angle of incidence equals minus the angle of diffraction), the sampling region is positioned in an attempt to simultaneously capture the dark-field scattering of a maximum number of nanoantennas per measurement round. By aligning all their gaps with the slit aperture of the spectrometer, the effect of the DC field in a particular nanoantenna can be properly compared with other nanoantennas where no bias is applied. The nanoantennas are sufficiently distant thus the scattered light can be easily discriminated for each nanoantenna. Frames i and ii of Fig. 2.6.2 show real dark-field images of a different nanoantennas set. A coarse adjustment is made with the slit aperture broadly open (frame i), then the aperture is reduced to finely position the gap in the middle of the slit and exclude the scattered light from the surrounding structures (frame ii). The slit aperture is lastly closed at $200 \mu\text{m}$.

Figure 2.6.2(a) depicts the scattering spectra of six nanoantennas as a three-dimensional spectrogram. The position of the individual nanoantennas is given by the y -axis whereas the spectral scattering intensity is indicated by the pixel color (jet color scale) as a function of the photon wavelength between 500 nm and +1000 nm (x -axis). The dark-field spectra are integrated over $500 \mu\text{s}$. The incident light polarization is along the gaps. All the measurements are corrected for the spectral characteristics of the excitation light source but not that of the detectors.

2.6. Electrical control of the dark-field linear scattering

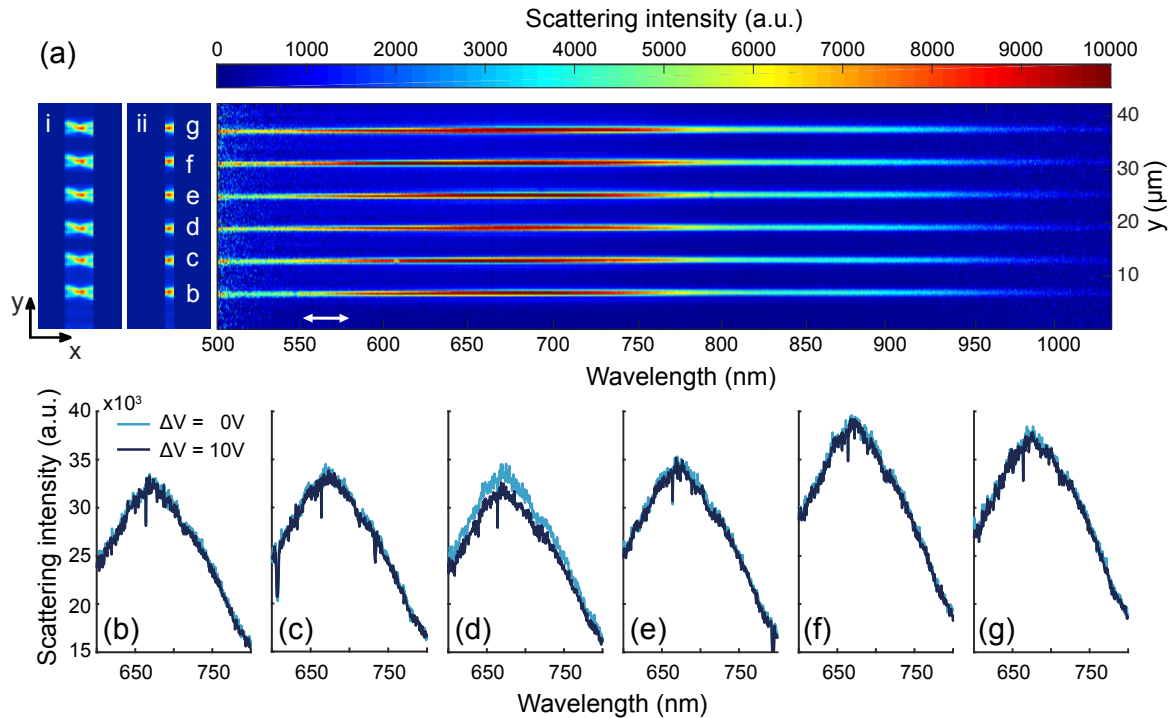


Fig. 2.6.2. Three dimensional spectrogram showing the dark-field spectra of six nanoantennas. The double arrow at the bottom left corner indicates the incident light polarization. Frames i and ii show the real image of the studied nanoantennas when the diffraction grating is at zero-order. (b,c,d,e,f,g) Corresponding binned spectra for every nanoantenna in (a).

Going back to the electrical control of the nanoantennas optical response, an electric field is now applied exclusively through the gap of the nanoantenna ‘d’. Figures 2.6.2(b,c,d,e,f,g) show the respective binned and averaged spectrum for every nanogap in the 600 nm – 800 nm wavelength range in two situations: when no bias is applied and during the action of a -10 V potential on nanoantenna ‘d’. The spectral lines corresponding to the particular scattering of each nanogap are separated and integrated. The shape of the spectra is very similar evidencing the structural resemblance among them. However, the changes on the spectra only manifest on the nanogap under the effect of the -10 V potential, i.e. nanoantenna ‘d’ which exhibits a reduced scattered light intensity. The rest of the nanogaps spectra remain unchanged discarding any sample drifting, defocussing or additional perturbations. A systematic study confirms this effect for several nanogaps.

It is worth noting the opposite effect of the electric field on the scattered light if compared to the spectra of Fig. 2.6.1. Although it seems *a priori* consistent with a change of the field polarity, the response should be polarity-independent given the extension of the studied area. In other words, the detector is ideally collecting the optical response from the center of the gap where the studied feature is symmetric. In reality, the resolution of the camera does not allow high-precision adjustment of the nanoantennas to match the exact center of the spectrometer slit and therefore different polarities can lead to opposite behaviors.

Although both the linearly scattered light and the nonlinear photoluminescence are modulated in the same device by practically identical electric fields the mechanisms behind both processes are fundamentally different. Evidently, in this situation, hot electrons are not playing any role. Nonetheless, it seems plausible to anew consider the surface density charge change as the main responsible. Macroscopically, from a simplified point of view, an effect similar to that of ref. [160] and the STM tip-sample system showed in Sec. 2.2.1 is taking place. The dielectric function of the metal is altered in a small volume where the carrier density is

most largely modified. The underlying mechanisms are probably related to a local change in the plasma frequency or in the number of electrons participating in the optical interaction as already suggested by [160].

2.7 Conclusion

An electro-plasmonic device based on gold optical gap antennas and capable of modulating linear and nonlinear optical responses of the metal was successfully fabricated. The nanofabrication protocol using UV and e-beam lithography techniques to produce this device, and the nanostructures studied throughout this thesis, were presented. The experimental setup and the implementation of experimental techniques like nonlinear confocal microscopy and dark-field microscopy to operate and characterize the device were detailed.

Most importantly, the effect of strong static electric fields on the nonlinear photoluminescence emission and the linear scattering response of gold optical gap antennas has been deeply studied. Throughout the chapter, different experiments confirmed the successful electrical modulation of both phenomena. The strength of the electric field applied across the gap of the nanoantennas defined the modulation depth, the stronger the field the more important the N-PL change. Another parameters like the laser power, the incident polarization, the specific nanoantenna morphology as well as the localization of the excitation spot showed to affect the N-PL response too. Depending on the position of the laser and the polarity of the electric field with respect to the constituent electrodes of the nanoantennas, N-PL emission dropped or rose with the modulus of the electric field, unequivocally implying an asymmetric process highly sensitive to the emission localization. Modeling the optical antenna as a nanocapacitor highlighted the possible effects of the surface charge density modifications on the N-PL response. Furthermore, different processes probably leading to N-PL modification with the static electric field were explored. Based on the thermal radiation occurring after NIR pulsed laser radiation upon noble metal structures, the influence on the absorption mechanisms generating hot electrons as well as on the subsequent broadband nonlinear emission were considered. Experimental data suggested that the emission yield is highly dependent on the carrier density which strongly modifies the thermalized electronic temperature.

Finally, due to the relatively slow response time of the N-PL modulation, additional mechanisms taking place on the dynamics of the process are considered. Mechanical and charge trapping effects resulting from the high electrical stress are systematically contrasted. However, several mechanisms may be simultaneously involved and interrelated in a very complex way.

In the next chapter, the successful generation of N-PL on gold nanostructures microns away from the excitation point is presented. Going a step further, electrical modulation of this delocalized emission is also achieved.

Nonlinear optical transport in plasmonic nanowires

3.1 Introduction

Small objects such as nanoparticles or the bow-tie antennas presented in chapter II feature nonlinear responses which are spatially restricted to the excitation region provided by a focused laser beam. Pumping of extended plasmonic structures leads to a significantly different situation. Thanks to the enhanced electromagnetic field associated with surface plasmon propagation and its scattering at defects and terminations, nonlinear signals are no longer confined to the excitation area, but are now distributed throughout the entire structure [221–223]. These responses may take different natures including incoherent and broadband nonlinear continuum emission, i.e. N-PL.

An obvious consequence of this delocalization is the possibility to transport nonlinear optical signals in complex devices via an engineering of the underlying surface plasmon modal landscape [192]. Despite repeated successful observations of delocalized optical nonlinearities [221, 222], the mechanisms responsible for the spatial extension remain unclear and no attempts have been made to locally describe and characterize the nonlinear transport. In this context, a particularly interesting model structure is a simple metal nanowire. Nanowires are considered as suitable candidates for sub-wavelength confining, tailoring and guiding optical signals in highly integrated optical circuits [154, 224, 225] and its plasmonic modal decomposition is easy to predict [226, 227]. Importantly, the different spatial distributions of the nonlinear continuum along a nanowire provide different advantages. For instance, the local response may be used as a spectral probe to detect absorbing species within an extremely compact detection area. Metal nanowires have already been deployed to remotely excite and detect various optical processes like Raman scattering [228, 229] and up-converted luminescence from a distant crystal [230]. Also, and unlike standard phase-matched nonlinear processes occurring in dielectric waveguides (e.g. fibers) requiring a dispersion engineering of the index of refraction and thus very long propagation distances ($\gg \lambda$), the continuum generated by the plasmon-induced nonlinearity is formed in an extremely local interaction area ($\ll \lambda$). Such continuum may also have several applications in a nanowire-based circuitry as a wavelength converter process.

In this direction, the present chapter aims at developing novel strategies to route surface plasmon polaritons in one-dimensional metallic nanowires waveguides. Most importantly and in line with chapter II, we continue to seek the development of electrically active linear and nonlinear functionalities with reduced dimensionality. Specifically, a complete space-resolved analysis of the spectral signature of the broadband nonlinear up-converted emission in gold nanowires

3.2. Fabrication techniques and nonlinear wide-field microscopy

(AuNWs) is carried out to understand the origin of the spatially distributed nonlinear response. We systematically explore and discuss various mechanisms to explain the experimental data and unambiguously demonstrate that the spatial and spectral extension of the N-PL in the nanowire are mainly dictated by the propagation of a surface plasmon excited at the pump wavelength. We also present experimental signature of near-field excitation of a broadband continuum of surface plasmons excited locally throughout the N-PL emission spectrum. At the end of the chapter, a modified version of the device studied in Chapter II is presented, whereby the nonlinear emission emerging from the end of gold nanowires is successfully modulated. The implications of such achievement are further discussed.

3.2 Fabrication techniques and nonlinear wide-field microscopy

Polycrystalline AuNWs of different lengths $3.0 \mu\text{m} < L < 9.5 \mu\text{m}$ and widths $60 \text{ nm} < L < 160 \text{ nm}$ are fabricated on a glass substrate by means of standard electron beam lithography (Pioneer, e-line) and metal deposition followed by a lift-off process. The width of the nanowire is precisely varied by increasing the e-beam exposure dose. Electron-beam physical vapor deposition of 3 nm thick titanium acts as an adhesion layer for the subsequent thermal evaporation of a 50 nm thick gold layer. Basically, the fabrication protocol is identical to the first lithography step shown in chapter 2. SEM micrographs of Fig. 3.2.1(a) show several AuNWs with different widths achieved by varying the e-beam exposure parameters as well as the design specifications (nominal width). Additionally, higher doses tend to produce smoother nanowires edges. Optimal propagation and N-PL emission is observed for AuNWs widths that are around 160 nm. A CAD design defines sets of five nanowires with different lengths as shown in Fig. 3.2.1(b).

Given the high confinement nature of SPPs, the imaging of propagating SPPs through the nanowires utterly requires microscopy setups adapted to the subwavelength regime. Furthermore, thin nanowires as the ones studied in this chapter can only sustain SPP modes localized at the NW-glass interface with effective indices higher than the substrate (bound mode), only evanescent fields exist in the substrate, thus hindering far-field direct observation as they propagate. However, the scattering event produced at the distal end is a signature of this mode and can be used to extract relevant information about the SPPs properties as will be seen later in the chapter.

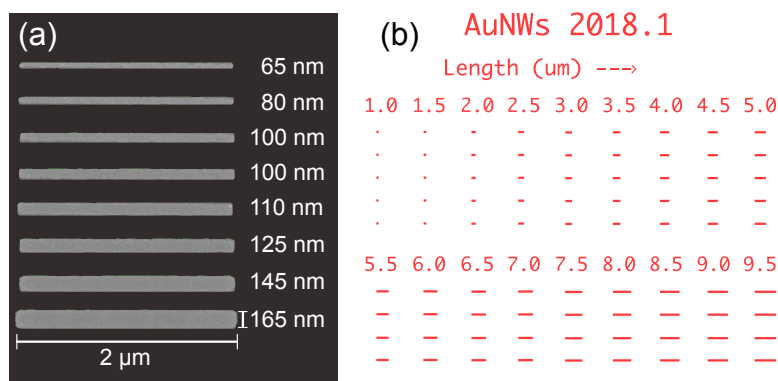


Fig. 3.2.1. (a) SEM micrographs of AuNWs showing the effect of the e-beam dose on the nanowire widths. (b) CAD design used to expose the resist and finally fabricate the AuNWs with different lengths.

The actual experimental setup slightly varies from that shown in chapter II. In this particular experiment, wide-field optical imaging and the two-dimensional piezo-electric stage allow to precisely adjust the nanowire to overlap one end face with the focused laser beam where the discontinuity provides the necessary momentum matching condition to optically excite propagating SPPs. Additionally, the tightly focused pulsed femtosecond laser beam tuned at NIR wavelengths generates, as in the case of chapter II, nonlinear photoluminescence emission in the AuNWs. The same objective collects the resulting linear and nonlinear optical responses produced by the sample. A set of relay lenses transfers the object and Fourier conjugate planes either to the imaging spectrometer or to a charge-coupled device (CCD) camera (Hamamatsu, C4742-80-12AG). The dichroic beam splitter and a set of filters (Thorlabs) are used to block the laser in the collection path when necessary.

3.3 Excitation of delocalized N-PL in gold nanowires

Nonlinear optical responses and in particular nonlinear photoluminescence from metallic nanostructures are clearly dictated by the surface plasmon resonances and the supported plasmonic modal landscape [121, 192, 221, 231].

Introductory concepts to plasmonics and surface plasmon polaritons were already presented in chapter one. However, the excitation of SPPs in metallic structures, which is not trivial, has not been discussed so far. Let us recall the derived dispersion relation from the Maxwell's equations considering the flat interface between a metal and a dielectric and the corresponding boundary conditions ($k_x = k\sqrt{\varepsilon_1\varepsilon_2/(\varepsilon_1 + \varepsilon_2)}$). At small k_x , the dispersion relation approaches the light line $\omega = c \times k_x$. For larger values of k_x , it bends and comes nearer to the limiting value of the plasmon resonance $\omega_p/\sqrt{2}$ given by $\varepsilon_1 = -\varepsilon_2$, with ε_1 corresponding to the dielectric. In this region, small variations of frequency lead to large changes on k_x . Figure 3.3.1 displays this case assuming an interface between semi-infinite glass and gold [232]. The SPP dispersion relation (orange solid line) is completely below the light cone in vacuum (solid line), i.e. the wave vector k_x is always larger than that of light in vacuum for a given energy. In order to excite SPPs, it is necessary to provide additional momentum Δk_x to the excitation photons.

The case for nanowires is, in this regard, qualitatively equivalent. SPPs propagating in one-dimensional waveguides require excitation light with an additional externally-provided momentum. Quantitatively, the geometry of the system affects the resulting dispersion. The dispersion relation for nanowires can be reconstructed from the spectral information by approximating the nanowire as a cylinder and using the Fabry-Perot resonator model [233, 234]. Counter-propagating plasmons interfere and generate maxima and minima corresponding to constructive and destructive interference respectively. In a resonator of length L , the plasmon wave vector is given by

$$k_{\text{spp}} = \frac{j\pi - \phi_r}{L} \approx \frac{j\pi}{L} \quad (3.3.1)$$

where j is the mode order and ϕ_r is the phase shift upon reflection at the ends of the nanowire. The dispersion relation also provides information about the group and phase velocities. The group velocity is defined by the relation $v_g = d\omega/dk_x$ i.e. the tangents of the dispersion curve while the phase velocity is equal to $ck/k_x = c/n_{\text{eff}}$ [235]. Figure 3.3.1 additionally shows the reconstructed dispersion relation for gold nanowires on a glass substrate by extinction spectroscopy (individual symbols taken from the work of [232]). Although similar in trend to the planar interface, k_x in nanowires is larger for a given frequency ω , therefore plasmon propagation group velocity is slower in gold nanowires than in a planar Au/glass interface, validating the high degree of optical confinement at the interface of such plasmonic structures.

3.3. Excitation of delocalized N-PL in gold nanowires

Evidently, plasmon resonances depend on the size and shape of the nanowires, which also directly affect the dispersion relation and the supported plasmonic modes. Roughly speaking, the dispersion relation for thin nanowires (< 100 nm) is below the light cone for a glass substrate, i.e. the plasmon momentum is too large to radiatively decay into far-field photons, thus the SPP mode is tightly bound to the surface of the nanowire (bound mode) [62]. In contrast, for thick nanowires (> 300 nm) bound and higher modes exist and can be leaky. The plasmon dispersion is above the light cone in glass resulting in a leaky mode [233]. Leaky plasmons are lossy and consequently have shorter propagation lengths. In the next chapter more details will be given about the different sustained modes by plasmonic nanowires.

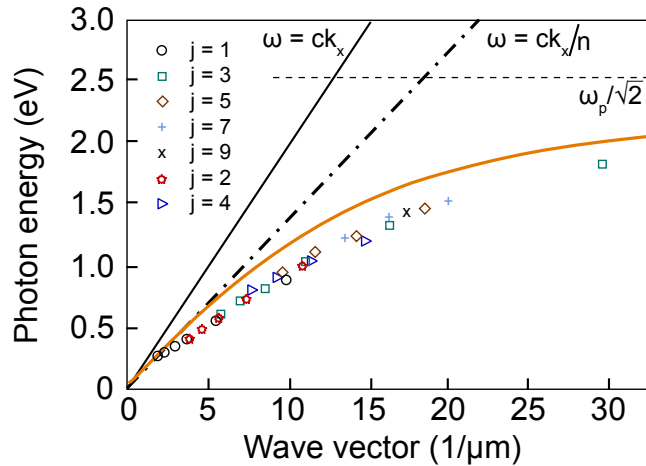


Fig. 3.3.1. Dispersion relation of surface plasmons for gold. The solid and dashed lines represent the light line in vacuum $\omega = ck$ and in quartz glass $\omega = ck/n$ respectively. In orange the dispersion curve for SPPs on a gold/glass interface. The limiting frequency $\omega_p/\sqrt{2}$ is represented by a dotted line. The symbols are the dispersion relation for gold nanowires reconstructed from $k_{\text{spp}} = j\pi/L$, j is the mode order. Adapted with permission from [232]. Copyright 2003 by the American Physical Society.

There exist several techniques to increase the wavevector of the excitation light and overcome the momentum matching constraints. The most widely known, namely evanescent coupling, allows to excite surface plasmons by means of evanescent waves created at the metal-dielectric [236] or dielectric-air [237] interface for dielectric media with $n > n_{\text{air}}$ (a glass prism) [65, 238]. Such refractive index tilts the light line by a factor of n since $\omega = ck/n$ (see Fig. 3.3.1). Another solution consists on modifying the planar metal surface by means of gratings and provide momentum ensuring momentum conservation [32]. Fluorescence emitted by quantum dots or molecules close to nanostructures can also couple in the form of SPPs [239]. As shown later in this chapter, nonlinear photoluminescence produced in gold nanowires is able to couple to the structure and propagate as a broadband plasmon [64]. Furthermore, the field confinement produced by optical antennas has shown to boost the coupling efficiency in adjacent nanostructures [240].

More recently and for the seek of simplicity, scattering produced at symmetry-broken points or defects has been used to provide the necessary momentum Δk_x . Random surface roughness, wire terminations [241], kinks [242], adjacent nanoparticles [243] or even fabricated defects can significantly ease the launching of SPPs [244]. In general, to excite propagating SPPs in nanowires, focused light is directed to the “defect” of the structure and scatters in all directions producing a broadband distribution of wave vectors including those matching that of the SPP [241, 245].

With the setup and the basics explained, let us now focus on the main subject matter of

this chapter, namely the origin of the delocalized nonlinear emission in gold nanostructures.

3.4 Unraveling the N-PL delocalization

Firstly, the incident light polarization as well as the position of the focused light determine the coupling efficiency of the SPP [246] and thus the N-PL generation on the structure. Figure 3.4.1 better exemplifies this by comparing the linear SPP propagation at the pump wavelength ($\lambda = \lambda_0$) and the N-PL emission under incident longitudinal and transverse polarizations with respect to the axis of a nanowire. Wide-field images of the linear scattering response and the filtered nonlinear photoluminescence emission of a $3.5 \mu\text{m}$ AuNW are shown in figures 3.4.1(a,c) and 3.4.1(b,d) respectively. The gold nanowire SPP bound mode is excited at the left end with a focused pulsed femtosecond laser at $\lambda_0 = 808 \text{ nm}$ (saturated region). At the distal end of the nanowire, a SPP is partially converted to free propagating photons through a scattering process [245]. The nonlocal distribution of light in both the linear and the nonlinear cases confirm the excitation of SPPs when the incident polarization is aligned with the nanowire. Gradually changing the polarization to transverse reduces the coupling efficiency as already reported [247,248]. As a result the distal light scattering and thus the nonlinear emission along the nanowire vanishes (see pointing arrow). For an easier view, the integrated intensities along the y -axis of the AuNWs of the linear and nonlinear images are shown in Fig. 3.4.1(e,f). The curves are normalized with their own maxima. Under longitudinal polarization, the linear and nonlinear curves show two peaks resulting from laser scattering and local N-PL generation at the excitation point (left) and scattering by the propagating SPPs when they reach the distal end. The second peak disappears for the transverse polarization (no coupled SPPs).

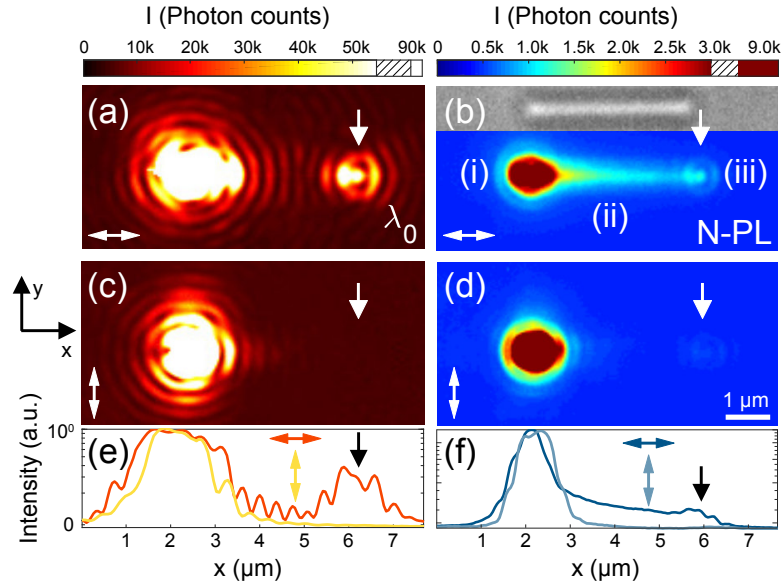


Fig. 3.4.1. Wide field images of the light distributed in a $3.5 \mu\text{m}$ AuNW at the excitation wavelength with (a) longitudinal and (c) perpendicular incident polarization. The AuNW is excited at the left end by a focused laser at $\lambda_0 = 808 \text{ nm}$. Wide-field images of the spectrally filtered nonlinear photoluminescence emission are also shown for (b) longitudinal and (d) perpendicular incident polarization. The inset is a bright-field optical image of the AuNW. (e,f) Normalized integrated intensity plots of the (e) linear scattering and (f) nonlinear emission along the y -axis showing the SPP excitation efficiency for two different incident polarizations. The double arrows indicate the incident beam polarization.

Remarkably, delocalization of the N-PL is ubiquitous in all studied nanowires and consistently follows the pattern exemplified in Fig. 3.4.1(b) where three different regions can be

3.4. Unraveling the N-PL delocalization

discriminated. (i) The strongest emission results from the excitation point (left), (ii) N-PL emission along the nanowire exponentially decays and finally (iii) gets increased at the distal end (right).

Let us now review the different scenarii that may be considered to explain the intensity distribution of the N-PL along the nanowire and at its distal end. The different cases are schematically pictured in Fig. 3.4.2. Figure 3.4.2(a) sketches the linear case where a SPP excited at the left end propagates along the AuNW and scatters at the distal end. As already discussed by our group in a previous report [221], the decay of the N-PL intensity along the nanowire and the presence of a brighter spot at the extremity strongly point toward an effect mediated by SPPs propagating in the nanowire. But, the challenging questions are which SPP and at which wavelength? Should we consider only the local nonlinear response of the AuNW upon excitation of a SPP developing at the pump wavelength as pictured in Fig. 3.4.2(b) or should we take into account secondary SPP excitations? For instance, Fig. 3.4.2(c) and (d) depict situations where the N-PL continuum produced at the excitation spot couples in the nanowire in the form of a broadband spectrum ($\lambda_{\text{N-PL}}$) of surface plasmons, akin to what was observed in thin films [249]. On one hand, these colored surface plasmons will eventually reach the AuNW termination and be scattered into photons, which is in accord with N-PL spots observed at the extremity in Fig. 3.4.1(b). This is schematically represented by Figs. 3.4.2(c) and (d). On the other hand, the end face of the nanowire is responsible for a localized electromagnetic enhancement [36,250,251], which may also explain the brighter N-PL response observed experimentally at the end faces. This effect is represented in Fig. 3.4.2(b). Finally, the N-PL signal distributed along the nanowire could be interpreted as the radiative signature of higher-order SPP modes leaking in the substrate [226] (Fig. 3.4.2(c)). In the following sections, we experimentally verify all these hypothesis by conducting cross-check experiments to identify the mechanisms at play.

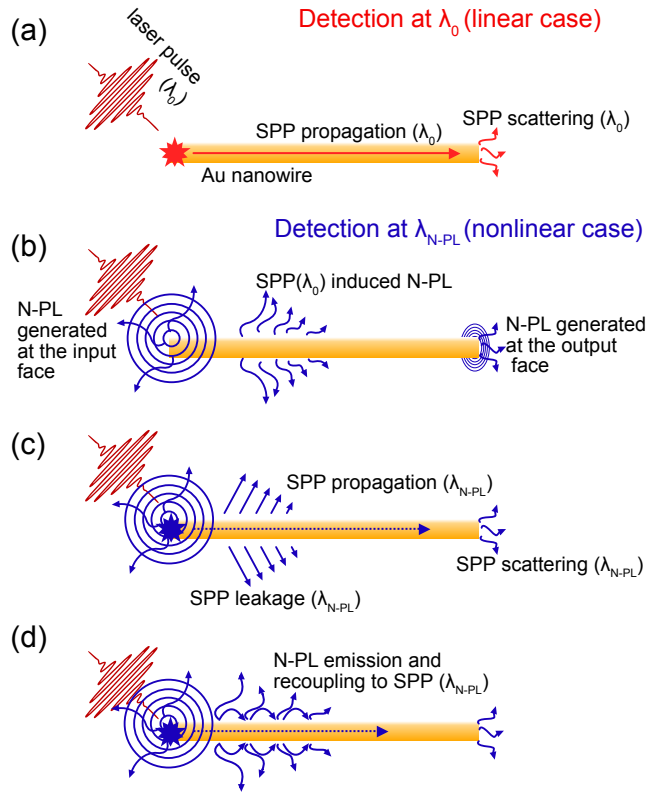


Fig. 3.4.2. (a) Sketch of the excitation, propagation and diffusion of the SPP at λ_0 . (b) to (d) Sketches of the different scenarii that may explain the spatial distribution of the nonlinear photoluminescence along the AuNW and at its distal end.

3.4.1 Propagation lengths

Our first analysis consists in estimating the propagation length of the SPP at the pump wavelength λ_0 and comparing it with the length dependence of the N-PL produced at the distal end. When light couples to a SPP it will propagate and gradually lose energy either by leakage radiation into the substrate and scattering defects or by absorption of the metal (non-radiatively). This non-radiative energy loss depends on the dielectric function of the metal. In chapter I the complex nature of the dielectric function of metals in the visible and NIR was exposed. In particular, the imaginary part of $\varepsilon(\omega)$ defines the ohmic damping of the conduction

electron oscillations in the metal. Therefore, the wavevector $k_x = k'_x + ik''_x$ will have also an imaginary part leading to solutions of the fields of the form $e^{-2k''_x x}$ with $k''_x = 1/2L_{\text{SPP}}$. It is valid then to define the intensity I_{SPP} of the surface plasmon propagating in an AuNW decreasing as [252]

$$I_{\text{SPP}} = I_0 e^{-x/L_{\text{SPP}}} \quad (3.4.1)$$

where L_{SPP} is the propagation length after which the intensity has decayed to $1/e$, x is the distance along the nanowire and I_0 is the SPP intensity at the coupling site.

A composition of scanning electron micrographs showing four AuNWs is illustrated in the insets of Fig. 3.4.3(a). Figure 3.4.3(a) also displays false-color wide-field images obtained at the pump wavelength $\lambda_0 = 808$ nm (each frame is integrated over 20 ms). The diffraction-limited focal area is clearly identified at the left of the images (saturated region). As introduced before, light emitted by the distal end confirms the excitation and propagation of SPPs. The in-plane position of the nanowire within the focal spot is precisely adjusted to maximize this signal [246]. We estimate L_{SPP} by measuring the out-coupled light intensity $I_{\text{out}}^{\text{SPP}}$ detected from the distal end at $x = L$ for AuNWs with different lengths [226, 253]. Experimentally, the intensity is extracted from a region-of-interest on the CCD images overlapping the extremity of the AuNW (dotted square in Fig. 3.4.3(a)). A semilogarithmic plot of I_{out} as a function of L for $\lambda_0 = 808$ nm is displayed on Fig. 3.4.3(c). For comparison, L_{SPP} is also estimated when the incident laser is tuned at $\lambda = 720$ nm. The exponential fits indicate $L_{\text{SPP}}(\lambda_0 = 808 \text{ nm}) = 2.96 \pm 0.78 \mu\text{m}$ and $L_{\text{SPP}}(\lambda_0 = 720 \text{ nm}) = 1.83 \pm 0.53 \mu\text{m}$ in agreement with the expected shorter propagation lengths for shorter wavelengths due to higher losses [94].

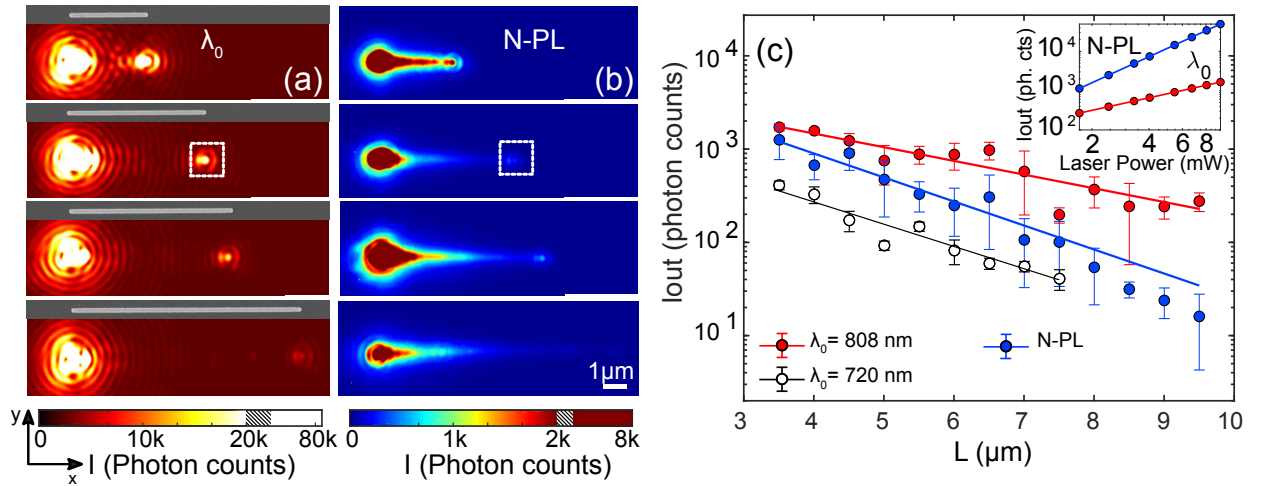


Fig. 3.4.3. (a) Image of the light distributed in AuNWs with different lengths L taken at the excitation wavelength. From top to bottom $L = 3.0 \mu\text{m}$, $L = 5.5 \mu\text{m}$, $L = 7.0 \mu\text{m}$ and $L = 9.5 \mu\text{m}$. Scanning electron micrographs of the AuNWs are shown in insets. The AuNWs are excited at the left end by the focused laser at $\lambda_0 = 808$ nm. The incident polarization is along the AuNWs. (b) Spectrally filtered images capturing the nonlinear photoluminescence emitted at $\lambda < 780$ nm by the nanowires. The dynamic of the images is saturated at the excitation area to reveal the weaker signals produced along the nanowires and at the distal ends. (c) Semilogarithmic plots of the linear ($\lambda_0 = 808$ nm and $\lambda_0 = 720$ nm) and nonlinear light intensity I_{out} (integrated for $\lambda < 780$ nm) out-coupled at the distal end of the nanowire vs. nanowire length with their corresponding exponential fit. The error bars represent the standard deviation measured on five nanowires. The inset is a log-log plot of the dependence of the integrated N-PL intensity on the incident power at the excitation point with a quadratic fitting (slope ≈ 2.2). The power dependence for the laser line λ_0 is also shown for reliability purpose with a slope of 1.

3.4. Unraveling the N-PL delocalization

We now turn our attention to Fig. 3.4.3(b) showing images capturing the nonlinear photoluminescence emitted by the AuNWs (the acquisition time is here 5 s). The excitation wavelength is filtered out from the detection path to only retain the spectrally integrated N-PL emitted at wavelengths $\lambda < 780$ nm. Note that the second harmonic co-generated with the N-PL is also rejected from the detection and the images are background corrected. We verify the nonlinear character of N-PL by interrogating its dependence with average laser power. A plot of the logarithm of the integrated intensity over the whole N-PL spectrum versus the logarithm of the average incident power is shown in the inset of Fig. 3.4.3(c). The linear fit gives a slope of ≈ 2.2 , revealing the quasi-quadratic dependence of the N-PL on the excitation power.

The largest N-PL signal in Fig. 3.4.3(b) is evidently produced within the focal region where the pump intensity is the highest. However, a clear extension of the N-PL directed along the nanowire is also readily observed. The intensity of this delocalized N-PL signal decreases with distance x . At $x = L$, a small but visible gain of the N-PL signal is observed.

Let us now estimate, by the same approach used to measure $L_{\text{SPP}}(\lambda_0)$, the changes on the N-PL intensity at the distal end of the AuNWs $I_{\text{out}}^{\text{N-PL}}$. The graph is shown in Fig.3.4.3(c) too.

The characteristic decay length $L_{\text{N-PL}}$ inferred from a linear fit in this semilogarithmic plot is about $1.69 \pm 0.46 \mu\text{m}$. In principle, this decay value could be related to the SPP excited at the pump wavelength λ_0 . By taking into account the power dependence of N-PL measured before we write [254]

$$I_{\text{out}}^{\text{N-PL}} \approx (I_{\text{SPP}})^{2.2} = I_0^{2.2} e^{-2.2y/L_{\text{SPP}}} \quad (3.4.2)$$

Equation 3.4.2 implies that $L_{\text{N-PL}} = L_{\text{SPP}}/2.2$, which is not in accord with the experimental data where $L_{\text{N-PL}}$ is 30% greater. Such discrepancy hints the presence of extra contributing processes occurring at the extremity not taken into account so far.

When the surface plasmon propagating at the pump wavelength reaches the end of the nanowire, the finite geometry of the termination creates the condition for locally enhancing the electromagnetic field through a lightning rod effect. This localized field-enhanced region at the nanowire's end has been exploited for developing remote Raman sensing [251, 255]. It is clear that the amplification factor will contribute at rising the N-PL signal level. However, it should not influence the characteristic decay length $L_{\text{N-PL}}$ and one has to look for additive contributions that would explain $L_{\text{N-PL}}$. Again reviewing the literature, Shegai *et al.* showed in 2010 that fluorescence spectra emitted from molecules adsorbed in silver nanowires varies as the excitation position changes, suggesting the possibility of near-field excitation of surface plasmons within the whole fluorescence spectrum [239]. A similar mechanism might be at play here whereby the N-PL signal produced along the nanowire would locally excite SPPs within a wavelength range dictated by the emitted luminescence spectrum. This situation is depicted by Fig. 3.4.2(d). Let us investigate whether or not the N-PL signal produced at the laser focus may couple to a continuum of SPPs.

3.4.2 N-PL plasmons coupling

Figure 3.4.4 shows a set of images when the laser excitation no longer overlaps one end facet but is moved to the middle of the nanowires. For this excitation location, the direct excitation of a SPP at the pump wavelength λ_0 is inefficient. The absence of a geometrical discontinuity along the polarization direction inhibits the momentum transfer required for SPP excitation [246]. Figure 3.4.4 (a) directly compares the excitation at the end and at the middle of the nanowire at the pump wavelength. The absence of signal detected at the distal end (arrow) when the focus is moved on the middle of the AuNW confirms the absence of SPP excitation. One can safely rule out any contribution generated from a direct excitation of SPP

at λ_0 in the nonlinear signal displayed in Fig. 3.4.4(b). Here, the N-PL response at the focal excitation area dominates the images, but there is a small signal emitted from both ends of the AuNWs. The N-PL intensity at the extremity $I_{\text{out}}^{\text{N-PL}}$ weakens for longer nanowires suggesting a loss-related process. This process can be identified by recording the spectra of $I_{\text{out}}^{\text{N-PL}}$ as shown in Fig. 3.4.4(c) for two different AuNWs (3.0 μm and 7.0 μm). Both graphs follow the typical broad photoluminescence shape with higher intensities at longer wavelengths. For the 7.0 μm long AuNW, the relative intensity in wavelength range 650 nm $< \lambda < 750$ nm is reduced. Because of the wavelength dispersion of the imaginary part of the plasmon effective index, SPPs excited in the blue region of the N-PL spectrum have shorter propagation length than SPPs excited in the red part of the continuum [94, 256]. This translates to a loss of the blue part of the spectrum for $L = 7.0 \mu\text{m}$.

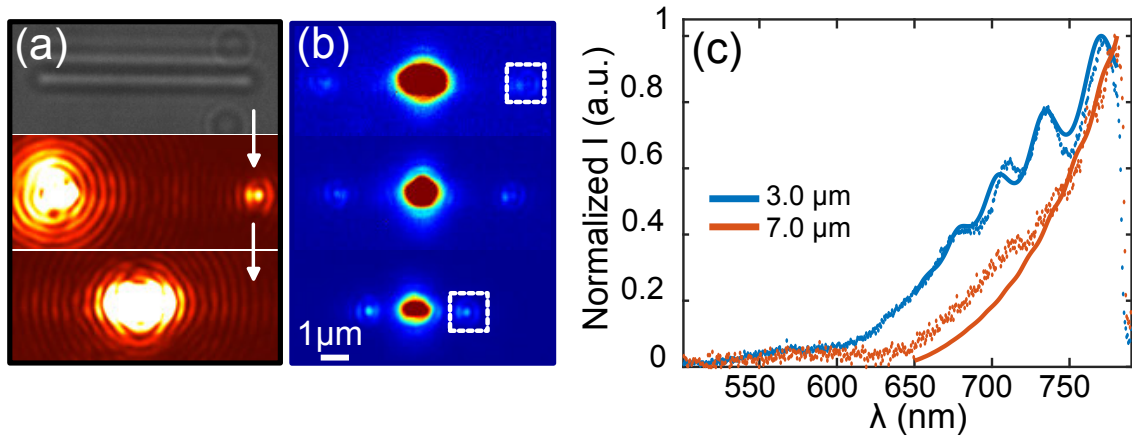


Fig. 3.4.4. (a) top frame: optical transmission image of a 7.0 μm AuNW. Center frame: SPP excitation at one end and propagation to the distal face (arrow). Image is taken at the excitation wavelength. Bottom frame: excitation at the middle of the AuNW showing an absence of SPP excitation and propagation at the laser wavelength. (b) Image of the filtered nonlinear optical response of AuNWs with different lengths (from top to bottom 7.0 μm , 5.5 μm and 3.0 μm) when excited approximately at the middle with $\lambda_0 = 808$ nm, incident polarization is along the AuNWs. (c) Data points: normalized spectra of the N-PL emitted by the end face (white dashed square in (b)). The spectra are normalized with their own maximum. Solid lines: simulated spectra considering a diffraction-limited broad-band source in the middle of a Fabry-Pérot cavity.

The oscillations observed in the N-PL spectrum emitted by the end of the shortest nanowire suggest the presence of Fabry-Pérot plasmon resonances. In this respect, one-dimensional structures such as nanowires or nanorods act as a cavity in analogy with Fabry-Perot resonators [65, 253]. The formalism described by Taminiau et al. is used to qualitatively reproduce the experimental spectra of the two nanowires with different lengths L_0 [257]. The model is schematically depicted in Fig. 3.4.5(a), it considers a source with a diffraction limited Gaussian spatial extension located inside a two-mirror cavity. The cavity has a length L and identical real-valued amplitude reflection coefficients r at both end faces. The source, located at $y = y_0$ emits a broad spectrum with a N-PL intensity exponentially growing with the wavelength mimicking the N-PL spectrum. Such N-PL wavelength dependence is characteristic of the emission of an out-of-equilibrium heated electron distribution following a blackbody radiation tailing in the visible region [9, 10, 145]. The complex wavevectors of the plasmon modes k_{SPP} and their wavelength dispersion are determined by a Finite-Element mode solver (COMSOL Multiphysics[®]) considering a 50 nm \times 160 nm two-dimensional Au nanowire placed on glass/air interface. If t is the transmission coefficient of the cavity, the electric field at the output $x = L$ writes

3.4. Unraveling the N-PL delocalization

$$E_{\text{out}}(x = L) = \frac{te^{ik_{\text{SPP}}L}(e^{-ik_{\text{SPP}}x_0} + re^{ik_{\text{SPP}}x_0})}{1 - r^2e^{2ik_{\text{SPP}}L}} \quad (3.4.3)$$

The solid lines in Fig. 3.4.4(c) are the simulated output spectra considering an effective cavity length $L = 3.15 \mu\text{m}$ and $L = 7.0 \mu\text{m}$. The reflection coefficient is set at $r = 0.5$ and the calculated effective index of the SPP at $\lambda_0 = 750 \text{ nm}$ is $n_{\text{eff}} = k_{\text{SPP}}/k_0 = 1.72 + i0.03$. The source is located at $y_0 = L/2$ and has a Gaussian lateral extension with a full-width at half maximum of 300 nm. The main features of the experimental spectra are qualitatively recovered by this simple model (spectral position, number of the oscillations) including the disappearance of the resonances for nanowire length significantly exceeding the propagation length of the mode ($L = 7.0 \mu\text{m}$).

Concatenating the information brought by Fig. 3.4.4, we conclude that a broad distribution of SPPs is thus excited at the focal spot within the N-PL continuum, and propagate with different attenuation lengths. This coupling mechanism mediated by the confinement of the nonlinear response and revealed for an excitation at the middle of the nanowire also occurs when the focal region overlaps one extremity (probably with greater efficiency due to scattering at the physical boundary).

The propagating bound mode of the AuNWs is further investigated in the substrate-AuNW-air system considered before. The complex effective index $n_{\text{eff}} = n' + in''$ of the corresponding SPP mode is calculated for a given set of frequencies. The real and imaginary parts of the SPP's momenta are derived from $k' = n'k_0$ and $k'' = n''k_0$ and finally $L_{\text{spp}} = 1/(2k'') = \lambda/(4\pi n'')$. Specifically, we again use FEM (COMSOL Multiphysics[®]) to characterize the guided mode and the dielectric constant is taken from Johnson and Christie [94]. The optical index of the glass substrate is fixed at $n = 1.5$ and the computation window is limited to $1 \mu\text{m}$. Since the bound mode is considered, we use perfect boundary conditions. Results are shown in the curve of Fig. 3.4.5(b). In the same figure, the experimental L_{spp} values obtained in the previous section are displayed for comparison, they clearly follow the same trend of the simulation.

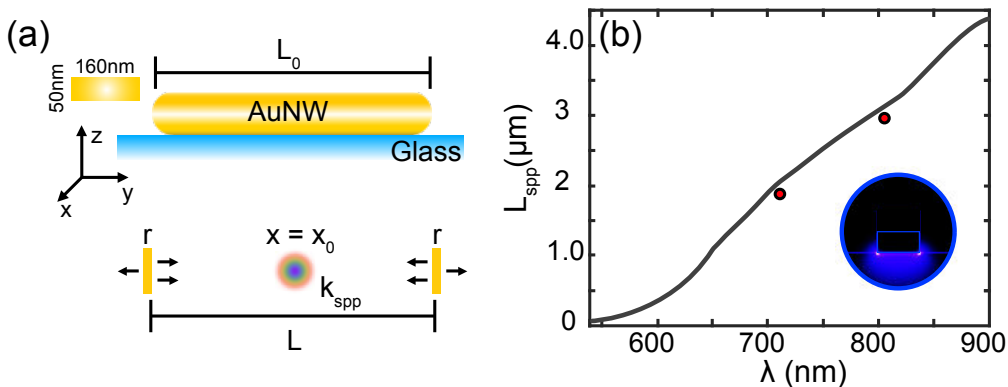


Fig. 3.4.5. (a) AuNW with a cross section of $50 \text{ nm} \times 160 \text{ nm}$ on a glass substrate that supports a wavevector k_{spp} . Simplified modelization of the AuNW as a 1D cavity with length L and reflection coefficient r . The source is located at $x = x_0$ and emits a broad spectrum mimicking a blackbody radiation. Adapted with permission from [257]. Copyright 2011 American Chemical Society. (b) Simulated surface plasmon propagation lengths for a $150 \text{ nm} \times 60 \text{ nm}$ height AuNW on a glass substrate. The points represent the L_{spp} values inferred in the previous section. The inset on the bottom right shows the field emission of the bound mode sustained by the nanowire.

3.4.3 Emission mechanisms of the delocalized N-PL

A major difference between N-PL emission with an excitation at the middle and with an excitation coinciding with one end is the lack of longitudinal extension of the nonlinear signal along the nanowire. Figure 3.4.6 graphically compares such situations where a $7.0 \mu\text{m}$ long AuNW is excited at the left end (a) and at approximately the middle (b). Integrated intensity profiles of the images along the x -axis complete the comparison, the grayed areas indicate the N-PL extension. Whereas the excitation at the extremity produces a longitudinally extended emission almost reaching the end of the nanowire, the middle excitation turns into a very localized emission ($< 2.5 \mu\text{m}$).

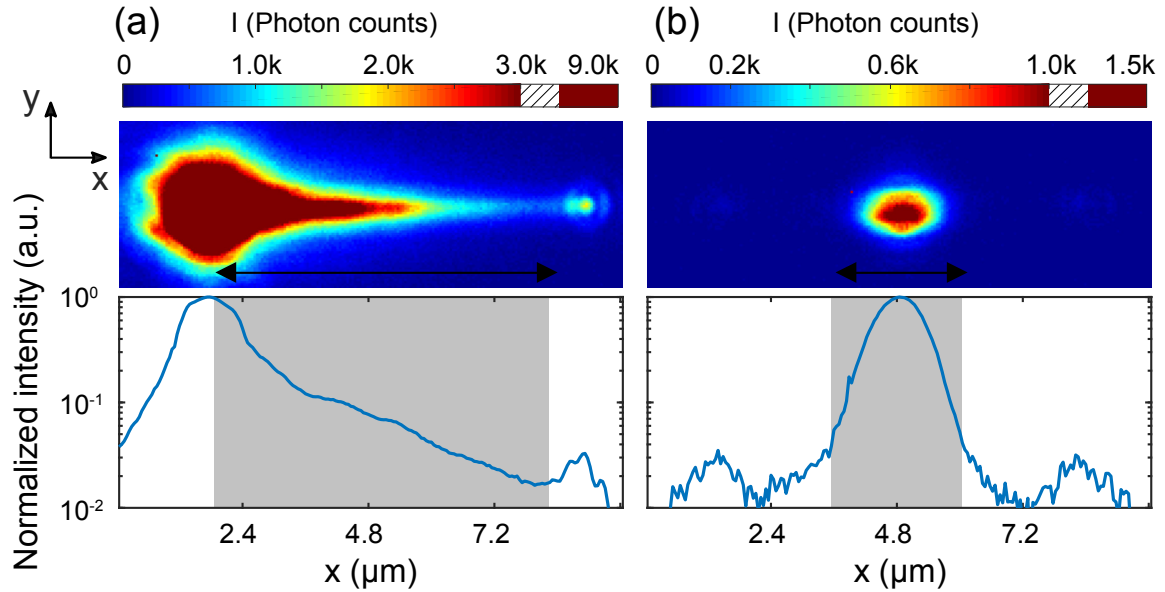


Fig. 3.4.6. Images of the filtered nonlinear optical response of a $7.0 \mu\text{m}$ long AuNW being excited (a) at the left end and (b) at approximately the center. The normalized integrated intensity profiles along the x -axis at the bottom of the images. Grayed areas indicated the longitudinal extension of the N-PL.

Clearly, when present, the longitudinal extension of the N-PL signal relates to the presence of SPP propagating at the pump wavelength. We cross-check in the following that the longitudinal distribution cannot be understood as SPP modes leaking in the substrate as sketched in Fig. 3.4.2(c). To start, higher-order leaky SPP modes are only existing above a cut-off width, typically $100 \text{ nm} - 200 \text{ nm}$ [227, 258]. Although, the nanowires have a rectangular cross-section ($50 \text{ nm} \times 160 \text{ nm}$), the higher-order modes that may be present would be strongly attenuated because they are propagating close to their cut-off. Furthermore, SPP leaky modes are easily recognized in images; the light is distributed in two well-defined lines located at the sides of the nanowire [226, 227]. Throughout the chapter, figures recorded at the pump wavelength indicate that only the SPP bound mode is present since there is no leakage visible during SPP propagation (See Figs. 3.4.1(a), 3.4.3(a), 3.4.4(a)). In the case of N-PL wavelengths (Figs. 3.4.1(b), 3.4.3(b), 3.4.6(a)), the signal is indeed distributed along the nanowire but not in the form of two parallel lines characteristic of leaky nanowire modes. Since the effective index of the mode increases for shorter wavelengths, the absence of a leaky mode at λ_0 indicates that the extension of the N-PL is of different origin. We unambiguously rule out the contribution of leaky modes in the signal in the next section by analyzing the wavevector distribution (k_x, k_y) in Fourier space.

3.4. Unraveling the N-PL delocalization

3.4.3.1 Wavevector distribution of the N-PL

Fourier plane (FP) imaging also known as back focal plane (BFP) imaging is a microscopy technique that unravels the angular emission of the sample. In contrast to real plane imaging where the information is encoded in spatial coordinates, Fourier imaging develops in angular coordinates. Fourier imaging provides access to the momentum distribution given the intimate relationship between the angular distribution of light and its momentum (wavevector \vec{k}). Fourier imaging is particularly important to resolve the angular emission pattern of nanoantennas [2, 233] as well as to understand complex optical processes as secondary emission [259, 260] and nonlinear scattering [261].

Although the resulting wavevector distribution can become very complex, the optical principle of Fourier imaging is relatively simple [262]. Light emerging from the sample plane can be expressed as a sum of plane waves emanating at different angles as shown in 3.4.7. When this light passes through the objective (Fourier transformer), its different components separate and transform into converging waves focused at a point in the Fourier plane.

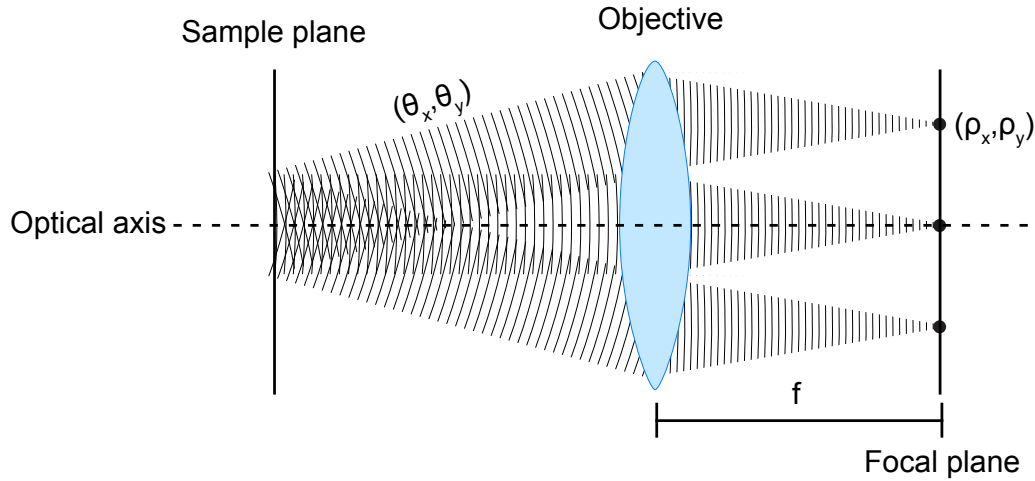


Fig. 3.4.7. (a) Schematic of the Fourier transform produced by an objective lens. Adapted with permission from [262].

The result is a pattern in the Fourier plane where every point (ρ_x, ρ_y) represents the angle of emission of the light emanated at the sample plane. Both quantities are related by [263]

$$\rho = fn \sin \theta \quad (3.4.4)$$

where θ is the angle of emission, ρ is the radial distance from the optical axis in the Fourier plane, f is the objective focal length and n is the immersion medium refractive index. As stated before, the angular emission and the wavevector distribution are related, specifically, the in-plane wavevector k_{\parallel} is proportional to ρ .

In practice, the Fourier plane of the objective is generated inside the barrel as schematically shown in Fig. 3.4.8(a) for a glass coverslip illuminated by a focused laser. However, relay optics allows to project it as far from the sample as necessary to an imaging device [226]. Given that excitation and collection are performed with the same objective and the transparent nature of the bare substrate (no features or structures), most of the collected light in this case comes from total internal reflection (TIR). Consequently, the Fourier plane pattern is basically a ring limited by the critical angle for the glass/air interface θ_{crit} and the numerical aperture of the objective (θ_{NA}). The intensity distribution in the Fourier plane I_{FP} as a function of the emission angle θ can be related to the fields generated by the emitter \vec{E}_{emitter} as [264]

$$I_{\text{FP}} \propto \frac{1}{\cos \theta} \left| \vec{E}_{\text{emitter}} \right|^2 \quad (3.4.5)$$

where the factor $1/\cos \theta$ corrects the amount of power collected by each angular section $d\theta$ by using a simple trigonometrical relation ($dr = ds \cos \theta$). This correction factor is better illustrated in Figure 3.4.8(a) which shows the projection of the emission onto the Fourier plane generated in the objective. The emission coming in a certain angular section $d\theta$ is captured in ds . Whereas dr decreases with θ , the projected power onto ds is invariant.

As already introduced, the Fourier plane can be transferred with relay lenses outside the microscope to a CCD camera in order to allow easier filtering and image acquisition. The exact positioning of these lenses can be easily set and confirmed by performing some measurements on the ring of the Fourier plane as shown in Fig. 3.4.8(b). Here, intensity profiles taken at the center of the FP (optical axis) and their derivative I' are used to check the ratio between the outer diameter ($D_{\text{out}} = 453$ pixels) corresponding to $NA = n_{\text{oil}} \sin \theta_{NA} = 1.49$ and the inner one ($D_{\text{in}} = 305$ pixels) which corresponds to $N_{\text{crit}} = n_{\text{glass}} \sin \theta_{\text{crit}} = 1$. The referential points for this measurement are indicated by arrows in the profile. A quick calculation corroborates the optimum lens configuration, this is

$$N.A. = \frac{D_{\text{out}}}{D_{\text{in}}} = 1.485 \quad (3.4.6)$$

which is very close to the expected value 1.49 given the limited resolution of the camera. Finally, the intensity inhomogeneity in this Fourier plane pattern comes from a preferred angular emission towards one of the semi-planes.

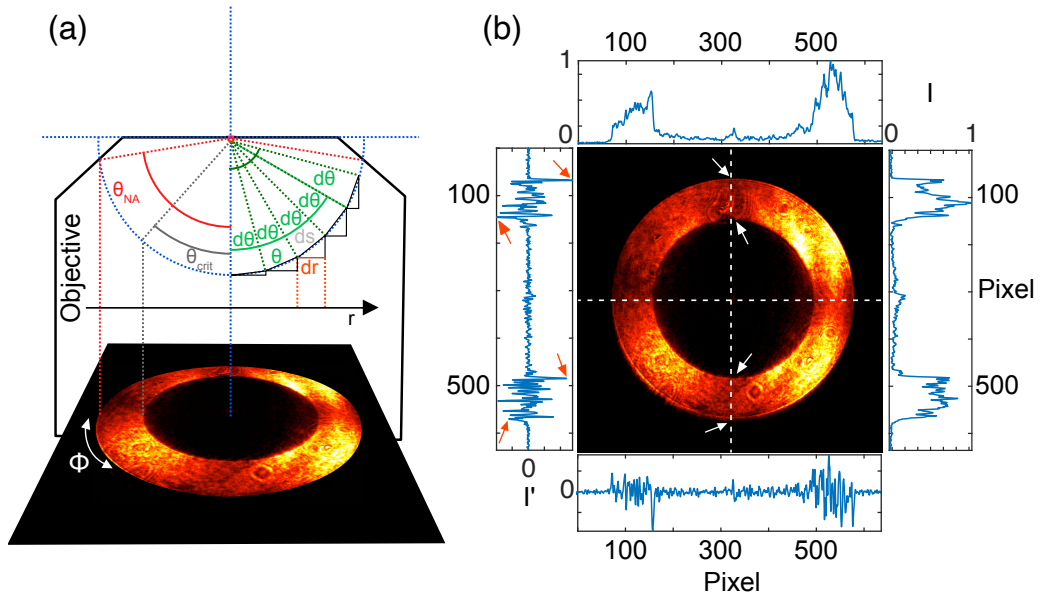


Fig. 3.4.8. (a) Resulting Fourier plane pattern as the scattered laser light from the sample substrate goes through the objective lens. The projection of the angular emission is schematically depicted. Image inspired by [265, 266]. (b) The same Fourier plane with the intensity profiles indicated by the dashed lines (top and right frames). The derivatives of the profiles are shown at the bottom and left frames. The arrows indicate the referential points taken to verify the positioning of the relay lens.

Fourier planes taken at the pump wavelength and across the N-PL spectrum are shown in respectively Fig. 3.4.9(a,b) and Fig. 3.4.9(c,d) for the $L = 3.0 \mu\text{m}$ and $L = 5.5 \mu\text{m}$ long nanowires. At λ_0 , the Fourier planes feature a well-defined fringe pattern, but there is no clear signature of the presence of a leaky mode [226, 246]. Known as Gibbs oscillations, they are

3.4. Unraveling the N-PL delocalization

the result of the bound mode sustained by the nanowire, as well as the Fourier transform, the coherence of the process and the finite dimension of the AuNW [246, 267, 268]. A cross section profile of the $3.0 \mu\text{m}$ nanowire Fourier plane at the position indicated by the dashed line is shown in Fig. 3.4.9(e). The oscillation period Δn of the fringes in the k_x axis relates to the length of the nanowire, with $L = \lambda_0/\Delta n$ [221]. Calculations for several nanowires demonstrate the relative accuracy of this method in Fig. 3.4.9(f). In spite of the experimental errors and the limited resolution of the microscope setup, the linear fit is close to 1 revealing a direct correspondence with the nominal length values of the AuNWs. In the k_y direction, i.e. perpendicular to the propagation direction, the fringes show no change, this is due to the confinement of the wavevector in one direction [265].

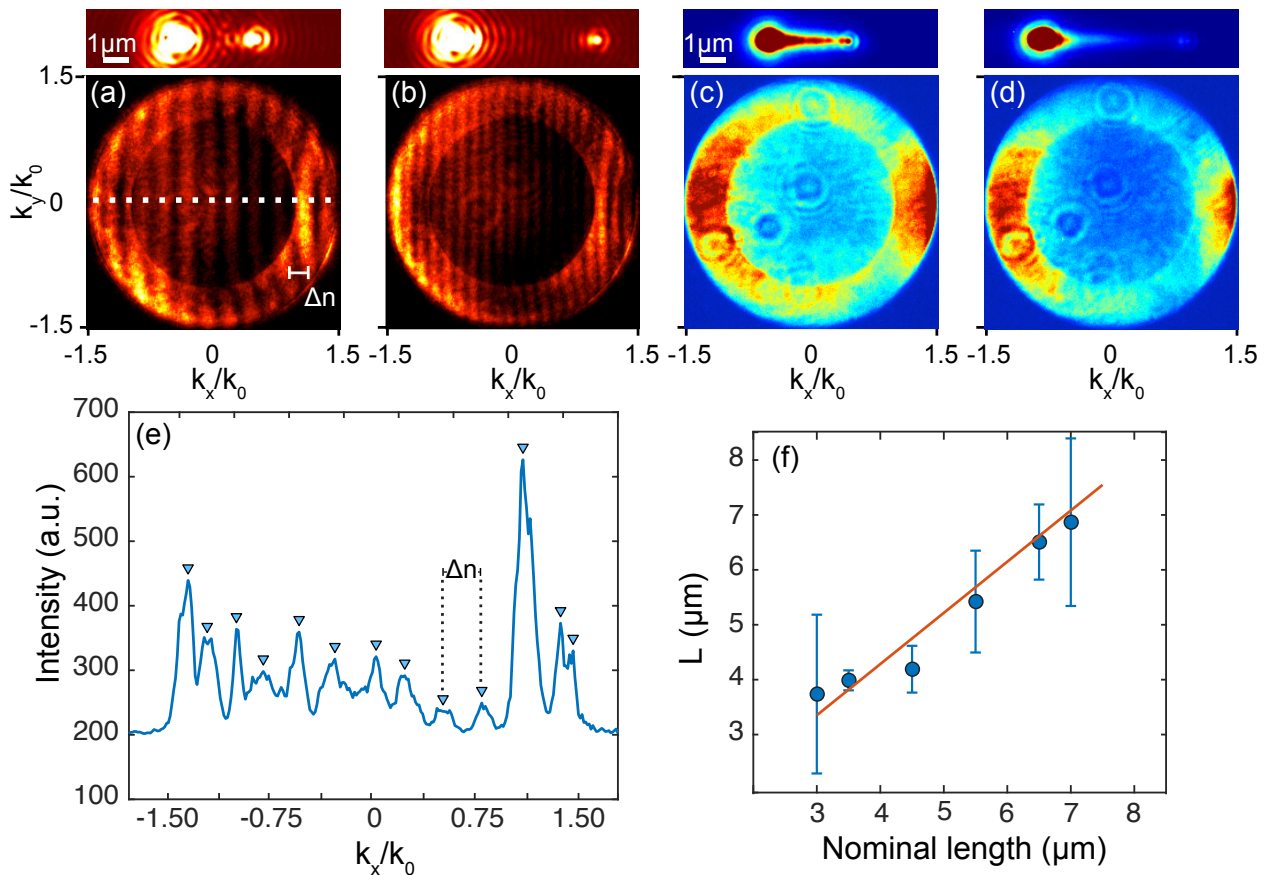


Fig. 3.4.9. Fourier space patterns of the (a,b) linear and (c,d) filtered nonlinear optical response for the (a,c) $3.0 \mu\text{m}$ and (b,d) $5.5 \mu\text{m}$ long AuNWs shown at the top obtained by imaging the back focal plane of the objective. The small concentric circles in (c) and (d) are diffraction rings produced by dust residues left on the optical elements. The excitation is located at one end of the AuNW. (e) Cross section profile indicated with a dashed line in (a). (f) Estimation of the nanowires length by using the fringe patterns of the linear back focal planes. The linear fit gives a slope of 0.93. The error bars indicate the standard deviation from several measurements in the Fourier plane fringes.

In contrast with the linear propagation, the Fourier planes recorded across the N-PL emission spectrum shown in Fig. 3.4.9(c,d) are completely free of fringes, a signature of the incoherent nature of this particular nonlinear process [221]. Here too, the distribution of wavevector confirms the absence of leaky modes at the N-PL spectral content. Most of the emission is located in two lobes oriented with the propagation. This pattern, already reported by Viarbitakaya *et al.* [221], is consistently observed on all the investigated nanowires. The increase of the N-PL intensity distributed toward larger $\pm k_x/k_0$ values confirms that the N-PL is emitted with

a broad distribution of in-plane wavevectors within the continuum; the objective collecting only those comprised below 1.49. Evidently, out of the large distribution of generated wavevectors, some of them are resonant with the effective index of bound SPP modes. Modes thus may be excited within the N-PL spectral continuum as already observed in Fig. 3.4.4 for an excitation in the middle of the AuNW. Furthermore, the successive near-field coupling of the generated N-PL as the SPP(λ_0) propagates is not discarded, nevertheless, the efficiency and yield of this process are very low.

The above discussion shows that the delocalized signal cannot be understood from leaky SPP modes; at this stage the question about how is the N-PL emitted remains unanswered. In this context, we investigate further the N-PL emission by measuring the polarization state of the distributed N-PL in the AuNWs in the next section. By doing so, we also confirm the near-field coupling mechanism.

3.4.3.2 Polarization resolved wavevector distribution of the N-PL in AuNWs

The wavevector distribution of the AuNWs N-PL emission is, as previously shown, mainly dictated by the nanowire orientation. Evidently, the excitation laser position and the coupling to the SPP at λ_0 defines the Fourier plane pattern too. Polarization resolved Fourier plane patterns of the delocalized N-PL in AuNWs are displayed in Fig. 3.4.10 for the cases of excitation at the end and at the middle of the gold nanowires. The excitation laser polarization is aligned with the axis of the nanowire.

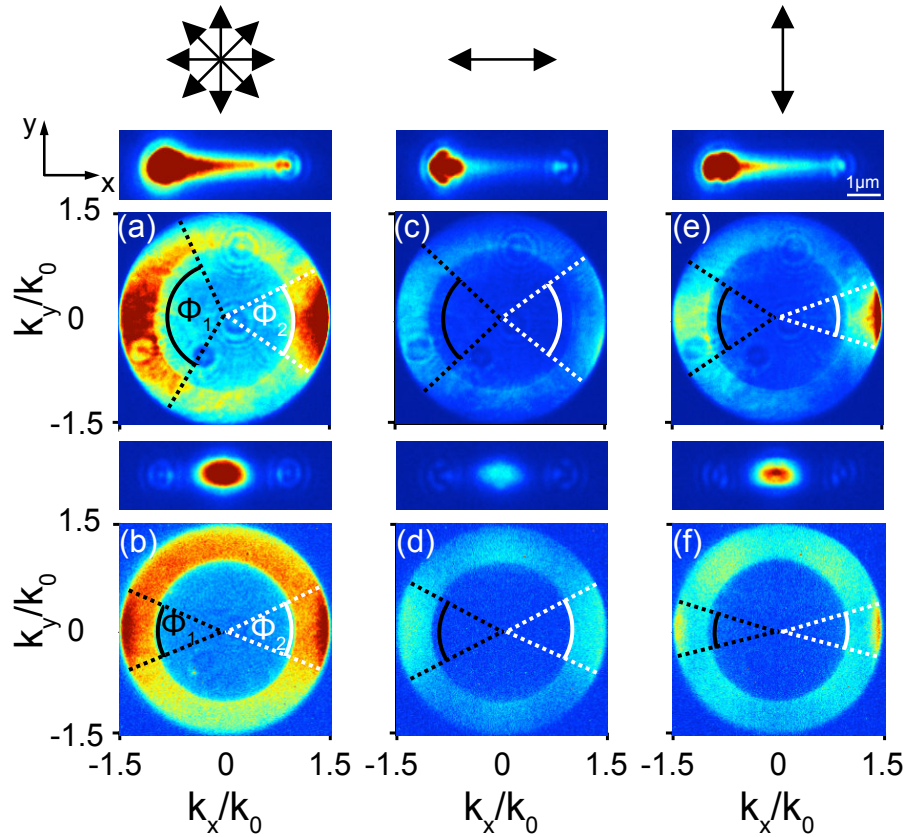


Fig. 3.4.10. Fourier plane patterns with different polarization analysis of the AuNWs N-PL emission with (a,b) no analyzer, analyzer (c,d) along and (e,f) transverse to the axis of the nanowire (see double-sided arrows on the top). ϕ_1 and ϕ_2 indicate the azimuthal spread angle of the wave vector distribution. The top insets show the corresponding real plane image of the presented FPs for (a,c,e) end-excitation and (b,d,f) middle excitation.

3.4. Unraveling the N-PL delocalization

For clarity, let us start with the situation when the analyzer is not present. Regarding end-excitation (see Fig. 3.4.10(a)), the emission is azimuthally confined in the direction of propagation ($+k_x/k_0$). Carefully looking at the Fourier plane, the in-plane azimuthal distribution of $-k_x$ vectors displays an angular spread at least two times larger than that of the $+k_x$ vectors ($\phi_1 = 120^\circ > \phi_2 = 58^\circ$). Essentially, the excited N-PL towards the $+k_x$ half-plane is directed by the AuNW. In contrast, that generated to the opposite $-k_x$ half-plane is able to out-couple to a wider range of wavevectors provided by the discontinuity. This is confirmed by the middle-excitation case showed in Fig. 3.4.10(b) where the FP exhibits a vertically symmetric pattern given by two well defined lobes. Both features indicate a very similar azimuthal spread ($\phi_1 \approx \phi_2 \approx 49^\circ$) where the polar angle of emission is very close to the maximum detection angle θ_{NA} fixed by the numerical aperture of the objective. In this particular excitation configuration, the nanowire is able to direct the N-PL emission along its axis. The horizontal asymmetry towards $+k_y/k_0$ is due to preferential excitation of the upper edge of the nanowire by a barely shifted laser spot with respect to the center of the nanowire.

If the longitudinally and transversely polarized contributions of the N-PL emission wavevector distribution are now discriminated with an analyzer, the transverse component shows a considerably higher generation efficiency than the longitudinal one. Furthermore, the azimuthal confinement along the axis of the nanowire is more important when the analyzer is transverse to the AuNWs (see table 3.4.1). These observations are a direct consequence of the N-PL generation processes occurring in the nanowire as further confirmed in the next section. Briefly, the transverse geometrical discontinuity of the nanowire facilitates the local scattering to free-space photons whereas the longitudinal invariant geometry hinders it. Hence, longitudinally polarized N-PL comes mainly from propagating SPPs scattering at the end face and the azimuthal confinement in the direction of propagation depends on the nanowire width. As the lateral confinement increases (thinner nanowires), the out-scattered light at the distal end spreads over a wider wavevector distribution (wider lobes). In our case, nanowires are relatively thin (160 nm) resulting in a wide distribution of wavevectors in the longitudinally polarized N-PL Fourier plane. On the other hand, the transversely polarized N-PL is mostly generated by local scattering at the generation point. The resulting Fourier plane can be interpreted as dipoles placed transverse to the nanowire which emission is directed by an antenna effect.

Table 3.4.1. Azimuthal wavevector spread angles for the Fourier plane images shown in fig. 3.4.10

		End	Middle
	ϕ_1	120°	49°
	ϕ_2	58°	49°
	ϕ_1	79°	60°
	ϕ_2	69°	57°
	ϕ_1	61°	31°
	ϕ_2	46°	32°

3.4.3.3 Polarized N-PL emission of AuNWs

The part of the N-PL continuum which couples as propagating SPPs in the AuNWs can be partially discriminated by carefully analyzing the polarization of $I_{\text{out}}^{\text{N-PL}}$. Indeed, SPP scattering at the end face is mainly polarized in the direction of propagation [247, 269], and such preferred field orientation should be visible in $I_{\text{out}}^{\text{N-PL}}$. Figure 3.4.11 shows integrated intensity profile graphs along the longitudinal axis of three of the nanowires studied before (3.0 μm ; 5.5 μm and 7.0 μm). The signal is measured for a longitudinal (N-PL $_{\parallel}$) and a transverse (N-PL $_{\perp}$) orientation of the analyzer. As hypothesized, the N-PL signals distributed along the nanowires length (blue-shaded area) and scattered at the extremity (red-shaded area) are partially polarized but feature opposite behaviors. The larger intensity of the out-coupled $I_{\text{out}}^{\text{N-PL}_{\parallel}}$ in comparison to $I_{\text{out}}^{\text{N-PL}_{\perp}}$ at the distal ends of all the AuNWs substantiates the scattering of a continuum of SPPs generated at the excitation spot and traveling in the nanowires.

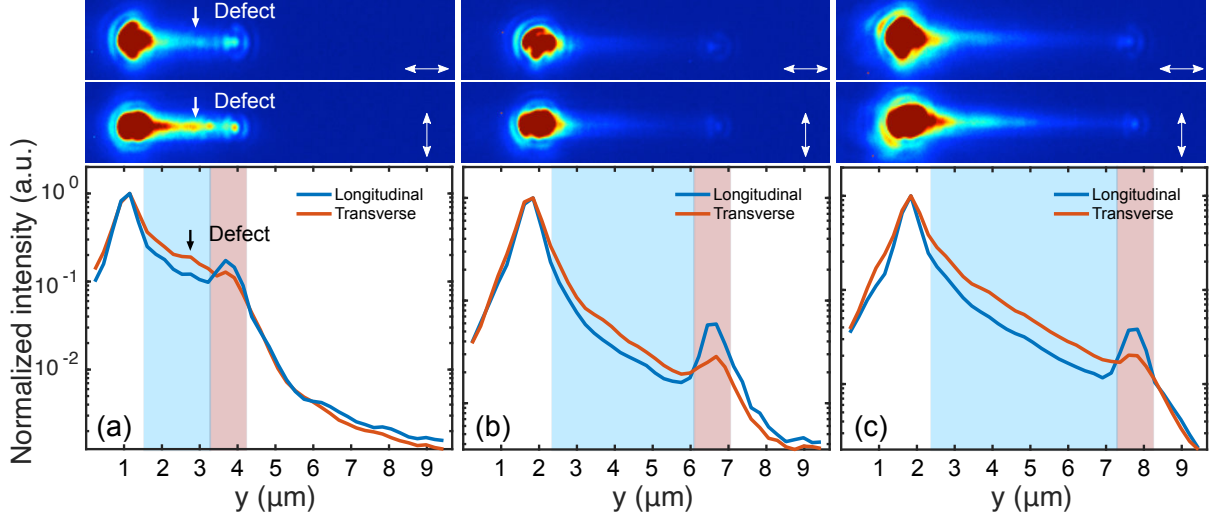


Fig. 3.4.11. Integrated intensity of the photoluminescence signal along the longitudinal axis of three AuNWs. The data is acquired for two orientations of the polarization analyzer and normalized with the maximum intensity. The blue-shaded area corresponds to the signal delocalized along the nanowire and the red area is the nanowire termination. The top insets show the polarization resolved image of the nonlinear photoluminescence distributed in the nanowire. The double arrow indicates the orientation of the analyzer.

We now have a better comprehension of the signal emitted from the termination. $I_{\text{out}}^{\text{N-PL}}$ is the additive contribution of the end-face amplification of the SPP field at the pump wavelength and the intensity scattered there by a continuum of SPPs. Their respective weight depends on the length of the nanowire.

N-PL emission may be interpreted as a surface effect mediated by momentum transfer that occurs when hot electrons interact with the walls of the metal. Such momentum transfer is reduced by the intrinsic invariant geometry of the nanowire along the longitudinal direction. Therefore, the emission intensity decreases in the case of the detection of N-PL_{\parallel} . On the contrary, N-PL_{\perp} is efficiently scattered to free-space photons because there is a strong geometrical discontinuity at the AuNW's edges. Defect mediated transfer is best observed for the shortest AuNW in Fig. 3.4.11(a) where local hot spots punctuates the N-PL distribution along the waveguide (see pointing arrows). Of course, the SPP excited at λ_0 is attenuated during its propagation, which readily explain the decay of the N-PL intensity distributed along the nanowire. The longitudinal N-PL decay along the nanowire follows an exponential with a characteristic length of $1.44 \mu\text{m}$. This value is very close to the $L_{\text{SPP}}/2.2$ expected from Eq. 3.4.2 confirming the indisputable role of the SPP propagated at λ_0 .

With the leaky modes discarded and the polarization analysis discussed just before, we hypothesize that the longitudinal extension of the N-PL along the nanowire is a local surface effect using the following argumentation: The SPP excited at the pump wavelength interacts with the surface of the metal nanowire where the plasmon field is maximum and locally produces the nonlinear photoluminescence observed along the waveguide. The local N-PL is partially emitted to free-space photons via a scattering process of hot electrons induced by the geometry of the nanowire and also via the mediation of surface defects.

3.5 Spatially resolved N-PL spectral emission

We now address the question about the spectral content of the distributed N-PL. To this aim, we measure the spectra for each position x along the AuNWs. Figure 3.5.1 displays

3.5. Spatially resolved N-PL spectral emission

the spatially-resolved N-PL spectra for the $7.0 \mu\text{m}$ long nanowire considered just before. The nanowire is excited at the bottom extremity. An image of the (x, y) spatial distribution is shown in the right hand side of the figure. Each horizontal line in the (λ, y) maps represents the spectrum at that specific position and is normalized with its own maximum intensity value. The spatial resolution is around $\Delta y = 230 \text{ nm}$. Again, as in section 3.4, we can identify three relevant areas: (i) the excitation spot located at $0.5 \mu\text{m} < y < 1.2 \mu\text{m}$, which has the brightest N-PL response and also the broadest spectrum. (ii) the out-coupling region at the AuNW extremity, where the sharp discontinuity introduced by the end of the AuNW acts as a scattering point enhancing the field and partially restoring the broad spectrum of N-PL. The same effect is observed in the presence of defects (local enhancers). (iii), the last interesting area is along the nanowire region of the AuNWs. In this part of the AuNW, there is a clear spatial evolution of the spectra: the bluer wavelengths are depleted with increasing distance. The SPP propagating at λ_0 loses energy as it propagates along the nanowire, affecting thus the N-PL spectral distribution.

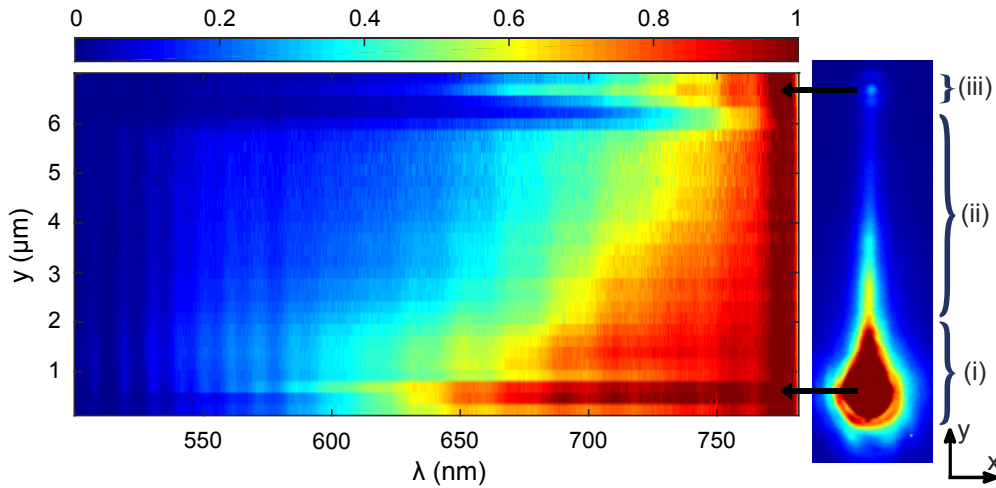


Fig. 3.5.1. Spatially resolved nonlinear photoluminescence spectral map for a $7.0 \mu\text{m}$ long AuNW excited at the bottom end. Each horizontal line represents the spectrum at that specific position and is normalized with its own maximum. The black arrows in the object plane image (right hand side) indicate the excitation and out-coupling regions.

The relative depletion of the bluer wavelengths for the extended N-PL is depicted on Fig. 3.5.2(a). Here, a few spectra are extracted from Fig. 3.5.1 at different y coordinates. The oscillations for $\lambda < 600 \text{ nm}$ arise from the transmittance of the shortpass filter used (Thorlabs, FES0800). The response observed in the 600 nm to 730 nm wavelength range near the excitation spot reduces with distance. To confirm the influence of the strength of the excitation on the spectral content of the nonlinear photoluminescence, we perform an analysis of the N-PL spectral shape by varying the average incident laser power. Spectra are measured at the excitation spot where the intensity is maximum; they are displayed in Fig. 3.5.2(b). Despite the differences on the evolution of the N-PL with the incident laser power (quadratic) and with the distance from the excitation point (exponential), there is a qualitative agreement between Fig. 3.5.2(a) and Fig. 3.5.2(b). When the laser power decreases, the contribution of 600 nm to 730 nm wavelength range becomes less dominant, a situation encountered in Fig. 3.5.1(a) for measurements obtained at the longer distances from the SPP excitation position. We checked that the trend of Fig. 3.5.2(b) is independent of the excitation laser position, the same depletion of the blue part of the spectrum is observed if the excitation spot is shifted along the nanowire. This experiment thus corroborates that the spectral shape of the N-PL response is dictated by the strength of the underlying SPP field.

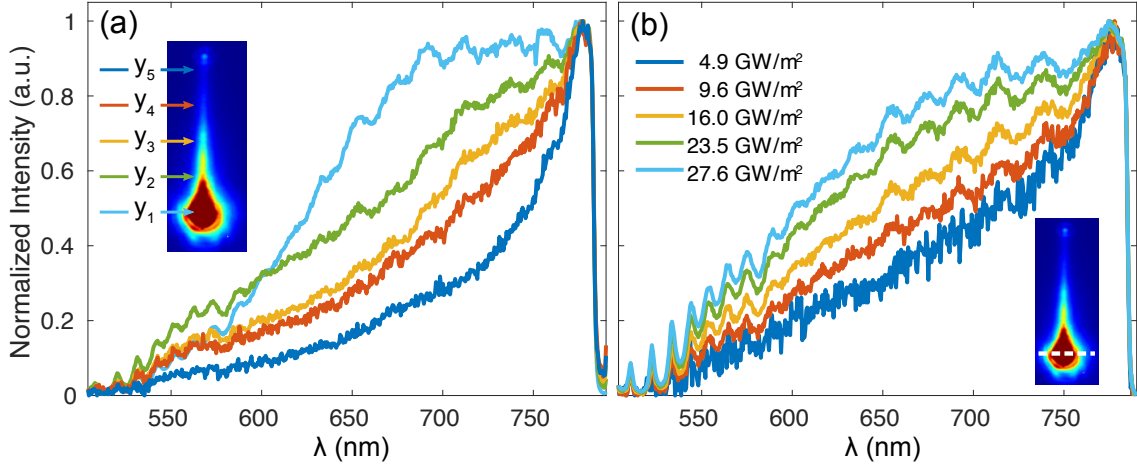


Fig. 3.5.2. Normalized N-PL spectra of the $7.0 \mu\text{m}$ studied AuNW (a) at different positions along the nanowire and (b) at the excitation spot but for different incident average laser powers. Insets indicate the position of the acquired spectrum.

For completeness, the space-resolved spectrum for the case of excitation at the middle of a $3.5 \mu\text{m}$ AuNW is also shown in Fig. 3.5.3. Here, we confirm once again the proposed mechanisms leading to the delocalization of the N-PL. Firstly, the absence of the propagating SPP(λ_0) limits the extension of the emission thus restricting the spectral content to the excitation point and the two ends of the nanowire. As stated before in the chapter, the coupling of SPP(λ_0) when exciting the AuNW in this particular fashion is negligible, therefore the observed nonlocal emission is principally generated by coupling of the N-PL continuum in the form of SPPs and scattering at the ends of the nanowire. The resulting spectra at both ends is then given by the dispersive nature of the material and the length of the nanowire as shown in the previous sections.

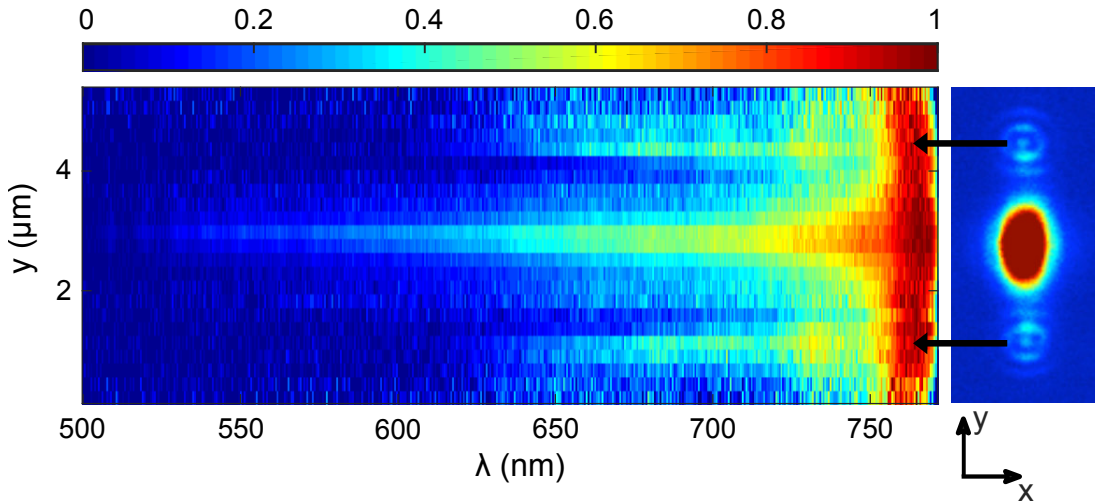


Fig. 3.5.3. (a) Spatially resolved nonlinear photoluminescence spectral map for a $3.5 \mu\text{m}$ long AuNW excited at the middle. Each horizontal line represents the spectrum at that specific position and is normalized with its own maximum. The black arrows in the object plane image (right hand side) indicate the out-coupling regions.

These results certainly open the way to a spatially tunable source originating from the delocalized N-PL in gold nanowires. As demonstrated, variations on the length of the nanowires, the excitation location or the incident power lead to different spectral emissions. Furthermore,

3.6. Remote electrical control of the N-PL emission

as presented and further investigated in the next chapter, the inclusion of scattering points such as an imperfection or a nanoparticle along the nanowire can completely change the coupling and emission characteristics of the gold nanowires. This can be particularly important for the development and improvement applications such as sensing, plasmonic waveguides and fast color switches. In the next section, another degree of control is included towards the achievement of a fully controllable active plasmonic device.

3.6 Remote electrical control of the N-PL emission

In nanophotonic devices based on nanowires, one of the main concerns on their performance is the precise manipulation of the SPPs propagation. Particularly important is the control of the linear and nonlinear scattering of the SPPs into photons. Such high level of control is essential in many applications focused on optical switches [270,271] and logic gates [272], light sources [273,274] and remote SERS excitation [228]. In this context, the electrical command of the local N-PL shown in chapter II and the understanding of the delocalized N-PL of the present chapter are brought together in an effort to extend the local control of the N-PL to a fully-remote activated and controlled N-PL emission.

In this section, we achieve the control of the N-PL scattered at the distal end of the nanowire by modulating the applied static electric field across the nanowire. A SEM micrograph of the nanostructure configuration is shown in Fig. 3.6.1(a). The gold nanostructures are yellow-colored for an easier view. A $5.0 \mu\text{m} \times 150 \text{ nm}$ gold nanowire very similar to the ones studied so far is separated on one edge $\approx 50 \text{ nm}$ from an electrode at the distal end. On the other edge the AuNW is contacted to another electrode. The bowtie shape of the electrodes seeks the enhancement of both the emission and the static electric field. A schematic figure of the dashed area of Fig. 3.6.1(a) shows a close-up of the electrical configuration (see Fig. 3.6.1(b)), similar to the procedure of Chapter II, a squared bias is applied through the gap. The nanowire is excited at the left end generating N-PL throughout the nanowire as displayed in Fig. 3.6.1(c).

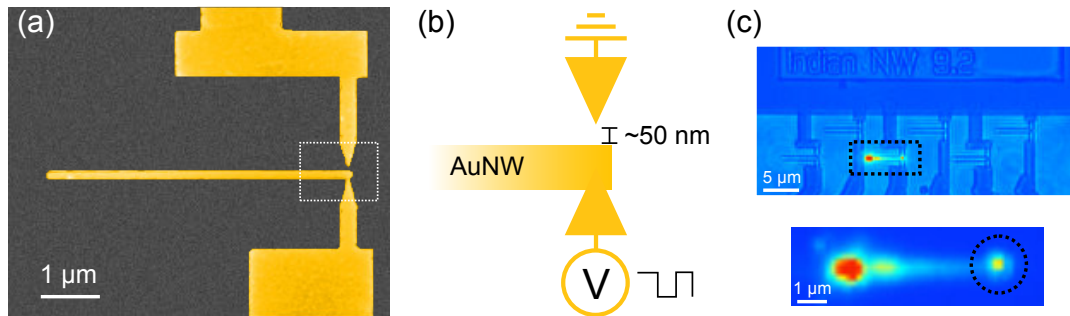


Fig. 3.6.1. (a) SEM micrograph of a $5 \mu\text{m} \times 150 \text{ nm}$ AuNW electrically contacted at the distal end. Another electrode is separated 50 nm from the nanowire to apply a potential difference across the gap. (b) Schematic of the electrical connection at distal-end region of the nanowire. (c) Excitation laser filtered optical image showing the generated N-PL throughout the AuNW. The dashed squared area is zoomed in and showed at the bottom of the image. The circle indicates the monitored area.

The changes on the emission intensity and spectrum at the distal end are investigated under the action of different electrical stresses. It is worth noting that only the distal-end response is monitored. The emission coming from the rest of the nanostructures is excluded by using a $300 \mu\text{m}$ diameter pinhole. The spatial filter improves the signal to noise ratio of the modulation given that the signal is not modulated in the rest of the nanowire. Figure 3.6.2 displays the time trace of the applied bias signal and the out-coupled N-PL at the distal end of the nanowire.

Clearly, the bias produces a quenching effect on the remotely generated N-PL. Modulations as high as $\approx 50\%$ are achieved.

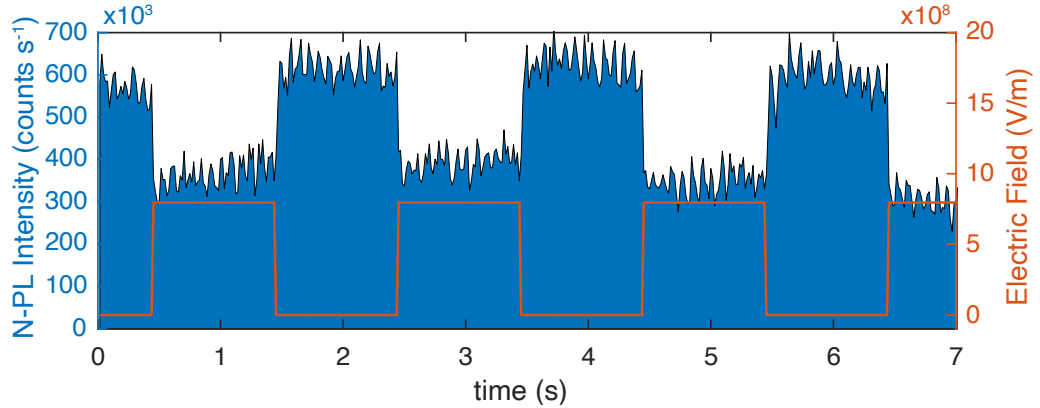


Fig. 3.6.2. Time trace of the N-PL coming from the distal-end of the AuNW (spatially filtered with a $300 \mu\text{m}$ pinhole).

Similarly to the local modulation presented in Chapter II, the N-PL response at the distal end shows spectral variations under the action of the high electric fields. Figure 3.6.3(a) shows the N-PL spectrum recorded at the region indicated by Fig. 3.6.3(b,c) which approximately corresponds to the out-coupled N-PL at the distal end of the nanowire. The spectra are integrated over 0.2 s for two different bias conditions (0 V and 14 V). As revealed on the time trace of the N-PL captured by the APDs, the bias considerably weakens the N-PL emission, making it noticeable even at the optical filtered images of Fig. 3.6.3(b,c).

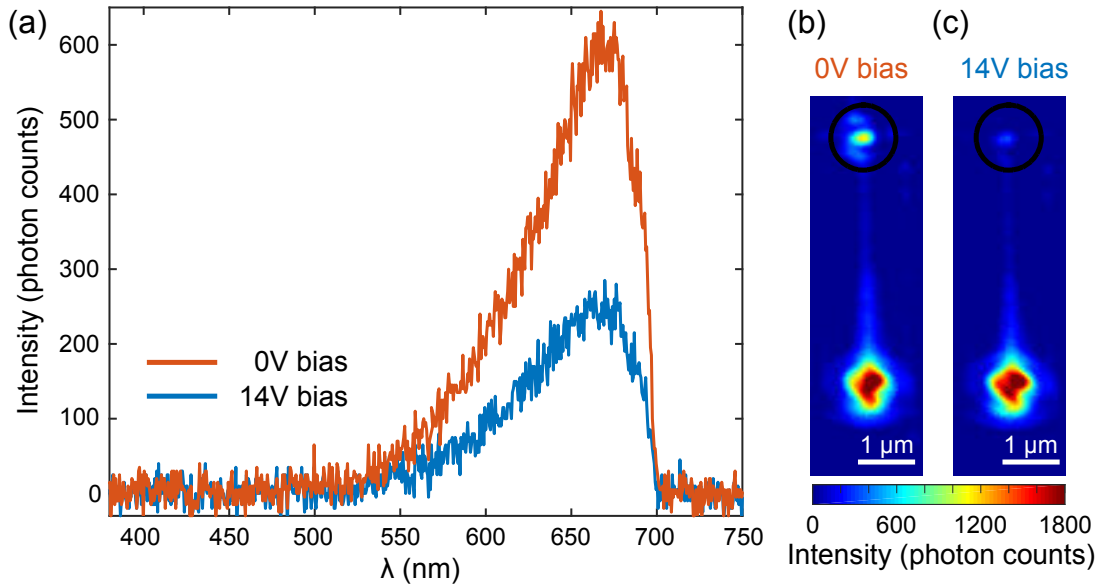


Fig. 3.6.3. (a) N-PL emission spectra at the distal end of a $5.0 \mu\text{m}$ long AuNW under the action of a 14 V bias and without any bias applied. The acquisition time is fixed at $t_{\text{acq}} = 0.2 \text{ s}$. Wide field optical images of the filtered nonlinear emission of the same nanowire under (b) 0 V and (c) 14 V bias applied.

The change on the nonlocal N-PL with the bias is expected to be driven by the same mechanisms proposed in Chapter II for the local case. However, the modulation capabilities and the implications of remotely modifying the emission properties of the nanowire termination open a broad range of applications. For instance, the incoherent emission emerging from the

3.7. Conclusion

distal-end can be further utilized to excite optical emitters such as molecules or quantum dots with precise control over the coupling between the N-PL photons and energy states of the optical emitter. Such capability may have direct implications in quantum nano-optoelectronics. Additionally, it can be used for the remote excitation of Raman scattering with the advantage of an excitation area of nanoscale dimensions. Hence, it allows to reduce heat effects, to avoid sample damage from the laser and also limits the background signals produced by diffraction-limited excitation volumes.

3.6.1 Single-crystalline nanostructures and the control of complex higher order modes

In top-down fabricated plasmonic devices, the achievement of advance functionalities is inevitably hampered by the high losses and scattering events resulting from the polycrystalline nature and structural defects which are inherent to thermal evaporation and lift-off processes [65]. As pointed out some sections ago (see Sec. 3.4.1), losses translate into a larger imaginary component of the dielectric permittivity and thus poorer propagation length, weaker field enhancement and lower performance. In this respect, mono-crystalline metal nanostructures produced by controlled chemical synthesis yield higher optical quality, improved structural uniformity and therefore stand out as a solution for complex plasmonic nanocircuitry and nanodevices. For instance, single-crystalline gold resonators with diabololo-like and double hexagon shapes [223, 275] as well as synthesized silver nanowire-based networks [276] can efficiently realize complex reconfigurable logic gate functions and information processing. Hence, the next reasonable step is to combine the electrical command of optical nonlinearities along with the complex functionalities provided by optimized nanostructures and their sustained higher order modes [277]. The next chapter presents some preliminary research on this matter and synthesized silver nanowires.

3.7 Conclusion

This study unequivocally confirms the essential role of the surface plasmon polariton modes to explain the longitudinal extension of the nonlinear photoluminescence observed in plasmonic nanowires. It is found that the origin of the signal depends on the observation area. For the nonlinear photoluminescence distributed along the nanowire, the spectral study and characterization demonstrate that this effect occurs locally at the surface by the plasmon field and cannot be explained by a continuum of plasmon mode leaking in the substrate. The spectral change of the photoluminescence along the nanowire results from the losses experienced by the underlying plasmon mode. For the photoluminescence signal emerging from the nanowire's distal end, two additive contributions are identified: a first one locally produced by the presence of an end-face enhancement of the surface plasmon field, and a second one resulting from scattering of a broad spectral distribution of secondary plasmon modes propagating in the system.

Naturally, the wavevector distribution of the gold nanowires' N-PL emission is determined by the nanowire orientation. Analyzing the nonlinear signal in real- and k -space reveals the out-coupling mechanisms of the N-PL to free-space photons which are mainly dictated by the geometry of the nanowire.

Additionally, the optical response modulation capabilities of the plasmonic device presented in Chapter II are extended to control the remote and delocalized nonlinear emission intensity produced at the gold nanowires distal-end. This undoubtedly expands the range of applications of such device.

The studies presented on this chapter are performed on a simple one-dimensional waveguide, but the analysis can be extended to more complex plasmon modal landscapes as will be presented in the following chapter. This would offer additional agility to control the intensity and the spectral content of nonlinear signals produced by propagating surface plasmons.

3.7. Conclusion

Control of the nonlinear properties of silver nanowires: towards the realization of plasmonic routers

4.1 Introduction

Among the variety of metallic nanostructure geometries that could be exploited for SPP-based studies, chemically synthesized silver nanowires (AgNWs) have shown great promise [235, 278]. Firstly because their single crystalline structure, excellent diameter uniformity and surface smoothness which, in contrast to top-down fabricated nanowires (see Fig. 3.4.3), mitigate the inner and surface scattering losses allowing longer propagation of higher plasmonic modes. Additionally, these one-dimensional nanostructures can be easily and consistently prepared using soft-solution processing methods. Furthermore, silver has the highest electrical conductivity among all the metals, which is essential for good electrical interconnections [278]. All these advantages give AgNWs a broad range of applications as signal processing components for integrated plasmonic circuits [271,276], as well as enhancers for sensing and detection purposes [279] among many others [278].

Chapter II was focused on the study of the N-PL dictated by the fundamental SPP bound mode propagating on polycrystalline gold nanowires. The goal here is to go a step further and also investigate optical nonlinearities produced by higher (leaky) and multiple SPP modes propagating in AgNWs which certainly allow better control on the light transmission in nanowire networks. We conceive then an additional unprecedented routing modality by introducing a plasmonic-enabled nonlinear wavelength and mode-conversion mechanism based upon the generation of the local nonlinear broadband continuum (N-PL).

4.2 Experimental methods

The experiment is conducted following the methodology of the previous chapters (see fig. 2.3.2). The NIR femtosecond laser and the high numerical aperture objective are used to excite SPPs and collect the linear and nonlinear responses of silver nanowires. Nonlinear wide-field microscopy as well as Fourier plane analysis and spectroscopy are again performed. Here, a solution of chemically synthesized silver nanowires is gently casted in a clean glass coverslip with previously fabricated micrometric position markers and let to dry at room temperature. Right after, the sample is transferred to the microscope stage for optical study.

4.2. Experimental methods

4.2.1 Silver nanowires' synthesis

Single crystalline silver nanowires are grown using a seed-mediated chemical process developed by Xia *et al.* [280] and following the polyol reduction of silver nitrate (AgNO_3) method. In practice, the procedure has been implemented and improved by the group of our collaborator G.V.P. Kumar in IISER Pune in India. Briefly, a 3 mL 0.1 M AgNO_3 solution and a 3 mL 0.5 M polyvinyl-pyrrolidone (PVP) solution, both in ethylene glycol (EG) and at room temperature are simultaneously and gradually injected in a preheated 160°C 5 mL EG (0.3 mL/min) solution. When the injection is completed, the final solution is again heated at 160°C and stirred for 1 h. Silver ions are reduced by the EG and form silver clusters followed by nucleation. The seeds grow into nanowires and other shapes like nanoparticles, nanocubes, nanorods, etc. After synthesis, the whole solution is cooled down and centrifuged at 2000 rpm in an effort to remove small particles and other impurities. This procedure yields a wide variety of single crystalline AgNW configurations with pentagonal cross-sectional shape, some of which are selected for this study. A high resolution TEM image taken from a typical AgNW synthesized by this particular procedure shows the lattice fringes and thus their single crystallinity nature in Fig. 4.2.1(a). Furthermore, applying a fast Fourier transform confirms the periodicity of the structure (see inset). A SEM micrograph of typical AgNWs is shown in Fig. 4.2.1(b). Additionally, figures 4.2.1(c,d) zoom on the spherical-like ends of the nanowire indicated by the red-dashed surrounding areas of Fig. 4.2.1(b). The SEM images reveal a thin layer of polyvinylpyrrolidone (PVP) surfactant covering the AgNW.

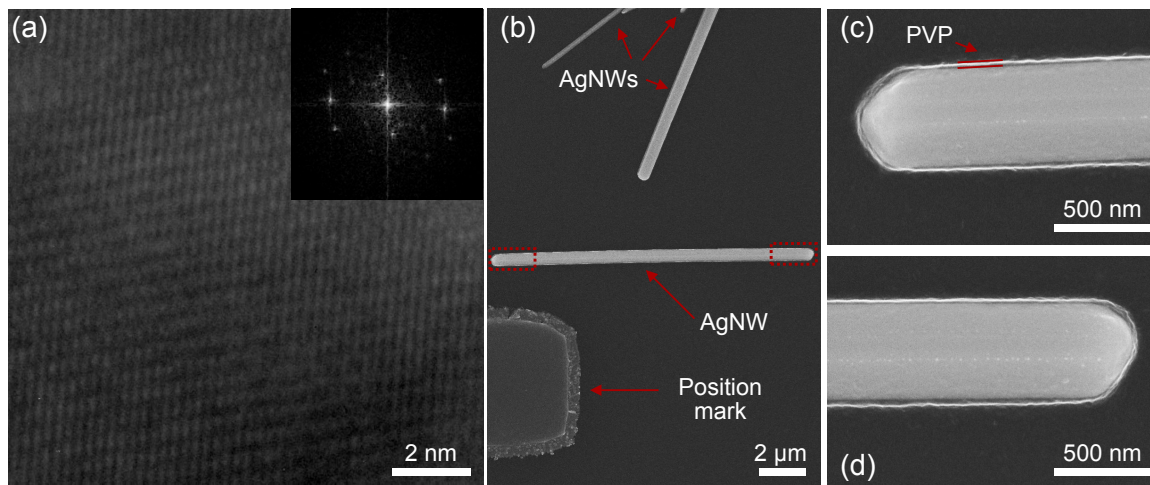


Fig. 4.2.1. (a) High resolution transmission electron microscope (HRTEM) image showing the crystallinity of the synthesized silver nanowires. Image provided by the group of G.V.P. Kumar in IISER Pune, India. The inset represents the corresponding fast Fourier Transform. SEM images of (b) a typical nanowire and its two terminations (c,d). The AgNW diameter is around 530 nm

While flat terminations impose incident polarization conditions to excite particular SPP modes, spherical-like terminations allow the excitation of multiple SPP modes regardless of the polarization [281,282]. Recently, Song *et al.* demonstrated the selective excitation of different plasmon modes by taking advantage of the inhomogeneous distribution of the field components inside the focus [246]. Unless contrarily indicated, in our experiments the incident polarization is always along the major axis of the nanowire (longitudinal) where the coupling shows to be more efficient.

4.2.2 Higher SPP modes detection by leakage radiation

As emphasized some sections ago, imaging of SPPs require specific microscopy setups. Near-field optical methods certainly allow to map the SPP propagation by collecting the near fields at the metal surface but can be very demanding and with long data acquisition times. Another method is based on the use of fluorescent dyes excited by the SPP near field, nevertheless, photo-bleaching of the electronic transitions of the dye makes quantitative analysis almost impossible. Newer techniques such as bleach-imaged plasmon propagation (BIIPP) [283] or transient absorption microscopy (TAM)-based approaches [227] offer alternative ways to study SPPs propagation and overcome the mentioned issues, however, they demand specific experimental setups. Fortunately, different configurations can open much simpler and versatile possibilities. For instance, in thin enough metal films (below 50 – 100 nm [284, 285]) and where the substrate optical constant is higher than that of the superstrate, SPPs can be detected. In such conditions depicted in Fig. 4.2.2, it is possible to detect in the far-field the leaking of the SPPs through the substrate where they can couple out into photons (leaky modes). The case of thick AgNWs on a glass substrate is similar. They can sustain leaky modes whose effective indexes are lower than that of the substrate. Leakage radiation (LR) is emitted in a very narrow angular range that requires an oil-immersion objective and under the phase-match angle θ defined by $k'_{\text{SPP}} = nk_0 \sin \alpha$ with n the effective index of the substrate (see the schematic picture of figure 4.2.2). This microscopy method, known as leakage radiation microscopy is widely used in the plasmonic community [286, 287].

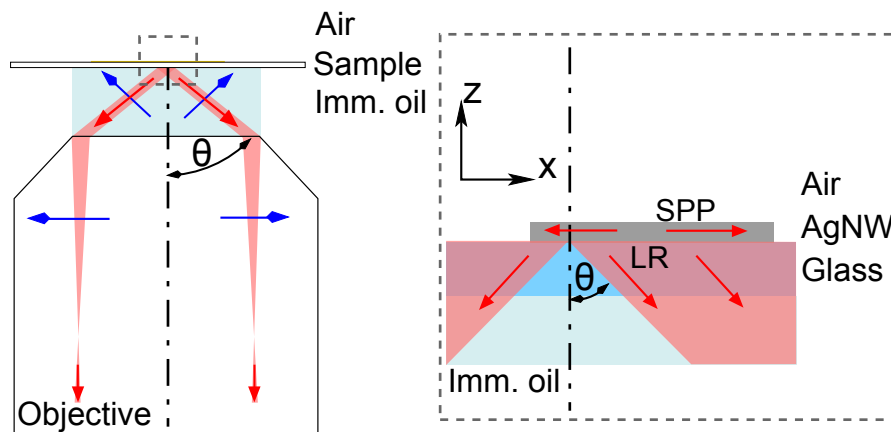


Fig. 4.2.2. SPPs are excited by a focused laser beam (not shown) and propagate through an AgNW. Leakage radiation (LR) is emitted under the phase-match angle range represented by θ . An oil-immersion objective collects the leakage radiation. The transversal polarization is indicated by the blue arrows. The zoomed area corresponds to the dashed square. Schematic inspired by [285]

4.3 Modal distribution and nonlinear optical emission in silver nanowires

In a general perspective, thick enough silver nanowires can support two kinds of plasmonic modes. The first kind, as in the case of the polycrystalline nanowires studied in chapter II, are the fundamental or bound modes. Highly confined at the NW-glass interface, they have higher effective refractive indexes than the substrate and can only be detected by scattering-mediated events at the extremities or defects. The losses suffered by these modes are mainly due to the high absorption of metals.

4.3. Modal distribution and nonlinear optical emission in silver nanowires

A typical thin silver nanowire wide-field image is shown in Fig. 4.3.1(a), where the bound mode is being excited by placing the nanowire's left end under the focused beam of a pulsed laser centered at $\lambda_0 = 808$ nm. As in the polycrystalline AuNWs, it manifests itself by the scattering event produced at the right end of the nanowire and by the presence of transverse fringes in k -space (see Fig. 4.3.1(b)). As explained in section 3.4.3.1, the period of the fringes is related to the excitation wavelength and the length of the nanowire ($L_{\text{AgNW}} \approx 6 \mu\text{m}$).

The second kind, which has been already introduced in the last section are the leaky modes supported only in thick nanowires. In thin nanowires leaky modes are at cutoff [227, 288]. In leaky modes, the field extends into the NW-air and NW-glass interfaces. Figure 4.3.2(a) displays the wide-field image of a thick and $12.6 \mu\text{m}$ long AgNW sustaining a leaky mode. The nanowire is again excited at the left end and the two bright parallel lines at the lateral edges are the signature of the mode. The rotational symmetry of the imaging lenses produce the interference fringes along the nanowire, similar to the fringes observed for the laser spot [289]. The relative intensity of the plasmon is extracted by plotting the profile along the two bright lines as shown in the semilogarithmic graph of fig. 4.3.2(b). The two lines follow a linear decaying trend and match almost perfectly. An exponential fit gives $L_{\text{spp}} = 2.6 \mu\text{m}$ using equation 3.4.1 in both data sets. A transverse profile along the x -axis displaying the two lines intensity is also shown in the inset.

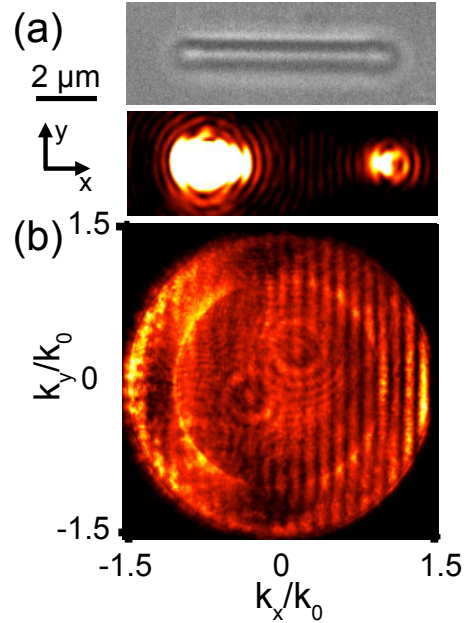


Fig. 4.3.1. (a) (Top) Optical transmission image of a $6 \mu\text{m}$ long AgNW and (bottom) SPP excitation at the left end. (b) corresponding wavevector distribution.

In Fourier space, a leaky mode is easily recognized by the presence of a thin straight line transverse to the direction of propagation (see inset of fig. 4.3.2(c)). It is interpreted as a strong confinement of the mode in the k_y/k_0 direction (broad k -vector range) and high directivity. Furthermore, the position of the line's peak represents the effective index of the SPP mode n_{eff} and the full width at half maximum (FWHM) gives information about the propagation length and thus losses. More generally, the intensity of leakage radiation in k -space can be described by a Lorentzian distribution given by [284]

$$I(k_x) \propto ((k_x - k'_{\text{spp}})^2 + k''_{\text{spp}})^{-1} \quad (4.3.1)$$

where, as just stated, the FWHM of the distribution is proportional to k''_{spp} and therefore to L_{spp} (see eq. 3.4.1). A cross section of the Fourier plane along $k_y/k_0 = 0$ is shown in fig. 4.3.2(c) with its respective Lorentzian fitting at the bright line position. It yields an effective index $n_{\text{eff}} = 1.02$ and FWHM = 0.06 which from the relationship 4.3.1 translates into a propagation length $L_{\text{spp}} = 2.1 \mu\text{m}$. Whereas n_{eff} matches well previous calculations [289], L_{spp} is slightly lower than the inferred value from the exponential fit of fig. 4.3.2(b) which is highly sensible to the fitting parameters and the background noise of the image.

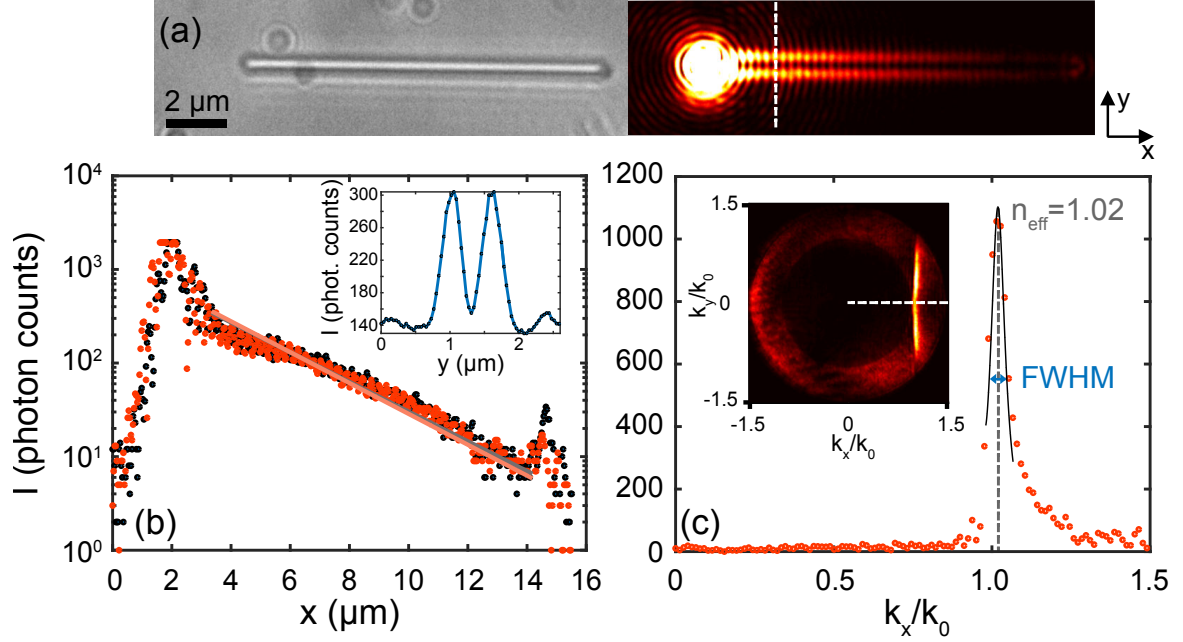


Fig. 4.3.2. (a) Wide-field image of the relative intensity distribution of the leaky mode in a $12.6 \mu\text{m}$ long AgNW. A bright-field image of the same nanowire is shown at the left. (b) Intensity profile along the two bright lines at the edges of the nanowire showed in (a). The inset shows the transverse profile along the dashed line in (a). (c) Cross section of the corresponding Fourier plane at $k_y/k_0 = 0$ for the leaky mode excitation showed in (a). The inset displays the full Fourier plane and indicates the cut position with a dashed line.

The plasmonic modal landscape in metal nanowires is not only dictated by the nanowires diameter. The shape of the cross-section or even the standardized use of the underlying substrate modify the supported plasmonic modes due to the substrate-induced hybridization of SPP modes [226,290,291]. Large diameter nanowires along with sharp edges and cross-sectional shapes lead to field localization at the edges and corners [281]. As the cross-section size is reduced, modes hybridize and give rise to a new and reduced set of supported modes. As expected, if the diameter is further reduced, modes converge to the cylindrical shape case.

For the thicker nanowires and in certain laser excitation positions and therefore incident linear polarizations, multiple modes can be simultaneously excited [235,291]. Figure 4.3.3(a) shows the LR image of a $10 \mu\text{m}$ long silver nanowire sustaining two leaky modes in addition to the bound mode. The light scattering at the right end reveals the excitation of the bound mode. Additionally, the leakage radiation pattern clearly shows an alternating beating pattern (zigzag) every $\Lambda_{\text{beat}} \approx 1.8 \mu\text{m}$ in average in both sides of the nanowire. Several modes with different phases are superposed coherently [235,291]. Maximum phase difference leads to a suppression of the net field intensity. The pattern results then from the different field distributions of the simultaneously excited modes (symmetric and antisymmetric) [235]. Profiles taken at the edges of the nanowire for the area indicated by a dashed square in Fig. 4.3.3(a) are plotted in the panel (c) of the same set of figures to better illustrate the oscillation of the intensity along the nanowire.

In the Fourier plane of Fig. 4.3.3(b), two parallel and straight lines corresponding to the radiation of the two modes are now distinguishable at $k_x/k_0 = 1.01$ and 1.46 as confirmed by the intensity profile shown in Fig. 4.3.3(d). Additionally, fringes are due to the excitation of the bound mode.

4.3. Modal distribution and nonlinear optical emission in silver nanowires

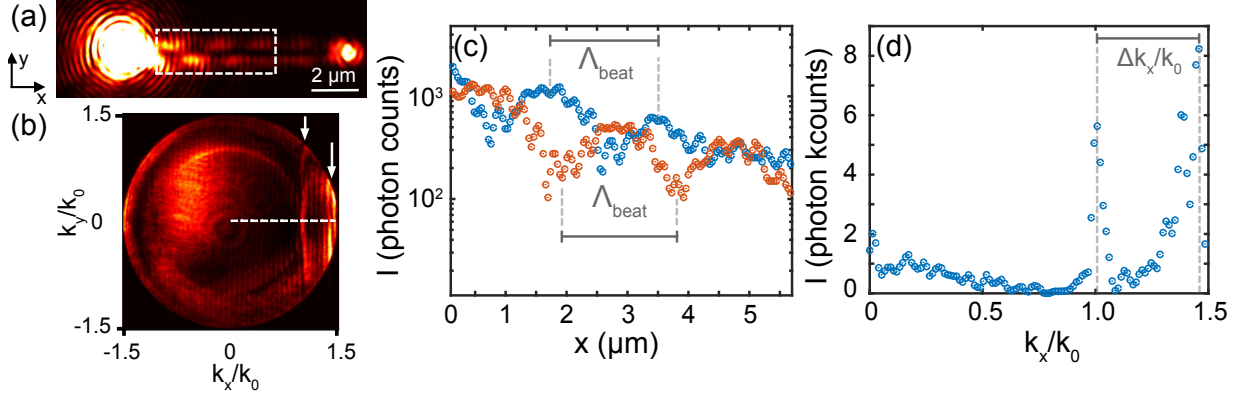


Fig. 4.3.3. (a) Wide-field image of the relative intensity distribution of the bound and multiple leaky modes being excited in a 10 μm long AgNW. (b) Fourier plane image corresponding to the real image shown in (a). Arrows point to the straight lines resulting from the excitation of two leaky modes. (c) Profiles at the edges of the nanowire for the dashed area indicated in (a). (d) Cross section of the Fourier plane shown in (b) at $k_y/k_0 = 0$ for the multiple leaky modes excitation showed in (a).

The beating period Λ_{beat} is given by the propagation constants of the two modes and thus depends on the nanowire parameters such as the width as well as on the environment medium. In terms of the effective indexes of the leaky modes $LM1$ and $LM2$ extracted from Fig. 4.3.3(b,d) it is given by [235]

$$\Lambda_{\text{beat}} = \frac{2\pi}{\text{Re}(\Delta k_x)} = \frac{\lambda_0}{(n_{\text{eff}}[LM1] - n_{\text{eff}}[LM2])} \approx 1.8 \mu\text{m} \quad (4.3.2)$$

which exactly matches the value extracted from the real image profile.

In close similarity with the polycrystalline nanowires of the previous chapter, AgNWs can also generate local and distributed nonlinear responses. Nonetheless, the crystallinity, modal landscape and surface smoothness of AgNWs open new possibilities for manipulating the transport, delocalization and emission mechanisms of such nonlinearities.

4.3.1 Optical nonlinearities in silver nanowires

A confocal map of a 13.5 μm AgNW obtained by raster scanning the nanowire through the focus reveals the nonlinear photoluminescence emission under pulsed laser excitation ($\lambda_0 = 808 \text{ nm}$) in fig. 4.3.4(a). The N-PL is recorded as a function of the (x, y) position. The map represents the probability of generating N-PL at (x, y) . Short-pass and notch filters ensure the rejection of the contribution from the laser. When necessary, SHG is filtered out too. At the top of the map, a bright-field optical transmission image shows the nanowire. As expected, the largest N-PL response is located at the extremities and edges of the nanowire whereas at the body of the nanowire the N-PL signal is at background level. Adsorbed species also constitute local hot-spots where the emission is enhanced.

To further characterize the nonlinear emission, the spectrum is shown in fig. 4.3.4(b), it is the result of 10 s integration time over the emission of the whole nanowire. Very similar to the nonlinear response of gold, it shows a broad peak from $\lambda \approx 450 \text{ nm}$ to $\lambda \approx 775 \text{ nm}$ where is cut by the short-pass filter. Second harmonic generation, although weak, is also present as shown by the inset. The N-PL to SHG intensity ratio strictly depends on the particular characteristics and configuration of the nanowire.

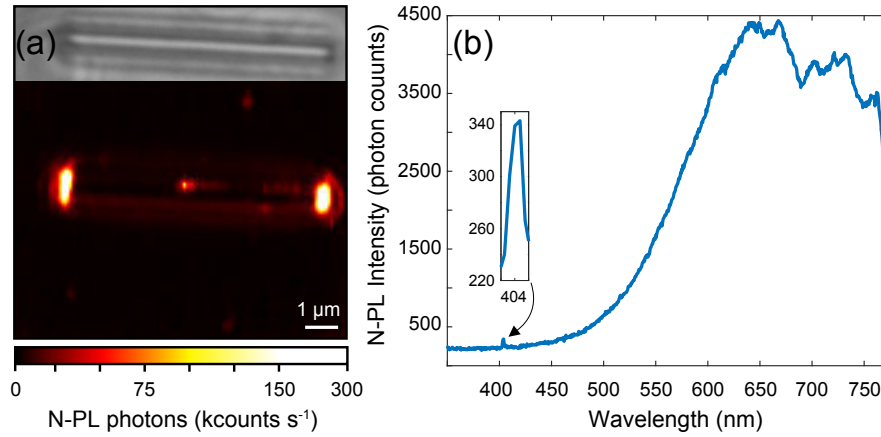


Fig. 4.3.4. (a) Nonlinear confocal map of a $13.5 \mu\text{m}$ long AgNW. The top frame is an optical transmission image of the same nanowire. (b) Nonlinear emission spectrum of the nanowire. The inset is an amplified image of the peak corresponding to SHG.

Remarkably, despite the fact that silver and gold have very different band structures and interband transitions (4.0 eV for silver and 2.4 eV for gold), both metals yield very similar broad emission throughout our conducted research on nanowires and nanoantennas (see Figs. 3.6.3, 3.5.2, 3.4.4, 2.5.3 and 1.4.3 for comparison). Such generality is hardly explained by interband recombination following multi-photon absorption processes and strengthens the hypothesis of thermal emission by a hot-electron gas.

Having confirmed the nonlinear emission in single-crystalline AgNWs, let us now explore the delocalized nonlinearities for the different supported plasmonic modes of the nanowires.

4.3.2 Linear and nonlinear modal distribution in AgNWs

Following the typical procedure, different plasmonic modes are excited in silver nanowires by focusing the laser at one end. As already shown in the previous chapter for polycrystalline gold nanowires, the effect on AgNWs is fundamentally equivalent. At high powers surface plasmons generate optical nonlinearities throughout the nanowires as they propagate. Figure 4.3.5(a) and (b) show, respectively, the real and Fourier space patterns for the excitation of the bound mode in a $9 \mu\text{m}$ long AgNW and the corresponding nonlinear emission.

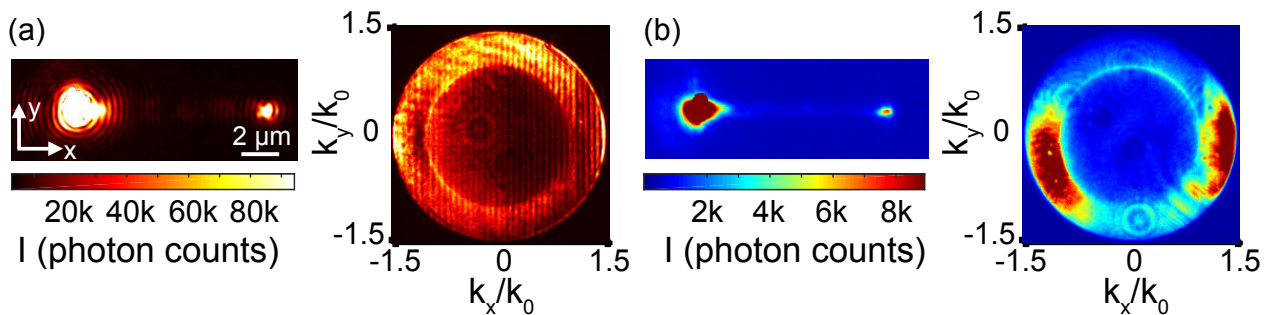


Fig. 4.3.5. Real and Fourier space patterns of the (a) linear and (b) filtered nonlinear optical response for the bound mode excitation. The excitation is located at the left end of the nanowire.

The linear scattering case follows, as expected, its characteristic pattern with some weak out-scattered light along the nanowire at adsorbed nanoparticles. Due to the reduced roughness of AgNWs and contrarily to e-beam lithographed nanowires, the nonlinear pattern follows that of the linear one with the emission mostly restricted to the excitation and the distal-end scattering

4.3. Modal distribution and nonlinear optical emission in silver nanowires

spots. The nonlinear Fourier plane reveals the antenna-like behavior and emission directionality brought by the nanowire.

For the leaky mode excitation (see fig. 4.3.6(a,b)), the situation is completely different. For the linear case shown in (a) the propagating plasmon shows, as expected, an exponential decay along the full nanowire and the Fourier plane readily displays the typical straight line transverse to the plasmon propagation direction. Interestingly, for the nonlinear case (fig. 4.3.6(b)) the nanowire exhibits a mostly homogeneous emission at the edges with much higher intensities at some particular hot-spots on the nanowire as pointed by the white arrow. In fact, the excitation area (left end) surprisingly shows a weak nonlinear emission comparable to other sites of the nanowire. Furthermore, the Fourier plane unexpectedly displays two straight lines at opposite sides of the k -space which can be explained as follows: The pump plasmon propagating in a single direction (+x) transports enough energy to locally activate a nonlinear continuum generation at a nanoparticle decorating the nanowire. In the subsequent step, the local continuum couples to a new set of modes propagating and leaking in the forward (+x) and backward (-x) direction as demonstrated by the emission diagrams. The process can be very efficient thanks to the large in-plane k -vector distribution of the continuum in the near-field which can match those of the SPPs in the nanowire. Profiles at $k_y/k_0 = 0$ of the linear and nonlinear Fourier planes are shown in fig. 4.3.6(c).

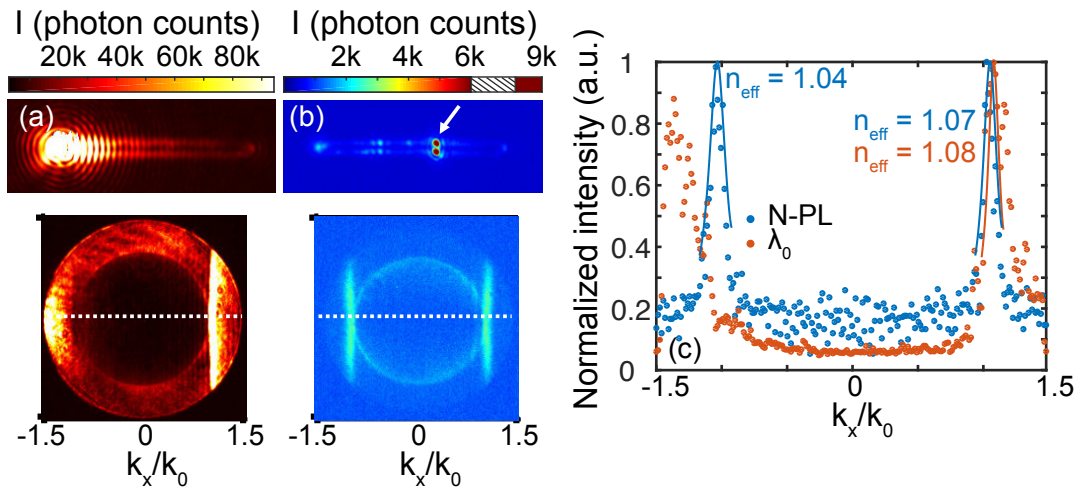


Fig. 4.3.6. Real and Fourier space patterns of the (a) linear and (b) filtered nonlinear optical response for the leaky modes excitation. The excitation is located at the left end of the nanowire. (c) Cross section profiles indicated with dashed lines in (a) and (b). The peaks are fitted with Lorentzian distributions (solid lines).

Lorentzian fits complete the graph at the leaky mode lines locations and provide an estimation of the effective indexes of the plasmonic modes. The peak of the linear Fourier plane yields $n_{\text{eff}}(\lambda_0) = 1.08$ whereas the two peaks for the nonlinear one correspond to $n_{\text{eff}1}(\text{NPL}) = 1.04$ and $n_{\text{eff}2}(\text{NPL}) = 1.07$. The dissimilarity between these values lies on the different wavelengths of the propagating SPPs given the different SPP coupling in opposite directions. The nonlinear emission from the nanoparticle couples as a broad range of plasmons with different wavelengths. For similar reasons, the FWHMs also differ with larger values for the N-PL thanks to the broad spectrum of SPPs.

Further studies in other nanowires confirm this mechanism. Figures 4.3.7(a,b) show as before the resulting linear and nonlinear real and Fourier plane patterns for another AgNW with a scattering defect. The laser excites simultaneously the bound and the leaky mode, the latter being partially suppressed in the linear case by the mentioned defect. Contrarily,

the nonlinear pattern in real space shows a high enhancement of the emission at the defect location. The nonlinear Fourier plane exhibits two straight lines indicating the presence of plasmons propagating in both directions in a leaky mode. To fairly characterize the nanowire and its defects, Fig. 4.3.7(c) displays SEM micrographs of the nanowire measuring $6.1 \mu\text{m}$ long by 230 nm wide. It shows spherical shape terminations as all the studied nanowires. Nanoparticles decorating the lateral edges of the nanowire enhance the nonlinear emission which then successfully couples towards both x and $-x$ directions as shown by the nonlinear Fourier plane of fig. 4.3.7(b).

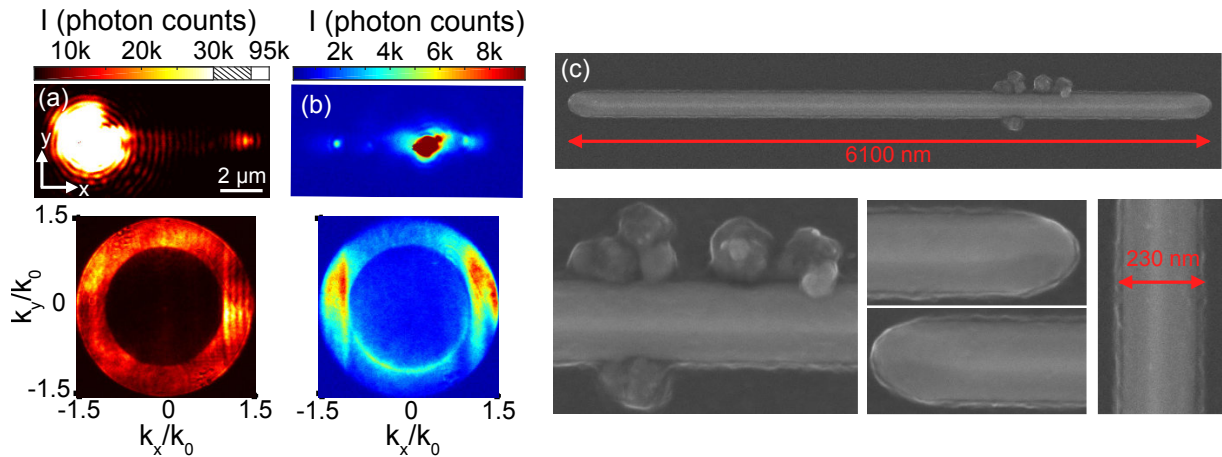


Fig. 4.3.7. Real and Fourier space patterns of the (a) linear and (b) filtered nonlinear optical response for the SPP excitation in an AgNW with a defect. The excitation is located at the left end of the nanowire. (c) SEM images of the same nanowire showing the nature of the defect.

As discussed in the beginning of the section for the linear case, the zigzag propagation results from the coherent multi-modal superposition which can be tuned by the incident polarization. Such approach is not suitable for advanced functions and practical applications which require local and direct control of the supported plasmonic modes in the nanowire. Conveniently, this single- to multi-mode conversion can be achieved by introducing a local structural defect in the nanowire and activating its broadband nonlinear emission. Figures 4.3.8(a,b) demonstrate the successful conversion from a single leaky mode (x -direction) to multiple leaky modes in opposite direction ($-x$ -direction).

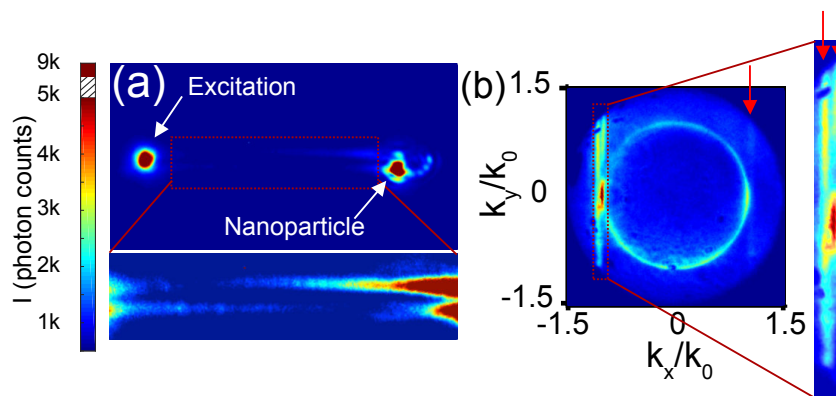


Fig. 4.3.8. Filtered (a) Real and (b) Fourier plane nonlinear images of a $12 \mu\text{m}$ long AgNW being excited at the left end with a pulse laser centered at $\lambda_0 = 808 \text{ nm}$. The red arrows highlight the excitation of multiple leaky modes in opposite directions.

4.4. Conclusion

In Fig. 4.3.8(a) the real plane nonlinear image shows two high emission spots at the excitation location and at the scattering center, both with similar intensity and saturating the CCD camera. Increasing the contrast in the middle of the nanowire (bottom frame) reveals the beating of the nonlinear mode which alternates between on and off at the edges. The Fourier plane of Fig. 4.3.8(b) confirms the presence of several leaky modes by the splitting of the straight line in the $-k_x$ semi-space (see zoomed frame on the right). Remarkably, the enhancement site performs and induces a modal and a wavelength conversion.

Figures 4.3.9(a,b) display the corresponding linear real and Fourier plane patterns where only a single leaky mode in the x -direction is excited. A zoomed frame of the real propagation image shows a weakened scattering intensity at the nanoparticle site whereas the white light transmission image shows a smooth nanowire.

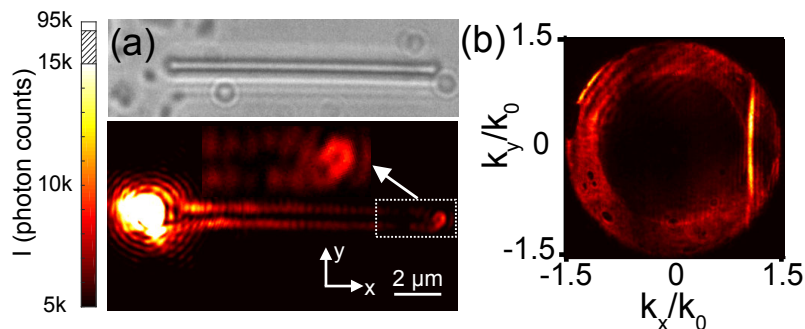


Fig. 4.3.9. Corresponding (a) real and (b) Fourier plane images of the pump plasmon propagating in the nanowire of Fig. 4.3.8.

The mode, wavelength and spatial conversions are crucial aspects for the design and implementation of plasmonic circuits. Furthermore, the different spatial distributions of the nonlinearities along the nanowires may be deployed advantageously. Evidently, the modal and wavelength conversion efficiency at the adsorbed species depends on the precise geometry of the spot generating the continuum. The coupling also strongly depends on the wave-vector distribution and polarization state of the confined nonlinear emission. Therefore, engineering of the different involved processes can enable the active control of complex switching and routing tasks in nanowire networks-based devices.

4.4 Conclusion

In summary, a preliminary study of the plasmon propagation in synthesized silver nanowires and the associated nonlinearities in real and Fourier spaces has been presented. Multiple modes were simultaneously excited in thick nanowires. In both the linear and nonlinear regimes the interference of single modes leads to nontrivial distributions of new plasmonic modes.

Interestingly, adsorbed species on the nanowires significantly change the modal, spectral and directional properties of the nonlinear emission. However, many aspects have to be addressed. Firstly, the distribution of the nonlinear continuum in relationship with the underlying plasmonic modal landscape needs to be further investigated. Furthermore, it is necessary to fully understand what are the parameters defining the local formation of the continuum (role of the termination, presence of adjunct field-enhancing nanoparticles or defects, nature of the nanowire, etc.). Therefore, different measurement protocols need to be deployed including polarization analysis of the angular emission diagram and testing various geometrical morphologies of the coupling area.

Finally, electrical activation and optical complex operations can be brought together yielding an active plasmonic spatial, modal and wavelength multiplexer as presented later in the research prospect.

Summary & outlook

Throughout this work, nonlinear optical phenomena and more specifically nonlinear photoluminescence developing in gold and silver nanostructures have been extensively studied. The aim was always towards the electrical manipulation of such responses and the realization of a nanometric active plasmonic device.

In a first approach, bowtie optical antennas were electrically connected inducing a potential difference across their gap. The N-PL emission coming from the gap region consistently showed a strong dependence on the applied static electric field. The modulation response was asymmetric with respect to the field polarity. Moreover, space-resolved measurements of the modulated N-PL emission confirmed the asymmetry and revealed deeper modulations for the locations under the action of *a priori* stronger electric fields. In connection with the induced charge density with opposite signs on both sides of the nanoantenna, N-PL emission systematically exhibited a decrease in the grounded half whereas the other side displayed the inverse behavior. N-PL has proven to be a thermal radiation driven by hot electrons under pulsed excitation. Therefore, we linked the N-PL modulation to a change in the hot electrons temperature caused by an alteration on the surface carrier density. The model is compatible with calculations comprising realistic values of the induced charge and the necessary temperature variation for a modified emission intensity. Generally speaking, the response time of the modulation is relatively slow. Charge trapping mechanisms occurring in the substrate constitute a plausible explanation. Further experiments should confirm it.

Then, in a logical move, we widen the study to extended plasmonic nanostructures, i.e. metal nanowires. The objective was to understand the mechanisms behind the transport of nonlinearities along these basic elements and use them in favor of the electrical modulation in a more complex device. Indeed, as emphasized in the manuscript, nanowires are a good candidate for becoming elementary building blocks in nanophotonic circuitry considering that they can perform multiple functions such as routing, detection and light generation in ultra small dimensions and with reduced power consumption.

The experiments demonstrated delocalized nonlinear emission dictated by the modal distribution of surface plasmon polaritons. The plasmon excited at the pump wavelength was the main responsible for the N-PL generation in the nanowire as it is propagated. A complete spectral analysis of the N-PL extension on the nanowires revealed the energy loss of the propagating plasmons given the dispersive nature of the material. N-PL emission resulted to be redder as the distance from the excitation end of the nanowire increased enabling a tunable light source. Such study also indicated the near-field coupling of multiple plasmons propagating within the broadband N-PL continuum created at the excitation area. Concerning the

out-scattering mechanisms of the N-PL to free-space photons, these were mainly dictated by the geometry of the nanowire as validated by a polarization analysis of the nonlinear emission.

Combining the proved strong optical and electrical enhancement of the nonlinearities provided by bowtie optical antennas and the nonlinear transporting features of plasmonic nanowires, we conceived an unprecedented remotely activated device capable of modulating nonlinear signals at the nanowire termination which remarkably were microns away from the excitation point. Such achievement allows independent control over the excitation area and the emission at distant locations of the nanowire. It could certainly find a broad number of applications including noninvasive on-chip sensing, networking and information processing.

Our device was mainly inspired by the enhanced nonlinear response produced in nanocavities along with the generation of huge electric fields with chip-level voltage signals. However, more complex designs and structures could offer more efficient control and tunability over the plasmonic modal landscape and thus the generated N-PL and the modulation achieved. In this regard, we investigated the nonlinear properties of synthesized silver nanowires which, thanks to its single-crystalline structure and reduced losses, can sustain higher order modes. Additionally, the nonlinear features of silver nanowires showed to be enriched by adsorbed nanometric species at their surface. As a matter of fact, promising modal, wavelength and spatial conversion were achieved in a single excited nanowire. Yet, these are still preliminary results and the influence of several parameters such as the diameter and length of the nanowire, the position, shape and size of the adsorbed species need to be characterized.

We may draw two main conclusions. Firstly, N-PL and optical nonlinearities in general are incredibly fertile and promising phenomena both technologically and scientifically. Furthermore, fundamentally speaking, N-PL mechanisms still intrigue the photonics research community opening the way to a wide variety of interesting experiments. On the applicability side, nonlinearities in physics always imply enhanced localization. Hence, they are a must in the seek of smaller footprints and complex operations for highly integrated photonic circuitry. Secondly, our device undoubtedly proved active nonlinear plasmonic capabilities. In fact, it may play a part in the development of optical functionality in ultra-compact nanophotonic platforms. For instance, it could help on the implementation of tunable on-chip light sources. Actually, many techniques to separate optical signals of different wavelengths face the difficulty of integration. Fibers, as pointed out before, require either dispersion engineering of the index of refraction or the use of prisms and diffraction gratings which definitely translates into bulky devices. Contrarily, the up-converted continuum generated by the plasmon-stimulated nonlinearity is formed in an extremely local interaction area. Such continuum may be applied as a wavelength and mode converting process to route the optical signals in a nanowire-based circuitry. Moreover, the electrical modulation of the N-PL adds another degree of control over the activation of the process.

In this context, Fig. X.1 schematically illustrates a conceptual prototype of an ultra-compact electrically controlled nanowire-based optical multiplexer. It can perform simultaneous spatial, modal and wavelength multiplexing along with modulation of the optical signals. It includes an input port, a series of output nanowires and a set of control electrodes. Surface plasmons excited by a pulsed laser beam at the input port propagate and interact with the nanowire triggering the nonlinear continuum at the predefined enhancement site. The resulting nonlinear continuum induces the optical coupling of different plasmon modes which are spatially and spectrally separated and transported to output ports through designated nanowires. This is achieved by controlling the geometry and the nature of the nanowire. One important aspect of the device is the electrically controlled coupling of the nonlinear continuum at the enhancement site and therefore the output strength by modulating the light intensity. The modulation is activated with a relatively low control voltage as already demonstrated which ensures low power

consumption.

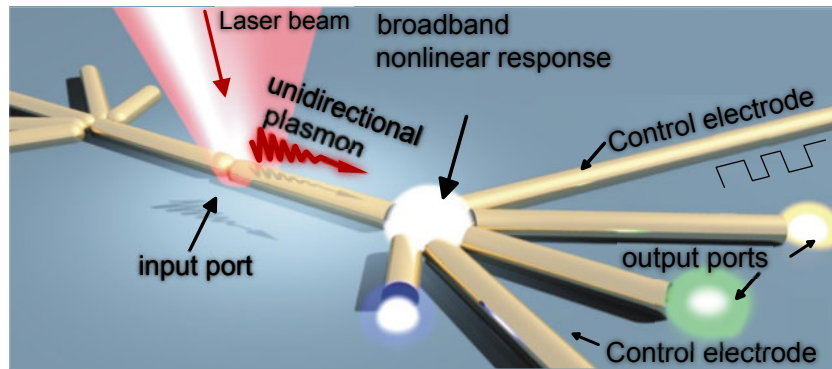


Fig. X.1. Illustration of a 1 to N broadband plasmonic multimode (spatial, spectral and modal) division multiplexer based on metal nanowires.

The device can be assembled using either chemically synthesized nanowires or electron beam lithographed polycrystalline nanowires. The advantages of top-down fabricated techniques lie on the precise control over the geometry of the device whereas chemically grown nanowires provide a robust and reliable fabrication method along with crystalline structure. A combination of both techniques is, perhaps, the most suitable approach. Indeed, e-beam lithography and crystalline nanowires integration has been already developed by the group [292] and may constitute a plausible technological approach for the problem.

The basic concept is applicable to more complex 2D structures and their intrinsic plasmonic modes which would bring a whole new set of sophisticated functionalities. Reconfigurable logic gates based in the nonlinear emission of plasmonic crystalline metal cavities, for example, would strongly benefit from the extra degree of control provided by the electrical modulation of the intensity. A gating electrode in close proximity to the optical output would activate or deactivate the logical operation. The electronic temperature and therefore the spontaneous emission of hot electrons in electron fed optical antennas is, in principle, also adjustable using the same three-terminal gating configuration. Finally, controlling the hot electrons temperature by electrical means would be also of great importance in many applications concerning photocatalytic effects in chemical reactions.

List of Figures

1.2.1 Charge oscillations on a dipole as a function of time. In the case of an electric dipole, the driving current is supplied externally in the circuit. For optical antennas, the oscillations are generated by the incident EM field. Inspired by [55].	5
1.2.2 Interface along the $x - y$ plane between a metal and a dielectric.	6
1.2.3 Scanning electron micrographs of different optical antenna designs. (a) Hertzian dimmer antenna. Reprinted with permission from [79]. Copyright 2012 American Chemical Society. (b) Dipole antenna. Reprinted with permission from [80]. Copyright 2008 by the American Physical Society. (c) Bowtie antenna and (d) Yagi-Uda antenna. SEM image courtesy of Xiao Yu, PhD student at the ICB lab.	8
1.3.1 Real and imaginary parts of the dielectric function for gold in the optical regime. Black dots correspond to experimental data. The red and blue lines correspond to fits to the Drude and Drude-Lorentz models. Reprinted with permission from [68]. Copyright 2011 American Chemical Society.	11
1.3.2 (a) Approximative band structure of gold. The red dashed squares point to its interband transitions (b). Adapted from [8] and [23].	11
1.4.1 Resonances and excited-stated dynamics contributing to the $\chi^{(3)}$ nonlinearities. (a) one-photon absorption, (b) direct two-photon resonance mediated by a virtual state, (c) resonant sequential two-photon absorption, (d) relaxed sequential absorption. Adapted with permission from [120]. Copyright 1994 American Chemical Society	16
1.4.2 Schematic representation of the hot electron generation in gold nanostructures. (a) A gold nanostructure is initially in thermal equilibrium at $T = T_0$. (b) A femtosecond laser pulse generates surface plasmons in the particle which exponentially decay into hot electrons and holes within ≈ 10 fs. (c) Coulomb electron-electron interactions lead to the decay of the most energetic electrons in a few tenths of femtoseconds and eventually relax back to ambient temperature in the picosecond scale thanks to the coupling with phonons. Shaded areas represent the initial Fermi-Dirac distribution of electronic states, points indicate the occupancies of different energy levels. The solid curve in (c) is the Fermi-Dirac distribution at a higher temperature T . Adapted with permission from [130]. Copyright 2016 American Chemical Society.	17

1.4.3 (a) Emission spectra of gold nanostructures for different excitation powers. (b) Log-log plot of the N-PL intensity dependence on the excitation power with its corresponding slope. The laser intensities have been proportionally reduced to avoid overlapping of the curves.	18
1.4.4 Representative band diagram for gold near the X and L symmetry points in the first Brillouin zone. The first IR photon (1) excites an electron in the <i>sp</i> -band, while the second (2) excites an electron from the <i>d</i> -band to the <i>sp</i> -band. Electron-electron and electron-hole scattering events move the electrons closer to the Fermi level. Visible emission is generated when the electron relaxes from the <i>sp</i> -band back to the <i>d</i> -band. Adapted with permission from [23]. Copyright 2009 by the American Physical Society.	19
1.4.5 (a) Emission spectrum of a single luminescent spot in a silver nanoparticle film being excited at 770 nm by a femtosecond laser (blue) or by a CW laser (red). The solid and the dashed lines represent a laser excitation power of 100 W/cm ² and 1 kW/cm ² respectively. The blank space in the 1.52 – 1.72 eV range is a consequence of the filtering of the elastically scattered light. (b) Spectrally resolved power-law exponent for the incident laser dependence of the emitted photons. Figure adapted with permission from [9]. Copyright 2015 by the American Physical Society	20
1.4.6 Estimated effective electron temperature as a function of the tunnel current for two energies (1.7eV; 2.06eV). (b) Light intensity versus electron temperature (semi-logarithmic scale). The red points are the inferred electron temperature and the solid line is the evolution of the light intensity at 1.7 eV. (c) Emission spectra of the device for different bias voltages. Figure adapted and reprinted with permission from [145]. Copyright 2015 American Chemical Society.	22
1.4.7 (a) Emission spectra of a small particle aggregate on a glass surface for increasing irradiation (dark red, 4.8 kW/cm ² ; red, 8.7 kW/cm ² ; orange, 11.0 kW/cm ²). Scattered light is cut off by filters. (b) Power-law exponents <i>p</i> for several laser powers over a limited range of irradiation (dark red, 1.8 – 4.9 kW/cm ² ; red, 2.6 – 8.7 kW/cm ² ; orange, 4.5 – 11.0 kW/cm ²). Adapted with permission from [10]. Copyright 2017 American Chemical Society.	23
2.2.1 (a) Schematic of a plasmonic EFISH device. A gold nanoslit filled with a dielectric medium is surrounded by a grating-based optical antenna. The two electrodes are connected to external circuits for electrical control. (b) Normalized change in the frequency doubled intensity versus the external applied voltage. Figures adapted with permission from [178]. (c) Measured fluorescence emission spectra for different applied DC bias voltages across the nanogap filled with quantum dots. Figure adapted by permission from [184]. Copyright 2011. (d) Dielectric function variation plotted versus δ for three sphere radii, the inset shows the effect of the strong electric field on the sphere. Figure adapted with permission from [160]. Copyright 2016 by the American Physical Society.	28
2.2.2 Electrically controlled plasmonic device. (a) Schematic representation of the device operation. Two gold electrodes are separated by a nanometric gap to form an optical gap antenna. A femtosecond laser excites the structure and generates N-PL which is modulated by an applied electric field across the gap. (b) Real graphic representation of the plasmonic device. SEM micrographs of (c) all the nanoantennas, (d) zoomed at the top 6 nanoantennas and (e) a single nanoantenna.	29

2.3.1 Schematic representation of the spin-coating process for a double layer of PMMA.	30
2.3.2 Schematic representation of the complete fabrication process of the plasmonic device. A combination of e-beam and UV lithography defines a set of nanoantennas and the connecting electrodes respectively.	31
2.3.3 (a) Nonlinear photoluminescence confocal map of a bow-tie optical antenna. The inset shows a SEM micrograph of the same structure. (b) Experimental setup. Ti:Sapphire laser (Chameleon, Coherent) at a wavelength of 810nm, \approx 120fs pulses and 80 MHz repetition rate. $\lambda/2$ Half wave plate. DBS Dichroic beam splitter, TL Tube lens, APD Avalanche photodiode, OBJ 1.49 100x numerical aperture objective, I/V converter, VA Voltage amplifier, RHK Scanning probe microscope control system, Function generator, Spec Spectrometer, CCD charge-coupled device camera.	32
2.4.1 Recorded N-PL in the gap region as a function of the applied voltage for nanoantennas with (a) \approx 100nm and (b) \approx 150nm gaps. (c) Change rate of the N-PL with the voltage applied. (d,e) SEM micrographs of typical studied nanoantennas with gaps similar to (a) and (b). The dotted lines indicate the zero bias N-PL in (a) and (b) and the zero N-PL change rate in (c).	34
2.4.2 In blue, the time trace of the N-PL emission (left ordinate axis) for a 75 nm gap nanoantenna. In orange, the applied squared electrical signal (right ordinate axis). The red dashed line and the double red arrow indicate approximately the values of $I_{N-PL}(E = 0)$ and $\Delta_{N-PL}(E = E_0)$ respectively.	35
2.4.3 (a) Time trace of the N-PL emission (blue shaded area and left axis) of the optical antenna under different applied electric fields (orange, right axis). The inset is a confocal map of the N-PL emission of the same optical antenna. The orange lines help the eye to see the nanostructure location. The blue arrow points to the acquisition area of the N-PL. A SEM image is also shown. (b) Evolution of N-PL mean rate (left axis) and the relative modulation depth Δ_r (right axis) during the on-state as a function of the voltage applied (lower scale) or electric field (upper scale) for the two voltage sweeps illustrated in (a). The horizontal dotted line and the gray zone indicate the off-state N-PL value and its standard deviation evaluated from $8 \text{ s} < t < 12 \text{ s}$ in (a). The solid line is a linear fit taking into account the complete data set.	36
2.4.4 (a,b,c,d,e) Corresponding time traces of the N-PL for each marked position in (b). The horizontal dashed line showing the approximated OFF state of the N-PL emission. (f) Confocal map of the N-PL emission of a 75 nm gap nanoantenna. The nanostructure is traced with orange lines. Each excitation point (laser tip position) is indicated with letters. The incident laser polarization is indicated by the double arrow.	37
2.4.5 Effect of the electric field polarity inversion on the recorded N-PL emission in the gap of a bow-tie antenna (100 nm gap). (a) Time trace of the N-PL and the electric signal. The dotted horizontal line refers to the no bias state. (b) N-PL confocal map of the nanoantenna. The inset shows an SEM micrograph of the antenna. The double arrow indicates the incident laser polarization.	38
2.4.6 COMSOL Multiphysics [®] simulation of a nanocapacitor with shape and dimensions similar to the studied nanoantennas. (a) Model configuration and different performed calculations. Electric (b) potential, (c) field and (d) surface charge density distribution in the gap region of the nanocapacitor. (e) Surface charge density along the dotted line indicated in (d).	39

2.4.7	Time trace of the recorded N-PL in a ≈ 80 nm gap under the action of time-varying 10 V pulses. Each color represents a different electrical pulse duration starting at 30 ms and increasing in 10 ms steps until reaching 200 ms. The insets show the dependence of the N-PL modulation depth as a function of the pulse duration and a N-PL confocal map of the studied nanoantenna.	40
2.4.8	(a) Rise (blue-shaded area) and fall (red-shaded areas) times measured on a highly time-resolved trace of the N-PL under the action of 10 V and 200 ms pulses. The red and green crosses indicate the referential points for the high and low values of the N-PL respectively. (b) Evolution of the FWHM of the N-PL pulses with the electric pulse duration. The inset shows the measured points for an N-PL pulse under the action of a 200 ms and 10 V pulse.	41
2.4.9	(a) time trace of the emitted N-PL of a nanoantenna under the action of 8 V and 200 ms pulses. (b) Rise (blue-shaded area) and fall (red-shaded areas) times measured on a highly time-resolved trace of the N-PL indicated by the red square on (a). The red and green crosses indicate the referential points for the high and low values of the N-PL respectively.	41
2.4.10	N-PL time trace of an optical antenna for two incident laser powers and under the action of a squared time-varying voltage function with an amplitude of 20 V and a period $T = 2$ s.	42
2.4.11	Time trace of the recorded N-PL under the action of a 20 V squared electric signal for different incident laser polarizations. The relative modulation depth is pointed out as $\Delta_{\text{N-PL}}$. The white arrows show the polarization state with respect to the nanoantenna shown in the inset at that specific time. An N-PL confocal map and a SEM micrograph of the nanoantenna are shown in the inset.	43
2.5.1	(a) Phonon and (b) surface collision assisted absorption of a quantum of electromagnetic energy $\hbar\omega$ in a metal.	44
2.5.2	Simplified diagram of the charge accumulation and electron temperature effects on the nanoantennas N-PL emission.	45
2.5.3	N-PL spectra of an optical gap antenna under different applied voltages. The inset shows the spectra at the corresponding SHG wavelength.	46
2.5.4	Different types of electron emission in a metal insulator metal (MIM) system. (i) Fowler-Nordheim tunneling. (ii) Thermionic emission. (iii) Poole-Frenkel effect. (iv) Direct tunnel emission. (v) Jumping. Modified from [209].	48
2.5.5	Time traces of both SHG and N-PL signals as a 7 V amplitude square waveform is applied.	49
2.6.1	(a) Dark-field spectra as the voltage across the gap of a bow-tie antenna is ramped-up. The insets show a SEM micrograph of the nanoantenna and the spectra for the subsequent ramping down. (b) Cross-section at $\lambda = 650$ nm of (a).	50
2.6.2	Three dimensional spectrogram showing the dark-field spectra of six nanoantennas. The double arrow at the bottom left corner indicates the incident light polarization. Frames i and ii show the real image of the studied nanoantennas when the diffraction grating is at zero-order. (b,c,d,e,f,g) Corresponding binned spectra for every nanoantenna in (a).	52
3.2.1	(a) SEM micrographs of AuNWs showing the effect of the e-beam dose on the nanowire widths. (b) CAD design used to expose the resist and finally fabricate the AuNWs with different lengths.	56

- 3.3.1 Dispersion relation of surface plasmons for gold. The solid and dashed lines represent the light line in vacuum $\omega = ck$ and in quartz glass $\omega = ck/n$ respectively. In orange the dispersion curve for SPPs on a gold/glass interface. The limiting frequency $\omega_p/\sqrt{2}$ is represented by a dotted line. The symbols are the dispersion relation for gold nanowires reconstructed from $k_{\text{spp}} = j\pi/L$, j is the mode order. Adapted with permission from [232]. Copyright 2003 by the American Physical Society. 58
- 3.4.1 Wide field images of the light distributed in a $3.5 \mu\text{m}$ AuNW at the excitation wavelength with (a) longitudinal and (c) perpendicular incident polarization. The AuNW is excited at the left end by a focused laser at $\lambda_0 = 808 \text{ nm}$. Wide-field images of the spectrally filtered nonlinear photoluminescence emission are also shown for (b) longitudinal and (d) perpendicular incident polarization. The inset is a bright-field optical image of the AuNW. (e,f) Normalized integrated intensity plots of the (e) linear scattering and (f) nonlinear emission along the y -axis showing the SPP excitation efficiency for two different incident polarizations. The double arrows indicate the incident beam polarization. 59
- 3.4.2 (a) Sketch of the excitation, propagation and diffusion of the SPP at λ_0 . (b) to (d) Sketches of the different scenarii that may explain the spatial distribution of the nonlinear photoluminescence along the AuNW and at its distal end. 60
- 3.4.3 (a) Image of the light distributed in AuNWs with different lengths L taken at the excitation wavelength. From top to bottom $L = 3.0 \mu\text{m}$, $L = 5.5 \mu\text{m}$, $L = 7.0 \mu\text{m}$ and $L = 9.5 \mu\text{m}$. Scanning electron micrographs of the AuNWs are shown in insets. The AuNWs are excited at the left end by the focused laser at $\lambda_0 = 808 \text{ nm}$. The incident polarization is along the AuNWs. (b) Spectrally filtered images capturing the nonlinear photoluminescence emitted at $\lambda < 780 \text{ nm}$ by the nanowires. The dynamic of the images is saturated at the excitation area to reveal the weaker signals produced along the nanowires and at the distal ends. (c) Semilogarithmic plots of the linear ($\lambda_0 = 808 \text{ nm}$ and $\lambda_0 = 720 \text{ nm}$) and nonlinear light intensity I_{out} (integrated for $\lambda < 780 \text{ nm}$) out-coupled at the distal end of the nanowire vs. nanowire length with their corresponding exponential fit. The error bars represent the standard deviation measured on five nanowires. The inset is a log-log plot of the dependence of the integrated N-PL intensity on the incident power at the excitation point with a quadratic fitting (slope ≈ 2.2). The power dependence for the laser line λ_0 is also shown for reliability purpose with a slope of 1. 61
- 3.4.4 (a) top frame: optical transmission image of a $7.0 \mu\text{m}$ AuNW. Center frame: SPP excitation at one end and propagation to the distal face (arrow). Image is taken at the excitation wavelength. Bottom frame: excitation at the middle of the AuNW showing an absence of SPP excitation and propagation at the laser wavelength. (b) Image of the filtered nonlinear optical response of AuNWs with different lengths (from top to bottom $7.0 \mu\text{m}$, $5.5 \mu\text{m}$ and $3.0 \mu\text{m}$) when excited approximately at the middle with $\lambda_0 = 808 \text{ nm}$, incident polarization is along the AuNWs. (c) Data points: normalized spectra of the N-PL emitted by the end face (white dashed square in (b)). The spectra are normalized with their own maximum. Solid lines: simulated spectra considering a diffraction-limited broad-band source in the middle of a Fabry-Pérot cavity. 63

3.4.5 (a) AuNW with a cross section of $50 \text{ nm} \times 160 \text{ nm}$ on a glass substrate that supports a wavevector k_{spp} . Simplified modelization of the AuNW as a 1D cavity with length L and reflection coefficient r . The source is located at $x = x_0$ and emits a broad spectrum mimicking a blackbody radiation. Adapted with permission from [257]. Copyright 2011 American Chemical Society. (b) Simulated surface plasmon propagation lengths for a $150 \text{ nm} \times 60 \text{ nm}$ height AuNW on a glass substrate. The points represent the L_{spp} values inferred in the previous section. The inset on the bottom right shows the field emission of the bound mode sustained by the nanowire. 64

3.4.6 Images of the filtered nonlinear optical response of a $7.0 \mu\text{m}$ long AuNW being excited (a) at the left end and (b) at approximately the center. The normalized integrated intensity profiles along the x -axis at the bottom of the images. Grayed areas indicated the longitudinal extension of the N-PL. 65

3.4.7 (a) Schematic of the Fourier transform produced by an objective lens. Adapted with permission from [262]. 66

3.4.8 (a) Resulting Fourier plane pattern as the scattered laser light from the sample substrate goes through the objective lens. The projection of the angular emission is schematically depicted. Image inspired by [265, 266]. (b) The same Fourier plane with the intensity profiles indicated by the dashed lines (top and right frames). The derivatives of the profiles are shown at the bottom and left frames. The arrows indicate the referential points taken to verify the positioning of the relay lens. 67

3.4.9 Fourier space patterns of the (a,b) linear and (c,d) filtered nonlinear optical response for the (a,c) $3.0 \mu\text{m}$ and (b,d) $5.5 \mu\text{m}$ long AuNWs shown at the top obtained by imaging the back focal plane of the objective. The small concentric circles in (c) and (d) are diffraction rings produced by dust residues left on the optical elements. The excitation is located at one end of the AuNW. (e) Cross section profile indicated with a dashed line in (a). (f) Estimation of the nanowires length by using the fringe patterns of the linear back focal planes. The linear fit gives a slope of 0.93. The error bars indicate the standard deviation from several measurements in the Fourier plane fringes. 68

3.4.10 Fourier plane patterns with different polarization analysis of the AuNWs N-PL emission with (a,b) no analyzer, analyzer (c,d) along and (e,f) transverse to the axis of the nanowire (see double-sided arrows on the top). ϕ_1 and ϕ_2 indicate the azimuthal spread angle of the wave vector distribution. The top insets show the corresponding real plane image of the presented FPs for (a,c,e) end-excitation and (b,d,f) middle excitation. 69

3.4.11 Integrated intensity of the photoluminescence signal along the longitudinal axis of three AuNWs. The data is acquired for two orientations of the polarization analyzer and normalized with the maximum intensity. The blue-shaded area corresponds to the signal delocalized along the nanowire and the red area is the nanowire termination. The top insets show the polarization resolved image of the nonlinear photoluminescence distributed in the nanowire. The double arrow indicates the orientation of the analyzer. 71

3.5.1 Spatially resolved nonlinear photoluminescence spectral map for a $7.0 \mu\text{m}$ long AuNW excited at the bottom end. Each horizontal line represents the spectrum at that specific position and is normalized with its own maximum. The black arrows in the object plane image (right hand side) indicate the excitation and out-coupling regions. 72

3.5.2	Normalized N-PL spectra of the 7.0 μm studied AuNW (a) at different positions along the nanowire and (b) at the excitation spot but for different incident average laser powers. Insets indicate the position of the acquired spectrum. . . .	73
3.5.3	(a) Spatially resolved nonlinear photoluminescence spectral map for a 3.5 μm long AuNW excited at the middle. Each horizontal line represents the spectrum at that specific position and is normalized with its own maximum. The black arrows in the object plane image (right hand side) indicate the out-coupling regions.	73
3.6.1	(a) SEM micrograph of a 5 $\mu\text{m} \times 150$ nm AuNW electrically contacted at the distal end. Another electrode is separated 50 nm from the nanowire to apply a potential difference across the gap. (b) Schematic of the electrical connection at distal-end region of the nanowire. (c) Excitation laser filtered optical image showing the generated N-PL throughout the AuNW. The dashed squared area is zoomed in and showed at the bottom of the image. The circle indicates the monitored area.	74
3.6.2	Time trace of the N-PL coming from the distal-end of the AuNW (spatially filtered with a 300 μm pinhole).	75
3.6.3	(a) N-PL emission spectra at the distal end of a 5.0 μm long AuNW under the action of a 14 V bias and without any bias applied. The acquisition time is fixed at $t_{\text{acq}} = 0.2$ s. Wide field optical images of the filtered nonlinear emission of the same nanowire under (b) 0 V and (c) 14 V bias applied.	75
4.2.1	(a) High resolution transmission electron microscope (HRTEM) image showing the crystallinity of the synthesized silver nanowires. Image provided by the group of G.V.P. Kumar in IISER Pune, India. The inset represents the corresponding fast Fourier Transform. SEM images of (b) a typical nanowire and its two terminations (c,d). The AgNW diameter is around 530 nm	80
4.2.2	SPPs are excited by a focused laser beam (not shown) and propagate through an AgNW. Leakage radiation (LR) is emitted under the phase-match angle range represented by θ . An oil-immersion objective collects the leakage radiation. The transversal polarization is indicated by the blue arrows. The zoomed area corresponds to the dashed square. Schematic inspired by [285]	81
4.3.1	(a) (Top) Optical transmission image of a 6 μm long AgNW and (bottom) SPP excitation at the left end. (b) corresponding wavevector distribution.	82
4.3.2	(a) Wide-field image of the relative intensity distribution of the leaky mode in a 12.6 μm long AgNW. A bright-field image of the same nanowire is shown at the left. (b) Intensity profile along the two bright lines at the edges of the nanowire showed in (a). The inset shows the transverse profile along the dashed line in (a). (c) Cross section of the corresponding Fourier plane at $k_y/k_0 = 0$ for the leaky mode excitation showed in (a). The inset displays the full Fourier plane and indicates the cut position with a dashed line.	83
4.3.3	(a) Wide-field image of the relative intensity distribution of the bound and multiple leaky modes being excited in a 10 μm long AgNW. (b) Fourier plane image corresponding to the real image shown in (a). Arrows point to the straight lines resulting from the excitation of two leaky modes. (c) Profiles at the edges of the nanowire for the dashed area indicated in (a). (d) Cross section of the Fourier plane shown in (b) at $k_y/k_0 = 0$ for the multiple leaky modes excitation showed in (a).	84

4.3.4	(a) Nonlinear confocal map of a $13.5 \mu\text{m}$ long AgNW. The top frame is an optical transmission image of the same nanowire. (b) Nonlinear emission spectrum of the nanowire. The inset is an amplified image of the peak corresponding to SHG.	85
4.3.5	Real and Fourier space patterns of the (a) linear and (b) filtered nonlinear optical response for the bound mode excitation. The excitation is located at the left end of the nanowire.	85
4.3.6	Real and Fourier space patterns of the (a) linear and (b) filtered nonlinear optical response for the leaky modes excitation. The excitation is located at the left end of the nanowire. (c) Cross section profiles indicated with dashed lines in (a) and (b). The peaks are fitted with Lorentzian distributions (solid lines).	86
4.3.7	Real and Fourier space patterns of the (a) linear and (b) filtered nonlinear optical response for the SPP excitation in an AgNW with a defect. The excitation is located at the left end of the nanowire. (c) SEM images of the same nanowire showing the nature of the defect.	87
4.3.8	Filtered (a) Real and (b) Fourier plane nonlinear images of a $12 \mu\text{m}$ long AgNW being excited at the left end with a pulse laser centered at $\lambda_0 = 808 \text{ nm}$. The red arrows highlight the excitation of multiple leaky modes in opposite directions.	87
4.3.9	Corresponding (a) real and (b) Fourier plane images of the pump plasmon propagating in the nanowire of Fig. 4.3.8.	88
X.1	Illustration of a 1 to N broadband plasmonic multimode (spatial, spectral and modal) division multiplexer based on metal nanowires.	93

List of Tables

2.3.1 Recipes for spin coating the two PMMA layers needed for e-beam lithography.	30
2.3.2 Recipes for spin coating the AZ nLOF 2070 photoresist.	31
3.4.1 Azimuthal wavevector spread angles for the Fourier plane images shown in fig. 3.4.10	70

List of publications

- **Adrian Agreda**, Sviatlana Viarbitskaya, Gérard Colas des Francs, and Alexandre Bouhelier. Electrical Command of the Nonlinear Photoluminescence in Plasmonic Antennas. Preparing for submission.
- **Adrian Agreda**, Deepak K. Sharma, Julien Barthes, Sviatlana Viarbitskaya, Gérard Colas des Francs, G.V. Pavan Kumar, and Alexandre Bouhelier. Wavevector analysis of the Nonlinear Photoluminescence in Gold Nanowires. Preparing for submission.
- Romain Hernandez, Renato Juliano Martins, **Adrian Agreda**, Marlene Petit, Jean-Claude Weeber, Alexandre Bouhelier, Benoit Cluzel, and Olivier Demichel. Delocalized Hot Electron Generation with Propagative Surface Plasmon Polaritons. ACS Photonics 2019 6 (6), 1500-1505. DOI: 10.1021/acsp Photonics.9b00245.
- **Adrian Agreda**, Deepak K. Sharma, Sviatlana Viarbitskaya, Romain Hernandez, Benoit Cluzel, Olivier Demichel, Jean-Claude Weeber, Gérard Colas des Francs, G.V. Pavan Kumar, and Alexandre Bouhelier. Spatial Distribution of the Nonlinear Photoluminescence in Au Nanowires. ACS Photonics 2019 6 (5), 1240-1247. DOI: 10.1021/acsp Photonics.9b00181

List of conference contributions

Talks

- Spatial Distribution of the Nonlinear Photoluminescence in Au Nanowires GDR Or-Nano 2019 Rennes, France
- Electrical Control of Broadband Light Emission in Gold Nanostructures Flashtalks of ICB Lab 2018 Dijon, France
- Electrical Command of the Nonlinear Photo-luminescence of Plasmonic Gap Antennas Surface Plasmon Photonics 8 SPP8 2017 Taipei, Taiwan
- Electrical Command of the Linear and Nonlinear responses of Plasmonic Gap Antennas Journées de l'École Doctorale Carnot-Pasteur 2017 Dijon, France
- Electrical Command of the Nonlinear Photoluminescence of Plasmonic Gap Antennas Summer School on Plasmonics 4 SSOP4 2017 Porquerolles, France

Posters

- Spatial Distribution of Hot Electron Nonlinear Photoluminescence in Au Nanowires Hot-electron science and microscopic processes in plasmonics and catalysis Faraday Discussion 2019 London, UK
- Spectral Dynamics of the Delocalized Nonlinear Photoluminescence in Gold Nanowires 15th international conference of Near-field Optics and Nanophotonics (NFO-15) 2018 Troyes, France
- Electrical Control of Broadband Light Emission in Plasmonic Gap Antennas 15th international conference of Near-field Optics and Nanophotonics (NFO-15) 2018 Troyes, France
- Spectral Dynamics of the Delocalized Nonlinear Photoluminescence in Gold Nanowires Journées de l'École Doctorale Carnot-Pasteur 2018 Besançon, France
- Electric Field Induced TPL Emission in Optical Gap Antennas GDR Ondes Workshop in Nonlinear and Quantum Plasmonics 2016 Marseille, France

Bibliography

- [1] Yuri S. K. Nonlinear optics: The next decade. *Optics Express*, 16(26):22126–22128, 2008.
- [2] L. Novotny and N. Van Hulst. Antennas for light. *Nature Photonics*, 5:83–90, 2011.
- [3] A. Wokaun, J. G. Bergman, J. P. Heritage, A. M. Glass, P. F. Liao, and D. H. Olson. Surface second-harmonic generation from metal island films and microlithographic structures. *Physical Review B*, 24(2):849, 1981.
- [4] D. Ricard, P. Roussignol, and C. Flytzanis. Surface-mediated enhancement of optical phase conjugation in metal colloids. *Optics Letters*, 10(10):511–513, 1985.
- [5] F. Hache, D. Ricard, and C. Flytzanis. Optical nonlinearities of small metal particles: surface-mediated resonance and quantum size effects. *Journal of the Optical Society of America B*, 3(12):1647–1655, 1986.
- [6] G. T. Boyd, T. Rasing, J. R. R. Leite, and Y. R. Shen. Local-field enhancement on rough surfaces of metals, semimetals, and semiconductors with the use of optical second-harmonic generation. *Physical Review B*, 30(2):519, 1984.
- [7] G. T. Boyd, Z. H. Yu, and Y. R. Shen. Photoinduced luminescence from the noble metals and its enhancement on roughened surfaces. *Physical Review B*, 33:7923–7936, 1986.
- [8] M. R. Beversluis, A. Bouhelier, and L. Novotny. Continuum generation from single gold nanostructures through near-field mediated intraband transitions. *Physical Review B*, 68:115433, 2003.
- [9] T. Haug, P. Klemm, S. Bange, and J. M. Lupton. Hot-electron intraband luminescence from single hot spots in noble-metal nanoparticle films. *Physical Review Letters*, 115:067403, 2015.
- [10] L. Roloff, P. Klemm, I. Gronwald, R. Huber, J. M. Lupton, and S. Bange. Light emission from gold nanoparticles under ultrafast near-infrared excitation: Thermal radiation, inelastic light scattering, or multiphoton luminescence? *Nano Letters*, 17(12):7914–7919, 2017. PMID: 29182344.
- [11] N. Jiang, X. Zhuo, and J. Wang. Active plasmonics: principles, structures, and applications. *Chemical reviews*, 118(6):3054–3099, 2017.

Bibliography

- [12] P-Y. Chen and A. Alù. Optical nanoantenna arrays loaded with nonlinear materials. *Physical Review B*, 82:235405, 2010.
- [13] N. Large, M. Abb, J. Aizpurua, and O. L. Muskens. Photoconductively loaded plasmonic nanoantenna as building block for ultracompact optical switches. *Nano Letters*, 10(5):1741–1746, 2010.
- [14] F. Zhou, Y. Liu, Z-Y. Li, and Y. Xia. Analytical model for optical bistability in nonlinear metal nano-antennae involving kerr materials. *Optics express*, 18(13):13337–13344, 2010.
- [15] M. Kauranen and A. V. Zayats. Nonlinear plasmonics. *Nature photonics*, 6(11):737, 2012.
- [16] J. Butet, P-F. Brevet, and O. J. F. Martin. Optical second harmonic generation in plasmonic nanostructures: From fundamental principles to advanced applications. *ACS Nano*, 9(11):10545–10562, 2015.
- [17] M. Lippitz, M. A. van Dijk, and M. Orrit. Third-harmonic generation from single gold nanoparticles. *Nano Letters*, 5(4):799–802, 2005.
- [18] J. Renger, R. Quidant, N. van Hulst, and L. Novotny. Surface-enhanced nonlinear four-wave mixing. *Physical Review Letters*, 104:046803, 2010.
- [19] A. Mooradian. Photoluminescence of metals. *Physical Review Letters*, 22:185–187, 1969.
- [20] C. K. Chen, A. R. B. de Castro, and Y. R. Shen. Surface-enhanced second-harmonic generation. *Physical Review Letters*, 46:145–148, 1981.
- [21] V. Knittel, M. P. Fischer, T. de Roo, S. Mecking, A. Leitenstorfer, and D. Brida. Nonlinear photoluminescence spectrum of single gold nanostructures. *ACS Nano*, 9(1):894–900, 2015. PMID: 25548827.
- [22] P. Biagioni, D. Brida, J-S. Huang, J. Kern, L. Duo, B. Hecht, M. Finazzi, and G. Cerullo. Dynamics of four-photon photoluminescence in gold nanoantennas. *Nano Letters*, 12(6):2941–2947, 2012. PMID: 22551099.
- [23] P. Biagioni, M. Celebrano, M. Savoini, G. Grancini, D. Brida, S. Mátéfi-Tempfli, M. Mátéfi-Tempfli, L. Duò, B. Hecht, G. Cerullo, and M. Finazzi. Dependence of the two-photon photoluminescence yield of gold nanostructures on the laser pulse duration. *Physical Review B*, 80:045411, 2009.
- [24] X-F. Jiang, Y. Pan, C. Jiang, T. Zhao, P. Yuan, T. Venkatesan, and Q-H. Xu. Excitation nature of two-photon photoluminescence of gold nanorods and coupled gold nanoparticles studied by two-pulse emission modulation spectroscopy. *The Journal of Physical Chemistry Letters*, 4(10):1634–1638, 2013.
- [25] F. Hache, D. Ricard, C. Flytzanis, and U. Kreibig. The optical kerr effect in small metal particles and metal colloids: The case of gold. *Applied Physics A*, 47(4):347–357, 1988.
- [26] B. Palpant. *Third-Order Nonlinear Optical Response of Metal Nanoparticles*, pages 461–508. Springer Netherlands, Dordrecht, 2006.
- [27] R. W. Boyd, Z. Shi, and I. De Leon. The third-order nonlinear optical susceptibility of gold. *Optics Communications*, 326:74–79, 2014.

-
- [28] M. Conforti and G. Della Valle. Derivation of third-order nonlinear susceptibility of thin metal films as a delayed optical response. *Physical Review B*, 85(24), 2012.
- [29] R. del Coso and J. Solis. Relation between nonlinear refractive index and third-order susceptibility in absorbing media. *Journal of the Optical Society of America B*, 21(3):640–644, 2004.
- [30] J. Mertens, M-E. Kleemann, R. Chikkaraddy, P. Narang, and J. J. Baumberg. How Light Is Emitted by Plasmonic Metals. *Nano Letters*, 17(4):2568–2574, 2017.
- [31] W. L. Barnes, A. Dereux, and T. W. Ebbesen. Surface plasmon subwavelength optics. *Nature*, 424:824–830, 2003.
- [32] L. Novotny and B. Hecht. *Principles of Nano-Optics*. Principles of Nano-optics. Cambridge University Press, 2012.
- [33] R. W. Boyd. *Nonlinear optics*. Academic Press, San Diego, 3rd edition, 2008.
- [34] M. Agio and A. Alù. *Optical Antennas*. Cambridge University Press, 2013.
- [35] P. Bharadwaj, R. Beams, and L. Novotny. Nanoscale spectroscopy with optical antennas. *Chemical Science*, 2:136–140, 2011.
- [36] G. V. P. Kumar. Plasmonic nano-architectures for surface enhanced raman scattering: a review. *Journal of Nanophotonics*, 6:6 – 6 – 20, 2012.
- [37] J. N. Anker, W. P. Hall, O. Lyandres, N. C. Shah, J. Zhao, and R. P. Van Duyne. Biosensing with plasmonic nanosensors. *Nature Materials*, 7(6):442–453, 2008.
- [38] P. Offermans, M. C. Schaafsma, S. R. K. Rodriguez, Y. Zhang, M. Crego-Calama, S. H. Brongersma, and J. Gómez Rivas. Universal scaling of the figure of merit of plasmonic sensors. *ACS Nano*, 5(6):5151–5157, 2011. PMID: 21574624.
- [39] L. Tang, S. E. Kocabas, S. Latif, A. K. Okyay, D-S. Ly-Gagnon, K. C. Saraswat, and D. A. B. Miller. Nanometre-scale germanium photodetector enhanced by a near-infrared dipole antenna. *Nature Photonics*, 2(4):226–229, 2008.
- [40] R. F. Oulton, V. J Sorger, T. Zentgraf, R-M. Ma, C. Gladden, L. Dai, G. Bartal, and X. Zhang. Plasmon lasers at deep subwavelength scale. *Nature*, 61:629–632, 2009.
- [41] A. H. Schokker and A. F. Koenderink. Lasing at the band edges of plasmonic lattices. *Physical Review B*, 90:155452, 2014.
- [42] S. Pillai, K. R. Catchpole, T. Trupke, and M. A. Green. Surface plasmon enhanced silicon solar cells. *Journal of Applied Physics*, 101(9), 2007.
- [43] S. Kühn, U. Håkanson, L. Rogobete, and V. Sandoghdar. Enhancement of single-molecule fluorescence using a gold nanoparticle as an optical nanoantenna. *Physical Review Letters*, 97:017402, 2006.
- [44] P. Anger, P. Bharadwaj, and L. Novotny. Enhancement and quenching of single-molecule fluorescence. *Physical Review Letters*, 96:113002, 2006.
- [45] H. Gersen, M. F. García-Parajó, L. Novotny, J. A. Veerman, L. Kuipers, and N. F. van Hulst. Influencing the angular emission of a single molecule. *Physical Review Letters*, 85:5312–5315, 2000.

- [46] S. I. Bozhevolnyi, J. Erland, K. Leosson, P. M. W. Skovgaard, and J. M. Hvam. Waveguiding in surface plasmon polariton band gap structures. *Physical Review Letters*, 86:3008–3011, 2001.
- [47] V. E. Ferry, L. A. Sweatlock, D. Pacifici, and H. A. Atwater. Plasmonic nanostructure design for efficient light coupling into solar cells. *Nano Letters*, 8(12):4391–4397, 2008. PMID: 19367883.
- [48] C. Rockstuhl, S. Fahr, and F. Lederer. Absorption enhancement in solar cells by localized plasmon polaritons. *Journal of Applied Physics*, 104(12):123102, 2008.
- [49] P. Bharadwaj, B. Deutsch, and L. Novotny. Optical antennas. *Advances in Optics and Photonics*, 1(3):438–483, 2009.
- [50] W. L. Stutzman and G. A. Thiele. *Antenna Theory and Design*. Antenna Theory and Design. Wiley, 2012.
- [51] E.H. Synge. A suggested method for extending microscopic resolution into the ultra-microscopic region. *The London, Edinburgh, and Dublin Philosophical Magazine and Journal of Science*, 6(35):356–362, 1928.
- [52] J. Wessel. Surface-enhanced optical microscopy. *Journal of the Optical Society of America B*, 2:1538–1541, 1985.
- [53] U. Ch. Fischer and D. W. Pohl. Observation of single-particle plasmons by near-field optical microscopy. *Physical Review Letters*, 62:458–461, 1989.
- [54] R. D. Grober, R. J. Schoelkopf, and D. E. Prober. Optical antenna: Towards a unity efficiency near-field optical probe. *Applied Physics Letters*, 70(11):1354–1356, 1997.
- [55] T. J. Cui, D. Smith, and R. Liu. *Metamaterials, Theory, Design, and Applications*. Springer US, 2010.
- [56] Y. Li. Optical properties of plasmonic materials. In *Plasmonic Optics: Theory and Applications*, pages 1–41. International Society for Optics and Photonics, 2017.
- [57] S. G. Rodrigo, F. J. García-Vidal, and L. Martín-Moreno. Influence of material properties on extraordinary optical transmission through hole arrays. *Physical Review B*, 77(7):075401, 2008.
- [58] S. Enoch and N. Bonod. *Plasmonics: from basics to advanced topics*. Springer, 2012.
- [59] S. A. Maier. *Plasmonics: Fundamentals and Applications*. Springer US, 2007.
- [60] J. D. Jackson. *Classical electrodynamics*. Wiley, 3rd ed. edition, 1999.
- [61] S. A. Maier, P. G. Kik, and H. A. Atwater. Optical pulse propagation in metal nanoparticle chain waveguides. *Physical Review B*, 67(20):205402, 2003.
- [62] P. Berini. Plasmon-polariton waves guided by thin lossy metal films of finite width: Bound modes of asymmetric structures. *Physical Review B*, 63:125417, 2001.
- [63] R. Hernandez, R. Juliano Martins, A. Agreda, M. Petit, J-C. Weeber, A. Bouhelier, B. Cluzel, and O. Demichel. Delocalized hot electron generation with propagative surface plasmon polaritons. *ACS Photonics*, 2019.

- [64] A. Agreda, D. K. Sharma, S. Viarbitskaya, R. Hernandez, B. Cluzel, O. Demichel, J-C. Weeber, G. Colas des Francs, G. V. P. Kumar, and A. Bouhelier. Spatial distribution of the nonlinear photoluminescence in au nanowires. *ACS Photonics*, 6(5):1240–1247, 2019.
- [65] H. Ditlbacher, A. Hohenau, D. Wagner, U. Kreibig, M. Rogers, F. Hofer, F. R. Aussenegg, and J. R. Krenn. Silver nanowires as surface plasmon resonators. *Physical Review Letters*, 95:257403, 2005.
- [66] S. I. Bozhevolnyi, V. S. Volkov, E. Devaux, and T. W. Ebbesen. Channel plasmon-polariton guiding by subwavelength metal grooves. *Physical Review Letters*, 95(4):046802, 2005.
- [67] F. López-Tejeira, S. G. Rodrigo, L. Martín-Moreno, F. J. García-Vidal, E. Devaux, T. W. Ebbesen, J. R. Krenn, I. P. Radko, S. I. Bozhevolnyi, M. U. González, et al. Efficient unidirectional nanoslit couplers for surface plasmons. *Nature Physics*, 3(5):324, 2007.
- [68] V. Giannini, A. I. Fernández-Domínguez, S. C. Heck, and S. A. Maier. Plasmonic nanoantennas: Fundamentals and their use in controlling the radiative properties of nanoemitters. *Chemical Reviews*, 111(6):3888–3912, 2011. PMID: 21434605.
- [69] P. Mie. Beiträge zur optik trüber medien, speziell kolloidaler metallösungen. *Annalen der Physik*, 330:377–624, 1908.
- [70] R. Gans. über die form ultramikroskopischer goldteilchen. *Annalen der Physik*, 342:881–900, 1912.
- [71] K. Yee. Numerical solution of initial boundary value problems involving maxwell’s equations in isotropic media. *IEEE Transactions on Antennas and Propagation*, 14:302–307, 1966.
- [72] V. Myroshnychenko, J. Rodríguez-Fernández, I. Pastoriza-Santos, A. M. Funston, C. Novo, P. Mulvaney, L. M. Liz-Marzán, and F. J. García de Abajo. Modelling the optical response of gold nanoparticles. *Chemical Society Reviews*, 37:1792–1805, 2008.
- [73] K. B. Crozier, A. Sundaramurthy, G. S. Kino, and C. F. Quate. Optical antennas: Resonators for local field enhancement. *Journal of Applied Physics*, 94(7):4632–4642, 2003.
- [74] G. W. Bryant, F. J. García de Abajo, and J. Aizpurua. Mapping the plasmon resonances of metallic nanoantennas. *Nano Letters*, 8(2):631–636, 2008. PMID: 18189444.
- [75] M. Liu, P. Guyot-Sionnest, T-W. Lee, and S. K. Gray. Optical properties of rodlike and bipyramidal gold nanoparticles from three-dimensional computations. *Physical Review B*, 76:235428, 2007.
- [76] P. Zijlstra and M. Orrit. Single metal nanoparticles: optical detection, spectroscopy and applications. *Reports on Progress in Physics*, 74(10):106401, 2011.
- [77] P. J. Schuck, D. P. Fromm, A. Sundaramurthy, G. S. Kino, and W. E. Moerner. Improving the mismatch between light and nanoscale objects with gold bowtie nanoantennas. *Physical Review Letters*, 94:017402, 2005.
- [78] D. P. Fromm, A. Sundaramurthy, P. J. Schuck, G. Kino, and W. E. Moerner. Gap-dependent optical coupling of single “bowtie” nanoantennas resonant in the visible. *Nano Letters*, 4(5):957–961, 2004.

- [79] F. Wen, J. Ye, N. Liu, P. Van Dorpe, P. Nordlander, and N. J. Halas. Plasmon transmutation: Inducing new modes in nanoclusters by adding dielectric nanoparticles. *Nano Letters*, 12(9):5020–5026, 2012. PMID: 22924627.
- [80] P. Ghenuche, S. Cherukulappurath, T. H. Taminiau, N. F. van Hulst, and R. Quidant. Spectroscopic mode mapping of resonant plasmon nanoantennas. *Physical Review Letters*, 101(11):116805, 2008.
- [81] K. Guo, A. Antoncicchi, X. Zheng, M. Sallam, E. A. Soliman, G. A. E. Vandenbosch, V. V. Moshchalkov, and A. F. Koenderink. Dendritic optical antennas: scattering properties and fluorescence enhancement. *Scientific Reports*, 7(1):6223, 2017.
- [82] Novotny L. From near-field optics to optical antennas. *Physics Today*, 64(7):47, 2011.
- [83] M. W. Knight, H. Sobhani, P. Nordlander, and N. J. Halas. Photodetection with active optical antennas. *Science*, 332(6030):702–704, 2011.
- [84] T. Ishi, J. Fujikata, K. Makita, T. Baba, and K. Ohashi. Si nano-photodiode with a surface plasmon antenna. *Japanese Journal of Applied Physics*, 44(No. 12):L364–L366, 2005.
- [85] H. G. Frey, S. Witt, K. Felderer, and R. Guckenberger. High-resolution imaging of single fluorescent molecules with the optical near-field of a metal tip. *Physical Review Letters*, 93(20), 2004.
- [86] M. F. Garcia-Parajo. Optical antennas focus in on biology. *Nature Photonics*, 2(4):201–203, 2008.
- [87] S. Nie. Probing single molecules and single nanoparticles by surface-enhanced raman scattering. *Science*, 275(5303):1102–1106, 1997.
- [88] M. Righini, P. Ghenuche, S. Cherukulappurath, V. Myroshnychenko, F. J. García de Abajo, and R. Quidant. Nano-optical trapping of rayleigh particles and escherichia coli bacteria with resonant optical antennas. *Nano Letters*, 9(10):3387–3391, 2009.
- [89] S. Lal, S. E. Clare, and N. J. Halas. Nanoshell-enabled photothermal cancer therapy: Impending clinical impact. *Accounts of Chemical Research*, 41(12):1842–1851, 2008.
- [90] A. Alù and N. Engheta. Wireless at the nanoscale: Optical interconnects using matched nanoantennas. *Physical Review Letters*, 104(21), 2010.
- [91] A. Dasgupta, M-M. Mennemanteuil, M. Buret, N. Cazier, G. Colas-des Francs, and A. Bouhelier. Optical wireless link between a nanoscale antenna and a transducing rectenna. *Nature Communications*, 9(1), 2018.
- [92] A. Emboras, C. Hoessbacher, C. Haffner, W. Heni, U. Koch, P. Ma, Y. Fedoryshyn, J. Niegemann, C. Hafner, and J. Leuthold. Electrically controlled plasmonic switches and modulators. *IEEE Journal of Selected Topics in Quantum Electronics*, 21(4):276–283, 2014.
- [93] D. Gall. Electron mean free path in elemental metals. *Journal of Applied Physics*, 119(8):085101, 2016.
- [94] P. B. Johnson and R. W. Christy. Optical constants of the noble metals. *Physical Review B*, 6:4370–4379, 1972.

-
- [95] R. E. Hummel. *Electronic properties of materials*. Springer Science & Business Media, 2011.
- [96] J. Leuthold, C. Koos, and W. Freude. Nonlinear silicon photonics. *Nature Photonics*, 4(8):535–544, Jul 2010.
- [97] J. A Dionne, L. A. Sweatlock, M. T. Sheldon, A. P. Alivisatos, and H. A. Atwater. Silicon-based plasmonics for on-chip photonics. *IEEE Journal of Selected Topics in Quantum Electronics*, 16(1):295–306, 2010.
- [98] P. A. Franken, A. E. Hill, C. W. Peters, and G. Weinreich. Generation of optical harmonics. *Physical Review Letters*, 7:118–119, 1961.
- [99] T. H. Maiman. Stimulated optical radiation in ruby. *Nature*, 187(4736):493–494, 1960.
- [100] X. Younan and G. M. Whitesides. Soft lithography. *Annu Rev Mater Sci*, 28:153–184, 1998.
- [101] J. Serbin, A. Egbert, A. Ostendorf, B. N. Chichkov, R. Houbertz, G. Domann, J. Schulz, C. Cronauer, L. Fröhlich, and M. Popall. Femtosecond laser-induced two-photon polymerization of inorganic–organic hybrid materials for applications in photonics. *Optics Letters*, 28(5):301–303, 2003.
- [102] J. Henzie, M. H. Lee, and T. W. Odom. Multiscale patterning of plasmonic metamaterials. *Nature nanotechnology*, 2(9):549, 2007.
- [103] B. Kobrin, E. S. Barnard, M. L. Brongersma, M. K. Kwak, and L. J. Guo. Rolling mask nanolithography: the pathway to large area and low cost nanofabrication. In *Advanced Fabrication Technologies for Micro/Nano Optics and Photonics V*, volume 8249, page 82490O. International Society for Optics and Photonics, 2012.
- [104] W. A. Murray and W. L. Barnes. Plasmonic materials. *Advanced materials*, 19(22):3771–3782, 2007.
- [105] V. E. Ferry, M. A. Verschuuren, H. B. T. Li, R. E. I. Schropp, H. A. Atwater, and A. Polman. Improved red-response in thin film a-si: H solar cells with soft-imprinted plasmonic back reflectors. *Applied physics letters*, 95(18):183503, 2009.
- [106] S. Kawata, H-B. Sun, T. Tanaka, and K. Takada. Finer features for functional microdevices. *Nature*, 412(6848):697, 2001.
- [107] J. Fischer and M. Wegener. Three-dimensional optical laser lithography beyond the diffraction limit. *Laser & Photonics Reviews*, 7(1):22–44, 2013.
- [108] A. I. Kuznetsov, R. Kiyari, and B. N. Chichkov. Laser fabrication of 2d and 3d metal nanoparticle structures and arrays. *Optics express*, 18(20):21198–21203, 2010.
- [109] A. Bouhelier, M. Beversluis, A. Hartschuh, and L. Novotny. Near-field second-harmonic generation induced by local field enhancement. *Physical Review Letters*, 90:013903, 2003.
- [110] G. Lu, L. Hou, T. Zhang, J. Liu, H. Shen, C. Luo, and Q. Gong. Plasmonic sensing via photoluminescence of individual gold nanorod. *The Journal of Physical Chemistry C*, 116(48):25509–25516, 2012.

Bibliography

- [111] K-Q. Lin, J. Yi, J-H. Zhong, S. Hu, B-J. Liu, J-Y. Liu, C. Zong, Z-C. Lei, X. Wang, J. Aizpurua, et al. Plasmonic photoluminescence for recovering native chemical information from surface-enhanced raman scattering. *Nature communications*, 8:14891, 2017.
- [112] X. Wu, T. Ming, X. Wang, P. Wang, J. Wang, and J. Chen. High-photoluminescence-yield gold nanocubes: for cell imaging and photothermal therapy. *ACS nano*, 4(1):113–120, 2009.
- [113] Y. Fang, W-S. Chang, B. Willingham, P. Swanglap, S. Dominguez-Medina, and S. Link. Plasmon emission quantum yield of single gold nanorods as a function of aspect ratio. *ACS Nano*, 6(8):7177–7184, 2012.
- [114] H. Hu, H. Duan, J. K. W. Yang, and Z. X. Shen. Plasmon-modulated photoluminescence of individual gold nanostructures. *ACS Nano*, 6(11):10147–10155, 2012.
- [115] Y-Y. Cai, J. G. Liu, L. J. Tauzin, D. Huang, E. Sung, H. Zhang, A. Joplin, W-S. Chang, P. Nordlander, and S. Link. Photoluminescence of gold nanorods: Purcell effect enhanced emission from hot carriers. *ACS Nano*, 12(2):976–985, 2018.
- [116] Y-Y. Cai, E. Sung, R. Zhang, L. J. Tauzin, J. G. Liu, B. Ostovar, Y. Zhang, W-S. Chang, P. Nordlander, and S. Link. Anti-stokes emission from hot carriers in gold nanorods. *Nano Letters*, 19(2):1067–1073, 2019.
- [117] J. T. Hugall and J. J. Baumberg. Demonstrating photoluminescence from au is electronic inelastic light scattering of a plasmonic metal: The origin of sers backgrounds. *Nano Letters*, 15(4):2600–2604, 2015.
- [118] J. Huang, W. Wang, C. J. Murphy, and D. G. Cahill. Resonant secondary light emission from plasmonic au nanostructures at high electron temperatures created by pulsed-laser excitation. *Proceedings of the National Academy of Sciences*, 111(3):906–911, 2014.
- [119] B. Neupane, L. Zhao, and G. Wang. Up-conversion luminescence of gold nanospheres when excited at nonsurface plasmon resonance wavelength by a continuous wave laser. *Nano Letters*, 13(9):4087–4092, 2013.
- [120] M. E. Orczyk, J. Swiatkiewicz, G. Huang, and P. N. Prasad. Study of resonant third-order nonlinear optical susceptibilities by the phase-tuned optically heterodyned kerr gate technique. *The Journal of Physical Chemistry*, 98(30):7307–7312, 1994.
- [121] P. Mühlischlegel, H.-J. Eisler, O. J. F. Martin, B. Hecht, and D. W. Pohl. Resonant optical antennas. *Science*, 308(5728):1607–1609, 2005.
- [122] T. Hanke, G. Krauss, D. Träutlein, B. Wild, R. Bratschitsch, and A. Leitenstorfer. Efficient nonlinear light emission of single gold optical antennas driven by few-cycle near-infrared pulses. *Physical Review Letters*, 103:257404, 2009.
- [123] N. Pfullmann, C. Waltermann, M. Kovačev, V. Knittel, R. Bratschitsch, D. Akemeier, A. Hütten, A. Leitenstorfer, and U. Morgner. Nano-antenna-assisted harmonic generation. *Applied Physics B*, 113(1):75–79, 2013.
- [124] M. Danckwerts and L. Novotny. Optical frequency mixing at coupled gold nanoparticles. *Physical Review Letters*, 98:026104, 2007.

- [125] V. Knittel, M. P. Fischer, M. Vennekel, T. Rybka, A. Leitenstorfer, and D. Brida. Dispersion of the nonlinear susceptibility in gold nanoantennas. *Physical Review B*, 96(12), 2017.
- [126] H. Baida, D. Mongin, D. Christofilos, G. Bachelier, A. Crut, P. Maioli, N. Del Fatti, and F. Vallée. Ultrafast nonlinear optical response of a single gold nanorod near its surface plasmon resonance. *Physical Review Letters*, 107:057402, 2011.
- [127] R. H. M. Groeneveld, R. Sprik, and A. Lagendijk. Femtosecond spectroscopy of electron-electron and electron-phonon energy relaxation in ag and au. *Physical Review B*, 51:11433–11445, 1995.
- [128] E. Carpenne. Ultrafast laser irradiation of metals: Beyond the two-temperature model. *Physical Review B*, 74:024301, 2006.
- [129] Y. Guillet, M. Rashidi-Huyeh, and B. Palpant. Influence of laser pulse characteristics on the hot electron contribution to the third-order nonlinear optical response of gold nanoparticles. *Physical Review B*, 79(4):045410, 2009.
- [130] J. R. M. Saavedra, A. Asenjo-Garcia, and F. J. García de Abajo. Hot-electron dynamics and thermalization in small metallic nanoparticles. *ACS Photonics*, 3(9):1637–1646, 2016.
- [131] N. Del Fatti and F. Vallée. Ultrafast optical nonlinear properties of metal nanoparticles. *Applied Physics B: Lasers and Optics*, 73(4):383–390, 2001.
- [132] C. Voisin, N. Del Fatti, D. Christofilos, and F. Vallée. Ultrafast electron dynamics and optical nonlinearities in metal nanoparticles. *The Journal of Physical Chemistry B*, 105(12):2264–2280, 2001.
- [133] M. Nisoli, S. Stagira, S. De Silvestri, A. Stella, P. Tognini, P. Cheyssac, and R. Kofman. Ultrafast electronic dynamics in solid and liquid gallium nanoparticles. *Physical Review Letters*, 78:3575–3578, 1997.
- [134] Y. Hamanaka, J. Kuwabata, I. Tanahashi, S. Omi, and A. Nakamura. Ultrafast electron relaxation via breathing vibration of gold nanocrystals embedded in a dielectric medium. *Physical Review B*, 63:104302, 2001.
- [135] K. D. Ko, A. Kumar, K. H. Fung, R. Ambekar, G. L. Liu, N. X. Fang, and K. C. Jr. Toussaint. Nonlinear optical response from arrays of au bowtie nanoantennas. *Nano Letters*, 11(1):61–65, 2011.
- [136] A. Bouhelier, R. Bachelot, G. Lerondel, S. Kostcheev, P. Royer, and G. P. Wiederrecht. Surface plasmon characteristics of tunable photoluminescence in single gold nanorods. *Physical Review Letters*, 95(26), 2005.
- [137] O. Demichel, M. Petit, S. Viarbitskaya, R. Méjard, F. de Fornel, E. Hertz, F. Billard, A. Bouhelier, and B. Cluzel. Dynamics, efficiency, and energy distribution of nonlinear plasmon-assisted generation of hot carriers. *ACS Photonics*, 3(5):791–795, 2016.
- [138] G. T. Boyd, Z. H. Yu, and Y. R. Shen. *Bulletin of the American Physical Society*, 27, 1982.
- [139] R. A. Farrer, F. L. Butterfield, V. W. Chen, and J. T. Fourkas. Highly efficient multiphoton-absorption-induced luminescence from gold nanoparticles. *Nano Letters*, 5(6):1139–1142, 2005.

Bibliography

- [140] M. Rashidi-Huyeh and B. Palpant. Thermal response of nanocomposite materials under pulsed laser excitation. *Journal of applied physics*, 96(8):4475–4482, 2004.
- [141] B. Y. Mueller and B. Rethfeld. Relaxation dynamics in laser-excited metals under nonequilibrium conditions. *Physical Review B*, 87(3):035139, 2013.
- [142] M. Perner, P. Bost, U. Lemmer, G. von Plessen, J. Feldmann, U. Becker, M. Mennig, M. Schmitt, and H. Schmidt. Optically induced damping of the surface plasmon resonance in gold colloids. *Physical Review Letters*, 78:2192–2195, 1997.
- [143] R. Méjard, A. Verdy, M. Petit, A. Bouhelier, B. Cluzel, and O. Demichel. Energy-resolved hot-carrier relaxation dynamics in monocrystalline plasmonic nanoantennas. *ACS Photonics*, 3(8):1482–1488, 2016.
- [144] J. Lambe and S. L. McCarthy. Light emission from inelastic electron tunneling. *Physical Review Letters*, 37:923–925, 1976.
- [145] M. Buret, A. V. Uskov, J. Dellinger, N. Cazier, M-M. Mennemanteuil, J. Berthelot, I. V. Smetanin, I. E. Protsenko, G. Colas-des Francs, and A. Bouhelier. Spontaneous hot-electron light emission from electron-fed optical antennas. *Nano Letters*, 15(9):5811–5818, 2015.
- [146] P. Tomchuk and R. Fedorovich. *Soviet Physics Solid State*, pages 276–278, 1966.
- [147] E. Gamaly. *Femtosecond Laser-Matter Interaction : theory, experiments and applications*. World Scientific, Singapore London, 2011.
- [148] K. Joulain, R. Carminati, J-P. Mulet, and J-J. Greffet. Definition and measurement of the local density of electromagnetic states close to an interface. *Physical Review B*, 68:245405, 2003.
- [149] A. V. Shchegrov, K. Joulain, R. Carminati, and J-J. Greffet. Near-field spectral effects due to electromagnetic surface excitations. *Physical Review Letters*, 85:1548–1551, 2000.
- [150] M. V. Klein. Equivalence of resonance raman scattering in solids with absorption followed by luminescence. *Physical Review B*, 8:919–921, 1973.
- [151] J. R. Solin and H. Merkelo. Resonant scattering or absorption followed by emission. *Physical Review B*, 12:624–629, 1975.
- [152] X. Xie and D. G. Cahill. Thermometry of plasmonic nanostructures by anti-stokes electronic raman scattering. *Applied Physics Letters*, 109(18):183104, 2016.
- [153] M. L. Brongersma and V. M. Shalaev. The case for plasmonics. *Science*, 328(5977):440–441, 2010.
- [154] E. Ozbay. Plasmonics: Merging photonics and electronics at nanoscale dimensions. *Science*, 311(5758):189–193, 2006.
- [155] T. W. Ebbesen, C. Genet, and S. I. Bozhevolnyi. Surface-plasmon circuitry. *Physics Today*, 61(5):44–50, May 2008.
- [156] M. A. Noginov, G. Zhu, A. M. Belgrave, R. Bakker, V. M. Shalaev, E. E. Narimanov, S. Stout, E. Herz, T. Suteewong, and U. Wiesner. Demonstration of a spaser-based nanolaser. *Nature*, 460:1110–1168, 2009.

- [157] J. Seidel, S. Grafström, and L. Eng. Stimulated emission of surface plasmons at the interface between a silver film and an optically pumped dye solution. *Physical Review Letters*, 94(17):177401, 2005.
- [158] J. Grandidier, G. Colas des Francs, S. Massenot, A. Bouhelier, L. Markey, J-C. Weeber, C. Finot, and A. Dereux. Gain-assisted propagation in a plasmonic waveguide at telecom wavelength. *Nano Letters*, 9(8):2935–2939, 2009. PMID: 19719111.
- [159] Y. Wu, C. Zhang, N. M. Estakhri, Y. Zhao, J. Kim, M. Zhang, X-X. Liu, G. K. Pribil, A. Alù, C-K. Shih, et al. Intrinsic optical properties and enhanced plasmonic response of epitaxial silver. *Advanced Materials*, 26(35):6106–6110, 2014.
- [160] V. Kalathingal, P. Dawson, and J. Mitra. Scanning tunneling microscope light emission: Effect of the strong dc field on junction plasmons. *Physical Review B*, 94(3):035443, 2016.
- [161] G. A. Wurtz, R. Pollard, W. Hendren, G. P. Wiederrecht, D. J. Gosztola, V. A. Podolskiy, and A. V. Zayats. Designed ultrafast optical nonlinearity in a plasmonic nanorod metamaterial enhanced by nonlocality. *Nature nanotechnology*, 6(2):107, 2011.
- [162] Z. Sun, W. Ni, Z. Yang, X. Kou, L. Li, and J. Wang. ph-controlled reversible assembly and disassembly of gold nanorods. *Small*, 4(9):1287–1292, 2008.
- [163] R. A. Pala, K. T. Shimizu, N. A. Melosh, and M. L. Brongersma. A nonvolatile plasmonic switch employing photochromic molecules. *Nano Letters*, 8(5):1506–1510, 2008.
- [164] J. Gosciniak and S. I. Bozhevolnyi. Performance of thermo-optic components based on dielectric-loaded surface plasmon polariton waveguides. *Scientific reports*, 3:1803, 2013.
- [165] J. Berthelot, A. Bouhelier, C. Huang, J. Margueritat, G. Colas-des Francs, E. Finot, J-C. Weeber, A. Dereux, S. Kostcheev, H. I. E. Ahrach, et al. Tuning of an optical dimer nanoantenna by electrically controlling its load impedance. *Nano Letters*, 9(11):3914–3921, 2009.
- [166] Y. R. Leroux, J. C. Lacroix, K. I. Chane-Ching, C. Fave, N. Félidj, G. Lévi, J. Aubard, J. R. Krenn, and A. Hohenau. Conducting polymer electrochemical switching as an easy means for designing active plasmonic devices. *Journal of the American Chemical Society*, 127(46):16022–16023, 2005.
- [167] D. Martín-Becerra, J. B. González-Díaz, V. V. Temnov, A. Cebollada, G. Armelles, T. Thomay, A. Leitenstorfer, R. Bratschitsch, A. García-Martín, and M. U. González. Enhancement of the magnetic modulation of surface plasmon polaritons in au/co/au films. *Applied Physics Letters*, 97(18):183114, 2010.
- [168] K. F. MacDonald, Z. L. Sámson, M. I. Stockman, and N. I. Zheludev. Ultrafast active plasmonics. *Nature Photonics*, 3(1):55, 2009.
- [169] A. V. Krasavin, K. F. MacDonald, N. I. Zheludev, and A. V. Zayats. High-contrast modulation of light with light by control of surface plasmon polariton wave coupling. *Applied physics letters*, 85(16):3369–3371, 2004.
- [170] J. Gosciniak, S. I. Bozhevolnyi, T. B. Andersen, V. S. Volkov, J. Kjelstrup-Hansen, L. Markey, and A. Dereux. Thermo-optic control of dielectric-loaded plasmonic waveguide components. *Optics express*, 18(2):1207–1216, 2010.

- [171] A. L. Lereu, A. Passian, J. P. Goudonnet, T. Thundat, and T. L. Ferrell. Optical modulation processes in thin films based on thermal effects of surface plasmons. *Applied Physics Letters*, 86(15):154101, 2005.
- [172] A. V Krasavin and N. I. Zheludev. Active plasmonics: Controlling signals in au/ga waveguide using nanoscale structural transformations. *Applied Physics Letters*, 84(8):1416–1418, 2004.
- [173] G. Soavi, G. Wang, H. Rostami, D. G. Purdie, D. De Fazio, T. Ma, B. Luo, J. Wang, A. K. Ott, D. Yoon, et al. Broadband, electrically tunable third-harmonic generation in graphene. *Nature nanotechnology*, 13(7):583, 2018.
- [174] J. A Dionne, K. Diest, L. A. Sweatlock, and H. A Atwater. Plasmostor: a metal- oxide-si field effect plasmonic modulator. *Nano Letters*, 9(2):897–902, 2009.
- [175] M. J. Dicken, L. A. Sweatlock, D. Pacifici, H. J Lezec, K. Bhattacharya, and H. A. Atwater. Electrooptic modulation in thin film barium titanate plasmonic interferometers. *Nano Letters*, 8(11):4048–4052, 2008.
- [176] Sukanya R., S. Lachèze, J. Renger, A. Bouhelier, R. Espiau de Lamaestre, A. Dereux, and R. Quidant. Performance of electro-optical plasmonic ring resonators at telecom wavelengths. *Optics Express*, 20(3):2354–2362, 2012.
- [177] A. Agrawal, C. Susut, G. Stafford, U. Bertocci, B. McMorran, H. J Lezec, and A. A. Talin. An integrated electrochromic nanoplasmonic optical switch. *Nano Letters*, 11(7):2774–2778, 2011.
- [178] W. Cai, A. P. Vasudev, and M. L. Brongersma. Electrically controlled nonlinear generation of light with plasmonics. *Science*, 333(6050):1720–1723, 2011.
- [179] A. Melikyan, N. Lindenmann, S. Walheim, P. M. Leufke, S. Ulrich, J. Ye, P. Vincze, H. Hahn, Th. Schimmel, C. Koos, W. Freude, and J. Leuthold. Surface plasmon polariton absorption modulator. *Optics Express*, 19(9):8855–8869.
- [180] W. Dickson, G. A. Wurtz, P. R. Evans, R. J. Pollard, and A. V. Zayats. Electronically controlled surface plasmon dispersion and optical transmission through metallic hole arrays using liquid crystal. *Nano Letters*, 8(1):281–286, 2008.
- [181] T. J. Kim, T. Thio, T. W. Ebbesen, D. E. Grupp, and H. J. Lezec. Control of optical transmission through metals perforated with subwavelength hole arrays. *Optics Letters*, 24(4):256–258, 1999.
- [182] K. Thyagarajan, R. Sokhoyan, L. Zornberg, and H. A. Atwater. Millivolt modulation of plasmonic metasurface optical response via ionic conductance. *Advanced Materials*, 29(31):1701044, 2017.
- [183] R. A. Maniyara, D. Rodrigo, R. Yu, J. Canet-Ferrer, D. S. Ghosh, R. Yongsunthon, D. E. Baker, A. Rezikyan, F. J. García de Abajo, and V. Pruneri. Tunable plasmons in ultrathin metal films. *Nature Photonics*, 13(5):328, 2019.
- [184] Y. C. Jun, K. C. Y. Huang, and M. L. Brongersma. Plasmonic beaming and active control over fluorescent emission. *Nature communications*, 2:283, 2011.

- [185] I. Berline, C. Royal, L. Douillard, F. Charra, and C. Fiorini-Debuisschert. Stm induced second harmonic generation: towards near-field nonlinear optical microscopy. In *Nanophotonics II*, volume 6988, page 69880M. International Society for Optics and Photonics, 2008.
- [186] C. Sentein, C. Fiorini, A. Lorin, L. Sicot, and J-M. Nunzi. Study of orientation induced molecular rectification in polymer films. *Optical Materials*, 9(1-4):316–322, 1998.
- [187] K. Becker, J. M. Lupton, J. Müller, A. L. Rogach, D. V. Talapin, H. Weller, and J. Feldmann. Electrical control of förster energy transfer. *Nature Materials*, 5(10):777, 2006.
- [188] S-J. Park, S. Link, W. L. Miller, A. Gesquiere, and P. F. Barbara. Effect of electric field on the photoluminescence intensity of single cdse nanocrystals. *Chemical Physics*, 341(1-3):169–174, 2007.
- [189] L. De Sio, A. Cunningham, V. Verrina, C. M. Tone, R. Caputo, T. Bürgi, and C. Umeton. Double active control of the plasmonic resonance of a gold nanoparticle array. *Nanoscale*, 4(24):7619–7623, 2012.
- [190] F Watt, A. A. Bettiol, J. A. Van Kan, E. J. Teo, and M. B. H. Breese. Ion beam lithography and nanofabrication: a review. *International Journal of Nanoscience*, 4(03):269–286, 2005.
- [191] R. Gauderon, P. B. Lukins, and C. J. R. Sheppard. Effect of a confocal pinhole in two-photon microscopy. *Microscopy research and technique*, 47(3):210–214, 1999.
- [192] S. Viarbitskaya, A. Teulle, R. Marty, J. Sharma, C. Girard, A. Arbouet, and E. Dujardin. Tailoring and imaging the plasmonic local density of states in crystalline nanoprisms. *Nature Materials*, 12(5):426, 2013.
- [193] N. D. Lang and W. Kohn. Theory of metal surfaces: induced surface charge and image potential. *Physical Review B*, 7(8):3541, 1973.
- [194] C. T. Black and J. J. Welser. Electric-field penetration into metals: consequences for high-dielectric-constant capacitors. *IEEE Transactions on Electron Devices*, 46(4):776–780, 1999.
- [195] R. R. Kumal, T. E. Karam, and L. H. Haber. Determination of the surface charge density of colloidal gold nanoparticles using second harmonic generation. *The Journal of Physical Chemistry C*, 119(28):16200–16207, 2015.
- [196] J. B. Khurgin. How to deal with the loss in plasmonics and metamaterials. *Nature nanotechnology*, 10(1):2, 2015.
- [197] J. B. Khurgin. Hot carriers generated by plasmons: where are they generated and where do they go from there? *Faraday Discussion*, pages 1–24, 2019.
- [198] C. López-Bastidas, J. A. Maytorena, and A. Liebsch. Hot-electron dynamics at noble metal surfaces. *Physical Review B*, 65(3):035417, 2001.
- [199] C. López-Bastidas. Thermalization time of noble metal nanoparticles: effects of the electron density profile. *The European Physical Journal B*, 85(2):79, 2012.
- [200] V. T. Binh and N. Garcia. Atomic metallic ion emission, field surface melting and scanning tunneling microscopy tips. *Journal de Physique I*, 1(5):605–612, 1991.

Bibliography

- [201] L. de Knoop, M. J. Kuisma, J. Löfgren, K. Lodewijks, M. Thuvander, P. Erhart, A. Dmitriev, and E. Olsson. Electric-field-controlled reversible order-disorder switching of a metal tip surface. *Physical Review Materials*, 2(8):085006, 2018.
- [202] A. V. Lugovskoy and I. Bray. Ultrafast electron dynamics in metals under laser irradiation. *Physical Review B*, 60(5):3279, 1999.
- [203] A. P. Kanavin, I. V. Smetanin, V. A. Isakov, Yu. V. Afanasiev, B. N. Chichkov, B. Wellegehausen, S. Nolte, C. Momma, and A. Tünnermann. Heat transport in metals irradiated by ultrashort laser pulses. *Physical Review B*, 57:14698–14703, 1998.
- [204] M. Zapata Herrera, J. Aizpurua, A. K. Kazansky, and A. G. Borisov. Plasmon response and electron dynamics in charged metallic nanoparticles. *Langmuir*, 32(11):2829–2840, 2016.
- [205] R. W. Schoenlein, W. Z. Lin, J. G. Fujimoto, and G. L. Eesley. Femtosecond studies of nonequilibrium electronic processes in metals. *Physical Review Letters*, 58(16):1680, 1987.
- [206] M. B. Agranat, S. I. Ashitkov, A. V. Ovchinnikov, D. S. Sitnikov, A. A. Yurkevich, O. V. Chefonov, L. T. Perel'man, S. I. Anisimov, and V. E. Fortov. Thermal emission of hot electrons in a metal. *JETP letters*, 101(9):598–602, 2015.
- [207] J. G. Mihaychuk, J. Bloch, Y. Liu, and H. M. Van Driel. Time-dependent second-harmonic generation from the si-sio₂ interface induced by charge transfer. *Optics Letters*, 20(20):2063–2065, 1995.
- [208] P. Pantazis, J. Maloney, D. Wu, and S. E. Fraser. Second harmonic generating (shg) nanopropes for in vivo imaging. *Proceedings of the National Academy of Sciences*, 107(33):14535–14540, 2010.
- [209] Y. Maneglia. *Analyse en profondeur des défauts de l'interface Si-SiO₂ par la technique du pompage de charges*. PhD thesis, Institut National Polytechnique de Grenoble-INPG, 1998.
- [210] M. J. A. Smith, B. T. Kuhlmeier, C. M. de Sterke, C. Wolff, M. Lapine, and C. G. Poulton. Electrostriction enhancement in metamaterials. *Physical Review B*, 91(21):214102, 2015.
- [211] C. Lumdee, B. Yun, and P. G. Kik. Effect of surface roughness on substrate-tuned gold nanoparticle gap plasmon resonances. *Nanoscale*, 7:4250–4255, 2015.
- [212] L. de Knoop, F. Houdellier, C. Gatel, A. Masseboeuf, M. Monthieux, and M. Hÿtch. Determining the work function of a carbon-cone cold-field emitter by in situ electron holography. *Micron*, 63:2 – 8, 2014. David J.H. Cockayne.
- [213] R. C. Miller. Optical second harmonic generation in piezoelectric crystals. *Applied Physics Letters*, 5(1):17–19, 1964.
- [214] C. Matranga and P. Guyot-Sionnest. Absolute intensity measurements of the optical second-harmonic response of metals from 0.9 to 2.5 eV. *The Journal of Chemical Physics*, 115(20):9503–9512, 2001.
- [215] C. Garrett and F. Robinson. Miller's phenomenological rule for computing nonlinear susceptibilities. *IEEE Journal of Quantum Electronics*, 2(8):328–329, 1966.

- [216] B. Metzger, T. Schumacher, M. Hentschel, M. Lippitz, and H. Giessen. Third harmonic mechanism in complex plasmonic fano structures. *ACS photonics*, 1(6):471–476, 2014.
- [217] M. Hentschel, T. Utikal, H. Giessen, and M. Lippitz. Quantitative modeling of the third harmonic emission spectrum of plasmonic nanoantennas. *Nano Letters*, 12(7):3778–3782, 2012.
- [218] K. O’Brien, H. Suchowski, J. Rho, A. Salandrino, B. Kante, X. Yin, and X. Zhang. Predicting nonlinear properties of metamaterials from the linear response. *Nature Materials*, 14(4):379, 2015.
- [219] J. Butet and O. J. F. Martin. Evaluation of the nonlinear response of plasmonic metasurfaces: Miller’s rule, nonlinear effective susceptibility method, and full-wave computation. *Journal of the Optical Society of America B*, 33(2):A8–A15, 2016.
- [220] M. D. Wissert, A. W. Schell, K. S. Ilin, M. Siegel, and H-J. Eisler. Nanoengineering and characterization of gold dipole nanoantennas with enhanced integrated scattering properties. *Nanotechnology*, 20(42):425203, 2009.
- [221] S. Viarbitskaya, O. Demichel, B. Cluzel, G. Colas des Francs, and A. Bouhelier. Delocalization of nonlinear optical responses in plasmonic nanoantennas. *Physical Review Letters*, 115:197401, 2015.
- [222] A. de Hoogh, A. Opheij, Ma. Wulf, N. Rotenberg, and L. Kuipers. Harmonics generation by surface plasmon polaritons on single nanowires. *ACS Photonics*, 3(8):1446–1452, 2016.
- [223] U. Kumar, S. Viarbitskaya, A. Cuche, C. Girard, S. Bolisetty, R. Mezzenga, G. Colas des Francs, A. Bouhelier, and E. Dujardin. Designing plasmonic eigenstates for optical signal transmission in planar channel devices. *ACS Photonics*, 5(6):2328–2335, 2018.
- [224] D. K. Gramotnev and S. I. Bozhevolnyi. Plasmonics beyond the diffraction limit. *Nature Photonics*, 4:83–91, 2010.
- [225] S. Lal, S. Link, and N. J. Halas. Nano-optics from sensing to waveguiding. *Nature Photonics*, 1:641–648, 2007.
- [226] M. Song, A. Bouhelier, P. Bramant, J. Sharma, E. Dujardin, D. Zhang, and G. Colas des Francs. Imaging Symmetry-Selected Corner Plasmon Modes in Penta-Twinned Crystalline Ag Nanowires. *ACS Nano*, 5(7):5874–5880, 2011.
- [227] P. Johns, G. Beane, K. Yu, and G. V. Hartland. Dynamics of surface plasmon polaritons in metal nanowires. *The Journal of Physical Chemistry C*, 121(10):5445–5459, 2017.
- [228] N. Coca-López, N. F. Hartmann, T. Mancabelli, J. Kraus, S. Günther, A. Comin, and A. Hartschuh. Remote excitation and detection of surface-enhanced raman scattering from graphene. *Nanoscale*, 10:10498–10504, 2018.
- [229] A. Dasgupta, D. Singh, and G. V. P. Kumar. Dual-path remote-excitation surface enhanced raman microscopy with plasmonic nanowire dimer. *Applied Physics Letters*, 103(15):151114, 2013.
- [230] A. Prymaczek, M. Cwierzona, J. Grzelak, D. Kowalska, M. Nyk, S. Mackowski, and D. Piatkowski. Remote activation and detection of up-converted luminescence via surface plasmon polaritons propagating in a silver nanowire. *Nanoscale*, 10(26):12841–12847, 2018.

Bibliography

- [231] C. Hubert, L. Billot, P-M. Adam, R. Bachelot, P. Royer, J. Grand, D. Gindre, K. D. Dorkenoo, and A. Fort. Role of surface plasmon in second harmonic generation from gold nanorods. *Applied physics letters*, 90(18):181105, 2007.
- [232] G. Schider, J. R. Krenn, A. Hohenau, H. Ditlbacher, A. Leitner, F. R. Aussenegg, W. L. Schaich, I. Puscasu, B. Monacelli, and G. Boreman. Plasmon dispersion relation of au and ag nanowires. *Physical Review B*, 68:155427, 2003.
- [233] T. Shegai, V. D. Miljkovic, K. Bao, H. Xu, P. Nordlander, P. Johansson, and M. Kall. Unidirectional broadband light emission from supported plasmonic nanowires. *Nano Letters*, 11(2):706–711, 2011.
- [234] Y. Peng and K. Kempa. Controlling light propagation with nanowires. *Applied Physics Letters*, 100(17):171903, 2012.
- [235] H. Wei, D. Pan, S. Zhang, Z. Li, Q. Li, N. Liu, W. Wang, and H. Xu. Plasmon waveguiding in nanowires. *Chemical reviews*, 118(6):2882–2926, 2018.
- [236] E. Kretschmann. Die bestimmung optischer konstanten von metallen durch anregung von oberflächenplasmaschwingungen. *Zeitschrift für Physik A Hadrons and nuclei*, 241(4):313–324, 1971.
- [237] A. Otto. Excitation of nonradiative surface plasma waves in silver by the method of frustrated total reflection. *Zeitschrift für Physik A Hadrons and nuclei*, 216(4):398–410, 1968.
- [238] M. Allione, V. V. Temnov, Y. Fedutik, U. Woggon, and M. V. Artemyev. Surface plasmon mediated interference phenomena in low-q silver nanowire cavities. *Nano Letters*, 8(1):31–35, 2008. PMID: 18052228.
- [239] T. Shegai, Y. Huang, H. Xu, and M. Käll. Coloring fluorescence emission with silver nanowires. *Applied Physics Letters*, 96(10):103114, 2010.
- [240] Z. Fang, L. Fan, C. Lin, D. Zhang, A. J. Meixner, and X. Zhu. Plasmonic coupling of bow tie antennas with ag nanowire. *Nano Letters*, 11(4):1676–1680, 2011.
- [241] J-C. Weeber, A. Dereux, C. Girard, J. R. Krenn, and J-P. Goudonnet. Plasmon polaritons of metallic nanowires for controlling submicron propagation of light. *Physical Review B*, 60(12):9061, 1999.
- [242] D. Singh, M. Raghuvanshi, and G. V. P. Kumar. Propagation of light in serially coupled plasmonic nanowire dimer: Geometry dependence and polarization control. *Applied Physics Letters*, 101(11):111111, 2012.
- [243] M. W. Knight, N. K Grady, R. Bardhan, F. Hao, P. Nordlander, and N. J. Halas. Nanoparticle-mediated coupling of light into a nanowire. *Nano Letters*, 7(8):2346–2350, 2007.
- [244] A. W. Sanders, D. A. Routenberg, B. J. Wiley, Y. Xia, E. R. Dufresne, and M. A. Reed. Observation of plasmon propagation, redirection, and fan-out in silver nanowires. *Nano Letters*, 6(8):1822–1826, 2006.
- [245] R. M. Dickson and L. A. Lyon. Unidirectional plasmon propagation in metallic nanowires. *The Journal of Physical Chemistry B*, 104(26):6095–6098, 2000.

- [246] M. Song, J. Dellinger, O. Demichel, M. Buret, G. Colas des Francs, D. Zhang, E. Dujardin, and A. Bouhelier. Selective excitation of surface plasmon modes propagating in ag nanowires. *Optics express*, 25(8):9138–9149, 2017.
- [247] P. Venugopalan, X. Lu Q. Zhang, and M. Gu. Polarization-sensitive characterization of the propagating plasmonic modes in silver nanowire waveguide on a glass substrate with a scanning near-field optical microscope. *Optics Express*, 21:15247–15252, 2013.
- [248] Z. Li, K. Bao, Y. Fang, Y. Huang, P. Nordlander, and H. Xu. Correlation between incident and emission polarization in nanowire surface plasmon waveguides. *Nano Letters*, 10(5):1831–1835, 2010. PMID: 20369891.
- [249] A. B. and G. P. W. Surface plasmon rainbow jet. *Optics Letters*, 30:884, 2005.
- [250] J. R. Lombardi and R. L. Birke. A unified view of surface-enhanced raman scattering. *Accounts of Chemical Research*, 42(6):734–742, 2009.
- [251] R. Chikkaraddy, D. Singh, and G. V. P. Kumar. Plasmon assisted light propagation and raman scattering hot-spot in end-to-end coupled silver nanowire pairs. *Appl. Phys. Lett.*, 100(4):043108, 2012.
- [252] H. Raether. *Surface Plasmons on Smooth and Rough Surfaces and on Gratings*, volume 111 of *Springer Tracts in Modern Physics*. Springer-Verlag, 1988.
- [253] P. Geisler, E. Krauss, G. Razinskas, and B. Hecht. Transmission of plasmons through a nanowire. *ACS Photonics*, 4(7):1615–1620, 2017.
- [254] B. Wild, L. Cao, Y. Sun, B. P. Khanal, E. R. Zubarev, S. K. Gray, N. F. Scherer, and M. Pelton. Propagation lengths and group velocities of plasmons in chemically synthesized gold and silver nanowires. *ACS Nano*, 6(1):472–482, 2012.
- [255] Y. Huang, Y. Fang, and M. Sun. Remote excitation of surface-enhanced raman scattering on single au nanowire with quasi-spherical termini. *The Journal of Physical Chemistry C*, 115:3558–3561, 2011.
- [256] A. Bouhelier and G. P. Wiederrecht. Excitation of broadband surface plasmon polaritons: Plasmonic continuum spectroscopy. *Physical Review B*, 71:195406, 2005.
- [257] T. H. Taminiau, F. D. Stefani, and N. F. van Hulst. Optical nanorod antennas modeled as cavities for dipolar emitters: Evolution of sub- and super-radiant modes. *Nano Letters*, 11(3):1020–1024, 2011.
- [258] E. Verhagen, M. Spasenović, A. Polman, and L. K. Kuipers. Nanowire plasmon excitation by adiabatic mode transformation. *Physical Review Letters*, 102:203904, 2009.
- [259] J. J. Baumberg, T. A. Kelf, Y. Sugawara, S. Cintra, M. E. Abdelsalam, P. N. Bartlett, and A. E. Russell. Angle-resolved surface-enhanced raman scattering on metallic nanostructured plasmonic crystals. *Nano Letters*, 5(11):2262–2267, 2005.
- [260] D. Piatkowski, N. Hartmann, T. Macabelli, M. Nyk, S. Mackowski, and A. Hartschuh. Silver nanowires as receiving-radiating nanoantennas in plasmon-enhanced up-conversion processes. *Nanoscale*, 7(4):1479–1484, 2015.

Bibliography

- [261] D. K. Sharma, S. K. Chaubey, A. B. Vasista, J. J. Karumancheril, R. P. N. Tripathi, A. Bouhelier, and G. V. P. Kumar. Directional second-harmonic generation controlled by sub-wavelength facets of an organic mesowire. *Applied optics*, 57(21):5914–5922, 2018.
- [262] A. B. Vasista, D. K. Sharma, and G. V. P. Kumar. Fourier plane optical microscopy and spectroscopy. *digital Encyclopedia of Applied Physics*, pages 1–14, 2018.
- [263] L. Dai, I. Gregor, I. von der Hocht, T. Ruckstuhl, and J. Enderlein. Measuring large numerical apertures by imaging the angular distribution of radiation of fluorescing molecules. *Optics express*, 13(23):9409–9414, 2005.
- [264] H. Weyl. Ausbreitung elektromagnetischer wellen über einem ebenen leiter. *Annalen der Physik*, 365(21):481–500, 1919.
- [265] N. Hartmann. *Coupling of emitters to surface plasmons investigated by back focal plane microscopy*. PhD thesis, lmu, 2013.
- [266] N. Coca López. *Confocal and antenna-enhanced microscopy and spectroscopy of graphene*. PhD thesis, lmu, 2018.
- [267] N. Hartmann, D. Piatkowski, R. Ciesielski, S. Mackowski, and A. Hartschuh. Radiation channels close to a plasmonic nanowire visualized by back focal plane imaging. *ACS Nano*, 7(11):10257–10262, 2013.
- [268] K. Hassan, A. Bouhelier, T. Bernardin, G. Colas des Francs, J-C. Weeber, A. Dereux, and R. Espiau de Lamaestre. Momentum-space spectroscopy for advanced analysis of dielectric-loaded surface plasmon polariton coupled and bent waveguides. *Physical Review B*, 87:195428, 2013.
- [269] Z. Wang, H. Wei, D. Pan, and H. Xu. Controlling the radiation direction of propagating surface plasmons on silver nanowires. *Laser & Photonics Reviews*, 4:596–601, 2014.
- [270] N. Moll, R. Harbers, R. F. Mahrt, and G-L. Bona. Integrated all-optical switch in a cross-waveguide geometry. *Applied physics letters*, 88(17):171104, 2006.
- [271] Y. Fang, Z. Li, Y. Huang, S. Zhang, P. Nordlander, N. J. Halas, and H. Xu. Branched silver nanowires as controllable plasmon routers. *Nano Letters*, 10(5):1950–1954, 2010.
- [272] Y. Zhang, Y. Zhang, and B. Li. Optical switches and logic gates based on self-collimated beams in two-dimensional photonic crystals. *Optics Express*, 15(15):9287–9292, 2007.
- [273] X. Guo, M. Qiu, J. Bao, B. J. Wiley, Q. Yang, X. Zhang, Y. Ma, H. Yu, and L. Tong. Direct coupling of plasmonic and photonic nanowires for hybrid nanophotonic components and circuits. *Nano Letters*, 9(12):4515–4519, 2009. PMID: 19995088.
- [274] S. Lal, J. H. Hafner, N. J. Halas, S. Link, and P. Nordlander. Noble metal nanowires: from plasmon waveguides to passive and active devices. *Accounts of Chemical Research*, 45(11):1887–1895, 2012.
- [275] U. Kumar. *Plasmon logic gates designed by modal engineering of 2-dimensional crystalline metal cavities*. PhD thesis, 2017.
- [276] H. Wei, Z. Wang, X. Tian, M. Käll, and H. Xu. Cascaded logic gates in nanophotonic plasmon networks. *Nature communications*, 2:387, 2011.

- [277] F. Dell’Ova. Nanofabrication et caractérisation optique de cavités plasmoniques modales. Master’s thesis, Institut national des sciences appliquées de Toulouse, Toulouse, 2019.
- [278] X. Xiong, C-L. Zou, X-F. Ren, A-P. Liu, Y-X. Ye, F-W. Sun, and G-C. Guo. Silver nanowires for photonics applications. *Laser & Photonics Reviews*, 7(6):901–919, 2013.
- [279] I. Yoon, T. Kang, W. Choi, J. Kim, Y. Yoo, S-W. Joo, Q-H. Park, H. Ihee, and B. Kim. Single nanowire on a film as an efficient sers-active platform. *Journal of the American Chemical Society*, 131(2):758–762, 2008.
- [280] Y. Sun, Y. Yin, B. T. Mayers, T. Herricks, and Y. Xia. Uniform silver nanowires synthesis by reducing AgNO_3 with ethylene glycol in the presence of seeds and poly (vinyl pyrrolidone). *Chemistry of Materials*, 14(11):4736–4745, 2002.
- [281] S. Nauert, A. Paul, Y-R. Zhen, D. Solis Jr, L. Vigderman, W-S. Chang, E. R. Zubarev, P. Nordlander, and S. Link. Influence of cross sectional geometry on surface plasmon polariton propagation in gold nanowires. *ACS nano*, 8(1):572–580, 2013.
- [282] H. Yang, M. Qiu, and Q. Li. Identification and control of multiple leaky plasmon modes in silver nanowires. *Laser & Photonics Reviews*, 10(2):278–286, 2016.
- [283] D. Solis Jr, W-S. Chang, B. P. Khanal, K. Bao, P. Nordlander, E. R. Zubarev, and S. Link. Bleach-imaged plasmon propagation (blipp) in single gold nanowires. *Nano Letters*, 10(9):3482–3485, 2010.
- [284] A. Drezet, A. Hohenau, D. Koller, A. Stepanov, H. Ditlbacher, B. Steinberger, F. R. Aussenegg, A. Leitner, and J. R. Krenn. Leakage radiation microscopy of surface plasmon polaritons. *Materials science and engineering: B*, 149(3):220–229, 2008.
- [285] A. Hohenau, J. R. Krenn, A. Drezet, O. Mollet, S. Huant, C. Genet, B. Stein, and T. W. Ebbesen. Surface plasmon leakage radiation microscopy at the diffraction limit. *Optics express*, 19(25):25749–25762, 2011.
- [286] D. G Zhang, X. Yuan, and A. Bouhelier. Direct image of surface-plasmon-coupled emission by leakage radiation microscopy. *Applied optics*, 49(5):875–879, 2010.
- [287] L. Zhu, D. Zhang, R. Wang, X. Wen, P. Wang, H. Ming, R. Badugu, and J. R. Lakowicz. Out-of-focal plane imaging by leakage radiation microscopy. *Journal of Optics*, 19(9):095004, 2017.
- [288] D. Zhang, Y. Xiang, J. Chen, J. Cheng, L. Zhu, R. Wang, G. Zou, P. Wang, H. Ming, M. Rosenfeld, et al. Extending the propagation distance of a silver nanowire plasmonic waveguide with a dielectric multilayer substrate. *Nano Letters*, 18(2):1152–1158, 2018.
- [289] M. Song. *Surface plasmon propagation in silver nanowires*. PhD thesis, université de Bourgogne, 2012.
- [290] S. Zhang and H. Xu. Optimizing substrate-mediated plasmon coupling toward high-performance plasmonic nanowire waveguides. *Acs Nano*, 6(9):8128–8135, 2012.
- [291] Z. Jia, H. Wei, D. Pan, and H. Xu. Direction-resolved radiation from polarization-controlled surface plasmon modes on silver nanowire antennas. *Nanoscale*, 8(48):20118–20124, 2016.

Bibliography

- [292] M. Song, A. Stolz, D. Zhang, J. Arocas, L. Markey, G. Colas des Francs, E. Dujardin, and A. Bouhelier. Evaluating plasmonic transport in current-carrying silver nanowires. *Journal of Visualized Experiments*, (82):e51048, 2013.